

PSFC/RR-03-2

DOE-ET-54512-345

**Physics and Application of Impurity Plume Dispersal
as an Edge Plasma Flow Diagnostic on
the Alcator C-Mod Tokamak**

S. Gangadhara

March 2003

Plasma Science and Fusion Center
Massachusetts Institute of Technology
Cambridge, MA 02139 USA

This work was supported by the U.S. Department of Energy, Cooperative Grant No. DE-FC02-99ER54512. Reproduction, translation, publication, use and disposal, in whole or in part, by or for the United States government is permitted.

**Physics and Application of Impurity Plume
Dispersal as an Edge Plasma Flow Diagnostic on
the Alcator C-Mod Tokamak**

by

Sanjay Gangadhara

B.S., Chemical Engineering and Nuclear Engineering (1994)
University of California, Berkeley

Submitted to the Department of Nuclear Engineering
in partial fulfillment of the requirements for the degree of
Doctor of Philosophy in Nuclear Science and Engineering

at the

MASSACHUSETTS INSTITUTE OF TECHNOLOGY

June 2003

© Massachusetts Institute of Technology 2003. All rights reserved.

Author
Department of Nuclear Engineering
February 19, 2003

Certified by
Brian LaBombard
Research Scientist, Plasma Science and Fusion Center
Thesis Supervisor

Read by
Ian H. Hutchinson
Professor of Nuclear Engineering
Thesis Reader

Accepted by
Jeffrey A. Coderre
Chairman, Department Committee on Graduate Students

Physics and Application of Impurity Plume Dispersal as an Edge Plasma Flow Diagnostic on the Alcator C-Mod Tokamak

by

Sanjay Gangadhara

Submitted to the Department of Nuclear Engineering
on February 19, 2003, in partial fulfillment of the
requirements for the degree of
Doctor of Philosophy in Nuclear Science and Engineering

Abstract

A unique system has been developed for studying impurity transport in the edge plasma of Alcator C-Mod. Impurity gas (which for these experiments is deuterated ethylene, C_2D_4) is injected locally into the scrape-off layer (SOL) through the end of a reciprocating fast-scanning probe, and the resultant emission (“plume”) is imaged from two near-perpendicular views. Plumes are generated at various SOL depths, while views are obtained using coherent fiber bundles optically coupled to gated, intensified CCD cameras through beam-splitters, allowing for the simultaneous acquisition of C^{+1} and C^{+2} emission.

Plume structure is observed to depend on local values of electron density and temperature, background parallel flow (v_{\parallel}), and radial electric field (\mathbf{E}_r). Emission resulting from sputtering of carbon deposited on the probe surface also contributes to the structure. For plumes generated in the near SOL, emission contours are non-elliptical and the parallel extent relative to the ionization mean-free path is large, indicating that transport of impurities near the probe is “jet”-like along \mathbf{B} . Plume results also suggest an elongation of the impurity ion density down the probe axis.

A Monte Carlo impurity transport code (LIM) was used to simulate the plumes. Results indicate that contributions to the emission from sputtering explain the cross-field plume width, and that the parallel extent of emission generated in the far SOL is well-described using a sputter launch-energy distribution for the impurities. In the near SOL, the presence of a localized parallel electric field arising from background ion recycling off the probe surface is necessary to explain the parallel extent of emission generated in this region. This electric field accelerates impurity ions formed near the probe tip away from the probe, causing jet-like behavior. LIM was also used to investigate causes for the vertical elongation of the impurity emission. Results suggest the existence of a probe-induced $\mathbf{E} \times \mathbf{B}$ drift, of order ~ 1000 m/s in the near SOL. This drift may be responsible for the transport of both impurity and bulk plasma ions down the probe axis.

Values for v_{\parallel} in the far SOL and \mathbf{E}_r in the near SOL have been extracted from the plume structure. A comparison between plume and probe results for \mathbf{E}_r suggests that calculations which employ a probe-sheath model may be in error, and that measurement of the poloidal propagation velocity of edge plasma fluctuations may be a more reliable means of inferring \mathbf{E}_r from probe data. Comparisons between plume- and probe-inferred values for the parallel Mach number suggest that the probe overestimates parallel flow to the divertor in the far SOL, where effects of short field line connection to the divertor are important. This result strengthens the argument for the main-chamber recycling view of particle flows in the Alcator C-Mod SOL.

Thesis Supervisor: Brian LaBombard

Title: Research Scientist, Plasma Science and Fusion Center

Acknowledgments

Where to begin. The process of obtaining a thesis has been one of the most difficult tasks I've ever undertaken. Without the support of a number of people, there is no way I would have finished. Here I take my opportunity to thank them.

First, my thanks to the entire Alcator C-Mod team. The hours spent by machinists, electricians, and vacuum specialists helping me to fix and optimize the design of various diagnostic components were innumerable. I would especially like to thank Josh Stillerman for his role in developing software for the plume imaging system. One of the wonderful things about working here was how comfortable I felt about approaching any of the research staff with questions, and special thanks are due to Drs. Bruce Lipschultz, Jim Terry, Spencer Pitcher, Earl Marmar, Robert Granetz, and Martin Greenwald for the many insights they supplied. Prof. Ian Hutchinson provided continuous financial support throughout my struggles, and his advice and counsel were valuable assets during my stay here. Kathy Powers and Jason Thomas at the PSFC Library were always available to answer questions and help me track down information. Any questions about faxes or mailings, reports or deadline, and I could always call on Valerie Censabella for assistance.

My deepest and most sincere thanks go to my advisor, Dr. Brian LaBombard. His contributions to this work, and to my entire learning experience while at M.I.T., were invaluable. I have come to the conclusion that he has more patience than anyone I have ever known, for during times when I was making no progress, confused and in despair, he was always ready with a new idea, and an unwavering commitment to solve the problem. I always went into his office with the phrase "I have a quick question", and more often than not would leave hours later, having come out with a greater understanding of physics and a renewed energy to move forward. I will always appreciate the time and effort that he gave to me during this process.

Thanks are also due to Steve Lisgo and Drs. Peter Stangeby and David Elder of the University of Toronto for their assistance in implementing LIM for plume simulations. They always answered my questions promptly and patiently, and as a result of our

discussions my knowledge of impurity transport physics has substantially improved.

During my time at the PSFC, I benefitted greatly from discussions with fellow graduate students, including Rob Nachtrieb, Jeff Schachter, Darren Garnier, Joe Sorci, Dmitri Pappas, Damien Hicks, Chris Boswell, Howard Yuh, and Jerry Hughes. These conversations were on range of topics, from plasma physics to human nature, and I learned a lot and laughed a lot as a result of them. I especially want to thank Rob, Chris, and Howard, for their time spent answering the many, many questions that I always seemed to come up with.

My experience in Boston was not limited to the PSFC, and I want to acknowledge a few of the many people who helped me enjoy the other side of life. Thanks to my roommates Ashok, Brent, Matt, Rohit, and Heather, who put up with my rantings when I came home from lab, and were always there to watch the game with me. Special thanks to Ashok, Sangeetha, Vikram, Nilesh, Rashmi, Vyju, Sandhya and Saritha, who helped me celebrate during the good times and provided moral support during the bad times, whether in person or over the phone.

Finally, my deepest thanks go to my mother, father, and brothers Sunil and Sandeep for their support throughout this time. Without their love and encouragement, I would not be where I am today.

Contents

1	Introduction	23
1.1	Background	24
1.1.1	Confinement Requirements	24
1.1.2	Magnetic Confinement Fusion Devices	26
1.1.3	Edge Plasmas	30
1.1.4	Impurities	33
1.2	Open Questions	34
1.2.1	“Plume” studies	38
1.2.2	Uniqueness of studies using GIFSP	40
1.3	Goals & Outline of Thesis	41
2	Diagnostic Hardware	45
2.1	Gas-Injecting Fast-Scanning Probe	45
2.1.1	Injection parameters	47
2.2	Probe views	50
2.2.1	Periscope design	50
2.2.2	Fiber bundles	55
2.2.3	Cameras	57
2.2.4	Beam-splitters	58
2.2.5	Image capture & Acquisition	62
2.3	In-vessel system integration	62
2.3.1	Relative & Absolute calibration	63
2.3.2	Distortion correction	70

2.3.3	Absolute view alignment	73
2.4	Image analysis	73
2.4.1	Generating plumes	76
2.4.2	Brightness calibration & uncertainties	78
2.4.3	Image alignment to the local magnetic field	81
2.4.4	SVC rotation correction	83
2.4.5	Moment Analysis	86
3	Plume Physics Overview	93
3.1	Experimental Observations	94
3.1.1	Typical plume characteristics	94
3.1.2	Variation of plume structure with discharge conditions	98
3.1.3	Two-source model for impurity emission	106
3.1.4	SVC/TVC asymmetry	110
3.2	Simple plume analysis	115
3.2.1	Ionization mean-free paths	115
3.2.2	Particle & Power balance	117
3.3	Plume database	123
3.3.1	Plume characterization	123
3.3.2	Variation of jet behavior with background conditions	125
3.3.3	Characteristics of plumes without jet	132
4	Plume modelling tools	135
4.1	Analytic fluid modelling	135
4.1.1	Development of 1-D & 2-D fluid models	135
4.1.2	Limitations of analytic modelling	140
4.2	LIM modelling	141
4.2.1	Code overview	142
4.2.2	Code modifications	145
4.2.3	Benchmarking	149
4.3	Generating impurity plume images in LIM	161

4.3.1	Emissivity Calculation	161
4.3.2	Determining brightness	163
4.4	Sputter source model in LIM	165
4.5	Recycling D ₂ plume simulation using LIM	169
4.6	Injected D plume simulation using LIM	174
5	Plume analysis & simulation	175
5.1	SVC/TVC plume width investigation	176
5.1.1	Carbon recycling model	176
5.1.2	Probe-induced $\mathbf{E} \times \mathbf{B}$ drifts	177
5.2	Results from Sputter Source Model	186
5.3	Possible causes for jet behavior	192
5.4	Results from density perturbation model	197
5.4.1	D ⁺ plume arising from D ₂ recycling	197
5.4.2	D ⁺ plume arising from C ₂ D ₄ injection	205
5.4.3	Density perturbation arising from injected carbon	208
5.5	Jet modelling in LIM	208
5.5.1	Parallel electric field	209
5.5.2	Jet plume results	214
5.5.3	Unresolved issues for the jet model	215
5.6	Plume modelling results	219
5.7	Plume variation with plasma conditions	223
5.7.1	Background profile variation	223
5.7.2	Poloidal flow effects	227
5.7.3	Parallel flow effects	228
5.7.4	Diffusion effects	230
5.8	Conclusions from plume analysis & simulation	231
6	Plasma flows inferred from Impurity Plumes	237
6.1	Jet-inferred $\mathbf{E} \times \mathbf{B}$ flows	237
6.1.1	Comparison with probe-inferred $\mathbf{E} \times \mathbf{B}$ flows	240

6.2	Parallel flows in the far SOL	247
7	Summary	255
7.1	Results	255
7.1.1	Diagnostics	255
7.1.2	Overview of impurity dispersal results	256
7.1.3	Probe-induced perturbations	258
7.1.4	Application of plumes as an edge flow diagnostic	260
7.2	Future Work	262
7.2.1	Diagnostic upgrades	262
7.2.2	Plume physics modelling	263
	Bibliography	265

List of Figures

1-1	Binding Energy per nucleon vs. nucleon number.	25
1-2	Fusion reaction rate parameter vs. temperature for a few reactions of interest.	27
1-3	Schematic of a typical tokamak.	28
1-4	Types of edge plasma configurations.	31
1-5	A poloidal cross-section of Alcator C-Mod, with a typical diverted equilibrium shown. Poloidal flows exist in the outboard SOL as a result of both parallel flows and $\mathbf{E} \times \mathbf{B}$ flows.	36
1-6	Example of a CIII plume generated using gas injection through an inner wall capillary.	39
2-1	Close-up views of gas-injecting scanning probe.	46
2-2	Transparent view of fast-scanning probe head assembly showing gas feed and inertial valve location.	47
2-3	Test shot illustrating timing of gas injection relative to the probe insertion.	48
2-4	Injection of C_2D_4 through the scanning probe into an empty vacuum vessel, as a part of the injection system calibration.	50
2-5	Calibration “curve” for injection of C_2D_4 through the scanning probe.	51
2-6	Cross-section of the Alcator C-Mod vacuum chamber with a typical diverted equilibrium. Gas is injected at the end of stroke of a vertically-scanning probe. Impurity emission plumes are viewed from two near-perpendicular locations.	53

2-7	Layout of F-horizontal flange, indicating location of F-side persicope.	54
2-8	Calculation of the ionization mean-free path vs. electron density and temperature for C^{+1} and C^{+2} ions.	56
2-9	Schematic of a beam-splitter used to capture images of CII and CIII emission <i>simultaneously</i> at each view location.	60
2-10	Calibration curves for the SVC and TVC at a fixed pixel location. . .	65
2-11	Average vignetting fields for the SVC and TVC, used to provide a relative calibration for images obtained from each system.	66
2-12	Image of the Labsphere located at the FSP location, taken from the side view system. Using the known brightness of this source, this image may be used to provide an absolute calibration for the SVC.	67
2-13	Comparison between relative calibration results for the TVC from in-vessel calibration using a ground glass diffuser system and bench calibration using the Labsphere.	69
2-14	Image taken from the side view system of a back-illuminated grid, used for distortion correction.	71
2-15	Image taken from the top view system of a back-illuminated grid, used for distortion correction.	72
2-16	Un-distorted image from the side and top view systems of a back-illuminated grid (originals in Figures 2-14 and 2-15).	74
2-17	Superimposed alignment images from the F-side and F-top cameras. .	75
2-18	Example of exposure and image readout timing for the SVC camera system.	77
2-19	Example of a calibrated CIII SVC plume, illustrating how problems with the vignetting field affect the calibrated results.	80
2-20	Illustration of the method used to map plume emission from the TVC to field-aligned coordinates.	82
2-21	Example of CIII TVC emission which has been mapped to the image plane at the gas injection location, with corresponding field line trajectories overlaid.	83

2-22	Example of field-aligned CIII emission seen from the TVC (unaligned data shown in Figure 2-21).	84
2-23	Composite images from the SVC of an bulb placed at various locations in the vessel. Images were taken from before and after the run campaign.	85
2-24	Example of CIII SVC data exhibiting rotation.	87
2-25	Illustration of how the divot in the SVC plume data is used to determine the SVC rotation angle.	88
2-26	An example of results obtained from performing moment analysis for an experimental CIII TVC plume.	92
3-1	Typical data obtained from plume imaging system, side and top view.	95
3-2	Definition of the plume “boomerang angle”, in terms of the 1-D parallel centroid profile determined from moment analysis. This angle can be used to estimate the value of \mathbf{E}_r	97
3-3	Plumes generated at various values of electron density and temperature.	99
3-4	Plumes generated at various SOL depths.	100
3-5	Plots of the ratio of ionization time (τ_{ion}) to coulomb collision time (τ_{coul}) for C^{+1} and C^{+2}	102
3-6	Comparison between plumes formed near the separatrix during ohmic L-mode and ohmic H-mode.	104
3-7	Comparison between plumes formed in the intermediate SOL ($\rho = 4$ mm) during ohmic L-mode and ohmic H-mode.	105
3-8	Comparison between CIII SVC plumes generated inside and outside of the Quasi-Coherent (QC) mode layer during a pair of Enhanced D_α (EDA) H-mode discharges.	107
3-9	Data obtained from plume imaging system for a case with <i>no gas injection</i> , side and top view.	108
3-10	Plume images from three consecutive probe scans with no gas injection (only two for the side view, due to a problem with exposure gating for this camera during the third scan).	109

3-11 Comparison between CIII TVC plumes which exhibit varying degrees of “jet”-like behavior.	111
3-12 SVC and TVC CIII brightness data for a plume generated in the near SOL, illustrating the asymmetry in cross-field extent between the two views.	112
3-13 Comparisons between 1-D cross-field brightness profiles for CIII SVC and TVC data shown in Figure 3-12.	114
3-14 Variation of C^{+2} parallel mean-free path with electron density, for five different values of electron temperature (ranging from 15-50 eV).	116
3-15 Ratio of C^{+2} to C^{+1} ionization times as a function of electron temperature.	117
3-16 Parallel profiles of electron temperature calculated from a two-point model, for cases with and without gas injection. Conditions typical of both the near and far SOL are considered.	122
3-17 Plot of electron temperature vs. parallel Mach number for all points in the plume database.	124
3-18 An example of “ridge-line” analysis for a CIII TVC plume.	126
3-19 A plot of the potential drop inferred from ridge-line analysis vs. electron temperature for all points in the plume database.	127
3-20 A plot of normalized potential drop vs. ionization mean-free path of atomic deuterium for all plumes in the database.	129
3-21 Normalized plume asymmetry vs. parallel Mach number inferred from probe measurements, labeled by cross-field width and least-squares difference parameter.	130
3-22 Normalized plume asymmetry vs. parallel Mach number inferred from probe measurements, labeled by toroidal field direction.	131
3-23 Comparison between CII plume generated by injection through a capillary at the inner wall midplane and a CII plume generated by injection through the probe in the far SOL.	133

4-1	Comparison of normalized 1-D impurity density profiles with and without diffusion effects.	137
4-2	Fit to a 1-D cross-field brightness profile from a CIII TVC plume (the full plume is shown in Figure 3-8).	139
4-3	Schematic of the FSP probe head geometry implemented in LIM.	146
4-4	Parallel profiles of n_e , v_{\parallel} , and E_{\parallel} in the probe presheath.	150
4-5	Comparison between analytic and simulation results of a simple diffusion model test.	152
4-6	Comparison of CIII 1-D parallel profiles for two different radial bin sizes (1 mm vs. 2 mm).	155
4-7	Plot of the approximate ratio of the velocity diffusivity calculated from the NRL Plasma Formulary to the value calculated in LIM vs. $m_I T_{iB}/m_B T_I$	159
4-8	Plot of the velocity diffusivity calculated from the NRL Plasma Formulary including parallel drifts vs. parallel drift velocity.	160
4-9	Simple schematic illustrating the definition of the angles χ and β , used to determine the orientation of the velocity vector (\hat{v}) for a sputtered particle relative to the surface normal (\hat{n}) for a Thompson distribution.	168
4-10	Plot of the total current collected by the probe vs. the current density decay length.	173
5-1	Comparison between simulated CIII SVC 2-D plume emission for cases with and without carbon recycling off the probe surface.	178
5-2	Schematic of the probe geometry indicating the direction of the electric field which results from probe-induced variations in the plasma potential near the probe surface.	179
5-3	Schematic which illustrates the possible effect of a circulating $\mathbf{E} \times \mathbf{B}$ drift on the impurity ion distribution.	180

5-4	CIII SVC and TVC plumes for a simulation in which a vertical impurity ion drift has been included and the electron density has been assumed constant in the calculation of the emission excitation rate.	182
5-5	Comparison between simulated and experimental 1-D cross-field profiles of normalized brightness for the SVC and TVC. A vertical impurity ion drift has been included in the simulation, and the electron density has been assumed constant in the calculation of the emission excitation rate.	183
5-6	Comparison between simulated and experimental 1-D cross-field profiles of normalized brightness for the SVC and TVC. A vertical impurity ion drift has been included in the simulation, and the measured electron density profile has been used in the calculation of the emission excitation rate.	185
5-7	Comparison of simulated CIII TVC plumes for two values of λ (3, 12 mm).	189
5-8	Comparison between experimental and simulated CIII TVC plumes, where simulation results were generated using the non-jet background/sputter source model.	190
5-9	Comparison of 1-D CIII TVC parallel emission profiles for a pair of simulation runs in which the electron density was varied. The non-jet background/sputter source model was used in both cases.	193
5-10	Comparison between experimental and simulated CIII TVC plume results in the far SOL plasma using the non-jet background/sputter source model.	194
5-11	Schematic illustrating the process of background ion recycling off the probe surface.	196
5-12	Surface plots of the total electron density (background plus recycling-induced) at two radial coordinates ($x = 0$ mm and $x = -2$ mm), for conditions typical of the near SOL.	199

5-13	Plot of the electron density resulting from deuterium recycling vs. parallel coordinate for the field line passing above the probe tip. In this case, n_e and T_e profiles typical of the near SOL were used as inputs.	200
5-14	Parallel variation of the plasma potential and electric field resulting from ion recycling off the probe surface.	201
5-15	Plot of the electron density resulting from deuterium recycling vs. parallel coordinate for the field line passing above the probe tip. For this case, the parallel electric field shown in Figure 5-14 is included in the simulation to estimate its effect on the resulting density distribution.	203
5-16	Plot of the electron density resulting from deuterium recycling vs. parallel coordinate for the field line passing above the probe tip. In this case, n_e and T_e profiles typical of the far SOL were used as inputs.	204
5-17	Comparison between experimental and simulated profiles for the normalized potential drop vs. ionization mean-free path of deuterium neutrals recycling from the probe surface.	206
5-18	Plot of the electron density resulting from C_2D_4 injection vs. parallel coordinate for the field line passing through the gas injection location (i.e. above the probe tip).	207
5-19	Surface plots of the parallel electric field at two radial coordinates: $x = 0$ mm and $x = -2$ mm.	210
5-20	Example of a typical $E_{\parallel, pert}$ profile and its analytic fit.	211
5-21	Comparison between simulation runs in which the total potential drop experienced by the impurity ions is the same but the parallel electric field structure is different.	213
5-22	Comparison between an experimental CIII TVC plume generated in the near SOL and a simulation of the jet component of that plume.	216
5-23	Comparison between 1-D CIII TVC parallel emission profiles for experimental and numerical plumes shown in Figure 5-22.	217
5-24	Comparison between 1-D parallel emission profiles for an experimental CIII TVC plume in which two sets of calibration factors were applied.	220

5-25	Comparison between experimental and simulated CIII TVC results. The simulated plume was generated by summing together components arising from a point source launch into a jet background and a sputter source launch into a non-jet background with equal weight.	222
5-26	Comparison between simulated 2-D CII TVC plumes for cases in the near and far SOL.	224
5-27	Comparison between 2-D simulated CIII TVC plumes generated under conditions typical of the near SOL, for a case in which n_e and T_e vary with radial coordinate and a case in which these parameters are constant.	225
5-28	Emission centroid comparison between simulated CIII TVC plumes shown in Figure 5-27.	226
5-29	Emission centroid comparison between simulated CIII TVC plumes formed with and without poloidal flow.	228
5-30	Comparison between simulated CIII TVC 1-D parallel emission profiles for cases in the near SOL with and without background plasma flow.	229
5-31	Comparison between simulated CIII TVC 1-D parallel emission profiles for cases in the far SOL with and without background plasma flow. .	230
5-32	Comparison between simulated CIII TVC 1-D cross-field width profiles for cases with different cross-field diffusivities.	232
6-1	Plot of the 1-D integrated radial C^{+2} density distribution resulting from the presence of finite n_e and T_e gradients at the gas injection location.	239
6-2	2-D contour plot of the C^{+2} density distribution resulting from the presence of finite n_e and T_e gradients at the gas injection location. . .	240
6-3	Comparison between radial electric field values obtained from plume data and probe data for a number of ohmic L-mode discharges. The latter values are calculated from the radial gradient of the inferred plasma potential.	243

6-4	Comparison between $\mathbf{E} \times \mathbf{B}$ velocities obtained from plume and probe data (both FSP and ASP) for a number of ohmic L-mode discharges. The latter values are calculated by subtracting the drift-wave velocity from the poloidal propagation velocity of edge plasma fluctuations, neglecting effects of finite temperature fluctuations.	245
6-5	Comparison between $\mathbf{E} \times \mathbf{B}$ velocities obtained from plume and probe data (both FSP and ASP) for a number of ohmic L-mode discharges. The latter values are calculated by subtracting the drift-wave velocity from the poloidal propagation velocity of edge plasma fluctuations, including effects of finite temperature fluctuations (using $\beta = 1$ in Equation 6.4).	246
6-6	Comparison between electron temperature measurements made by the scanning probe on the upstream and downstream side of the probe head for conditions typical of the far SOL.	249
6-7	Comparison between experimental and simulated CIII TVC plume results in the far SOL for a normal field discharge.	250
6-8	Comparison between experimental and simulated CIII TVC plume results in the far SOL for a reversed field discharge.	251

List of Tables

2.1	Characteristics of periscopes used to view FSP.	55
2.2	Coherent fiber bundle characteristics for each view.	56
2.3	Summary of uncertainties in calibrated plume data	79

Chapter 1

Introduction

As the population of our planet increases, so does our need for energy. The study of nuclear fusion as a potential energy source is motivated by the observation of fusion “power plants” all around us – namely the sun and stars. The goal of magnetic confinement fusion research is to emulate those reactors here on Earth, in order to harness the power of fusion in a useful way. Though this task is challenging from both an engineering and physics standpoint, the potential benefits are numerous. Deuterium, which serves as a principle component of fusion fuel, is readily available in seawater, providing a nearly exhaustless fuel source. In addition, since fusion reactions do not burn fossil fuels, greenhouse gases would not be emitted by energy production in a fusion reactor. Finally, in a fusion reactor both the amount of radiation released and the amount of radioactive material requiring disposal would be significantly less than that produced in a fission reactor of comparable capacity [10].

Fusion reactor performance will depend critically on impurity and bulk ion transport in the edge plasma. To develop an understanding of these phenomena, it is necessary to have an accurate description for the edge plasma flow pattern in such a device. In this thesis, a physics model has been developed to assess the utility of impurity dispersal plumes as an edge plasma flow diagnostic in the Alcator C-Mod tokamak.

In this chapter, the need for the development of fusion as a reliable energy source is described, and some basic principles of magnetically confined fusion devices (e.g.

tokamaks) are presented. As mentioned above, the physics of the edge plasma and the production and transport of impurities play important roles in the realization of fusion reactors. Though much progress has been made in understanding impurity behavior and transport in fusion devices, some open questions remain. Previous work performed to address these questions is briefly reviewed, followed by a description of some of the unique aspects of the current impurity dispersal plume experiments. Finally, a thesis outline is presented, along with a complete description of the thesis goals.

1.1 Background

The need for alternative energy sources is clear, from the trends of both current and projected energy usage as well as from estimates of current energy supplies [1]. For a number of reasons, fusion is being explored as an option to meet these needs.

Energy release from fusing together light elements to form heavier ones results from the (general) increase in stability of nuclei as they become larger. This is illustrated in Figure 1-1, in which a plot of the binding energy per nucleon vs. nucleon number is shown for a number of naturally occurring elements. A maximum in this curve occurs near the element iron ($Z=26$, $A=56$), after which heavier nuclei become less stable. This results in the possibility of obtaining energy both from splitting heavy nuclei (i.e. fission) as well as from fusing light ones.

1.1.1 Confinement Requirements

In order for two nuclei to fuse together, the distance between them needs to be on the order of the nuclear dimension, i.e. a few femtometers. However, at these distances the electrostatic repulsion which exists between the nuclei is rather large, since this force varies as $\frac{1}{r^2}$. Nuclei which are brought close together by collision at high energy will in general scatter due to coulomb repulsion, and only a small percentage of them will actually fuse. Therefore, to generate a significant amount of energy from this process, a large number of nuclei need to be contained (**confined**) for a sufficiently long time

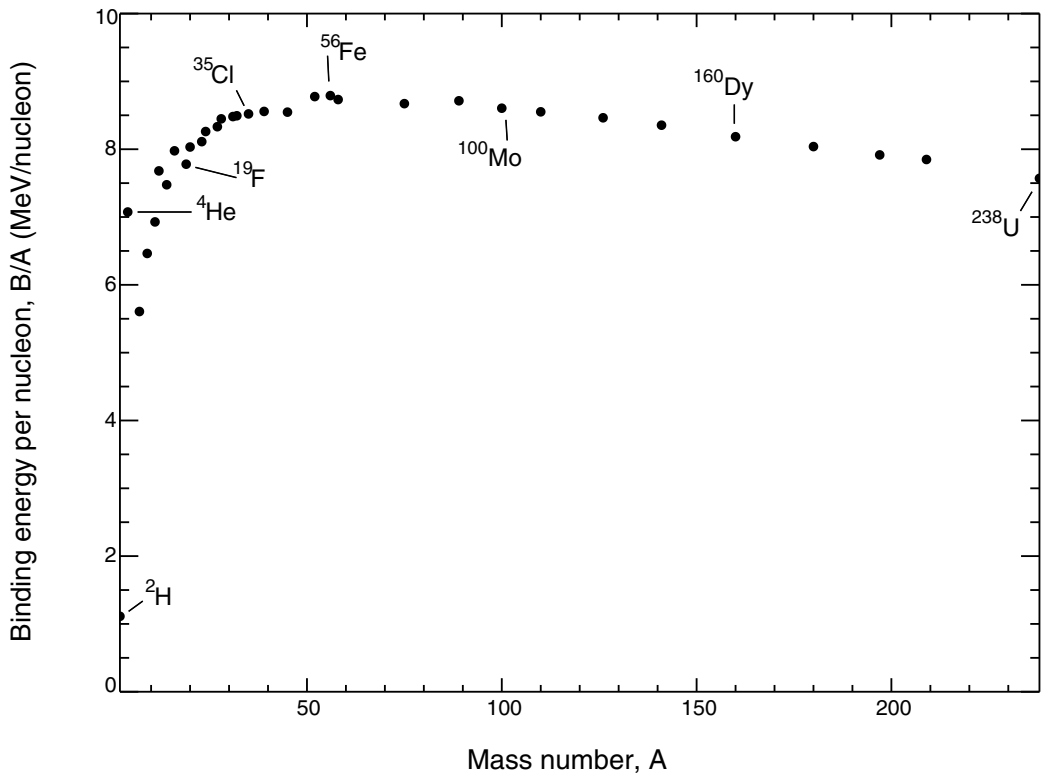
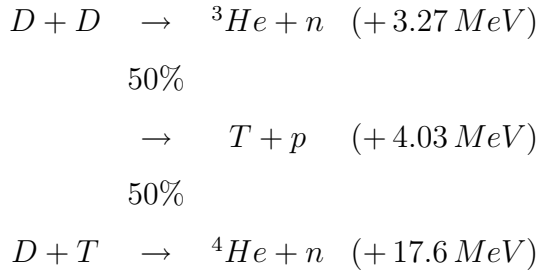


Figure 1-1: Binding Energy per nucleon vs. nucleon number. A peak occurs near the element iron ($Z=26$, $A=56$), allowing energy to be extracted both from splitting heavy nuclei (i.e. fission) as well as from fusing light ones. *Source:* K.S. Krane, Introductory Nuclear Physics, John Wiley & Sons, New York, 1988.

relative to the time scale over which fusion reactions will take place. In the sun and stars, this confinement is provided via gravity. However, it is impossible to simulate the gravitation field of such immense objects in laboratory experiments. In many experiments confinement is instead provided using magnetic fields (see section 1.1.2).

Since the coulomb force also scales with the charge of each interacting species, the fusion reaction with the lowest threshold energy is that between two hydrogen nuclei. Due to the presence of a resonance in the nuclear structure of ${}^5\text{He}$, fusion between deuterium (D) and tritium (T) occurs most readily. This can be quantified in terms of the fusion reaction rate parameter, $\langle \sigma v \rangle_{fusion}$; the number of fusion reactions per unit time is simply given by $n_1 n_2 \langle \sigma v \rangle_{(1,2)}$, where subscripts 1 and 2 refer to the reacting species and n is the particle density (m^{-3}). Plots of $\langle \sigma v \rangle_{fusion}$ vs. temperature are shown in Figure 1-2 for a few fusion reactions of interest, including the deuterium self-reaction (D-D) and the D-T reaction. Equations for the D-D and D-T reactions are:



1.1.2 Magnetic Confinement Fusion Devices

As indicated in Figure 1-2, temperatures required to achieve significant values for the fusion reaction rate parameter are large ($T \sim 25 \text{ keV}$). At these temperatures neutral species are fully ionized, resulting in the formation of a plasma.

Plasmas consist of charged particles which are subject to Lorentz forces. Specifically, consider the case of a particle with charge q moving with velocity \mathbf{v} in a magnetic field \mathbf{B} . The equation of motion for this particle is:

$$m \frac{d\mathbf{v}}{dt} = q (\mathbf{v} \times \mathbf{B}) \tag{1.1}$$

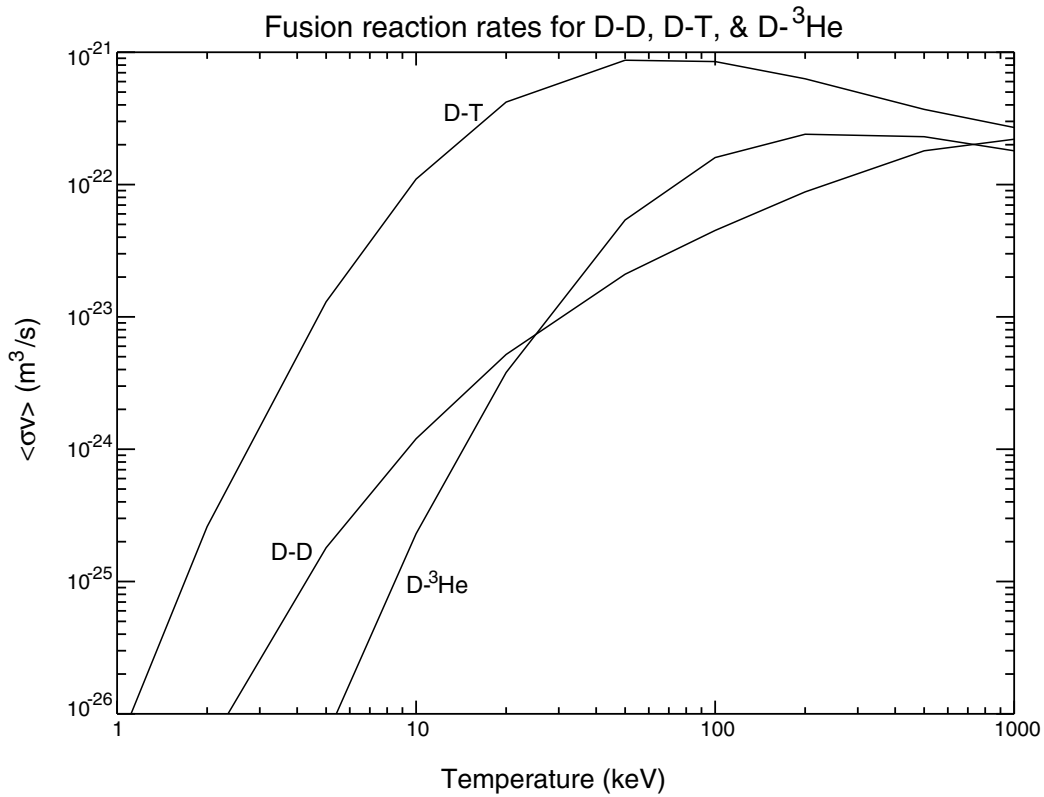


Figure 1-2: Fusion reaction rate parameter ($\langle \sigma v \rangle_{fusion}$) vs. temperature for a few reactions of interest. Over the range of experimentally achieved temperatures to date, ($\lesssim 25$ keV), D-T has the highest reaction rate parameter, and has therefore drawn the most attention in future reactor designs. *Source:* J.D. Huba, NRL Plasma Formulary, Naval Research Laboratory, Washington, DC, 1994, p. 45.

Solving this equation for the single particle system, the resulting particle trajectory is found to be a helical orbit about magnetic field lines. The radius of this orbit (the *gyroradius*) is determined by the energy of the particle and the magnetic field strength. In principle, transport across magnetic fields is possible only through collisions between particles, which lead to an effective particle (and energy) diffusivity. However, the transport of particles parallel to the magnetic field is unconfined in this simple picture. To control so-called “end-losses”, a toroidal geometry is employed in most fusion devices. A schematic of a typical toroidal fusion device, known as a tokamak, is shown in Figure 1-3.

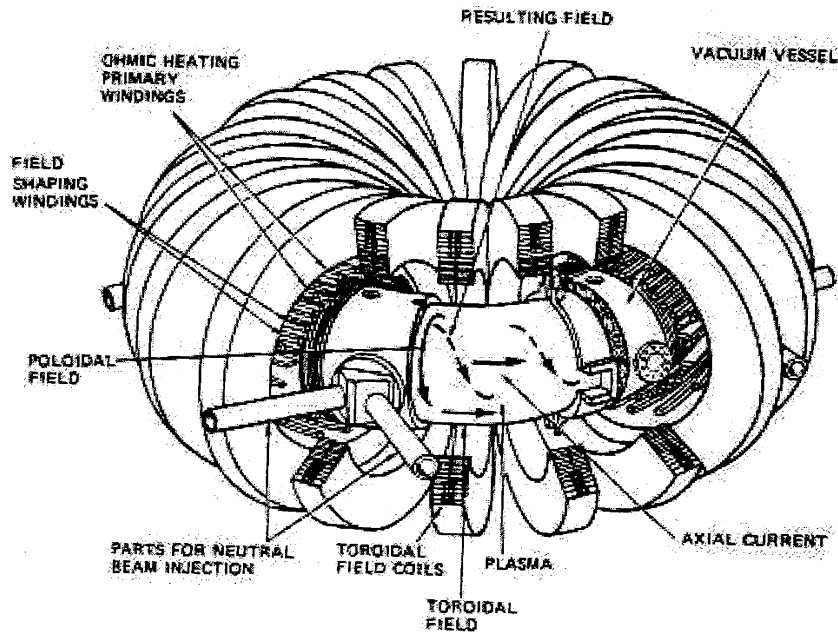


Figure 1-3: Schematic of a typical tokamak. Coils are required to generate a magnetic field (“toroidal field coils”) and a plasma current (“ohmic heating primary windings”) in the toroidal direction. The plasma current produces a magnetic field in the poloidal direction, which is required for plasma equilibrium. Coils are also present to allow for plasma shaping, which can be used to optimize reactor performance. *Source:* J.M. Rawls, et al., “Status of Tokamak Research”, DOE/ER-0034, 1979.

In a tokamak, coils are required to generate a magnetic field (“toroidal field coils”) and a plasma current (“ohmic heating primary windings”) in the toroidal direction. The plasma current produces a magnetic field in the poloidal direction, which is necessary for plasma equilibrium (more discussion below). Coils are also present to allow for plasma shaping, which can be used to optimize reactor performance.

The single particle picture is inadequate for describing much of the physics present in tokamak plasmas, since typically these systems contain a large number of particles ($\sim 10^{20}$). A more accurate description is given by a set of fluid equations known as the ideal MHD model [12]. As noted in reference [12], the MHD equations comprise the most basic self-consistent, single fluid model for determining the macroscopic equilibrium and stability properties of a plasma. In the two dimensional, axisymmetric geometry of a tokamak, this set of equations can be reduced to a single equation for describing the plasma equilibrium – the Grad-Shafranov equation:

$$\Delta^* \psi = -\mu_0 R^2 \frac{dp}{d\psi} - F \frac{dF}{d\psi} \quad (1.2)$$

where $p(\psi)$ and $F(\psi)$ are two free functions related to the plasma pressure and the toroidal magnetic field. ψ is function representing the magnetic flux:

$$\psi = \frac{1}{2\pi} \int \mathbf{B}_p \cdot d\mathbf{A} \quad (1.3)$$

In this analysis, the plasma pressure is considered to be a flux function, i.e. is constant along lines of constant magnetic flux.

An important result from ideal MHD theory is that a toroidal magnetic field (\mathbf{B}_ϕ) alone is insufficient to provide equilibrium confinement for toroidal plasmas. The required poloidal field (\mathbf{B}_θ) is generated in a tokamak by a toroidal plasma current (\mathbf{I}_p). This current is driven using an ohmic field coil (so-named because plasma current is also responsible for providing heating through ohmic dissipation), which acts as the primary of a transformer for which the plasma is the secondary. Together, the toroidal and poloidal magnetic fields provide plasma confinement in tokamak fusion devices.

1.1.3 Edge Plasmas

The presence of a poloidal field in a tokamak results in magnetic field lines which have a helical trajectory (see Figure 1-3). In general, these field lines do not close on themselves, but instead form surfaces of constant magnetic flux (ψ). Over most of the plasma cross-section these flux surfaces are closed. This is critical to maintaining good plasma confinement – if these surfaces were not closed, particles could flow freely towards the boundary along field lines contained in the surface. In the edge plasma, however, flux surfaces are open, resulting in magnetic field lines which intersect solid surfaces.

The edge plasma is defined as that region of plasma beyond the last closed flux surface (LCFS), also referred to as the separatrix. The existence of an edge plasma seems to be counter to the goal of magnetic confinement, which is to keep plasma away from the reactor walls. However, in reality, plasma-wall interactions are unavoidable. The “creation” of an edge plasma ensures that these interactions occur in a controlled manner.

Edge plasma regions can be formed by two means: by changes in the physical topology or in the magnetic topology. In the first case, a physical component (“limiter”) is introduced into the plasma at a given plasma radius. Beyond this radius the plasma density decays rapidly, so that the density in contact with the remaining reactor surfaces is greatly reduced (in turn reducing heat loads to the wall, and therefore erosion of the wall due to sputtering). The limiter is effectively “scraping-off” plasma at its radius – for this reason the region beyond the limiter is typically referred to as the Scrape-Off Layer (SOL). The magnetic flux surface tangent to the limiter surface is the last one which is closed, i.e. it is the LCFS – beyond the limiter field lines intersect solid surfaces. The poloidal cross-section of a limiter tokamak configuration is shown in Figure 1-4 (top panel).

Magnetic topology can also be used to form edge plasma regions. For example, if a toroidal coil located below the reactor vessel but on a plane parallel to the plasma axis is used to generate a current, this current will interact with the plasma current (\mathbf{I}_p) to distort the poloidal field inside the plasma. Depending on the location of the

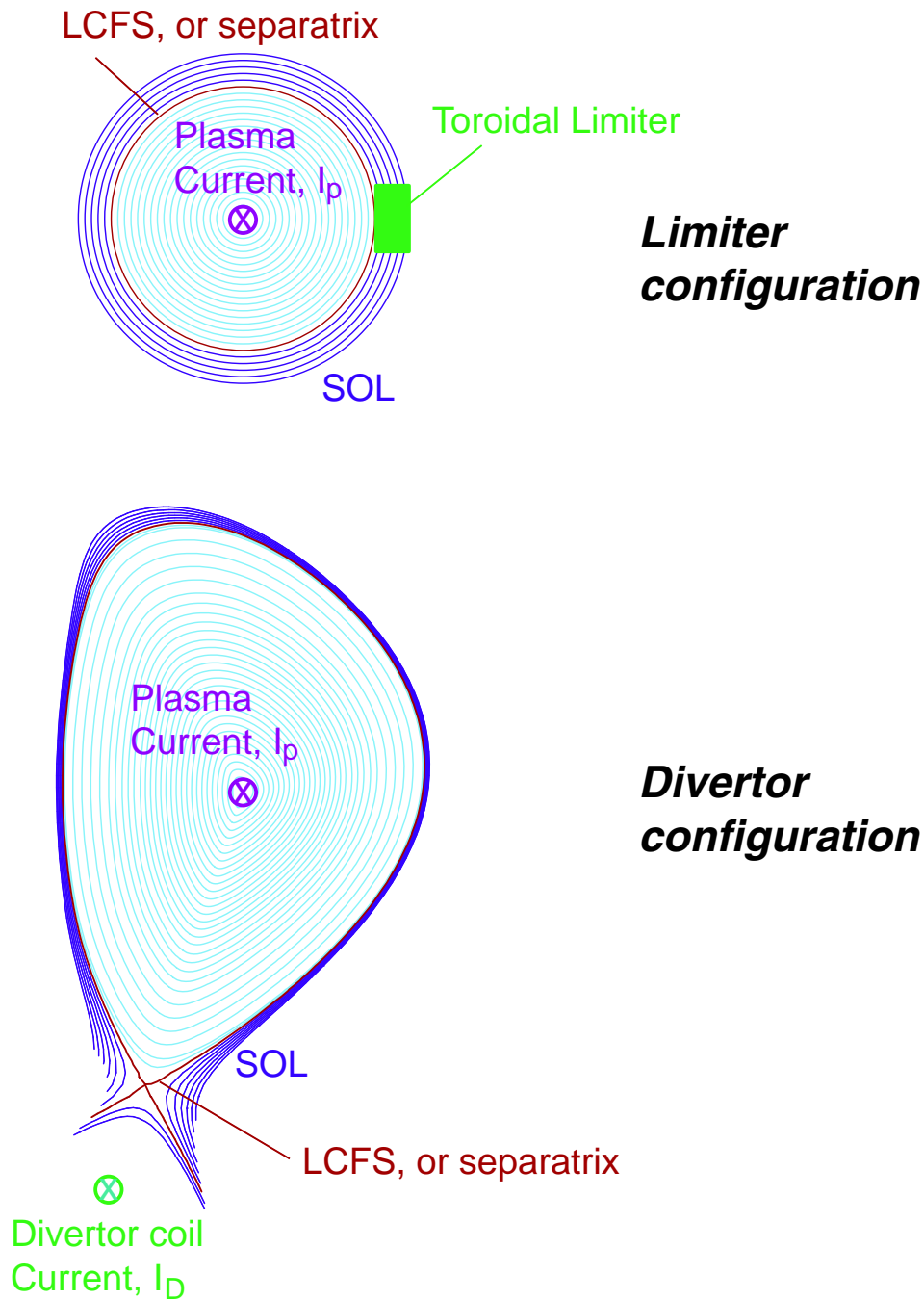


Figure 1-4: Types of edge plasma configurations. *Top panel:* Limiter configuration. The last-closed flux surface, or separatrix, is defined by the limiter radius in this geometry. Plasma density beyond this radius decays rapidly, reducing particle and heat loads to the remaining surfaces. *Bottom panel:* Divertor configuration. In this case the separatrix is defined by magnetic topology. Nonetheless, density still decays rapidly with distance away from the LCFS, due to the strong transport of particles along field lines.

coil and the strength of its current relative to \mathbf{I}_p , the distortion can be strong enough to create a region of zero net poloidal field, i.e. a poloidal field null. The position at which this occurs is typically referred to as the X-point, and simple calculations can be used to show that the surface containing the X-point will be the LCFS. Again, outside of this surface field lines will intersect the reactor walls. In a divertor tokamak, the geometry of the machine is designed to keep the plasma outside of the separatrix in a region separated from the core plasma. An example of a divertor configuration is shown in the bottom panel of Figure 1-4.

In a divertor geometry, the density profile outside of the LCFS is again expected to decay rapidly. In both limiter and divertor tokamaks this is a result of the same effect, namely the strong transport of particles to the wall along field lines in the edge plasma. Thus, in both geometries it is common to refer to the region outside of the LCFS as the SOL.

There are a number of aspects in which tokamak performance depends on processes occurring in the SOL. (i) **Plasma-wall interactions.** Plasma-wall interactions result in the creation of “impurities” (non-fuel species) via chemical and/or physical sputtering. Impurities can have a deleterious effect on core plasma performance (see section 1.1.4) – whether they make it to the core will depend on edge plasma transport. Large heat loads to the walls also result in degradation of material surfaces, requiring more frequent replacement of components. (ii) **Helium ash removal.** In a tokamak reactor in which D-T fusion is predominant, α -particle heating in the core is a key ingredient to reaching steady-state operation. However, once these particles have transferred their energy to the background fuel, they need to be removed from the plasma before they lead to significant fuel dilution. Efficient pumping of helium from the edge requires an enhancement of the helium edge concentration relative to the background. Whether this can be achieved will depend on the reactor geometry in this region as well as edge plasma transport. (iii) **Edge-core interaction.** Core plasma behavior also depends on physics in the SOL. For example, although particle fueling typically occurs at the edge, core density profiles tend to be somewhat peaked, suggesting the existence of a mechanism in the edge plasma which enhances inward

radial (across \mathbf{B}) particle transport. A number of experiments have demonstrated that density profile peaking can have a significant effect on plasma confinement properties (e.g. [15]), indicating that it is important to understand how density profiles are affected by edge plasma transport. Experiments have also been conducted in Alcator C-Mod [34] which indicate that as the plasma density increases, turbulence in the edge region begins to affect a larger proportion of the SOL, until this turbulence in fact crosses into closed flux surfaces and leads to a thermal quench of the plasma. This mechanism could be responsible for explaining the well established density limit [19] which is observed in all tokamaks.

1.1.4 Impurities

Impurities are defined as any plasma component which is not the main fusion fuel. Impurities exist naturally due to the inability to achieve a perfect vacuum in a tokamak reactor before fueling. Thus materials such as water vapor and nitrogen may be present in small amounts in plasma discharges. On Alcator C-Mod, a number of techniques are employed to reduce these impurity concentrations, including vessel baking and electron cyclotron discharge cleaning (ECDC).

However, impurities may also be generated during plasma discharges due to plasma-wall interactions. These interactions primarily cause material from the wall to be ejected into the plasma through sputtering. On Alcator C-Mod, where molybdenum serves as the first wall material, physical sputtering is the primary mechanism for surface erosion. On other machines, such as DIII-D and JET, where graphite is predominantly used for first wall material, chemical sputtering can also play a significant role.

The effect of impurities on tokamak performance is largely based on their location. In general, impurities can be responsible for large power losses due to bremsstrahlung radiation, which varies as the square of the ion charge state (Z^2). If significant concentrations of impurities exist in the core plasma, this can lead to degradation of core energy confinement and a thermal quench of the plasma. However, radiation from impurities may be beneficial in the edge plasma, where it can be used to reduce heat

loads to plasma-facing components. Experiments conducted on Alcator C-Mod [16] indicate that it is possible to run discharges with enhanced impurity levels in the edge – significant enough to dramatically reduce heat loads to the walls – while maintaining good core plasma properties.

1.2 Open Questions

Impurity concentration profiles in a reactor will depend on two factors: the source distribution and the transport of impurities in both the core and edge plasma. Impurity transport in the edge plays an especially important role, since it determines the “efficiency” with which impurities generated in this region penetrate to the core. Though significant effort has been spent on understanding these phenomena, there remain open questions regarding the influence of the following mechanisms on impurity dispersal in the edge plasma:

- *Reversed flows.* There have been observations on a number of machines, including Alcator C-Mod [37] and JT-60U [3], of parallel flows (v_{\parallel}) in the SOL changing direction near the separatrix, i.e. reversing (where the “normal” flow direction is designated as being towards the closest material surface). These measurements are typically made in the outboard SOL, and imply a large-scale poloidal flow of the background plasma from outer divertor to inner divertor. This flow could be responsible for transporting impurities generated at the outer divertor into the main chamber SOL, providing a mechanism of enhancing impurity concentrations in the core plasma. This flow may also result in the transport of impurities from outer to inner divertor, which has been suggested as a possible explanation for asymmetries in carbon deposition on the floor of JET [9].
- *$E \times B$ flows.* In the SOL, field lines intersect material surfaces and electron temperature varies with cross-field coordinate. The combination of these properties leads to the establishment of a radial electric field (\mathbf{E}_r) in the edge plasma.

This field results in an $\mathbf{E} \times \mathbf{B}$ force on charged species, leading to a flow which is in the poloidal (in the flux surface) direction. This flow occurs for all species, independent of any interaction between the bulk plasma and the impurity ions. \mathbf{E}_r is nominally in a direction which is outward in major radius in the outboard SOL and inward in major radius in the inboard SOL. In a “normal”-field configuration, in which the direction of \mathbf{B}_ϕ is clockwise when viewed from the top of the machine, the resulting $\mathbf{E} \times \mathbf{B}$ flows are directed from the inner to the outer divertor.

The poloidal flow resulting from reversed parallel flows and from $\mathbf{E} \times \mathbf{B}$ flows are in opposite directions in the outboard SOL (for normal field operation), as illustrated in Figure 1-5. On Alcator C-Mod, reciprocating fast-scanning probes are typically used to make measurements of parallel flows and radial electric fields in the edge plasma. Recent results [36] suggest that the poloidal projection of the parallel flow and the $\mathbf{E} \times \mathbf{B}$ flow tend to cancel near the separatrix (where reversed flows are typically observed), leading to a net toroidal rotation of the plasma. The implication for impurities is significant – if plasma flows lead to toroidal rotation only, then the dominant mechanism remaining for transporting impurities generated near outer divertor surfaces into the main chamber SOL (and beyond) is the thermal gradient force (arising from parallel gradients in the background electron and/or ion temperature, e.g. see Equation 6.21 in reference [62]). For typical SOL conditions in Alcator C-Mod, this force is small (see Equation 5.5), suggesting that impurity ions generated near divertor surfaces are in fact confined to regions of the SOL near the divertor. However, these results depend on the validity of the probe data, and independent measurements of v_{\parallel} and \mathbf{E}_r are therefore desired.

Independent flow measurements are also necessary to confirm probe results describing the effect of the edge plasma flow pattern on divertor performance. For example, recent results in Alcator C-Mod [38] indicate that over much of the SOL cross-field transport to the main-chamber walls dominates over parallel transport to the divertor, based in part on the measurement of low parallel flow velocities in the

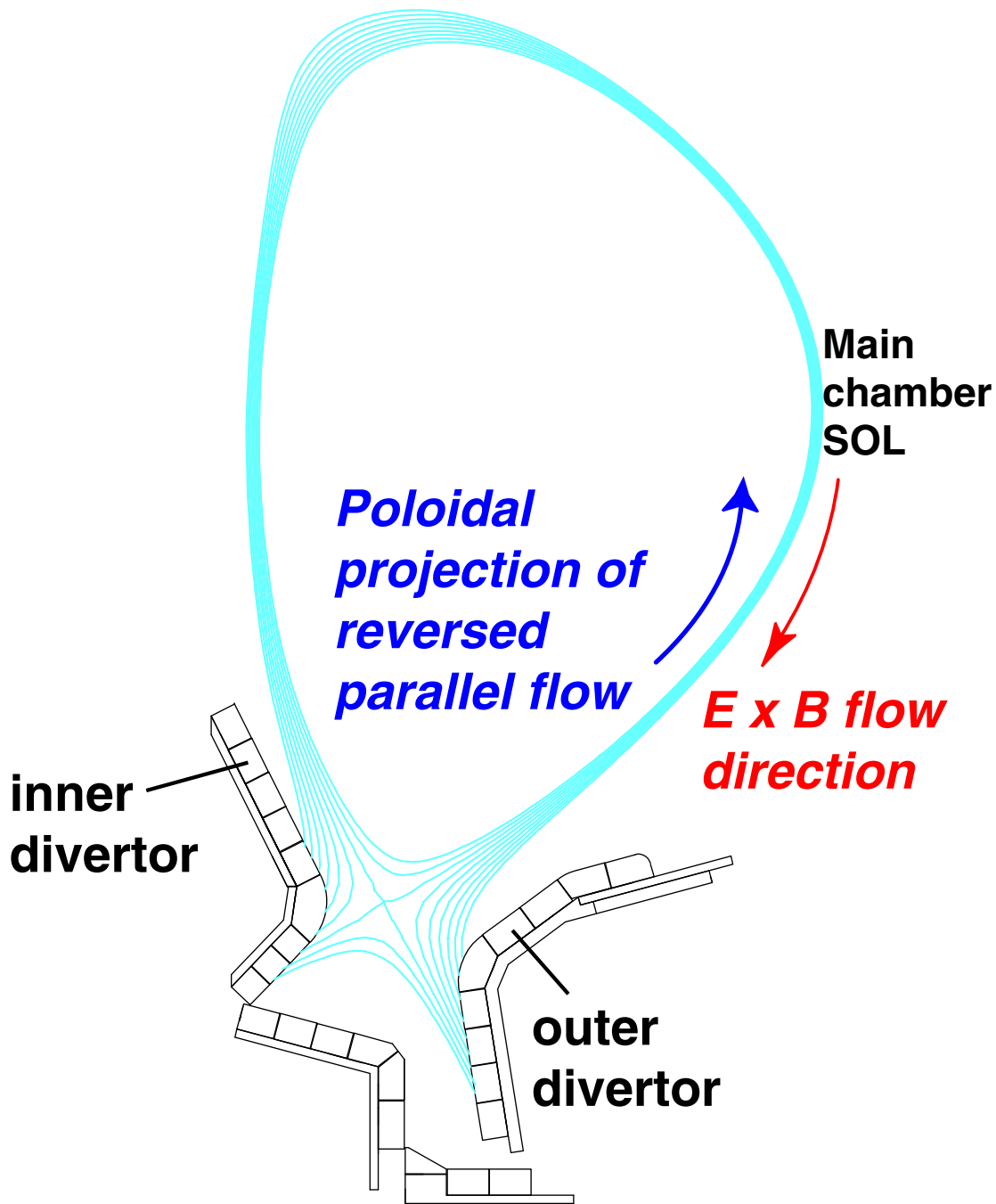


Figure 1-5: A poloidal cross-section of Alcator C-Mod, with a typical diverted equilibrium shown. Poloidal flows exist in the outboard SOL as a result of both parallel flows (blue) and $\mathbf{E} \times \mathbf{B}$ flows (red). Recent results suggest that near the separatrix, where parallel flows are observed to reverse (i.e. are away from the outer divertor), the poloidal projection of the parallel flow and the $\mathbf{E} \times \mathbf{B}$ flow cancel, leading to a net toroidal rotation of the plasma.

SOL by the scanning probe. Under such conditions, the role of the divertor as a means of maintaining plasma-surface interactions in a region separate from the core plasma is minimized. In addition, cross-field heat convection and charge exchange play a significant role in the scrape-off layer power balance in this case, which can lead to significant sputtering from main-chamber walls. In order to validate this main-chamber recycling view of particle flows in the Alcator C-Mod SOL, values of v_{\parallel} should be determined from measurements other than probes.

Doppler spectroscopy has been used in Alcator C-Mod [53], DIII-D [26],[27] and ASDEX Upgrade [13] to measure parallel impurity ion flows in the outboard SOL, and results indicate the existence of both normal and reversed flow regions for the impurities. Spectroscopic measurements have also been used to infer values for the background ion parallel flow in DIII-D [26] and ASDEX Upgrade [13], under the assumption of strong coupling between the background neutrals and ions (e.g. through charge exchange), and in Alcator C-Mod [53] under the assumption of strong coupling between impurity and background ions. Although this technique provides a simple means of determining parallel flows in the edge plasma, it has thus far found limited application in Alcator C-Mod. This is primarily due to problems with obtaining high signal throughput, which are made more difficult by the low emission strength typical in C-Mod for spectral lines of intrinsic impurities emitting in the visible range of the spectrum. In addition, the assumption of strong coupling between impurity and background ions which is necessary for relating the impurity ion flow velocity to the background flow velocity is questionable for cases in the near SOL.

Calculations of the radial electric field using a radial momentum balance and spectroscopic measurements of the poloidal and toroidal flow velocities (as well as density and temperature measurements) have also been performed on a number of devices (e.g. [55], [51], [21]). However, these calculations focus on plasma regions inside the separatrix – there exist no well-documented measurements of \mathbf{E}_r in the edge plasma other than from probes.

These results bring attention to the need for additional bulk and impurity plasma transport measurements in the edge plasma of Alcator C-Mod. Such measurements

have been conducted using impurity dispersal plumes.

1.2.1 “Plume” studies

A conceptually simple means to determine impurity transport in the SOL is to inject impurities locally in the edge plasma and then “watch” where they go. Experiments utilizing impurity gas injection into the edge plasma from limiter or wall-mounted capillaries have been conducted on a number of machines, including DITE [54], DIII-D [48], TEXTOR [49],[72], and Alcator C-Mod [28]. Results from these experiments are based on visible imaging of the resultant impurity dispersal “plumes” using CCD cameras with bandpass interference filters (e.g. see Figure 1-6). From an analysis of the emission structure, parameters which affect local impurity transport may be investigated. For example, results from DITE indicate that the frictional drag arising from the presence of plasma flows in the limiter presheath significantly impedes impurity transport away from the limiter along \mathbf{B} [54], while results from DIII-D suggest that a large background plasma flow along \mathbf{B} is necessary to explain the parallel (to \mathbf{B}) asymmetry of impurity emission generated near the divertor strike points [48]. In both DITE [54] and TEXTOR [49], effects arising from temperature differences between the impurity and background plasma ions are found to be important for describing the parallel impurity dispersal. In addition, results from TEXTOR [72] suggest that impurity ion recycling off the limiter surface may play an important role in determining the parallel transport of impurities away from the limiter, as does the presence of a parallel electric field above the injection location, generated as a result of the density perturbation arising from both the gas injection and background ion recycling off the limiter surface.

Plume experiments conducted by Jablonski et al. [28] on Alcator C-Mod employed gas injection through a capillary mounted on the inner wall midplane. A single CCD camera was used for these experiments, located at the outboard midplane, providing 2-D images of the emission in the toroidal-poloidal plane (emission images are integrated in the radial coordinate). Methane, nitrogen, and helium were used as working gases, with bandpass interference filters employed to view radiation from

specific line transitions in carbon (CII, CIII), nitrogen (NII), and helium (HeII) respectively.

An example of a C^{+2} (CIII) plume obtained from these experiments is shown in Figure 1-6. The emission is observed to be approximately aligned with the local magnetic field line, which is expected since ions are allowed to flow freely along field lines. In addition, there is a slight asymmetry in the extent of the emission along the field line relative to the injection location, which is indicative of a parallel flow in the impurity species (similar results for the parallel impurity dispersal have been observed in other experiments, e.g. [54],[48],[49],[72]). Deviation of emission from the field line is also observed. This deviation is thought to result from an $\mathbf{E} \times \mathbf{B}$ drift of the impurity ions, arising from the presence of a radial electric field in the SOL (radial electric fields are also thought to affect the impurity ion deposition on the local limiter in gas injection experiments conducted on TEXTOR [72]). The result is a “boomerang” shape to the emission, where the angle of the boomerang is set by a competition between parallel and cross-field transport.

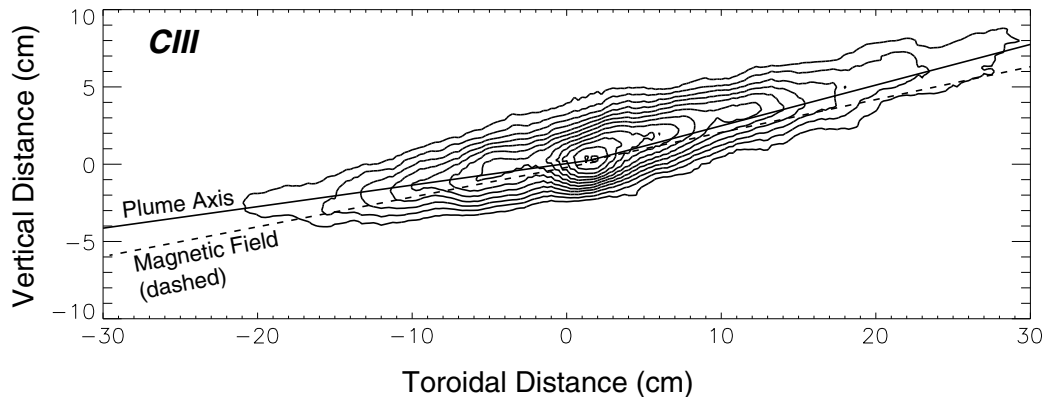


Figure 1-6: Example of a CIII plume generated using gas injection through an inner wall capillary. The image was obtained from a camera located at the outboard mid-plane. The plume exhibits elongation along \mathbf{B} , as well as deviation from the field line as a result of an $\mathbf{E} \times \mathbf{B}$ drift of impurity ions, which arises from the presence of a local radial electric field. Courtesy: B. LaBombard.

A $1\frac{1}{2}$ -D fluid model was developed by Jablonski to extract from the plume emission structure the following quantities: parallel flow velocity (v_{\parallel}); perpendicular flow

velocity (due to an $\mathbf{E} \times \mathbf{B}$ force, thus yielding \mathbf{E}_r); electron temperature (T_e). To solve for these quantities, however, measurements of the local electron density (n_e) were required. These were obtained from a reciprocating fast-scanning probe (FSP) located in the outer divertor. Probe measurements were then mapped from the outer SOL to the location of the gas injection assuming constant density along field lines. Comparisons between probe measurements of v_{\parallel} , \mathbf{E}_r , and T_e and plume measurements of these same quantities (assuming these values are also constant along field lines) suggest that the plumes provide a reasonable means for obtaining flow information in the SOL.

1.2.2 Uniqueness of studies using GIFSP

Plume studies conducted on Alcator C-Mod using wall-mounted capillaries suffer from a number of limitations. First, plumes tend to be formed close to the wall, since the ionization mean-free path is shorter than the SOL width for most impurities of interest. Helium provides a counter-example; however, helium ions have a wide radial distribution, making it difficult to localize the emission radially with a single camera view. Thus, in most cases plumes formed by gas injection through wall-mounted capillaries allow only the far SOL plasma to be studied. Second, plasma measurements required for plume modelling (i.e. electron density) are not made locally, which may introduce an error in the plume analysis. Similarly, any comparisons of flow parameters extracted from the plume emission with FSP measurements are questionable, since both v_{\parallel} and \mathbf{E}_r may vary along \mathbf{B} in the SOL.

To address these limitations, a novel diagnostic has been developed on C-Mod: a gas-injecting fast-scanning probe (GIFSP) [35]. This diagnostic allows impurity gas to be injected out the probe over a short period near the probe's end-of-stroke. Since the probe scans the entire edge plasma, up to the LCFS, gas can be injected anywhere in the SOL, allowing plume studies to be conducted as a function of SOL depth. Surrounding the gas-injection capillary are four Langmuir probes (more detail in section 2.1), which provide values of the local electron density and temperature as well as local estimates of v_{\parallel} and \mathbf{E}_r (similar to the gas-injecting limiter probe

used in DITE [54]). Thus for plumes formed with the GIFSP, quantities required for modelling are locally available. Similarly, flow quantities are locally measured, allowing a direct comparison to be made between plume and probe results.

The imaging component of the plume diagnostic system has also been upgraded relative to previous work on C-Mod. Two near-perpendicular views of the plume are available, allowing (in principle) for a full 3-D reconstruction of the emission. At each view location beam-splitters are used to obtain emission from two charge states simultaneously. Finally, gated, intensified CCD cameras are used to image the plume emission, allowing the gas injection to be reduced below perturbative levels. This system, which is described in more detail in section 2.2, allows plumes to be used as a flow diagnostic for any plasma discharge.

1.3 Goals & Outline of Thesis

The goals of this thesis are to gain an understanding of the physics of impurity dispersal plumes, and to assess their utility as a diagnostic of parallel flows and radial electric fields in the edge plasma. This is achieved by imaging plumes generated at a variety of SOL depths (up to the LCFS) and for a variety of plasma discharge conditions.

In Chapter 2, a description of the diagnostic system used to make the plume measurements is given, followed by a discussion of the invessel integration of the system. For comparison with modelling results, plumes are calibrated and mapped to a field-aligned coordinate system. The algorithms used to perform these transformations are presented. Finally, in order to simplify the comparison between experiment and modelling, emission is characterized in terms of moment parameters. The calculation of these parameters, and the implementation of error analysis in the calculations, is discussed.

In Chapter 3, characteristics of the plume emission are described, including their dependence on local plasma parameters. Experimental results are then presented which provide evidence for the existence of a sputter source for the emission, as well

as evidence that impurity transport near the probe is “jet”-like along \mathbf{B} in the near SOL and that the impurity ion distribution is extended down the probe axis. A simple model which is used to assess perturbations arising from the gas injection is then described. Finally, a database of plume results is constructed, allowing correlations to be developed between the plume structure and background parameters. The ionization mean-free path for deuterium neutrals recycling off the probe surface is found to play a key role in the formation of plumes which exhibit jet-like behavior.

In Chapter 4, initial analysis of the plumes using analytic fluid models is presented. The drawbacks of analytic modelling are then discussed, which indicate that the simple model employed by Jablonski is insufficient for describing plume emission generated from injection through the scanning probe. These results motivate the use of a more sophisticated tool for impurity plume simulation, namely the LIM 3-D impurity transport code. A description of modifications which were made to this code to allow for a more accurate simulation of the plume experiments is given. Among these were the development of various code options for including effects of sputtering and background ion recycling off the probe surface. Benchmarking results are then presented, and an algorithm is described which is used to transform the 3-D simulated data into 2-D plume images that can be compared directly with experimental results.

A physics model for the emission structure is presented in Chapter 5. This model features separate components for describing the sputter source of the emission, the mechanism leading to the impurity ion jet, and the cause of the vertical elongation in the impurity emissivity. During its development, new insights were acquired on the nature of perturbations induced by the scanning probe. These include the presence of a vertical $\mathbf{E} \times \mathbf{B}$ drift near the probe surface, responsible for transporting bulk and impurity plasma down the probe axis, and the presence of a localized parallel electric field above the probe tip, responsible for accelerating impurity ions away from the probe. This latter effect, which is the result of a localized density perturbation arising from background ion recycling off the probe surface, has been characterized for this first time in this work (although the effects of a density perturbation arising from localized gas injection and background ion recycling off the limiter surface were also

investigated to a limited extent in TEXTOR [72]). The density perturbation is found to be significant only in the near SOL, and the magnitude of the resultant parallel electric field is sufficient to explain the parallel extent of impurity emission generated in this region. In the far SOL, the parallel plume extent is reproduced using the sputter source component of the model. This component of the model also provides an explanation for the cross-field extent of emission generated in both the near and far SOL. Finally, results from sensitivity studies in LIM are presented, which are used to investigate the density and temperature profile dependence of the plume structure, as well as the influence of parallel and cross-field flows on the emission in the near and far SOL. Having developed a model for describing the plume emission, conclusions are reached as to the utility of the plumes as an edge plasma flow diagnostic.

In Chapter 6, results from the plume model are used to extract parallel and cross-field flow information from the emission structure. For plumes generated in the near SOL, estimates of the radial electric field are obtained from an analysis of the jet component of the emission. These values are then compared with probe estimates calculated from the radial gradient of the inferred plasma potential profile and from measurements of the poloidal propagation velocity of edge plasma fluctuations. Results of this comparison suggest that the latter technique may provide a more reliable means of determining the radial electric field in the edge plasma from probe data. Plume measurements are also used to infer values of \mathbf{E}_r inside and outside of the Quasi-Coherent (QC) mode layer during Enhanced D_α (EDA) H-mode. In the far SOL, estimates of the parallel flow velocity are inferred from parallel asymmetries in the plume emission structure using LIM. Results indicate that the plume measurements of parallel flow to the divertor are larger during reversed field operation compared to normal field operation, consistent with probe measurements. However, values for the parallel Mach number inferred from the plume data are also found to be smaller than values inferred from the probe data. Possible causes for this discrepancy are discussed, which suggest that the plume measurements may provide a constraint for the parallel flow structure in the far SOL. This result is important for assessing the effect of main-chamber recycling in the edge plasma of Alcator C-Mod.

Finally, a summary of results from the impurity plume experiments is presented in Chapter 7. Although plume measurements provide a means of cross-checking probe results in many cases, ultimately the sophisticated nature in which the plume structure is related to SOL flows suggests that the plumes cannot stand alone as a complete flow diagnostic. However, in many cases plumes serve as a valuable tool for determining the sign, as well as an estimate of the magnitude, of \mathbf{E}_r in the near SOL, especially during EDA H-mode, when fluctuations from the QC mode make it difficult to interpret probe measurements. Future work which could be performed to improve the plume imaging diagnostic is also discussed.

Chapter 2

Diagnostic Hardware

The impurity plume diagnostic consists of two main components: (1) the gas-injecting fast-scanning probe (FSP) and (2) optical views of the probe. The details of each system are described below.

2.1 Gas-Injecting Fast-Scanning Probe

A vertical fast-scanning probe [71] (FSP) has been operational on Alcator C-Mod since the beginning of plasma operation (1993). In 1996, the probe was modified to allow a controlled amount of impurity gas to be injected through the probe tip [35]. The probe consists of four 1.5 mm diameter tungsten wires embedded in a 1.6 cm diameter molybdenum probe head. The wires serve as Langmuir probes, making measurements of local electron density (n_e) and temperature (T_e) in the SOL. A close-up view of the probe head is shown in Figure 2-1. As shown in the figure, probe elements are labeled “north”, “east”, “south”, and “west”, based on their location relative to the pyramidal center when viewed from the front. Probe elements are positioned within the probe head such that one pair (east-west) has directional sensitivity along the local magnetic field line trajectory and the other has directional sensitivity across \mathbf{B} . For normal field operation (i.e. clockwise toroidal field direction when viewing the machine from the top), the west probe looks “downstream”, towards the divertor.

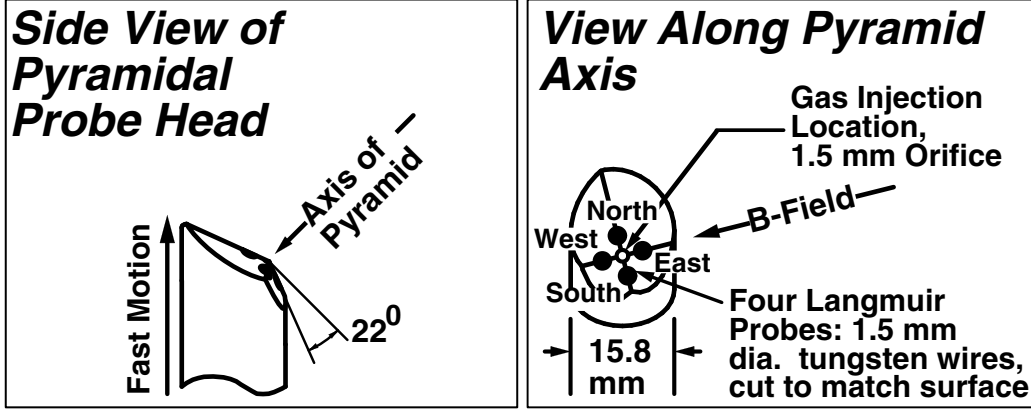


Figure 2-1: Close-up views of gas-injecting scanning probe (actual scale). The probe head is made from molybdenum, the wires which serve as Langmuir probes from tungsten, and the capillary tube and inertial valve from stainless steel. The Langmuir probes are oriented to have directional sensitivity both along and across \mathbf{B} , yielding information on local SOL flows in addition to values for electron density and temperature.

The local value of the parallel Mach number (M_{\parallel}) may be estimated from the ratio of saturation currents measured on the east and west probes, using:

$$M_{\parallel} = 0.45 \ln \left(\frac{j_{east}}{j_{west}} \right) \quad (2.1)$$

Equation 2.1 is based on a 2-D fluid analysis of ion collection by probes in a plasma with background flows and strong magnetic fields [23].

Centered between the probe elements is a 1 mm diameter stainless steel flexible capillary tube. The tube extends down the body of the probe and is connected to a nearby gas plenum. An inertial valve sits inside the capillary near the probe tip, and is designed to open under an acceleration of ≥ 30 g's. A diagram of the probe head showing the capillary and inertial valve is given in Figure 2-2. Gas in the capillary leaks out from the probe head only when the probe head experiences an acceleration greater than the acceleration required to open the valve. The acceleration of the probe is ≥ 30 g's for a period of ~ 8 -10 ms near its end-of-stroke; the peak acceleration of the probe during insertion is $\simeq 70$ g's. The timing of the valve opening relative to the probe insertion is illustrated in Figure 2-3. In this case a large gas injection was used

to perturb local plasma conditions (as detected by the south probe), with the timing of the perturbation establishing when the inertial valve is open. During this period, the probe moves ~ 6 mm, or ~ 4 mm perpendicular to magnetic flux surfaces (based on typical magnetic equilibria in the SOL). Thus gas deposition is highly *localized*.

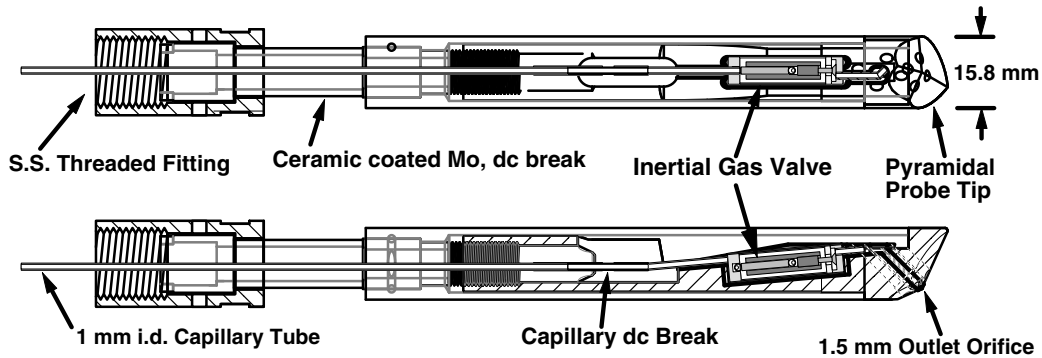


Figure 2-2: Transparent view of fast-scanning probe head assembly showing gas feed and inertial valve location.

2.1.1 Injection parameters

A series of parameters are chosen to optimize performance of the injection system, including injection gas species and rate of gas injection. The choice of the gas species is determined by the following requirements:

- That there exist charge states of the resultant impurities which emit line radiation in the visible (requirement for optics, see sections 2.2.2 and 2.2.3);
- That there exist impurity charge states which can exist over a large region of the SOL, where densities and temperatures vary strongly;
- That there exist impurity charge states which strongly couple with background plasma flows, so that impurity transport can be related to bulk plasma transport;
- That injection of the impurity have a non-perturbative effect on the bulk plasma.

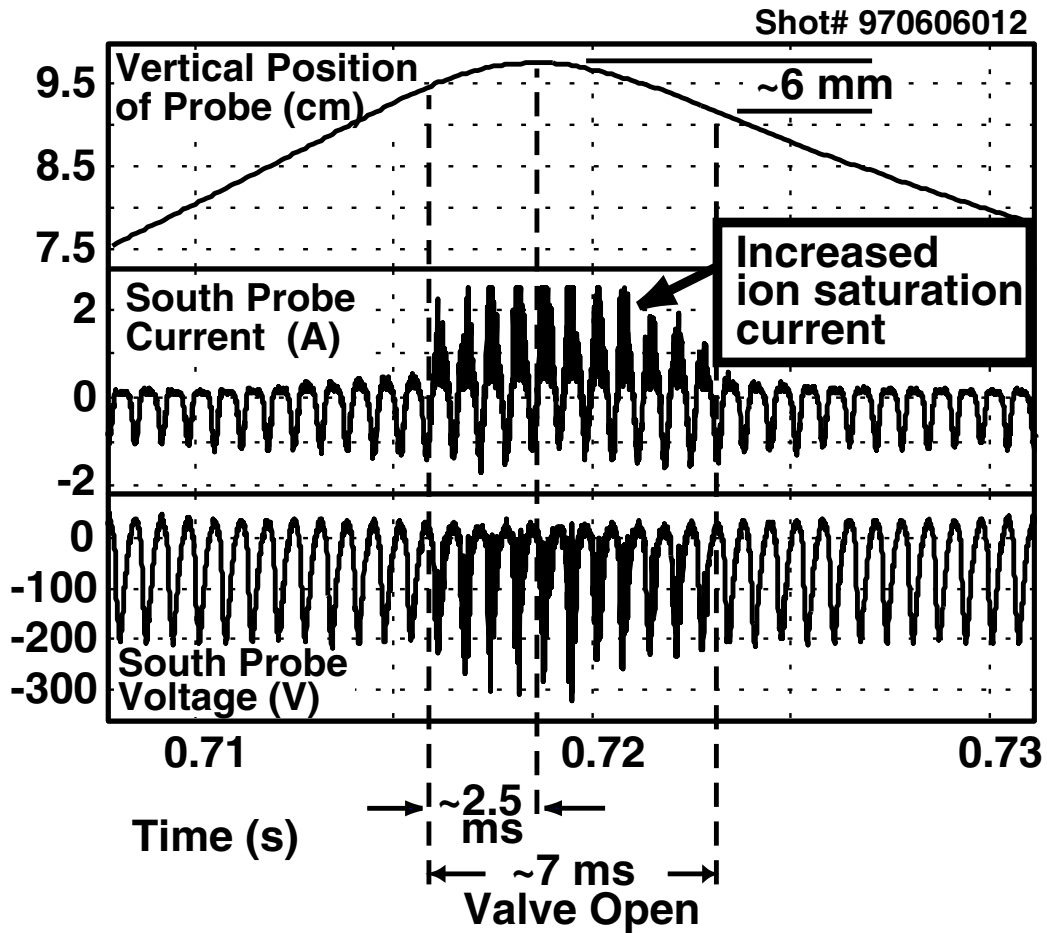


Figure 2-3: Test shot illustrating timing of gas injection relative to the probe insertion. In this case a large gas injection was used to induce a perturbation in the local plasma conditions (as detected by the south probe). The timing of the perturbation establishes when the inertial valve is open. This result indicates that the inertial valve opens only near the peak of the scan, i.e. that gas deposition is localized. Courtesy: B. LaBombard.

Previous experiments on Alcator C-Mod have been conducted using carbon impurity injection (in the form of methane gas) and nitrogen impurity injection (N_2) from both wall-mounted capillaries [28] as well as the fast-scanning probe [35]. Results of FSP-injection experiments using nitrogen revealed that low charge state ions of this impurity (which are the only ones to emit in the visible) have a short lifetime and therefore do not strongly couple to background flows for typical SOL conditions. Nitrogen plume emission structure is therefore only weakly correlated with bulk plasma transport. Results of nitrogen plume modelling using the LIM Monte Carlo impurity transport code [65] were consistent with this finding. Code results did indicate however that C^{+3} ions formed in conditions typical of the near scrape-off layer would be sufficiently long-lived to be well-coupled to the background, implying that measurement of C^{+3} plumes could be used to obtain information on background flows [35]. To address the criterion of non-perturbativeness (e.g. by minimizing the amounts of injected species not viewed), deuterated ethylene (C_2D_4) was chosen as the injection gas, with the hope of looking at CIV line radiation (specifically the 581.0 nm line). However, experiments conducted in the early portion of the 1999 C-Mod run campaign demonstrated that the emission strength for this line is too weak to be seen. Unfortunately, for carbon, only C^{+1} and C^{+2} ions emit strongly in the visible. To utilize C_2D_4 for plume studies, CII (at 514.3 nm) & CIII (at 465.1 nm) line radiation is viewed.

The amount of gas injected is primarily set by the plenum pressure. The injection system was calibrated by puffing gas into an empty vacuum vessel and recording the change in the pressure. Using a previously calibrated gauge, Δp can be expressed in terms of the total number of molecules injected, providing a relationship between plenum pressure and injection level. An example is shown in Figure 2-4 – in this case the plenum pressure was $\simeq 17$ torr, resulting in the injection of $\simeq 6 \times 10^{16}$ molecules of deuterated ethylene per puff (or probe scan). A calibration “curve” (consisting of points at 5 different plenum pressures) for C_2D_4 injection is shown in Figure 2-5. For a typical plume experiment, a plenum pressure of ~ 16 torr is used, resulting in $\sim 5 \times 10^{16}$ molecules injected per probe scan. Discussions on the gas perturbations are

given in section 3.2.2.

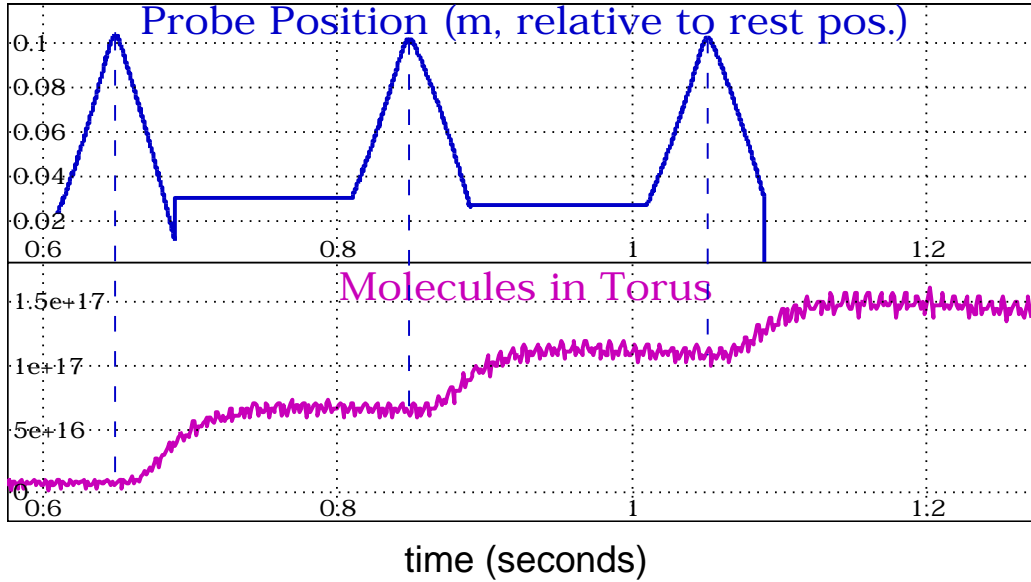


Figure 2-4: Injection of C_2D_4 through the scanning probe into an empty vacuum vessel. Using a calibrated gauge, the change in pressure inside the vessel can be related to the number of injected molecules. In this case, for a plenum pressure of 17 torr, $\sim 6 \times 10^{16}$ molecules of deuterated ethylene were injected per probe scan.

2.2 Probe views

Two near-perpendicular views of the probe are available on Alcator C-Mod, one viewing the probe from the top of the machine (F-top) and the other viewing horizontally from the outside (F-side). Views are obtained using coherent fiber bundles located in re-entrant periscopes. Each fiber is coupled to a gated, intensified CCD camera through a series of optics (lenses, mirrors, interference filters). Images from both cameras are captured simultaneously using a video framegrabber. Details on each of these components is given below.

2.2.1 Periscope design

A cross-section of Alcator C-Mod showing the locations of the two periscopes is given in Figure 2-6. Some characteristics of the periscopes are given in Table 2.1.

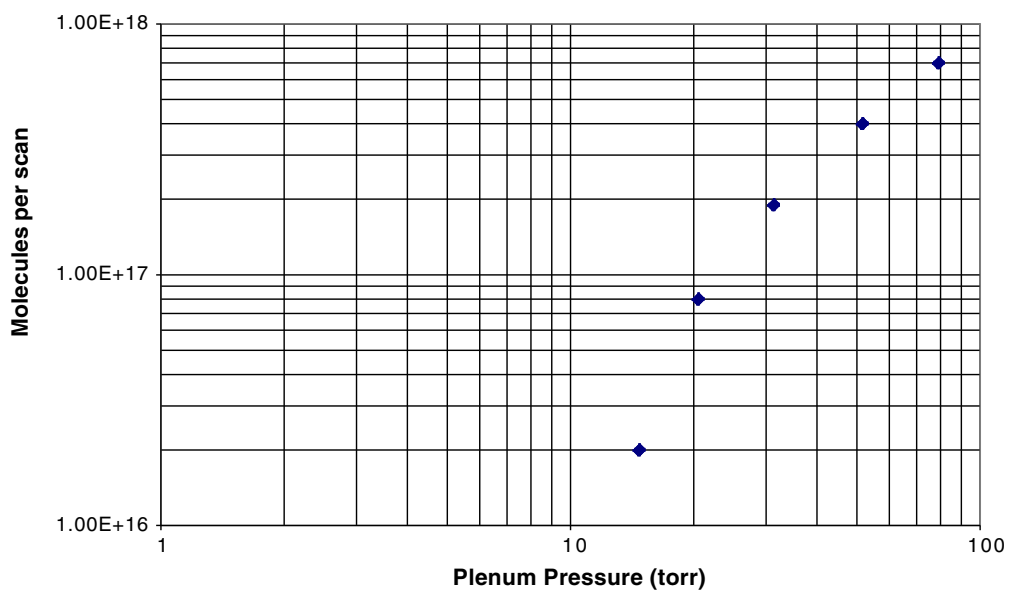


Figure 2-5: Calibration “curve” for injection of C_2D_4 through the scanning probe. For a typical plume experiment, the plenum pressure is ~ 16 torr, resulting in $\sim 5 \times 10^{16}$ molecules being injected per probe scan.

Here the term “periscope” refers to a pipe with a re-entrant window on the end. A coherent fiber bundle with a camera lens attached to its end is placed inside each tube, and each bundle looks through the corresponding window to provide a view of the scanning probe. Design of the F-top periscope was straight-forward, given the use of a standard $3\frac{3}{8}$ ” flange at this location, and was performed by Dr. B. LaBombard. The F-side periscope required special design so that it would fit within the flange layout at this port (see Figure 2-7), which was governed by the installation of the diagnostic neutral beam (DNB) and its associated diagnostics. The primary design considerations were the size of the periscope vacuum (conflat) flange, set at $1\frac{1}{8}$ ” by spatial constraints, and the ability to insert the periscope underneath the turbulence probe. Modifications to the conflat flange were necessary to allow for the periscope to be inserted – specifically, the flange was drilled out in two steps. Bench tests were conducted to verify that the structural integrity of the flange was not compromised by these modifications.

The outer diameter of the F-side periscope ($\frac{5}{8}$ ”) was chosen based on standard sizes offered by Larson Electronic Glass [44]. The inner diameter (0.555”) was chosen to accommodate the outer diameter ($\frac{1}{2}$ ”) of the coherent fiber bundle that would be inserted into it. For these range of sizes, Larson Glass only offers periscopes with sapphire windows. For a periscope tube outer diameter of $\frac{5}{8}$ ”, the window outer diameter is 0.660”. However, the nominal inner diameter of the copper gasket used to make the seal between the periscope and the conflat flange is 0.635”. Thus for the F-side periscope the gasket needed to be milled out to a larger diameter (0.665”). Tests were conducted in the Alcator C-Mod vacuum lab to ensure that a proper seal could be obtained with this thinner gasket, and they indicated that the integrity of the seal is maintained.

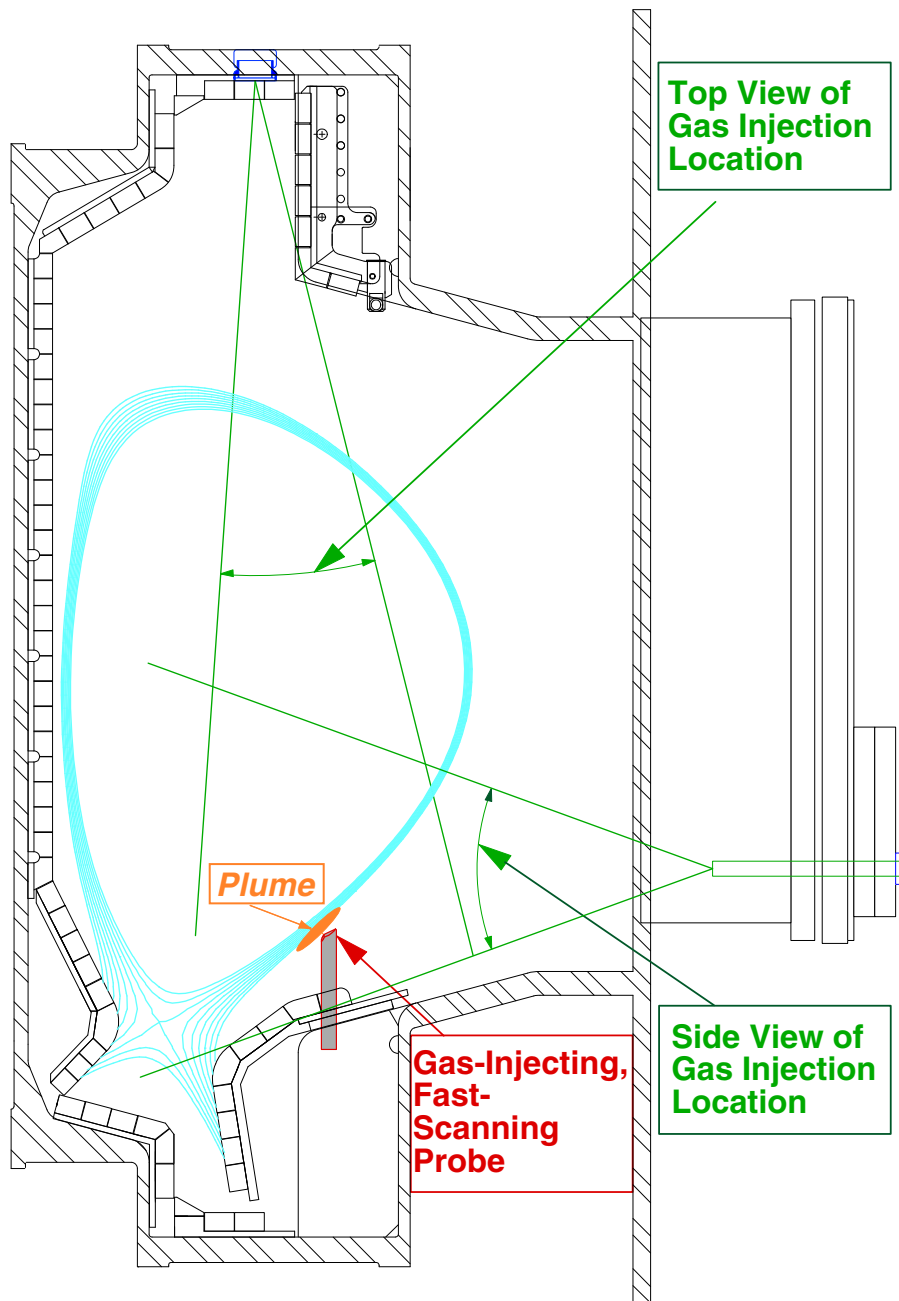


Figure 2-6: Cross-section of the Alcator C-Mod vacuum chamber with a typical diverted equilibrium. Gas is injected at the end of stroke of a vertically-scanning probe. Impurity emission plumes are viewed from two near-perpendicular locations.

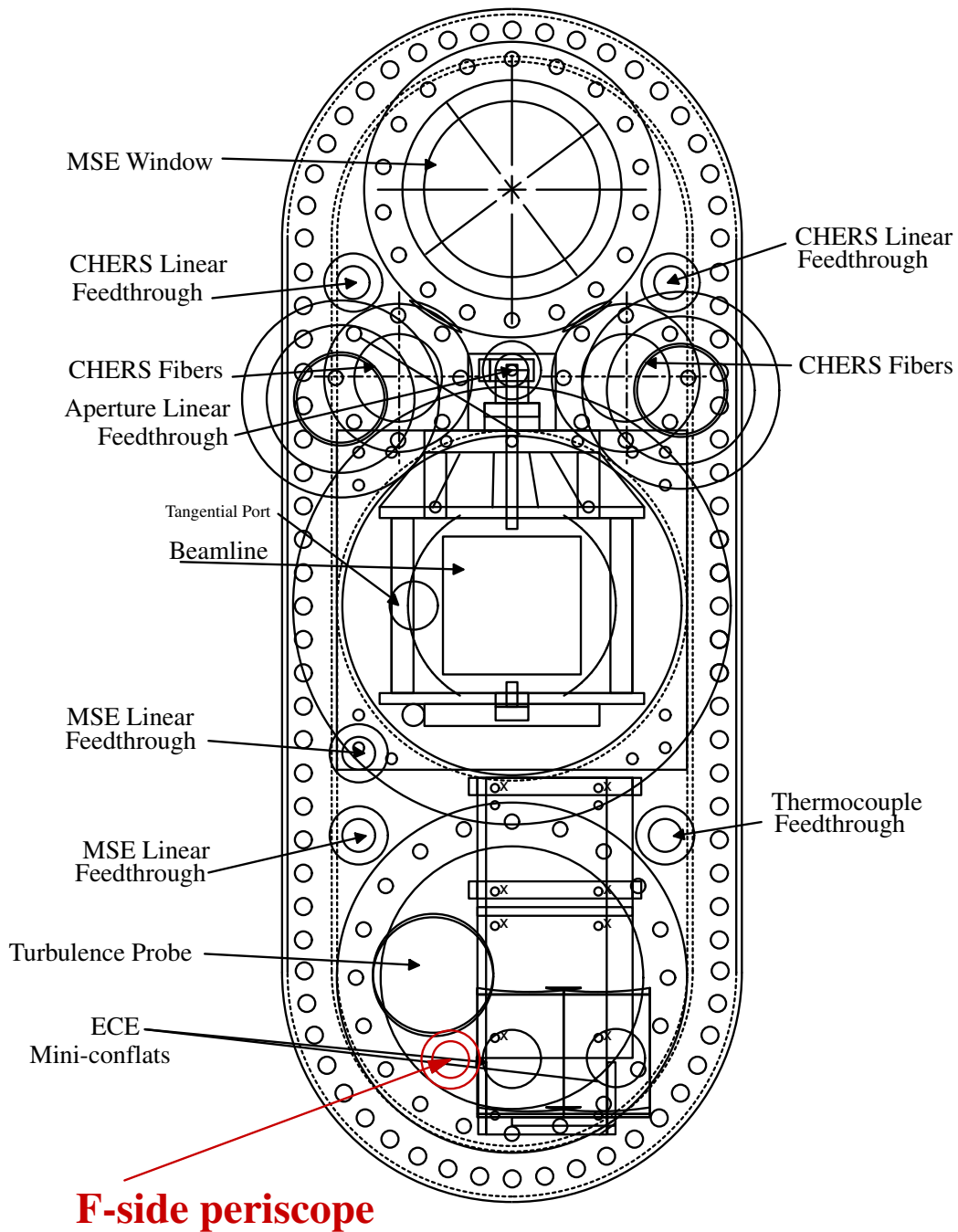


Figure 2-7: Layout of F-horizontal flange, indicating location of F-side persicope.

	<i>Side View</i>	<i>Top View</i>
Window type	Sapphire	Quartz
Length	8"	68"
Tube Outer dia.	0.625"	1.63"
Tube Inner dia.	0.555"	1.5"
Window Outer dia.	0.660"	1.8"

Table 2.1: Characteristics of periscopes used to view FSP.

2.2.2 Fiber bundles

The fiber bundles [58] are square format, $4 \text{ mm} \times 4 \text{ mm}$, containing 400×400 fibers each, and transmit primarily in the visible (starting at $\sim 350 \text{ nm}$).

Standard camera lenses are placed at either end of each fiber bundle for focusing. The focal length of the lens placed on the end looking into the machine is set by the desired viewing area at the given view location. These areas are determined by both the distance from the fiber to the probe and from the expected plume dimensions for the impurities being viewed. In Figure 2-8, values of the ionization mean-free path for C^{+1} (CII) and C^{+2} (CIII) for a variety of background electron densities and temperatures are shown ($T_{\text{carbon}} = T_e$ is assumed in each case); assuming that the parallel extent of the plume emission can be approximated by the ionization mean-free path (see section 3.2.1), parallel plume extents will be in the range of 5-10 cm for CII emission and 15-30 cm for CIII emission for conditions representative of the SOL. Focal lengths for the lenses (top view – 16 mm; side view – 6 mm) are chosen to ensure that the fiber views are at least as wide as the widest expected parallel extent for CIII emission. Since the fibers are square in format, the length of the view will be identical in each direction. This ensures full coverage of the plume, since the parallel extent of the impurity emission is much larger than the cross-field extent in almost all cases.

The resolution of each fiber bundle is determined from the following calculation:

$$Resolution = \frac{(4 \text{ mm}/400 \text{ fibers}) \times (\text{distance from fiber to probe})}{\text{focal length of lens viewing probe}} \quad (2.2)$$

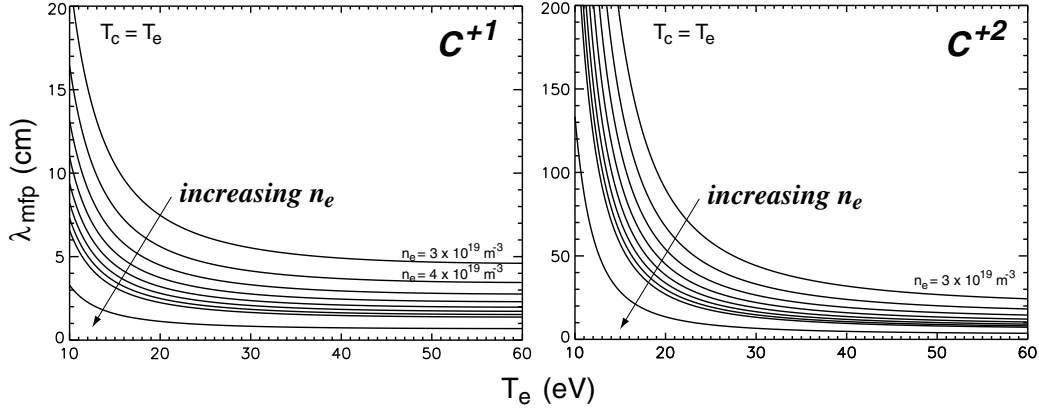


Figure 2-8: Calculation of ionization mean-free path vs. electron density and temperature for C^{+1} and C^{+2} ions. The density range is from $3 \times 10^{19} - 2 \times 10^{20} \text{ m}^{-3}$. The carbon temperature is assumed equal to the electron temperature in both cases.

Using the known distances from each fiber to the probe and the required view areas (which subsequently sets the focal lengths of each lens), the resolution for each system is determined to be $\sim 0.63 \text{ mm/fiber}$. These results are summarized in Table 2.2.

	<i>Side View</i>	<i>Top View</i>
Distance to fiber	41.7 cm	89.7 cm
View Area	27.7 cm^2	22.2 cm^2
Focal length of lens	6 mm	16 mm
Resolution	0.70 mm/fiber	0.56 mm/fiber

Table 2.2: Coherent fiber bundle characteristics for each view.

Sitting on top the lenses are wedge prisms, which are used to steer each fiber's view. These prisms are required because the fiber bundles are centered at locations which are different from the FSP axis (see Figure 2-6). The prisms are made of BK-7 glass – using the known index of refraction of this material [11], the angle that the view is steered by can be determined as a function the wedge angle from the following:

$$\cos \theta = [N \sin^2 \phi \pm \frac{\sin 2\phi}{2} (\csc^2 \phi - N^2)] \quad (2.3)$$

where ϕ is the wedge angle and θ is the angle that the view is steered by. Required θ values for the top and side view are determined by the distance from each view to the

FSP and the distance that each view is off-center from the FSP axis. The required wedge angles are then calculated using Equation 2.3. For the top view, a standard prism with a wedge angle of 4° is used. For the side view, a custom-made piece was required, with a wedge angle of 5.7° . These wedges are attached to the fiber lenses using standard RTV epoxy [57].

2.2.3 Cameras

Images obtained from the fiber bundles are digitized using CCD cameras. Discussion of the optical coupling between the bundles and the cameras is given in the next section.

The cameras are similar systems (*side view*: model ISG-250; *top view*: model ISG-202) developed by Xybion Electronic Systems [75]. Both cameras are on loan to Alcator C-Mod from outside facilities – the F-side camera from the Princeton Plasma Physics Laboratory (courtesy Dr. S. Zweben) and the F-top camera from the Los Alamos National Laboratory (courtesy Dr. R. Maqueda). Each CCD chip consists of a 2-D pixel array, from which a standard black and white analog video signal (RS-170 standard) is generated. This signal is then digitized (using 8-bit digitization) onto a separate 2-D array containing 640×480 pixels (see section 2.2.5). The F-side camera has an active pixel dimension of 768×493 pixels, corresponding to a physical dimension of 11.9×8.9 mm, while the F-top camera has an active pixel dimension of 754×484 pixels and a physical dimension of 12.7×9.6 mm. A high-voltage intensifier is available on each unit for increasing the light sensitivity. On the F-side camera the intensifier voltage can be controlled externally through a knob on the power supply, whereas for the F-top camera this voltage is fixed.

Each camera has the capability of being electronically shuttered, i.e. having an exposure time which is less than the nominal field time of 16.6 ms (since each frame is composed of two fields, “even” and “odd”, the corresponding frame rate of each camera is 30 Hz). Gates can be set externally through knobs on the cameras, or through a voltage signal sent to the proper pin on the cable connecting the camera to its power supply. The latter method is used during normal operation. Nominally

the exposure input pin is set low (0 V), corresponding to a full exposure window for the camera. When gating the camera, an initial high voltage (+2V) signal is sent, followed by a series of low voltage pulses, whose (variable) duration are the desired camera gate times. The cameras can be gated from 1 μ s to 16.6 ms. For typical operation camera gates are in the range of 0.1-1 ms.

Gating is desired in order to “freeze” the motion of the probe during acquisition of a given plume image. This is to ensure that the information obtained from the probe is truly localized, and not averaged over a series of flux surfaces. This is especially important for plumes generated in the near SOL, close to the separatrix, where plasma parameters may vary substantially over short distances. However, since gating is employed, intensification is required to improve the signal-to-noise of each camera.

In order for signals from each camera to be captured using a single video frame-grabber board, signals from both cameras need to be synchronized with each other. In the initial set of experiments [14], neither camera had the ability to synch directly to an inputted video signal. The F-side camera could only be synched by sending it horizontal drive (HD) and vertical drive (VD) pulses, while the F-top camera could only be synched using a line-driven source. Therefore, a circuit was developed to create synchronization signals that both cameras could accept. Following the 1999 run campaign, the F-side camera was sent to the manufacturer to have its video card replaced – this change allowed it to directly accept an external video signal as a synchronization signal. The old synch circuit was then used to synchronize the video frame times to the timing of the Alcator C-Mod shot cycle.

2.2.4 Beam-splitters

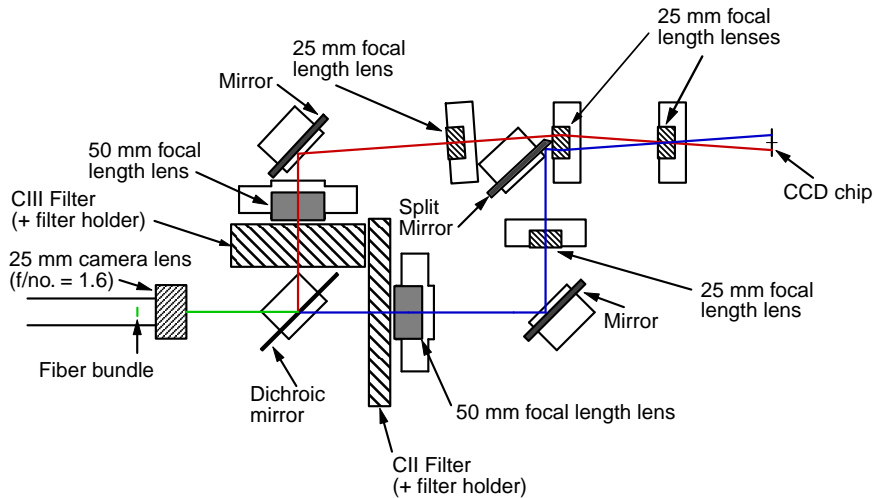
In almost all cases the extent of the impurity emission in the direction parallel to the local magnetic field will be extended compared to that in the cross-field direction. This “aspect ratio” is set by the ratio of the parallel diffusion (expansion) rate of the impurities, primarily governed by classical transport processes, and the cross-field drift of the impurities, set by anomalous transport processes. Since this ratio in most

cases is larger than 2-to-1, much of the viewing area on the CCD chip is blank for both cameras (roughly 1/2 - 2/3). This fact inspired the idea of capturing two images simultaneously on each chip through the use of beam-splitter optics.

Capture of CII and CIII emission simultaneously at each view location is done with the use of beam-splitters. A schematic of the beam-splitter design used for each camera is shown in Figure 2-9. Though the position of the beam-splitter optics are not identical for each camera due to the difference in camera CCD chip sizes, the basic designs are the same. Emission from the fiber bundle is first sent to a dichroic mirror. A 25 mm focal length camera lens is used on this end of the fiber bundle for both systems, with the focus set at ∞ to ensure that this emission is sent out as parallel rays. Emission below $\simeq 480$ nm is reflected off of the mirror, and emission above $\simeq 500$ nm is transmitted, making this component nearly ideal for the CII (514.3 nm) / CIII (465.1 nm) system. The mirror is 2.0 in², $\simeq 1$ mm thick, and made from soda-lime glass [46].

Once the signal is split with the dichroic mirror, each leg passes through a bandpass interference filter. The filters are 2" diameter, custom-made from Andover Optics [2]. The CII filters are centered at 514.5 nm with a bandwidth (FWHM) of 3.3 nm, while the CIII filters are centered at 465.7 nm with a bandwidth of 2.8 nm. All filters have a peak transmission of $\simeq 62\%$. The center wavelength of each filter is slightly blue-shifted relative to the wavelength of the corresponding carbon spectral line (CII: 514.3 nm, CIII: 465.1 nm) to optimize the amount of emission collected from light rays with non-normal incidence to the filter [2].

The remaining optics of the beam-splitter consist of achromatic lenses and mirrors, whose placement is set in order to steer the beam towards the camera CCD chip and to minimize light-loss/vignetting. At the point where the signals are recombined, a split-mirror containing a 30° bevel angle (custom-made from Cat I Manufacturing [8]) is used which allows signal from the upper leg to pass (relatively) unattenuated while reflecting signal from the lower leg into the proper beam path. All lenses were purchased from Edmund Industrial Optics [11], and each has a focal length of either 25 mm (stock no. K45-174) or 50 mm (stock no. K32-496). The f-number (the ratio of



- **25 mm lens on output of fiber bundle is used to make rays parallel**
- **Dichroic mirror is used to separate colors (CII, CIII)**
- **All other lenses are achromats**
 ==> 2 50 mm lenses (f/no. 1.67)
 ==> 4 25 mm lenses (f/no. 1.67)

Figure 2-9: Schematic of a beam-splitter used to capture images of CII and CIII emission *simultaneously* at each view location. A dichroic mirror is used to split the input signal: emission below $\simeq 480$ nm is reflected, emission above $\simeq 500$ nm is transmitted. Bandpass interference filters are used to pick out the radiation lines of interest, and then signals in each leg are sent through lenses and mirrors positioned to steer the beam towards the CCD chip while minimizing vignetting losses.

the focal length to diameter) for both the 25 mm and 50 mm lenses is 1.67. The mirrors are standard 2" square mirrors, coated for optimal reflection, and also obtained from Edmund Industrial Optics (stock no. K43-876).

The location of each of the components was initially set by simple ray-tracing calculations (the central ray for each leg in the splitter is shown in Figure 2-9: CII – blue, CIII – red). Component positions were then optimized on the bench using illuminated test patterns (e.g. an eye chart, a uniform grid), to ensure that each leg in the splitter gave the proper view dimensions and was optimally focused. In addition, for the side view system a HeNe laser beam was used to verify that the central ray passed through the center of each component. During these tests the decision was made to remove a pair of 25 mm achromatic lenses from the system, one from each leg of the beam-splitter, in order to improve image resolution at the expense of light loss from vignetting (these lenses are not included in Figure 2-9 – the original design called for a total of six 25 mm achromatic lenses). Finally, due to an error in construction of the beam-splitter housing, the location of the input fiber relative to the dichroic mirror was misplaced. However, there was enough tolerance in the design to correct for this error, and the final fiber input location was set by performing an invessel alignment which ensured that the center of each view was centered on the FSP.

The full fiber/beam-splitter system resolution is estimated from the pixel intensity variation in a line-out of an absolute calibration image (see section 2.3.1, Figure 2-12). In this case only a fraction of the CCD chip is illuminated. In an ideal system the boundary between the illuminated and non-illuminated portions of the image would also be sharp – in reality this boundary is smooth due to finite optical resolution, whose magnitude may be determined from the decay in pixel intensity across the boundary. For this system the average image resolution is found to be ~ 2.5 mm at the plane of the gas injection location. However, the final image resolution is in fact $\simeq 5$ mm for each view, resulting from the use of 9×9 pixel digital smoothing to minimize the contribution from random fluctuations arising from electronic noise. This is discussed further in section 2.4.1.

2.2.5 Image capture & Acquisition

Signals from both cameras are sent from the Alcator C-Mod cell to the C-Mod control room via fiber optic cables. Similarly, exposure timing data is sent from the control room to each camera via fiber optics. The fiber optic signals are converted to and from analog electrical signals using standard transmitter/receiver units [52]. Once signals are in the control room, they are sent to a video frame-grabber board for acquisition. The board being used (model Corona/4) is supplied by Matrox [47]. Software has been written [67] allowing the color board to accept black-and-white input signals on each of the individual color channels (R, G, and B); signals from both cameras are therefore acquired using the same board. A “dummy” camera located in the control room is used as a video signal buffer and plugged into the third color channel to set the timing of the frame-grabber board. This is required because video timing signals from the Xybion cameras were found to be unreliable when sent directly to the frame-grabber board. However, the dummy camera is itself synchronized to the F-top camera video, ensuring that the frame-grabber timing is indeed synchronized to the camera system.

The frame-grabber board is located within a PC dedicated for these experiments. Software has been written [67] to store the camera data locally into a file structure (data tree) similar to that used for the Alcator C-Mod database. Camera images are simply obtained by retrieving data from the proper node in the data tree (e.g. “\video:camera1”). The data tree can be accessed via the VMS or LINUX clusters, allowing data analysis to be done locally or remotely on a workstation.

The resulting output of the image capture system is a 2-D array of intensity values, which range from 0-255 pixel intensity units (PIU). These values are converted to units of brightness ($\text{W}/\text{m}^2/\text{ster}$) through an absolute calibration of the system.

2.3 In-vessel system integration

In this section, a brief description of the methods used to calibrate and align the imaging systems is presented.

2.3.1 Relative & Absolute calibration

Relative pixel calibrations were obtained *in-situ* for each imaging system by placing an illumination source directly in front of the corresponding periscope window and taking images at a number of different exposure levels. For relative calibration of the side view camera system (SVC), the source was one of constant, known brightness (the Labsphere) [42]. However, an *in-situ* relative calibration of the top view camera system (TVC) could not be performed with the Labsphere, as a result of in-vessel spatial constraints. Instead, an intense bulb was employed, whose output was made approximately uniform using a ground glass diffuser. The relative pixel calibration obtained from this setup was then compared to results obtained after the run campaign from a calibration conducted on the bench using the Labsphere. The comparison suggests that the output from the ground glass diffuser was indeed rather uniform (more details below). Therefore, for relative calibration of the TVC plume data, results obtained from the *in-situ* calibration are used.

During relative calibration of the SVC, bandpass interference filters were in place for each leg of the beam-splitter for all images. However, for the TVC, this was only true for small number of images taken at a single exposure level (16.6 ms). The TVC relative calibration was instead determined from images in which no bandpass interference filters were used, and a neutral density filter (ND=1, corresponding to a factor of 10 attenuation) was in place for the CII leg of the splitter. These conditions were necessary to maximize the dynamic range of the camera over which data were taken for each half of the CCD chip.

Calibration curves were generated detailing the response of any given pixel to the exposure time. An example of these curves for each camera system is shown in Figure 2-10. As one might expect, the variation in the pixel intensity with exposure time is roughly linear (especially after 9×9 pixel smoothing, using the SMOOTH function in IDL [25], is employed on the calibration images). Linear calibration coefficients are thus used for each pixel.

Since the input signals are uniform, any non-uniformities in images taken at fixed

exposure are due to variations in pixel response (e.g. due to vignetting losses). These variations are taken into account by requiring that all pixels in a half-image (i.e. in each leg of the beam-splitter) have the same intensity value as the center pixel in that half-image, which is expected to experience the least (and ideally no) vignetting. This results in the generation of a 2-D array of multiplicative factors for each imaging system, calculated at each pixel location by dividing the intensity value at the given pixel by the intensity value at the center pixel in the corresponding half-image. These 2-D arrays represent the relative calibration coefficients for each system, and are referred to as the “vignetting field”. Vignetting fields are calculated at each exposure for which calibration data were taken, and an average vignetting field is constructed from these data. The average vignetting fields for the SVC and TVC systems are shown in Figure 2-11.

The fields shown in Figure 2-11 represent the average response of each imaging system to a normalized uniform input. A strong decay of field intensity near the image boundaries is observed in both systems, suggesting that data near the boundaries may be unreliable as a result of strong vignetting occurring at those locations. In addition, application of the vignetting field from the top half of the SVC to the corresponding plume images results in the appearance of non-physical features in the calibrated CIII SVC data, indicating that this data may not be useful for quantitative analysis of the plume structure (more discussion in section 2.4.2). These fields are nonetheless used to provide a relative calibration for plume images captured from each imaging system.

Absolute calibration coefficients for the SVC are obtained by taking images of the Labsphere when it is placed at the FSP location. An example of such an image is shown in Figure 2-12. The dramatically different intensities in each half of the image result from the convolution of the wavelength dependence of the source output with the spectral response functions of the bandpass interference filters and the camera. In addition, due to the large distance between the probe location and the view, only a small fraction of the CCD chip is illuminated. Nonetheless, this image is more than sufficient to provide an absolute calibration. To determine values for the absolute

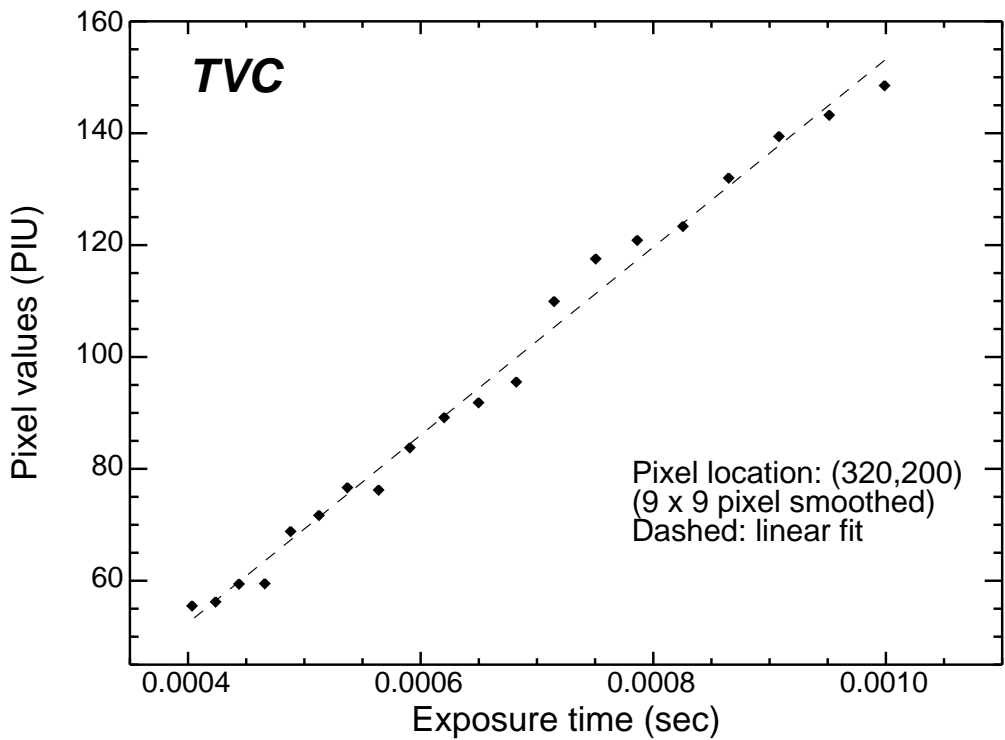
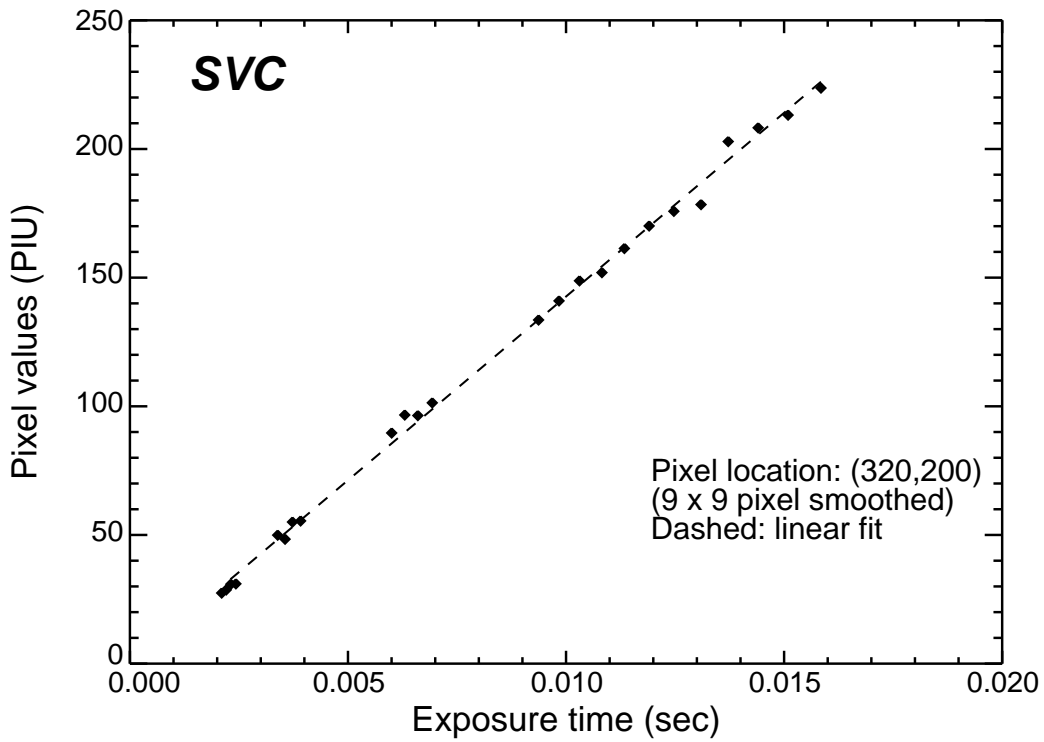


Figure 2-10: Calibration curves for the SVC and TVC at a fixed pixel (for both cases the pixel location is (320,200)). The response of pixel intensity to camera exposure is nearly linear over a wide range of exposure times. In both cases, calibration images are 9x9 pixel smoothed using the SMOOTH function in IDL.

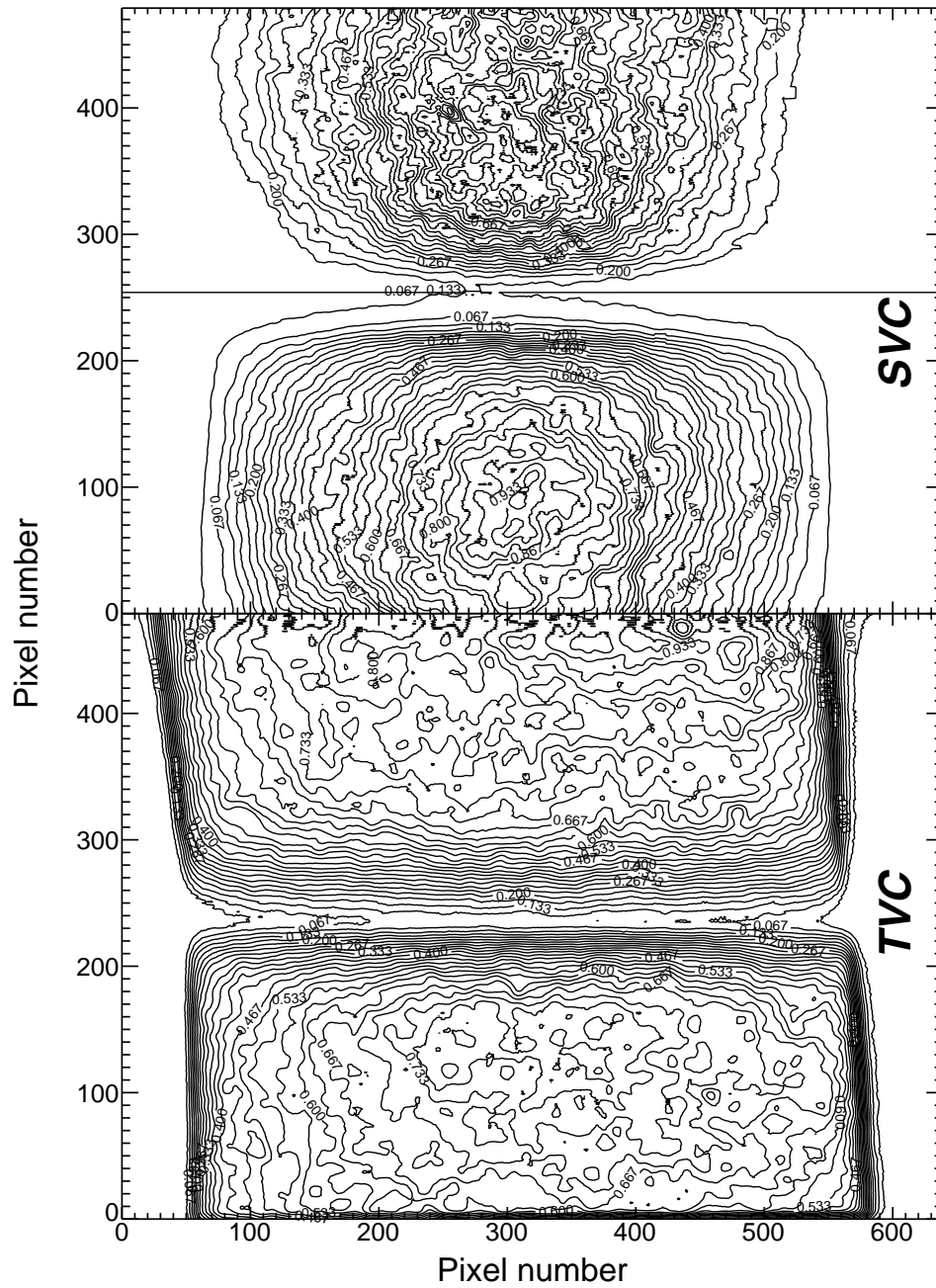


Figure 2-11: Average vignetting fields for the SVC and TVC, used to provide a relative calibration for images obtained from each system. The vignetting field exhibits a strong decay near the image boundaries in each case, suggesting that data near the boundaries may be unreliable.

calibration coefficients based on this image, relative pixel calibration factors (i.e. the vignetting field) for this system are first applied to the image, producing a nearly uniform output. The average pixel intensity value (PIU) of the output image is then set equal to the (convolved) brightness value of the light source ($\text{W}/\text{m}^2/\text{ster}$). Images were taken at 5 different exposure times, and averaging was employed to determine the final values for the CII and CIII absolute calibration coefficients. These values are $8.38 \pm 0.70 \times 10^{-6} \text{ J}/\text{m}^2/\text{ster}/\text{PIU}$ for CII and $2.60 \pm 0.32 \times 10^{-5} \text{ J}/\text{m}^2/\text{ster}/\text{PIU}$ for CIII (the camera exposure time was also included in the calculation – see Equation 2.4 for the exact relationship between pixel intensity and brightness).

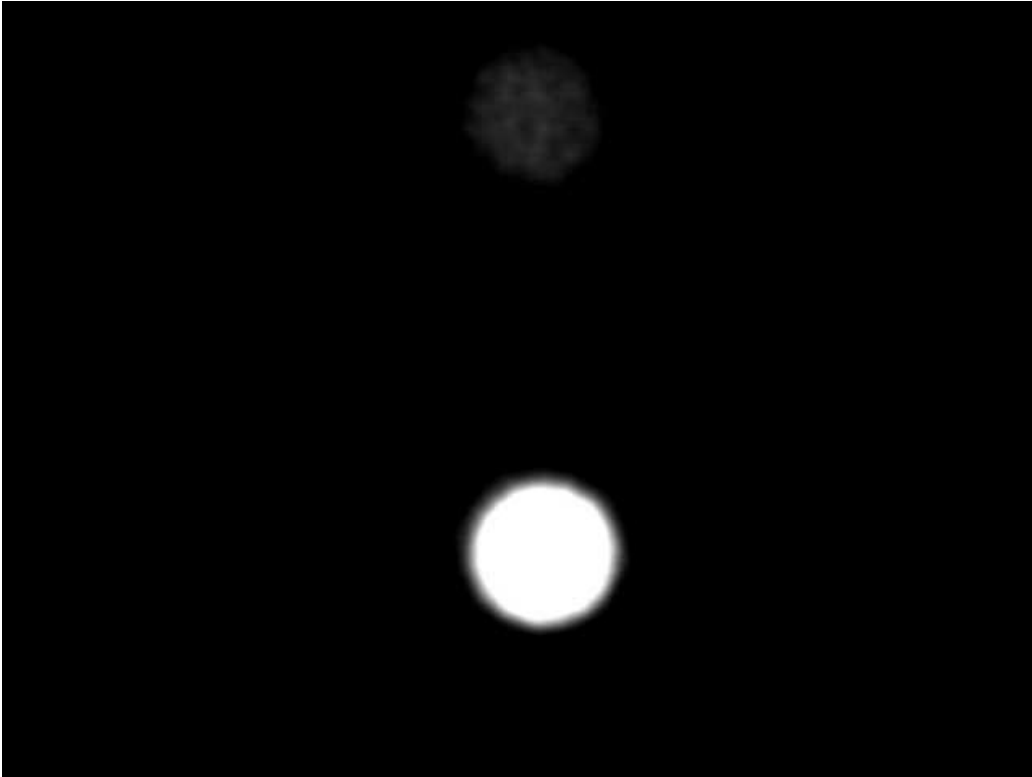


Figure 2-12: Image of the Labsphere located at the FSP location, taken from the side view system (no smoothing, no vignetting field applied). Using the known brightness spectra of this source, and the spectral response functions of the bandpass interference filters and the camera, an absolute calibration for the system can be obtained.

For the TVC, absolute calibration coefficients could not be obtained in the same manner, because images taken from this view of the Labsphere at the FSP location

were too dim to be useful. Values for these coefficients were instead determined from system calibrations conducted on the bench after the run campaign. These calibrations were also used to validate the relative calibration data obtained from the *in-situ* calibration. A comparison of relative calibration results from in-vessel calibration using the ground glass diffuser system and from bench calibration using the Labsphere is shown in Figure 2-13. In both cases results (given in terms of a normalized response to a normalized input) are averaged over the vertical pixel range corresponding to the CIII portion of the CCD chip. Note that the system configurations are not identical for the two cases, as a result of the imaging system being disassembled immediately after the run campaign and then re-assembled some time later. Nonetheless, the comparison indicates that the response of the TVC to the ground glass diffuser output and to the Labsphere is approximately the same (within the deviation of the results).

Absolute calibration coefficients for the TVC were obtained using a pair of images of the Labsphere, each taken with the output plane of the Labsphere slightly displaced from the input plane of the fiber bundle, and with bandpass interference filters in place for each leg of the beam-splitter. Again, the vignetting field for this imaging system, obtained from *in-situ* calibration results (Figure 2-11, bottom panel), is first applied to each image to produce a nearly uniform output. The average pixel intensity value of each resulting image is then set equal to the brightness value of the light source, calculated from a convolution between the wavelength dependence of the source output and the spectral response functions of the interference filters and the camera. Average values for the absolute calibration coefficients determined from this calculation are $5.34 \pm 1.02 \times 10^{-5}$ J/m²/ster/PIU for CII and $3.70 \pm 0.72 \times 10^{-5}$ J/m²/ster/PIU for CIII. There may be some uncertainty associated with applying these values to the plume data, since they were not obtained from images taken *in-situ* at the FSP location. However, results from a cross-calibration between the SVC and TVC plume data indicate that these values are appropriate (more details below).

Values of the absolute calibration coefficients for the TVC are found to be larger than corresponding values for the SVC. In addition, the relative variation between

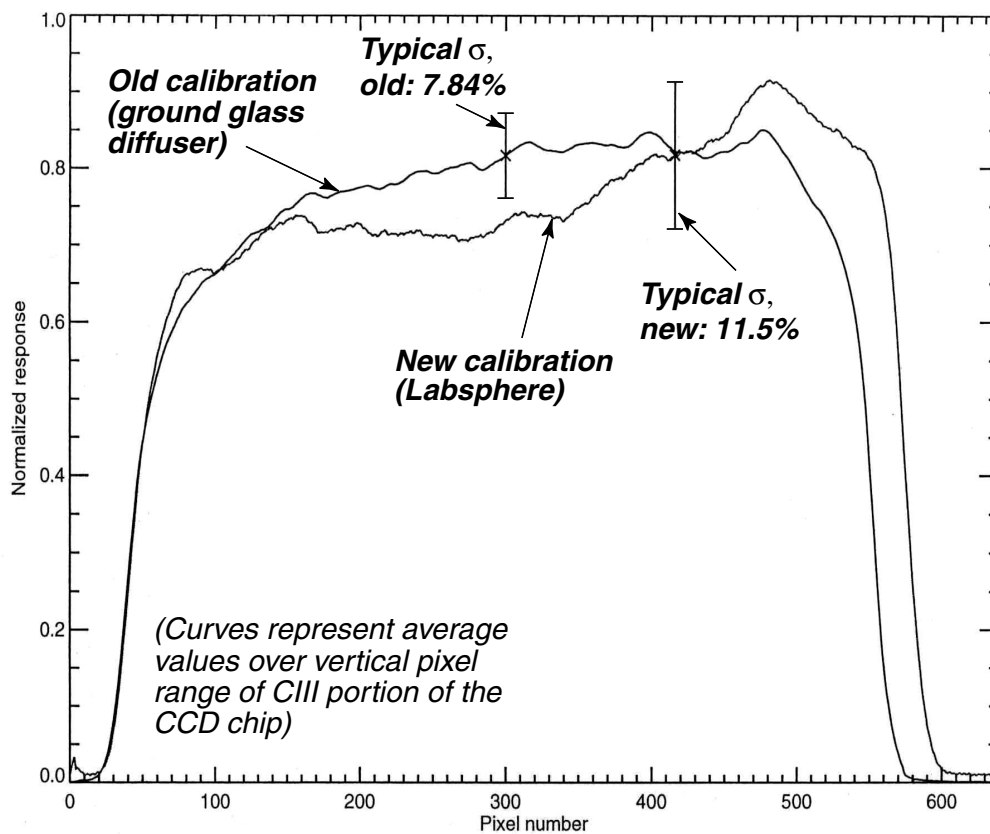


Figure 2-13: Comparison between relative calibration results for the TVC from in-vessel calibration using a ground glass diffuser system and bench calibration using the Labsphere. In both cases results (given in terms of a normalized response to a normalized input) are averaged over the vertical pixel range corresponding to the CIII portion of the CCD chip.

values of the CII and CIII coefficients differs for the SVC and TVC, indicating that the cameras have very different spectral response. These results are consistent with the weak intensity observed on both halves of the image during attempts to conduct an *in-situ* absolute calibration of the TVC using the Labsphere, explaining why such a calibration was not possible. Nonetheless, for a given plume, pixel intensity values observed on the SVC and the TVC are found to be comparable for comparable values of the camera exposure times (which are typically within a factor of 2). This suggests that the plume brightness viewed by the TVC ($\text{W}/\text{m}^2/\text{ster}$) can be larger than the plume brightness viewed by the SVC. A possible explanation for this discrepancy is an error in the calibration results. This is investigated by cross-calibrating the SVC and TVC plume data, which involves using data from each view to calculate an estimate for the total power per unit solid angle (W/ster) being emitted from a particular slice of the plume emission along **B**. These calculations were performed for a number of slices in a number of plumes, and it was found that estimates of the power per unit solid angle obtained from each view were approximately equal in each case (to within $\simeq 22\%$). This indicates that the calibration results are accurate, and that therefore the plume brightness viewed by the TVC is indeed larger than for the SVC. The cause of this difference is thought to be a vertical elongation of the plumes down the probe axis, which is discussed further in section 3.1.4.

2.3.2 Distortion correction

Distortions due to pin-cushioning and/or barrel effects are present in most optical systems [31]. For the plume imaging diagnostic, these distortions are calibrated out *in-situ* using a back-illuminated grid. The grid is constructed from an aluminum plate, in which 1/4" diameter holes were drilled in a regular pattern (1" spacing). A few off-center holes were also included to provide absolute reference points. Images of the grid, placed at the FSP location in an otherwise darkened vacuum vessel, were then taken from both views. These images are shown in Figures 2-14 and 2-15. A gross estimate for the grid centroids is determined (interactively) in IDL using the CURSOR function. Once these are obtained, a more precise calculation is performed

for each grid point using an intensity-weighted “center-of-mass” algorithm. In order to provide a distortion map for the entire image, false grid points are added to the boundaries – the centers are calculated from a linear extrapolation of the real grid points.

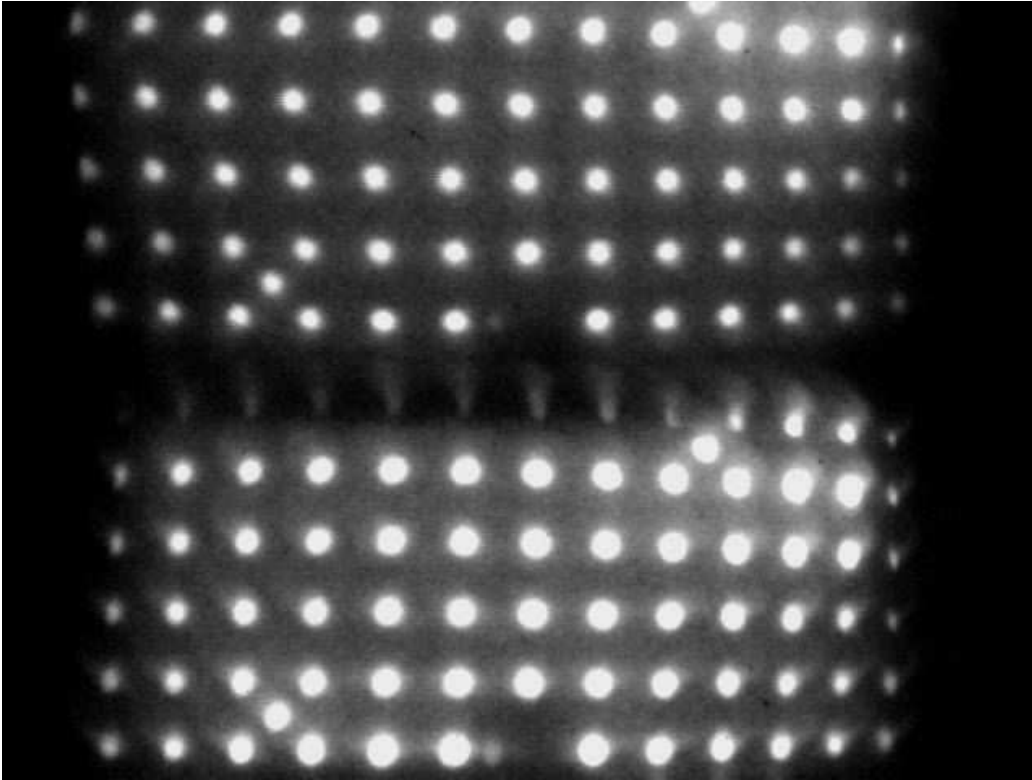


Figure 2-14: Image taken from the side view system of a back-illuminated grid. Interference filters were removed from each leg of the beam-splitter in this case. This image is used to obtain a distortion correction for the system.

If the images exhibited no distortion, then all grid points would align, both horizontally and vertically. The spacing between grid points (in pixel space) in this “ideal” image is determined by assuming that there is no distortion near the center of each half of the real image. This allows for the calculation of an “ideal” grid for each half of each view. The IDL function `WARP_TRI` is then used to map points in the distorted (real) space to points in the ideal space. Contour plots of the undistorted grid images are shown in Figure 2-16. The mapping obtained from these calculations is used to calibrate out distortion effects in the plume images. Finally, the data in

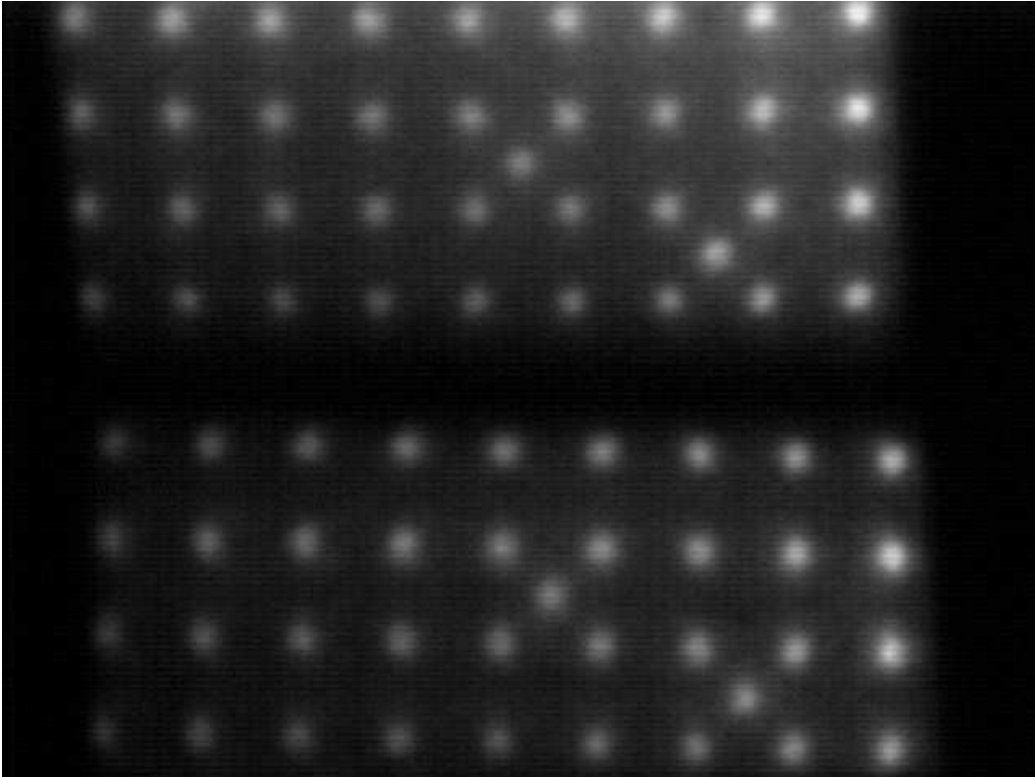


Figure 2-15: Image taken from the top view system of a back-illuminated grid. Interference filters were removed from each leg of the beam-splitter in this case. This image is used to obtain a distortion correction for the system.

Figure 2-16 also provides a relative mapping between pixels in the upper and lower halves of each CCD chip, allowing for a relative alignment between CII and CIII emission.

2.3.3 Absolute view alignment

To determine both where the plume emission is located in the SOL (e.g. near vs. far), as well as the position of the injection nozzle in each plume image, it is necessary to know where the emission is in machine coordinates. An absolute alignment of each view was determined by taking images of a small ($\frac{1}{4}$ " diameter) bulb placed at fixed locations inside an otherwise darkened vacuum vessel (*side view*: at the gaps along the inner wall; *top view*: at tile gaps along a fixed major radius). A composite image generated for all of the bulb locations is shown for each view in Figure 2-17 (*note*: images taken from the F-top camera exhibit poor resolution, due to condensation on the periscope window during alignment calibration). These images have been undistorted using the mapping determined from the back-illuminated grid calibration. In each image, bulb centroids are determined by first getting gross estimates for the pixel coordinates manually, and then using these results to obtain more accurate values from an intensity-weighted centroid calculation (the same algorithm used to determine grid centroids in the distortion correction). The distance between bulbs provides a scale (pixels/cm) for each image, which can be compared to values determined from the grid calibration. For both imaging systems, scale values obtained from both methods agree rather well with one another (to within $\lesssim 10\%$).

2.4 Image analysis

A series of algorithms have been developed to facilitate interpretation of the plume emission patterns. In this section, a brief description of these algorithms will be presented.

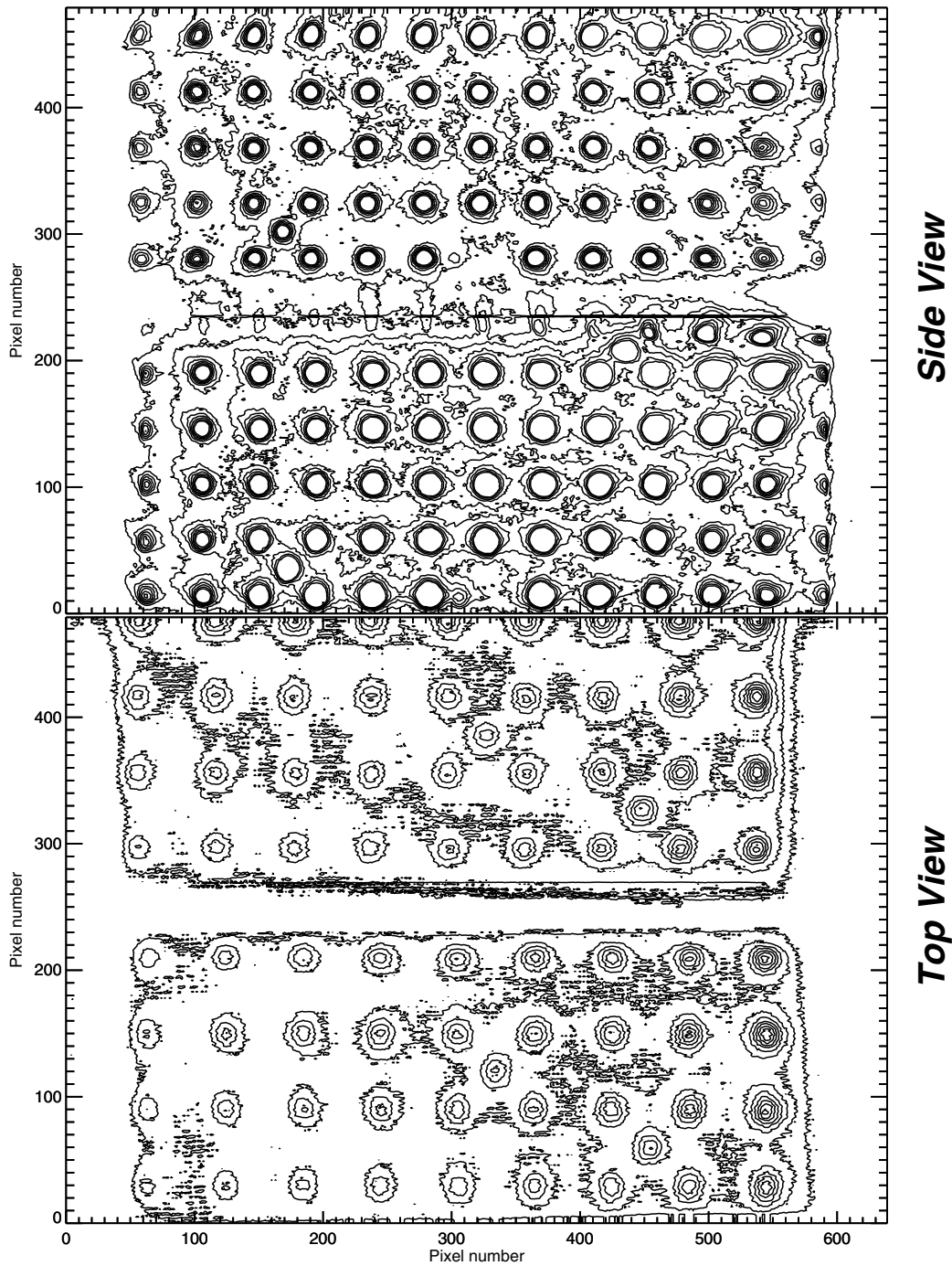


Figure 2-16: Un-distorted image from the side and top view systems of a back-illuminated grid (originals in Figures 2-14 and 2-15). The mapping used to undistort the original images will be used to undistort plume images.

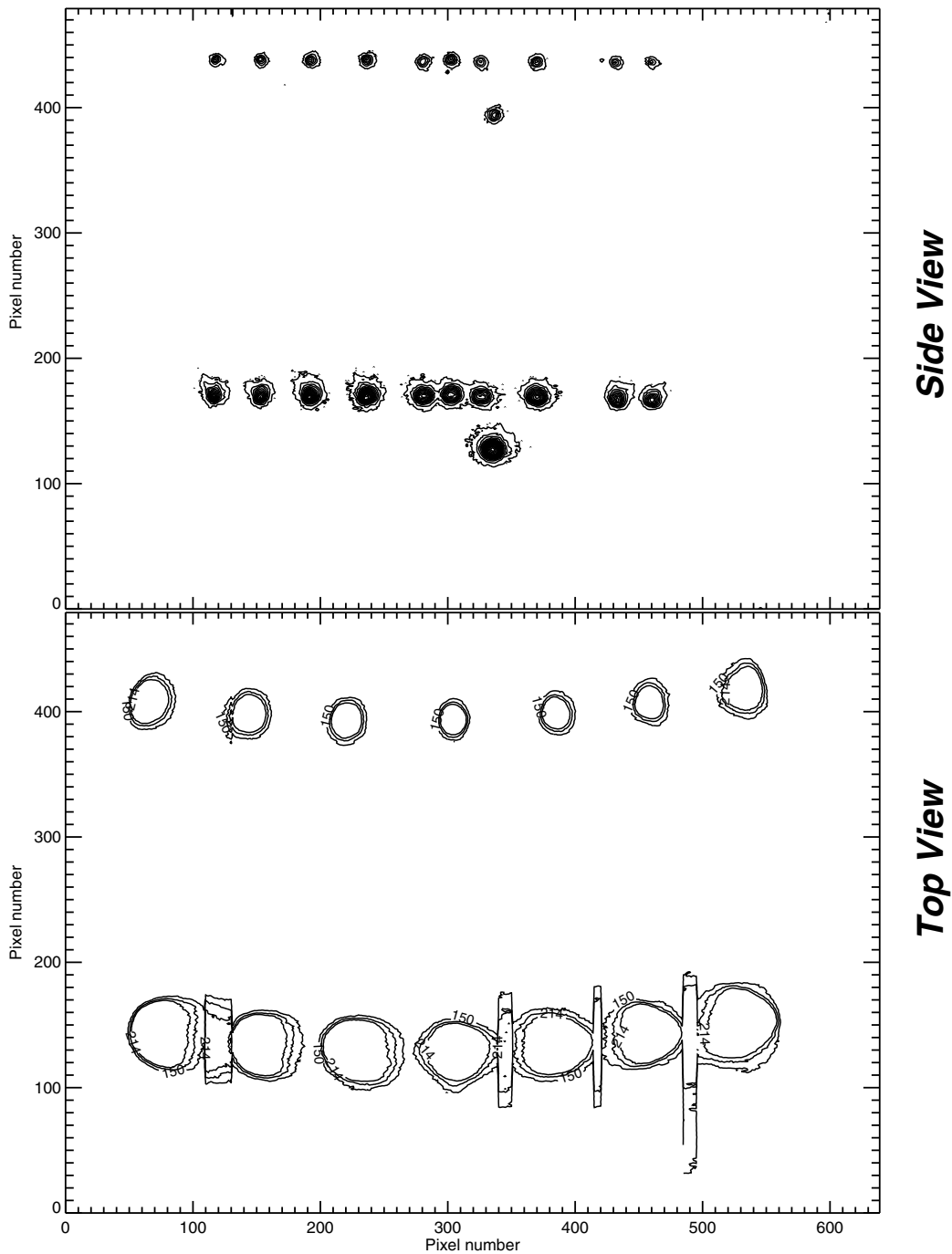


Figure 2-17: Superimposed alignment images from the F-side and F-top cameras. Images have been undistorted using mappings obtained from a back-illuminated grid calibration. These images provide a reference for the plume emission in machine coordinates, as well as a separate means of determining the pixel scale for each view.

2.4.1 Generating plumes

Plume images are captured using a video framegrabber and stored locally on a PC in a file structure similar to that used for data acquisition on C-Mod. Image data can then be read into IDL variables using MDS [66] commands.

An example of the exposure and readout timing for the SVC camera system is shown in Figure 2-18. As illustrated in the figure, exposure gates (top panel) are sent to the camera at times corresponding to the peak insertion of the probe (i.e. when gas is injected) and at a time halfway in between probe insertions. This intermediate exposure allows contributions from background radiation to be assessed. Triggers for data acquisition are sent to the video frame-grabber board (bottom panel) every 33 ms, corresponding to the frame rate of the camera. The first frame after an exposure gate (the capture trigger for this frame is shown in blue) is expected to correspond to the readout time of a plume or background image. However, in a number of cases for the SVC, and in all cases for the TVC, images from a single camera exposure would persist (at reduced intensity) over multiple frames. Apparently, the charge on the CCD chip is not completely transferred in one readout. In general, the readout is found to occur over the first 2-3 frames after an exposure gate is sent to the camera, which limits the time between camera exposures to be ≥ 100 ms. A full plume or background image at a given time is therefore constructed by summing together frames corresponding to a single exposure. An identical procedure was used to construct images used in the relative and absolute calibration of each system.

An average value for the background emission is then subtracted from the plume emission (typical values for this background are 5-10 PIU, compared to typical plume values of 200-300 PIU). This typically leads to some pixel intensity values becoming negative – primarily at those pixels near the edge of the chip, whose values were low to begin with. Since these initially low values contribute little to the plume emission, any negative values are set to zero. Finally, each image is 9×9 pixel smoothed using the IDL SMOOTH function. This function uses a box-car smoothing algorithm, so that at each pixel location the smoothed value is the average of pixel intensity values over a 9×9 window centered on the pixel in question. The window size was chosen

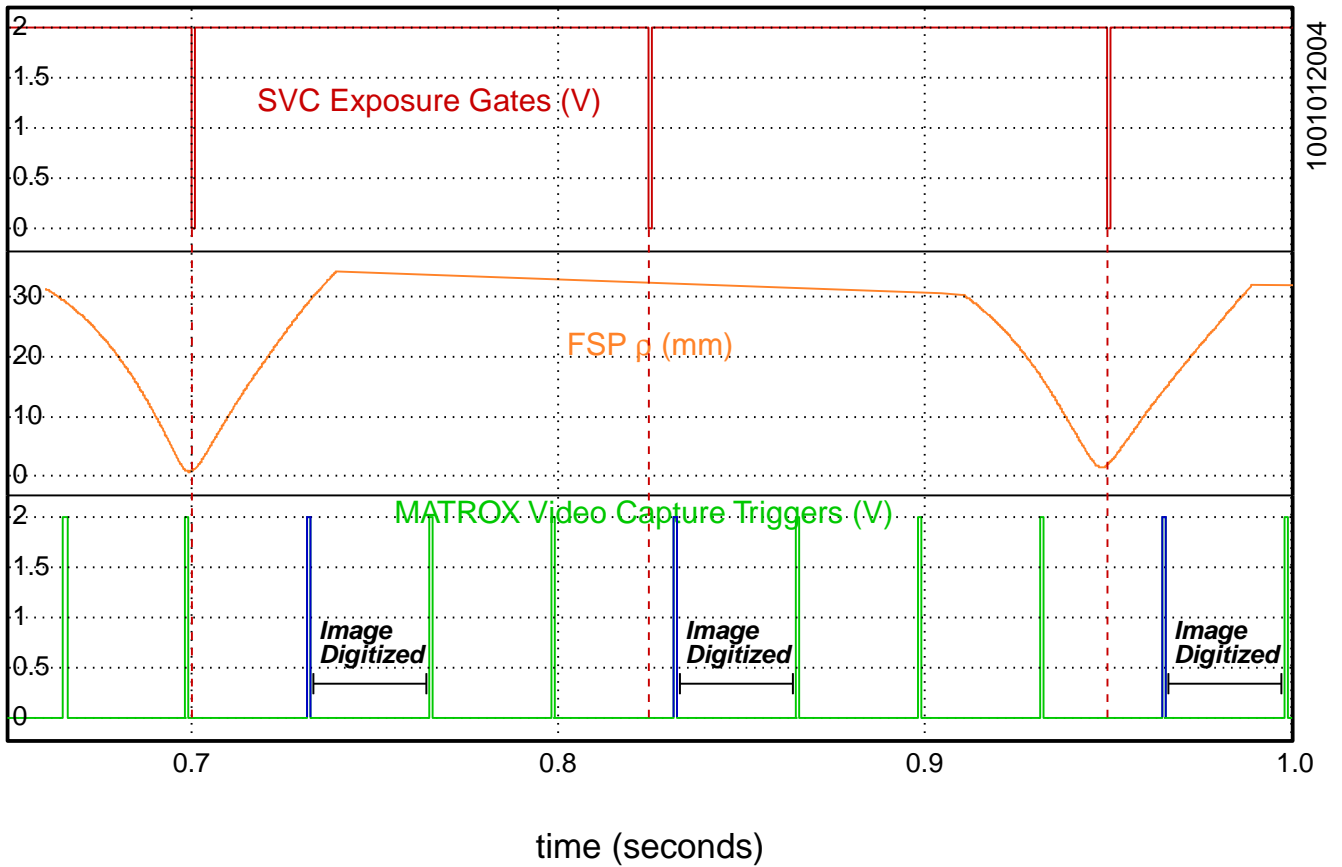


Figure 2-18: Example of exposure and image readout timing for the SVC camera system. Exposure gates (top panel) are sent to the camera at times corresponding to the peak insertion of the probe (i.e. when gas is injected) and at a time halfway in between probe insertions. Triggers for data acquisition are sent to the video frame-grabber board (bottom panel) every 33 ms, corresponding to the frame rate of the camera.

based on an optimization between maintaining good image resolution and minimizing fluctuations due to electronic noise. The final resolution of the imaging system set by this smoothing window is $\simeq 5$ mm for each view.

2.4.2 Brightness calibration & uncertainties

Two sources contribute to uncertainty in the calibrated emission data: random fluctuations in the pixel intensity values, and uncertainties in the relative calibration field. Fluctuations in pixel intensity values were determined for each imaging system by recording shot-to-shot variations in the pixel intensity for a fixed exposure to the corresponding uniform source (SVC: Labsphere; TVC: ground glass diffuser). For the SVC the standard deviation (σ_{pv}) was $\simeq 28$ PIU, while for the TVC the standard deviation was $\simeq 8$ PIU (in both cases these values represent an average over the CCD chip). This difference results from differences in the system designs – due to spatial constraints for the SVC periscope, the solid angle for the SVC view is much smaller than that for the TVC, and thus to utilize the full dynamic range of the camera a higher intensifier voltage is required for the SVC, leading to a larger contribution of electronic “shot noise”.

Uncertainties are present in the relative calibration fields because these represent average values of vignetting field data taken at a number of different exposures. A total of 15 images were used for the SVC, at exposure times ranging from $\simeq 2.1$ -16.6 ms, while for the TVC a total of 25 images were used with exposure times ranging from $\simeq 0.40$ -1.05 ms.

For the SVC, the standard deviation in the relative calibration value at a given pixel location (σ_{rc}) was found to be related to the random fluctuations in pixel intensity value (σ_{pv}). σ_{pv} values (and thus σ_{rc} values) for the SVC are found to differ from pixel-to-pixel, and a 2-D array of σ_{pv} values is stored along with the relative calibration data for use in generating standard deviation error fields for the SVC plume images.

For the TVC, uncertainties in the pixel intensity value at any given pixel location due to uncertainties in the relative calibration data were found to be proportional to

the value of the relative calibration factor at that location (i.e. $\sigma_{rc} \propto R_c$, where R_c is the relative calibration factor). In addition, for the TVC the uncertainty in pixel intensity value due to random fluctuations (σ_{pv}) was found to be roughly constant over the full range of pixels. These results are summarized in Table 2.3.

	σ_{pv} (PIU)	σ_{rc} (PIU)
Side View	28 (average; varies pixel-to-pixel)	$0.20 \sigma_{pv}$
Top View	8 (average; constant pixel-to-pixel)	$0.087 R_c$

Table 2.3: Summary of uncertainties in calibrated plume data (R_c is the relative calibration factor for the TVC, which varies pixel-to-pixel – see Figure 2-11).

Since values for the TVC relative calibration factors are between 1-10 over most pixels (see Figure 2-11), results from Table 2.3 suggest that uncertainties in the SVC data are significantly larger than for the TVC. In addition, when the SVC calibration field is applied to plume data, features result which are non-physical, e.g. the formation of emission “islands” in the CIII plumes (see Figure 2-19). As a consequence, the parallel extent of the emission (characterized by moment analysis – see section 2.4.5) tends to be much larger when viewed from the SVC than from the TVC, representing an inconsistency in the experimental data. These results suggest that the SVC data may have limited use in the quantitative analysis of the plume structure.

It is straightforward to compute absolutely calibrated brightness fields from plume images – the relative calibration fields are first applied to the pixel intensity values to generate relatively calibrated images, and these results are then multiplied by the absolute calibration coefficient and divided by the camera exposure time to yield an image in units of brightness ($\text{W}/\text{m}^2/\text{ster}$):

$$b = \frac{P_v R_c b_c}{\tau} \quad (2.4)$$

where b is the brightness on a given pixel, P_v is the pixel intensity value (PIU), R_c is the relative calibration factor for the pixel, b_c is the absolute calibration factor ($\text{J}/\text{m}^2/\text{ster}/\text{PIU}$), and τ is the camera exposure time (s). To generate the standard

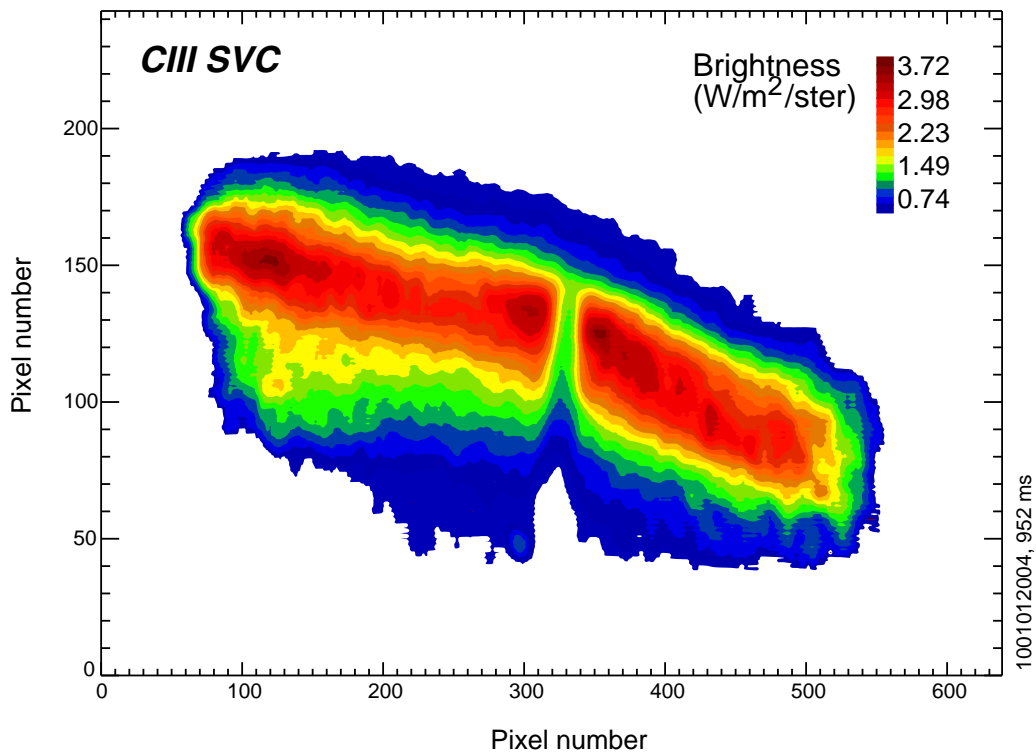


Figure 2-19: Example of a calibrated CIII SVC plume. Problems with the calibration field lead to non-physical results, such as the peaking of emission away from the injection location and/or the formation of emission “islands”.

deviation error fields, simple error propagation formulas are used, neglecting uncertainties in b_c and τ :

$$\sigma_b^2 = \left(\frac{P_v b_c}{\tau}\right)^2 \sigma_{rc}^2 + \left(\frac{R_c b_c}{\tau}\right)^2 \sigma_{pv}^2 \quad (2.5)$$

2.4.3 Image alignment to the local magnetic field

To distinguish between parallel and cross-field asymmetries in the emission data, plumes are mapped to field-aligned coordinates. The field line trajectory at the gas injection location is determined using the EFIT [43] magnetic reconstruction code. An absolute position in machine coordinates is required to determine the proper trajectory – this is achieved using the absolute alignment obtained during *in-situ* calibration (section 2.3.3). EFIT is also used to determine the trajectory perpendicular to \mathbf{B} . This provides an absolute origin for the emission data.

For each view, the brightness at any given pixel location represents the measurement of the integrated emission along the viewing chord. To map the plumes to a field-aligned coordinate system, this integrated emission is ascribed to a small volume located on the flux surface that the gas injection nozzle is located when the probe is at peak insertion. This is illustrated in Figure 2-20. To the extent that any cross-flux surface spreading in the plumes is small, and that the magnetic shear near the gas injection location is also small, this approximation will yield a valid estimate of the field line trajectories in the plume emission volume. Any field line trajectory on the flux surface may be determined by shifting the trajectory of a single field line passing through the gas injection location by a fixed toroidal angle.

Field line trajectories and plume emission data on the flux surface are then projected onto image planes at the injection location (see Figure 2-20) using an intersection algorithm developed by B. LaBombard [41]. In Figure 2-21, an example of CIII TVC data mapped to the appropriate image plane is shown, with corresponding field line projections overlaid.

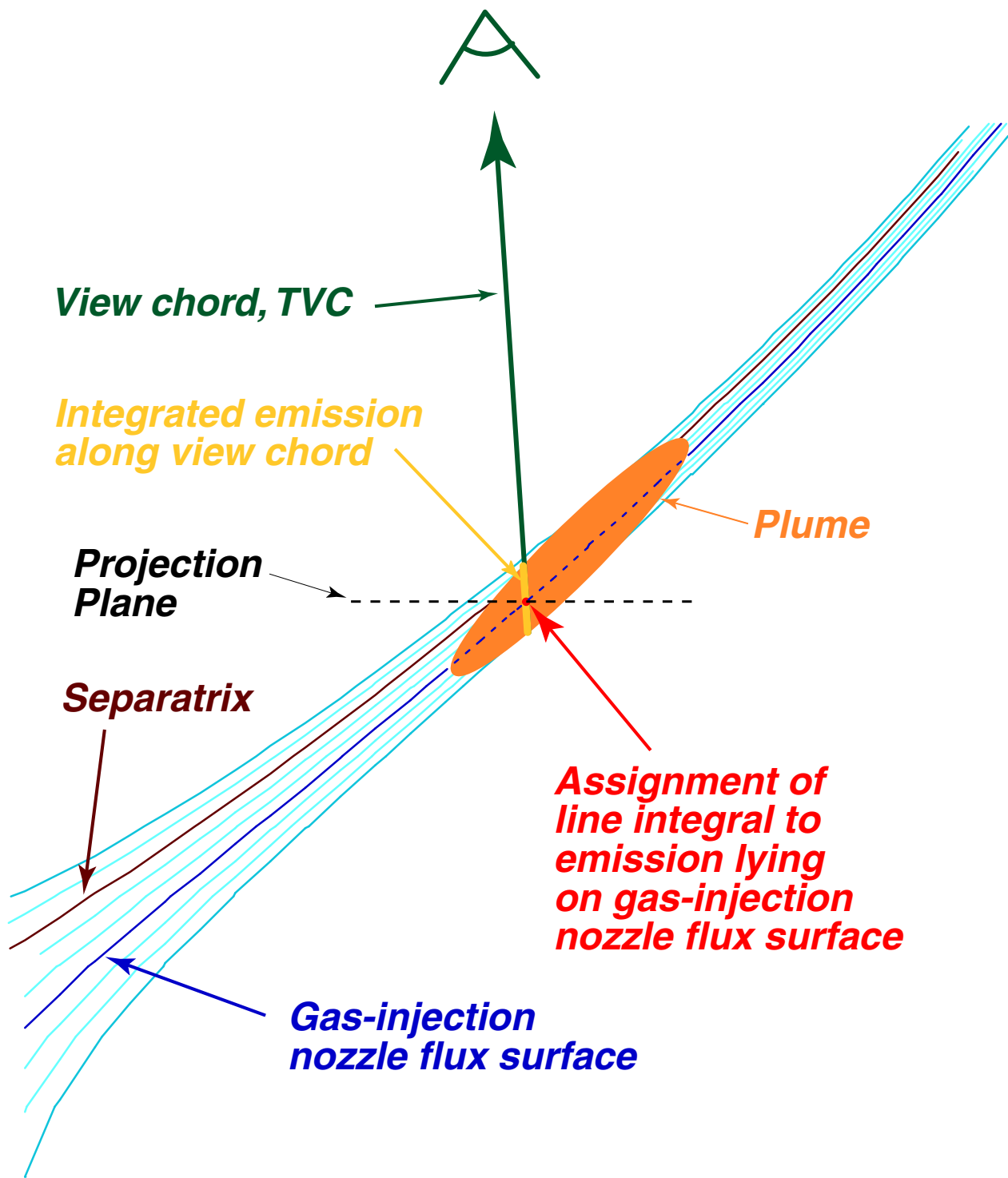


Figure 2-20: Illustration of the method used to map plume emission from the TVC to field-aligned coordinates. Any emission contributing to signal at a given pixel location is assumed to be localized to the flux surface at which the gas injection nozzle is located when the probe is at peak insertion. Field line trajectories on that flux surface are determined by shifting the trajectory of a single field line at the gas injection location by fixed amounts in toroidal angle.

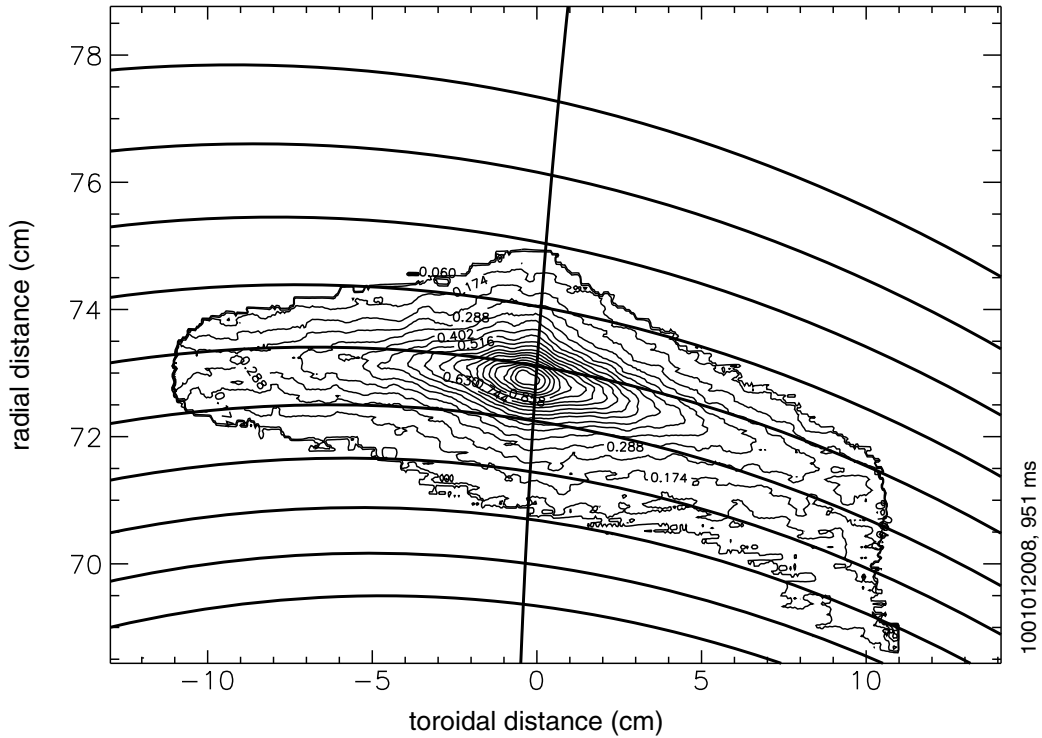


Figure 2-21: Example of CIII TVC emission which has been mapped to the image plane at the gas injection location, with corresponding field line trajectories overlaid. These trajectories are used to map the emission to field-aligned coordinates.

From the projected image and field line data, distances along and across field lines may be easily calculated. These distances define the field-aligned coordinate system for the plume emission. The IDL procedure WARP_TRI is used to map emission data from normal to field-aligned coordinates. In Figure 2-22, an example is shown of field-aligned CIII data seen from the TVC.

2.4.4 SVC rotation correction

It was determined that during the course of the 2000 run campaign the fiber bundle providing the side view of the FSP underwent rotation. The cause of the rotation is unclear, but is likely due both to the amount of activity that took place near the port in which the fiber is located as well as an inadequate mechanism for fastening the fiber inside its periscope.

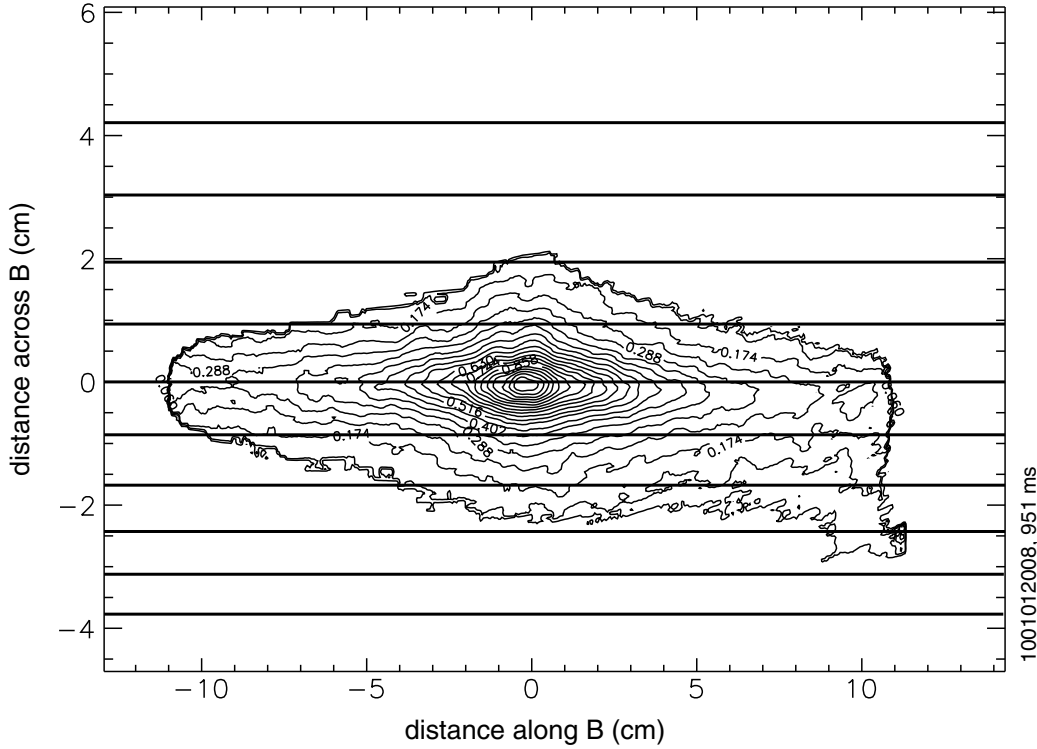


Figure 2-22: Example of field-aligned CIII emission seen from the TVC (unaligned data shown in Figure 2-21).

Just as a bulb was taken into the machine and imaged from both views to provide an absolute alignment for the imaging systems before the start of the campaign, at the end of the campaign the same set of alignment images were generated. Composite images for the SVC from before and after the campaign are shown in Figure 2-23. In both cases, the bulb was aligned horizontally along the inner wall.

It is clear from comparing before and after images that the fiber underwent rotation. The image resolution is also much poorer, suggesting that the camera lens attached to the fiber partially unscrewed during rotation, changing its effective focal length. Centroids were calculated for each set of bulb images in each half of the image, after which a linear fit to the centroid positions was performed. The intersection of the two lines provided the pixel location about which the rotation occurred in each half-image. The total rotation angle was also determined from this calculation, and was found to be $\simeq 10.6^\circ$.

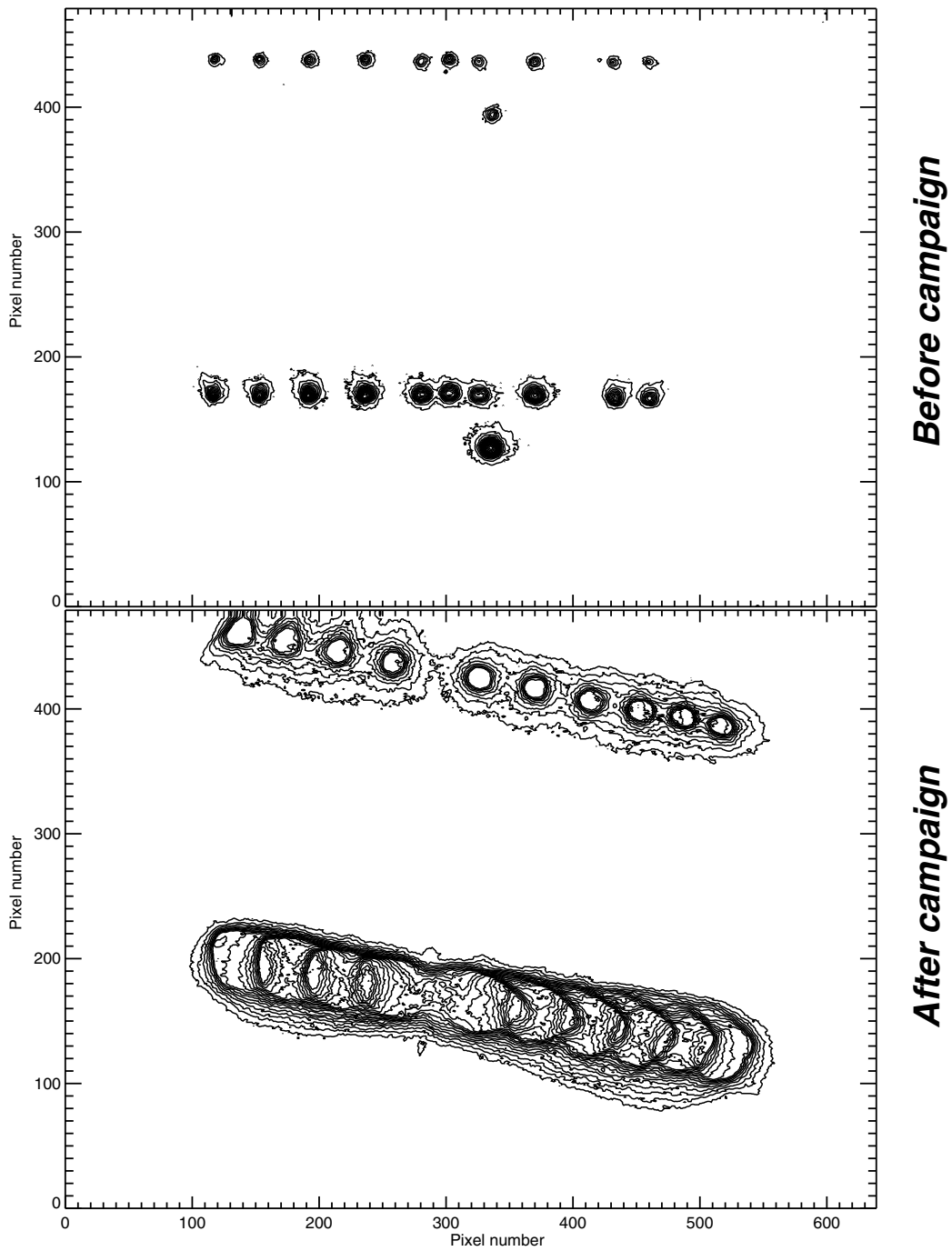


Figure 2-23: Composite images from the SVC of an bulb placed at various locations in the vessel. *Top*: Image from before the start of the run campaign. The bulbs were horizontally aligned along the inner wall. *Bottom*: Image from the end of the run campaign. Bulbs again were placed along a horizontal, but appear skewed due to the fiber rotation.

This angle likely represents the full rotation of the fiber, from start to end of run campaign. However, it is also likely that the fiber did not rotate this full amount all at once, but instead rotated by various amounts over the course of the campaign. To determine how much rotation occurred on a given run day, information present in the images themselves is utilized. An example of data taken from the SVC is shown in Figure 2-24. In this image, there is a “divot” due to the presence of the probe (because the probe body is situated between the gas-injection capillary and the view – see Figure 2-6). Since the view is perpendicular to the probe scan direction, this divot should be aligned vertically – however in the image it exhibits some tilt, indicative of the fiber rotation. An algorithm has been developed to determine the angle of rotation for the divot, based again on an intensity weighted centroid calculation. For the case shown in Figure 2-24, the rotation angle fit is shown in Figure 2-25. The image is rotated by the calculated divot angle, to “straighten it” out, using the IDL ROTATE function and the known center of rotation. The “straightened-out” image corresponding to the data in Figure 2-24 is also shown in Figure 2-25. This technique is used to correct for fiber rotation for any shot of interest.

2.4.5 Moment Analysis

To extract meaningful information out of the plume structure, simulation of the emission pattern will be undertaken. However, it is important to establish the criteria for determining a “match” between simulation and experiment. In principle, a direct comparison between experimental and simulated 2-D plumes provides one such measure. However, there are a number of problems with this technique, including what to do about emission near the probe head, which is not properly modelled in the simulation.

The wealth of information contained in each plume can be characterized in terms of a finite number of parameters using spatial moments of the 2-D emission pattern. Moment parameters can be calculated equivalently for both simulated and experimental data, eliminating ambiguity over the influence of the probe on the emission results. These calculations also allow a more direct means for performing sensitivity

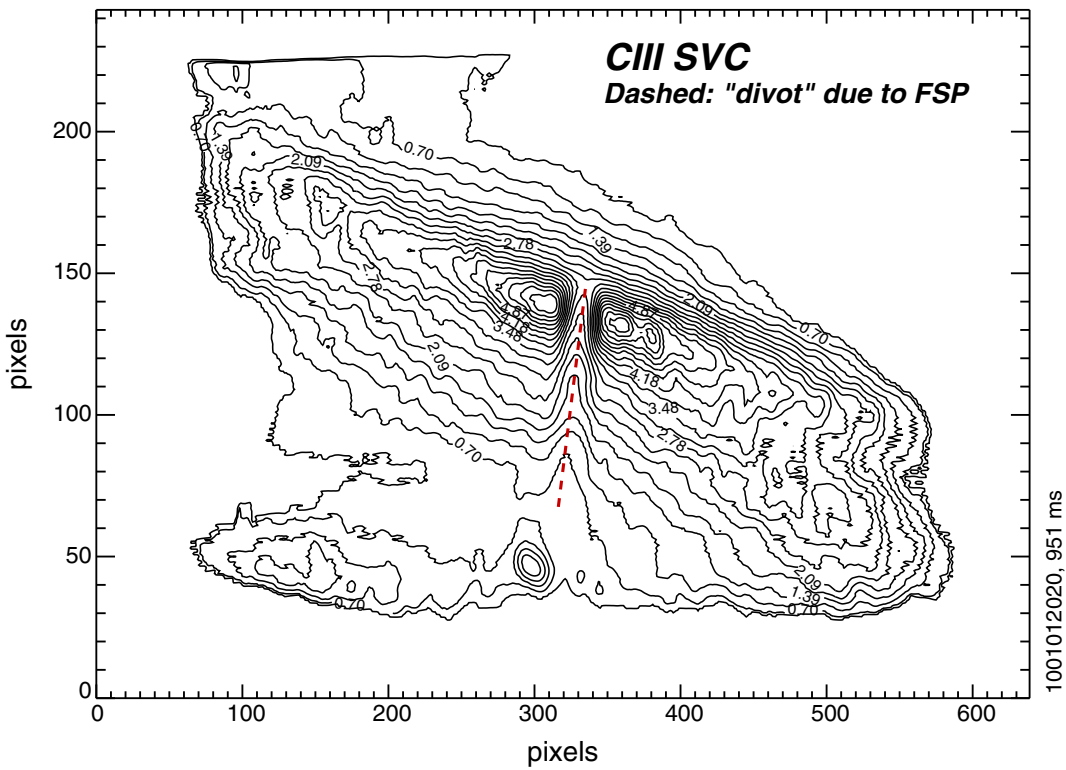


Figure 2-24: Example of CIII SVC data exhibiting rotation. The rotation angle is determined by trying to vertically align the “divot”, which is due to the presence of the probe.

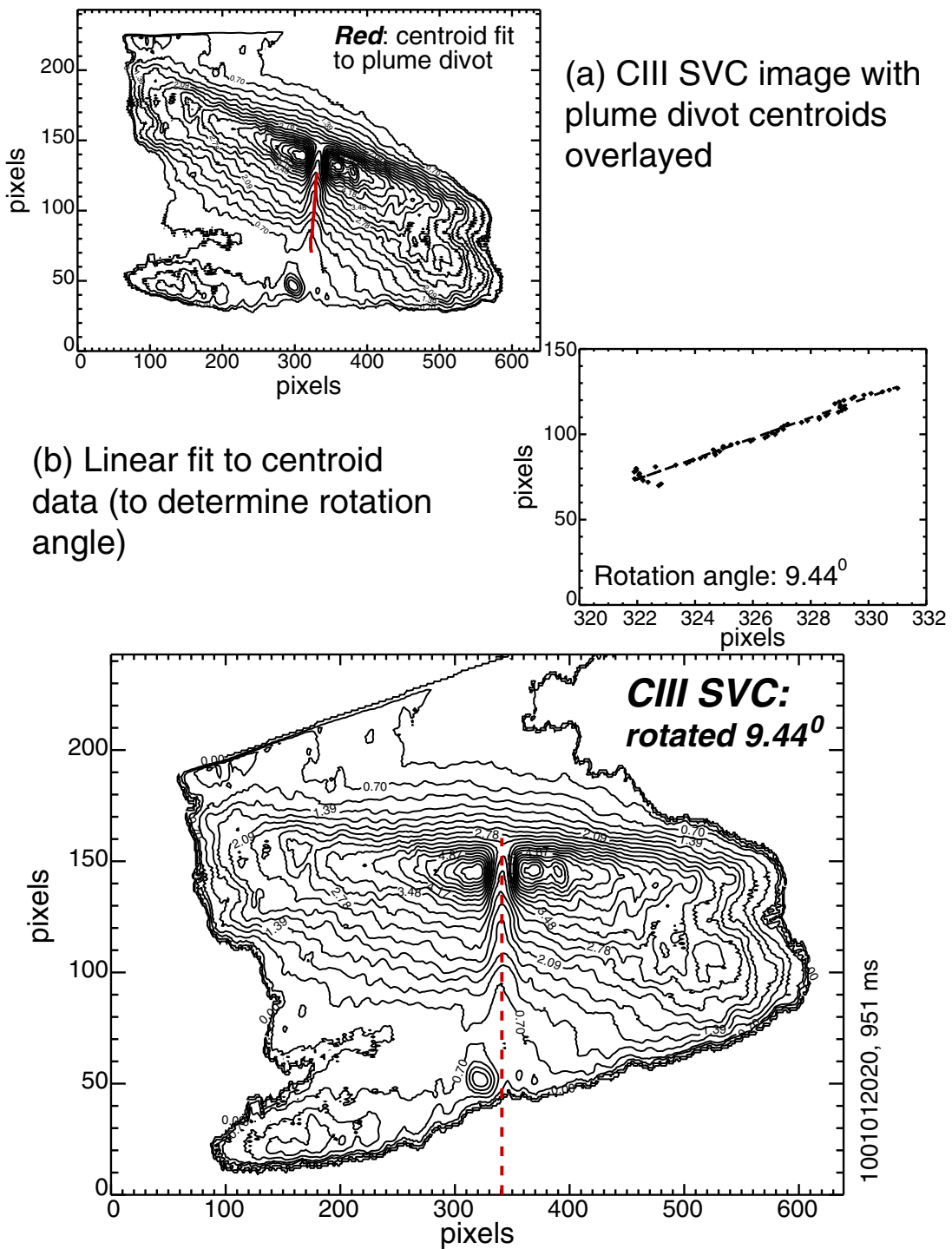


Figure 2-25: *Top: (a)* CIII SVC plume with calculated divot centroids overlaid. *(b)* Linear fit to divot centroids for determination of rotation angle. *Bottom:* Corrected SVC image, rotated using angle determined from fit. The ROTATE function in IDL is used to make the correction.

studies in the simulations (e.g. see section 5.7), since the variation of specific code inputs can be directly related to variation of specific moment parameters. From this analysis a clearer understanding of the physics involved in setting the plume structure may be obtained.

Definitions of various moments

For a function $f(x)$, the first three moments are defined as:

$$\bar{x} = \int_{-L}^L \frac{xf(x)}{F} dx \quad (\text{centroid}) \quad (2.6)$$

$$w^2 = \int_{-L}^L \frac{(x - \bar{x})^2 f(x)}{F} dx \quad (\text{variance}) \quad (2.7)$$

$$s = \int_{-L}^L \left(\frac{x - \bar{x}}{\sigma} \right)^3 \frac{f(x)}{F} dx \quad (\text{skewness}) \quad (2.8)$$

where $F = \int_{-L}^L f(x)dx$. The spatial moments are meaningful as long as $f(x)$ tends to zero near the boundaries ($[-L, L]$). For use with emission data, these equations are discretized.

At each parallel coordinate, a 1-D cross-field profile of the emission is available. Using the above equations, the centroid and width (square root of the variance) of the profile can be calculated. 1-D arrays of these values are generated as a function of the parallel coordinate for each plume. Since the influence of the probe head (*side view*: obscuring of the emission by the probe; *top view*: enhancement due to reflections) is not properly modelled in the simulations, data near the probe head is neglected (i.e. results from this region are not included in comparisons between experiment and simulation). The total integral of the 1-D cross-field profile may also be calculated at each parallel coordinate, resulting in a 1-D parallel emission profile for each plume.

The 1-D parallel emission profile is observed to decay exponentially on either side of the probe head. The parallel extent of the emission can therefore be characterized by decay lengths obtained from fits to the profile data. The 1-D array of centroid data is used to calculate the deviation of emission from field lines (i.e. the plume “boomerang” angle, which will be discussed further in Chapter 3), while an average

cross-field width for the plume is determined from the 1-D array of width data.

Practical considerations

The extent of the region near the probe head over which data is neglected in the moment calculations is given as an input to the algorithm. In addition, a minimum brightness level is set to limit the data used in the calculations (i.e. values below this threshold are not included). This typically eliminates data near the edges of the plume, which is desired since the edges represent regions of low signal-to-noise. The minimum brightness level is determined from an algorithm used to estimate the effective cross-field width of the emission, and is typically $\sim 10\%$ of the maximum plume brightness. The minimum brightness level determined for an experimental plume is also used for moment analysis of numerical plumes (see section 4.3) generated to simulate the experimental data. Finally, an additional constraint may be included to limit the parallel extent of the plume over which the calculations are performed. Again, the same parallel coordinates are used for calculations on both the experimental and simulation data.

Error propagation

Though the calculation of moment parameters (parallel decay lengths, boomerang angle, average cross-field width) is straightforward, these values have little meaning unless error bars are assigned to them. These are determined by subjecting the error fields which are generated for each plume (see section 2.4.2) to the same manipulations (distortion calibration, field-alignment) as the emission data, and then using those results in the moment analysis to estimate uncertainties.

In general, for a function $h = h(x, y)$, the uncertainty in h (σ_h) due to uncertainties in x (σ_x) and y (σ_y) is given by:

$$\sigma_h^2 = \sigma_x^2 \left(\frac{\partial h}{\partial x} \right)^2 + \sigma_y^2 \left(\frac{\partial h}{\partial y} \right)^2 \quad (2.9)$$

Using Equation 2.9, errors for the 1-D parallel profile, centroid data and width

data can be calculated. These errors are then propagated (again using Equation 2.9) into values for the decay lengths, boomerang angle, and cross-field width. For TVC data, errors in these values are typically less than a few percent. However, for SVC data, these errors are much larger, due to significantly larger uncertainties in the calibrated data. Thus much of the subsequent analysis will focus on interpretation of TVC results.

An example of results obtained from performing moment analysis for an experimental CIII TVC plume is shown in Figure 2-26. In the top left panel, a 2-D contour plot of the plume is given, with plots of the minimum contour level used in the calculations (dashed curve) and the 1-D centroid profile (solid) overlaid. A plot of the 1-D parallel emission profile is shown in the top right panel, with the region over which the probe is thought to influence the image indicated by the dashed lines. The 1-D profile of plume cross-field width is given in the bottom left panel – in this case the average width is found to be ~ 6 mm. However, near the injection location values for the cross-field width are even larger, $\gtrsim 8$ mm. The large cross-field width (relative to the injection diameter) is consistent with sputtering of deposited carbon off the molybdenum probe head – this will be discussed further in section 3.1.3. Finally, in the bottom right panel a plot of the 1-D logarithmic parallel emission profile is given. Fits to the decay length on both sides of the injection location are shown in blue. In this case, the decay lengths indicate that the parallel extent of the plume is much longer than the ionization mean free path of C^{+2} ions formed from sputtering and having undergone thermal spreading. More discussion will follow in section 3.2.1.

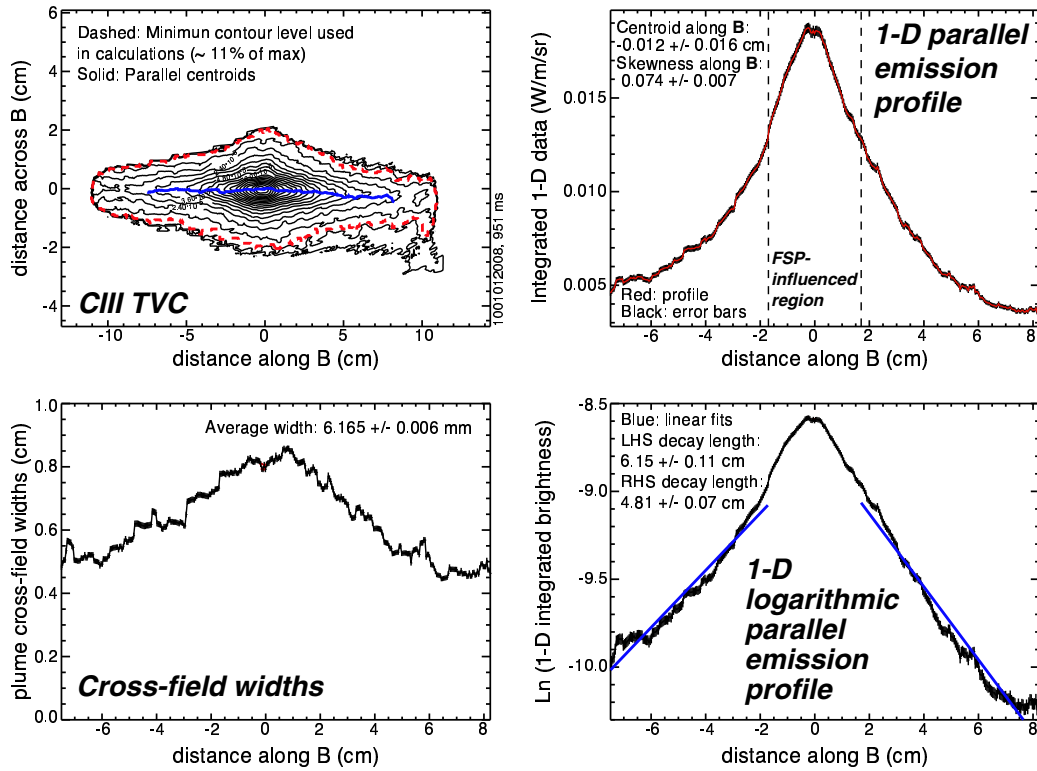


Figure 2-26: Example of moment analysis calculations performed for experimental CIII TVC data. *Top left:* 2-D contour plot of plume, with minimum contour level (dashed) and plume centroids (solid) overlaid. *Top right:* 1-D parallel emission profile, with the region over which the probe is thought to influence the image shown. *Bottom left:* 1-D profile of plume cross-field width. The cross-field extent is found to be large relative to the gas injection diameter. *Bottom right:* 1-D logarithmic parallel emission profile. The parallel extent of the emission is much longer than expected, based on estimates for the C^{+2} ionization mean-free path.

Chapter 3

Plume Physics Overview

In order to relate plume dispersal patterns to background transport, the physics of plume formation must first be understood. In this chapter, an overview is presented of conclusions regarding the physics of plumes. This begins with a summary of the plume experiments, and a discussion of the observed dependence of emission structure on background plasma conditions (section 3.1). Estimates for the parallel extent of the plume derived from a simple model for the impurity dispersal are then compared to experimental values (section 3.2). Analysis is also undertaken to quantify the perturbing effect of the gas injection on the background plasma. Finally, a plume database has been constructed, allowing correlations to be explored between emission structure and background conditions (section 3.3).

In many cases, qualitative and quantitative analyses presented in this chapter are based in part on results from detailed numerical computations described in later chapters. Therefore, this chapter also serves to motivate both the discussion of plume modelling tools (Chapter 4) and the numerical simulation of 3-D plume dispersal patterns (Chapter 5) in which the plume physics model is validated.

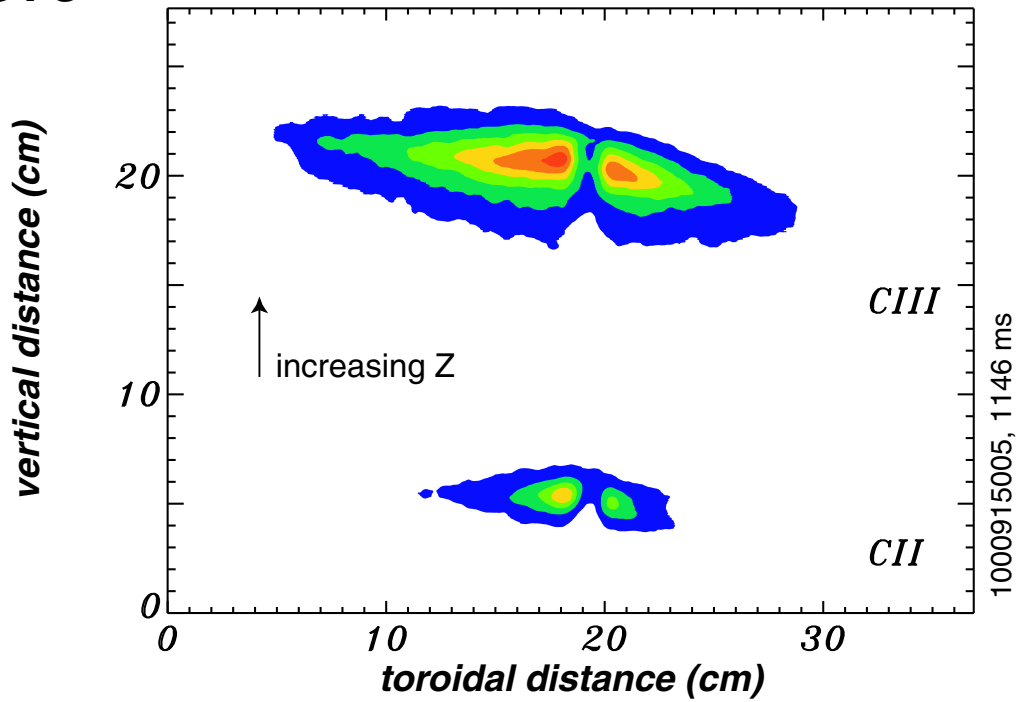
3.1 Experimental Observations

3.1.1 Typical plume characteristics

An example of data obtained from the plume imaging system is shown in Figure 3-1. Images in the top panel correspond to the side view of the plume, while images in the bottom panel correspond to the top view. In both cases C^{+1} (CII) emission is on the bottom half of the image, and C^{+2} (CIII) on the top half. Some simple observations can be made about the characteristics of the emission. First, the plumes are elongated in one direction – this is very clear for the CIII data. The direction of elongation is expected to align with the local magnetic field, since charged particle motion is unconfined along this direction. CIII plumes have a much longer elongation than CII plumes, which is consistent with C^{+2} ions having a longer ionization lifetime than C^{+1} ions (more details in section 3.2.1).

However, the aspect ratio of the plumes (extent along \mathbf{B} vs. across \mathbf{B}) is smaller than expected for both CII and CIII emission. The cross-field width of the ion emission is (nominally) set by two factors: (1) the neutral source width and (2) the cross-field diffusivity (D_{\perp}). In principle, the width of the neutral distribution is set by the injection capillary diameter (1 mm), while impurity spreading due to diffusion may be estimated as $\Delta \sim \sqrt{D_{\perp}\tau_{ion}}$, where τ_{ion} represents the ionization lifetime for the charge state of interest ($= \frac{1}{n_e \langle \sigma v \rangle_{ion}}$, where $\langle \sigma v \rangle_{ion}$ = ionization rate coefficient). Typical values for D_{\perp} , τ_{ion} (C^{+1}), and τ_{ion} (C^{+2}) in the SOL are $\sim 0.1 - 1 \text{ m}^2/\text{s}$, $0.2-0.5 \text{ }\mu\text{s}$, and $1-20 \text{ }\mu\text{s}$, respectively, with each parameter increasing in value with distance from the separatrix [38]. Based on these estimates, C^{+1} ions are expected to spread cross-field by $\sim 0.1 - 0.7 \text{ mm}$ during their lifetime, while C^{+2} ions will spread by $\sim 0.3 - 4.5 \text{ mm}$. Values for the impurity cross-field width are therefore expected to be $\lesssim 2 \text{ mm}$ for C^{+1} ions and $\sim 1 - 5 \text{ mm}$ for C^{+2} ions. These values are much smaller than those observed for most experimental plumes, which exhibit cross-field widths of order $\sim 5-10 \text{ mm}$ for CII and $\sim 10-15 \text{ mm}$ for CIII. This result suggests that the source width is in fact much larger than 1 mm.

SVC



TVC

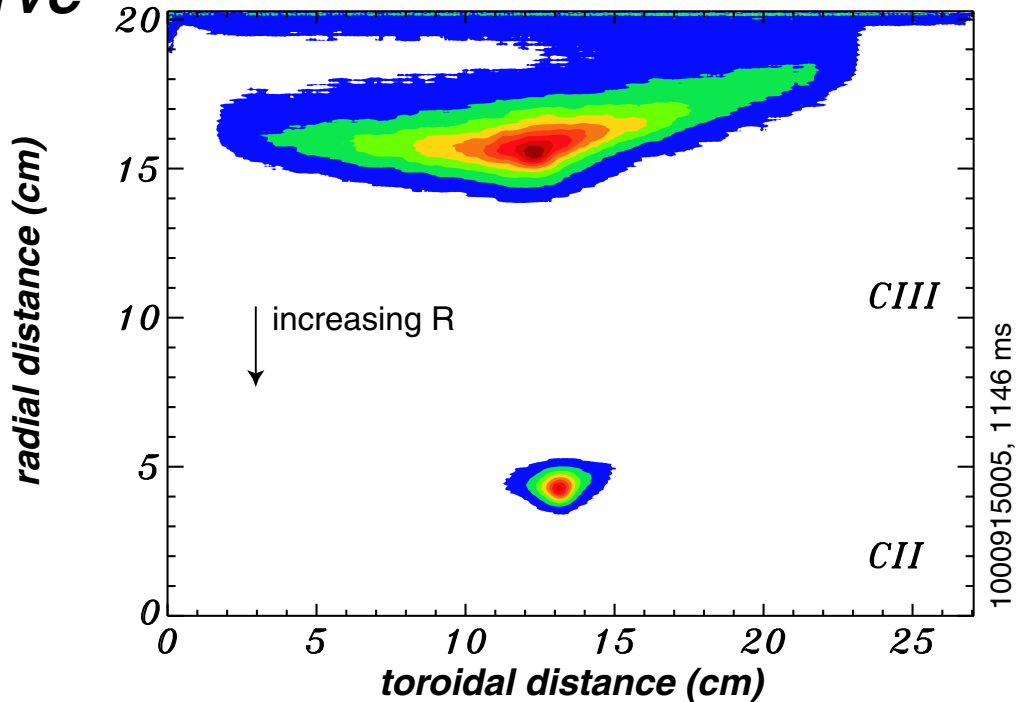


Figure 3-1: Typical data obtained from plume imaging system, side (*top panel*) and top (*bottom panel*) view. In both cases emission from C^{+1} is on the bottom half of the image and emission from C^{+2} is on the top half. Note: Raw image with 9×9 pixel smoothing.

One possible explanation is related to the re-deposition of carbon atoms onto the probe surface. As C_2D_4 molecules are injected into the plasma, they are broken up into their constituent atoms. This is expected to occur very close to the probe in most cases, since the dissociation mean-free path is small ($\sim 10\text{-}20 \mu\text{m}$) for typical SOL conditions. However, the break-up will in general involve a complicated set of processes, including the formation of molecular and atomic radicals. Based on the surface chemistry of the probe, there will be some probability of re-deposition of these species onto the probe head. Carbon deposited on the probe head can then be sputtered by the background plasma (by chemical and/or physical sputtering) and again contribute to the plume emission. In this model for the plume, the effective source width of the emission is governed by the probe head geometry, resulting in a cross-field width which is much greater than the injection capillary diameter. This is consistent with the observations. In addition, experimental evidence exists for the formation of a re-deposited carbon layer on the probe in the form of plumes generated *without gas injection*. These observations are discussed further in section 3.1.3.

Finally, plume emission centroids are observed to deviate from field lines, and the amount of deviation typically increases with distance (along \mathbf{B}) from the injection location. This results in plumes which have a “gull wing” or “boomerang” shape, which can be seen in Figure 3-1. The deviation is in part caused by a poloidal (in the flux surface) flow of the impurities resulting from the presence of a radial electric field at the injection location (i.e. from an $\mathbf{E} \times \mathbf{B}$ drift). Results from numerical modelling (section 5.7.1) indicate that in the absence of an electric field an emission boomerang can also arise from the cross-field variation of electron density and temperature (i.e. of the ionization rate). The total plume boomerang is therefore due to both $\mathbf{E} \times \mathbf{B}$ and ionization-rate variation effects. Nonetheless, in many cases the direction of the boomerang can be simply related to the sign of \mathbf{E}_r . Moreover, if the magnitude of ionization-rate variation effects can be estimated, then the boomerang angle (defined as $180^\circ - \theta_{total}$ – see Figure 3-2) can be used to directly estimate the value of \mathbf{E}_r . This type of analysis is presented in Chapter 6.

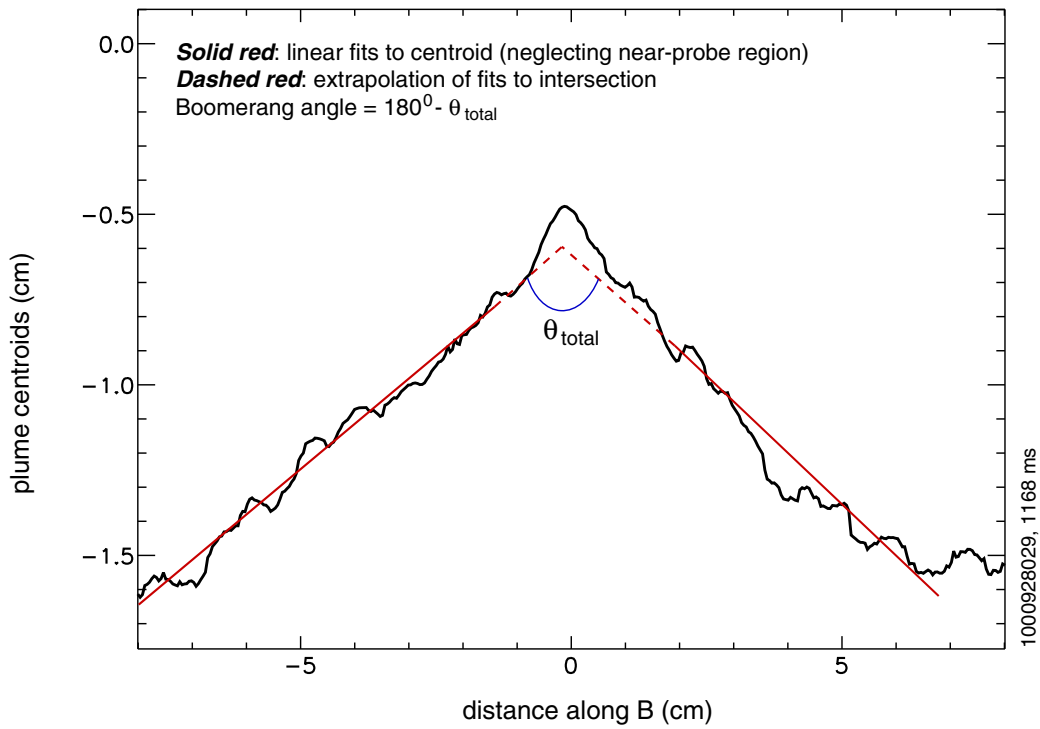


Figure 3-2: Definition of the plume “boomerang angle”, in terms of the 1-D parallel centroid profile determined from moment analysis. This angle can be used to estimate the value of \mathbf{E}_r .

3.1.2 Variation of plume structure with discharge conditions

Impurity plumes have been generated for a variety of background plasma conditions. These include varying electron density and temperature, SOL depth (up to the separatrix), and confinement regime. In this section, some qualitative observations will be made on how emission structure depends on plasma conditions.

Local n_e, T_e

An example of plumes generated at low ($n_e = 1.03 \times 10^{19} \text{ m}^{-3}$; $T_e = 12 \text{ eV}$) and high ($n_e = 1.34 \times 10^{20} \text{ m}^{-3}$; $T_e = 60 \text{ eV}$) density and temperature is given in Figure 3-3. In the low (n_e, T_e) case, the plumes exhibit a large aspect ratio, i.e. their extent along **B** is much longer than their cross-field width. This is true for both the CII and CIII emission. In the high (n_e, T_e) case, the CIII plume aspect ratio is slightly reduced, although the parallel extent of the plumes is still much larger than the cross-field width. In this case the CII emission is significantly smaller in size.

The parallel extent of the emission is related to the parallel mean-free path of the carbon ions, which is a function of both n_e and T_e (since $\langle \sigma v \rangle_{ion} = f(T_e)$). For instance, as the density and temperature increase, the ion mean-free path is reduced, resulting in a smaller parallel extent for the plumes. For CIII plumes, the effect is observed to be small – this is because at higher temperature perturbation effects due to the presence of the probe play a role in setting the parallel extent of the plumes (more discussion in sections 3.1.3 and 3.2.1). The cross-field width of the emission is observed to be relatively insensitive to local values of n_e and T_e . This is not surprising, since the overall width is thought to be determined by carbon sputtering off the probe head.

SOL depth

The location of plume formation in the SOL also affects the structure of the resulting emission. One reason is that n_e and T_e are a function of SOL position, and these parameters affect the parallel mean-free path of the impurity ions. However the

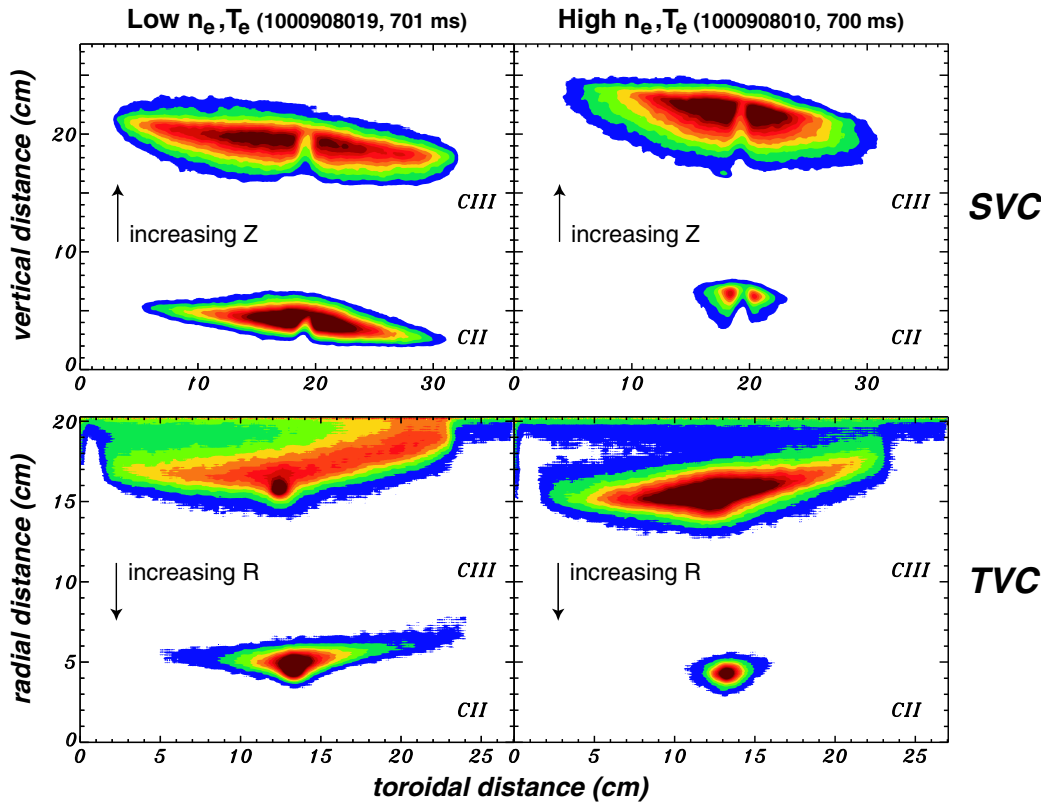


Figure 3-3: Plumes generated at various values of electron density and temperature. *Left panel:* Low n_e, T_e case (values at the injection location are $1.03 \times 10^{19} \text{ m}^{-3}$ and 12 eV, respectively). Both CII and CIII plumes exhibit a strong elongation along \mathbf{B} . *Right panel:* High n_e, T_e case (values at the injection location are $1.34 \times 10^{20} \text{ m}^{-3}$ and 60 eV, respectively). The elongation of the CIII plumes is slightly reduced, while the CII plumes are significantly smaller in size.

parallel asymmetry in the plume emission is also observed to depend on the SOL depth. An example of this variation is given in Figure 3-4, which shows plumes generated at three SOL positions: $\rho = 10, 5,$ and 0 mm, where ρ is the distance from the separatrix mapped to the midplane, determined using the known probe trajectory and EFIT [43].

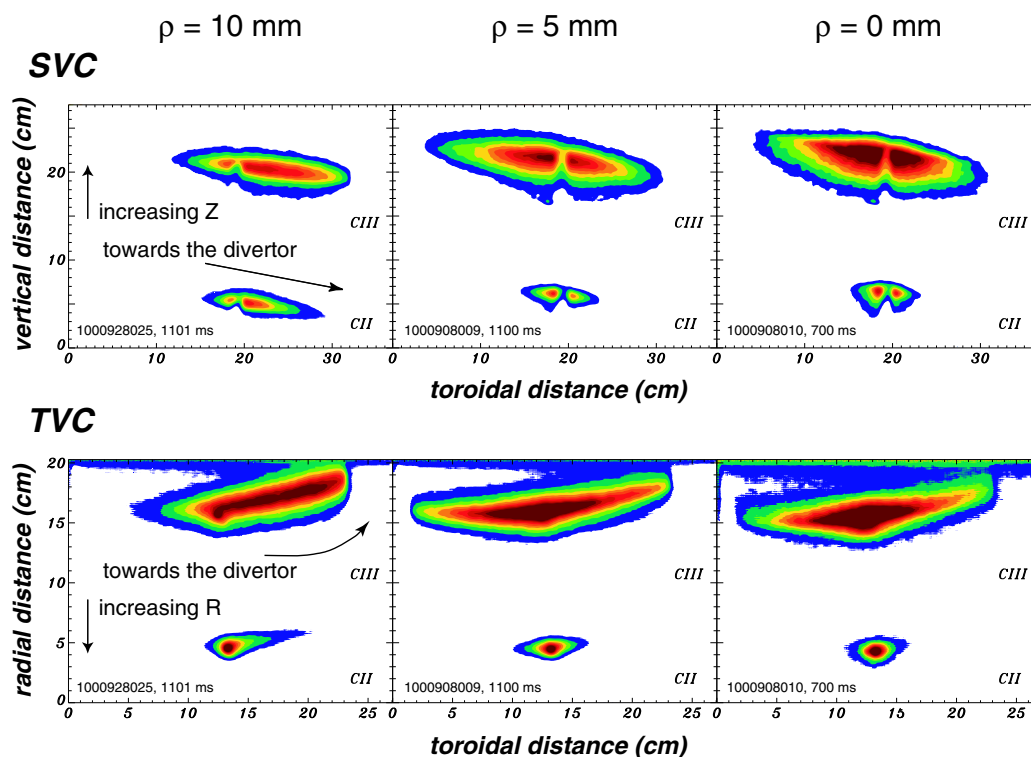


Figure 3-4: Plumes generated at various SOL depths. *Left panel:* $\rho = 10$ mm ($n_e = 8.7 \times 10^{19} \text{ m}^{-3}$, $T_e = 22$ eV). Plume asymmetry is strong, and consistent with parallel flows towards the divertor. *Middle panel:* $\rho = 5$ mm ($n_e = 7.06 \times 10^{19} \text{ m}^{-3}$, $T_e = 27$ eV). For the TVC, plume asymmetry is weak, and consistent with small parallel flows directed towards the divertor. For the SVC, the asymmetry is directed away from the divertor (i.e. *reversed*). *Right panel:* $\rho = 0$ mm ($n_e = 1.34 \times 10^{20} \text{ m}^{-3}$, $T_e = 60$ eV). Plume asymmetry is consistent with reversed parallel flows in both views, but is again weak for the TVC data.

In the far SOL ($\rho = 10$ mm), the plumes exhibit a strong asymmetry in their parallel extent, which is directed towards the outer divertor. This is clear for both CII and CIII emission. Closer to the separatrix ($\rho = 5$ mm), very little asymmetry is observed in the TVC plumes, whereas the SVC data indicate an asymmetry directed

away from the divertor (i.e. *reversed*). This discrepancy may be related to differences in camera response. Finally, plumes formed at the separatrix exhibit an asymmetry indicative of reversed flows in both views, but this asymmetry is weak for the TVC data. In the latter two cases the spatial extent of the CII emission is so small that asymmetries are difficult to identify.

The observed variation in TVC plume asymmetry with ρ is consistent with the variation of parallel flow (v_{\parallel}) measured by the scanning probe [37]. This seems to imply that the TVC plumes provide a direct measure of parallel SOL flows. However, the interpretation of this result needs to be more carefully considered. The extent to which impurity dispersal is influenced by background flows will depend on the strength of the coupling between the background and impurity charge state during its lifetime. If the coulomb collision time (τ_{coul}) between deuterium and carbon ions is small relative to the carbon ionization time (τ_{ion}), then the carbon ions will be strongly influenced by background flows. However, if the converse is true, i.e. $\tau_{coul} \gg \tau_{ion}$, then the carbon ion dispersal will have little direct dependence on background flows. Assuming that the distribution functions for the background plasma ions and electrons are Maxwellian, that the deuterium temperature is equal to the electron temperature, and that the carbon density is small (i.e. $n_e \simeq n_D$), then the ratio of τ_{ion} to τ_{coul} is simply a function of electron temperature and carbon ion charge state. Plots of this ratio for C^{+1} and C^{+2} are shown in Figure 3-5.

For C^{+1} , τ_{ion} is generally smaller than τ_{coul} for most SOL conditions ($T_e \gtrsim 10$ eV), implying that these ions are not well-coupled to the background except in the far SOL. For C^{+2} , the ratio $\frac{\tau_{ion}}{\tau_{coul}}$ is sufficiently large ($\gtrsim 1$) for these ions to be coupled to background flows over a substantial portion of the SOL. However, this is not the case in the near SOL, where $T_e \simeq 50$ eV. These results suggest that plume data may not be useful for inferring parallel plasma flows near the separatrix. Numerical modelling has been used to assess the potential of extracting parallel flows from the emission structure in the near and far SOL, and results from this analysis are discussed in Chapter 5 and Chapter 6.

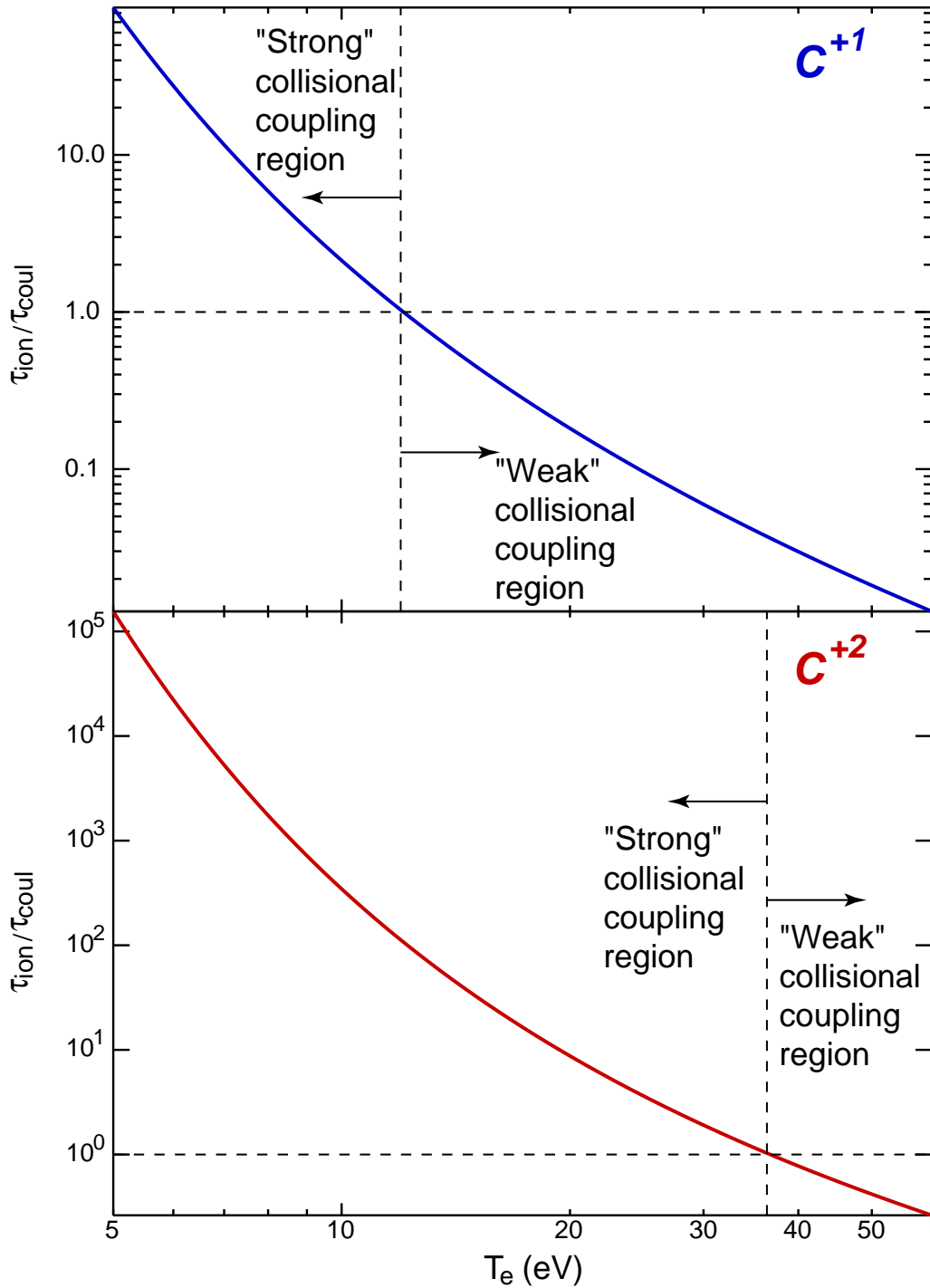


Figure 3-5: Plots of the ratio of ionization time (τ_{ion}) to coulomb collision time (τ_{coul}) for C^{+1} and C^{+2} . Assuming that $T_e = T_D$ and that $n_e \simeq n_D$ (i.e. $\frac{n_C}{n_D} \ll 1$), these ratios are a function only of electron temperature.

Confinement mode

An example comparing SVC and TVC data for L-mode vs. H-mode is shown in Figure 3-6. Plumes were generated during the same discharge at approximately the same location in the SOL, close to the separatrix. Time traces of the probe tip location in ρ -space, the plasma current, the toroidal field on axis, and the D_α signal (used to determine confinement mode) are also shown in the figure. In both cases the parallel and cross-field extent of the emission is comparable, and the plumes exhibit a boomerang angle consistent with $\mathbf{E}_r > 0$ (as expected in the SOL [63]). However, the boomerang angle is larger in H-mode, implying that \mathbf{E}_r at this location is larger in H-mode. This is consistent with probe measurements for this case. Further out in the SOL a counter-example is found (Figure 3-7), i.e. the boomerang angle, and thus the implied radial electric field, is larger in L-mode than in H-mode. This is again consistent with probe measurements, and the combination of these results suggest that during H-mode the \mathbf{E}_r profile becomes steeper and peaked near (or at) the separatrix.

The amount of boomerang angle exhibited by the plumes also depends on the type of H-mode. For example, plumes formed near the separatrix in ELM-free H-mode (EFH [18]) discharges tend to exhibit a larger boomerang angle than those formed in Enhanced D_α (EDA [17]) discharges, suggesting that \mathbf{E}_r is larger in EFH discharges. This is again consistent with probe measurements.

Finally, plumes have been obtained in both EFH and EDA discharges in which the direction of the emission boomerang implies a reversal of the radial electric field (i.e. $\mathbf{E}_r < 0$). As an example, a comparison between CIII SVC plumes formed inside and outside of the Quasi-Coherent (QC) mode [59] layer during a pair of EDA H-mode discharges is shown in Figure 3-8. Also shown in this figure are floating potential measurements from the gas-injecting scanning probe (FSP) and a horizontal fast-scanning probe (ASP) located slightly above the outboard midplane in Alcator C-Mod [33]. ASP results indicate that this probe was located inside the QC mode layer during both discharges, whereas FSP measurements suggest that this probe was located inside the mode layer during only the first discharge (bottom panels).

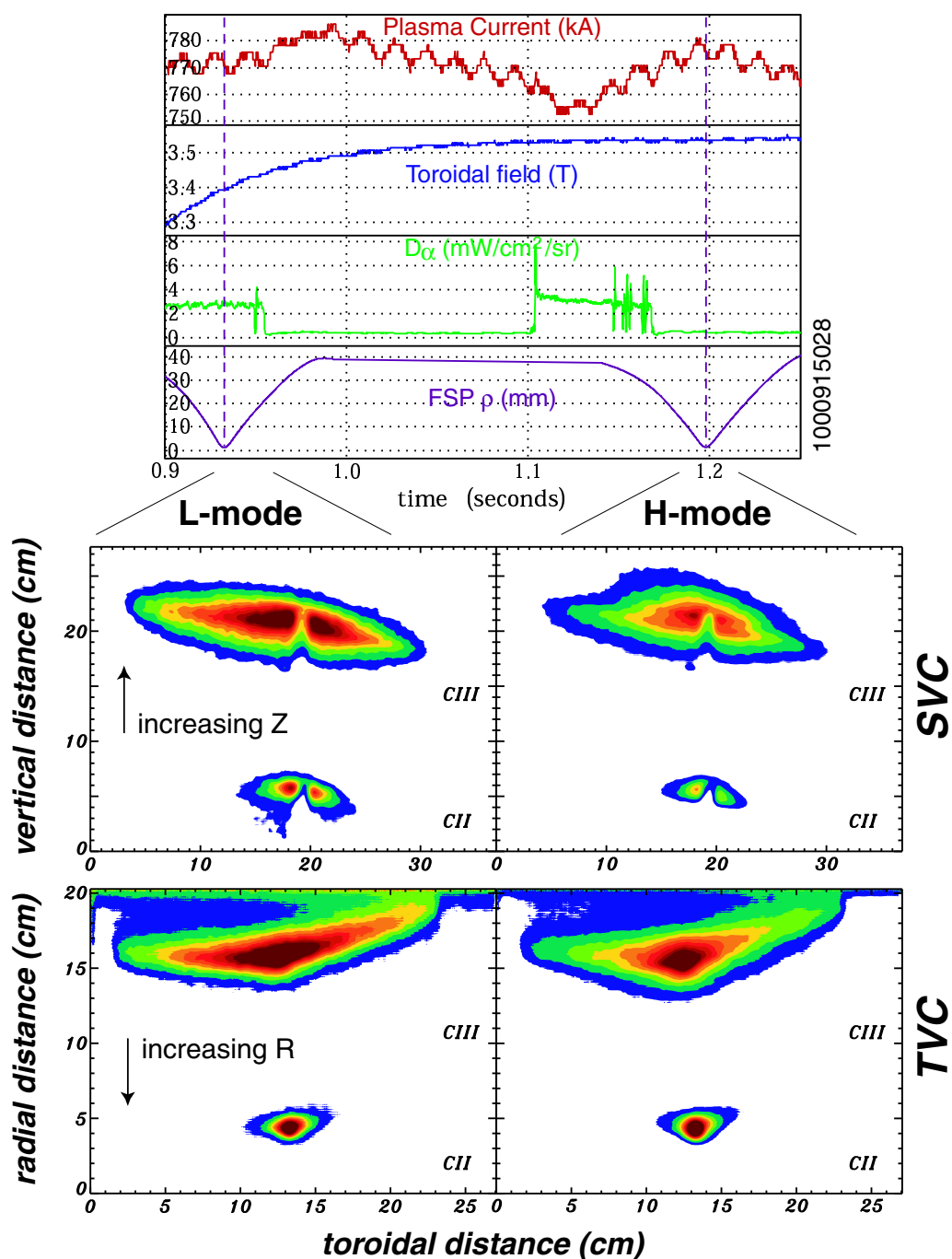


Figure 3-6: Comparison between plumes formed in ohmic L-mode and H-mode. Plumes were formed during the same discharge, at nearly the same SOL depth, near the separatrix. Traces of the probe tip location (in ρ -space), the plasma current, the toroidal field on axis, and the edge D_α signal (used to determine the plasma confinement mode) are given in the top panel. Results suggest that \mathbf{E}_r is larger during H-mode, consistent with probe measurements.

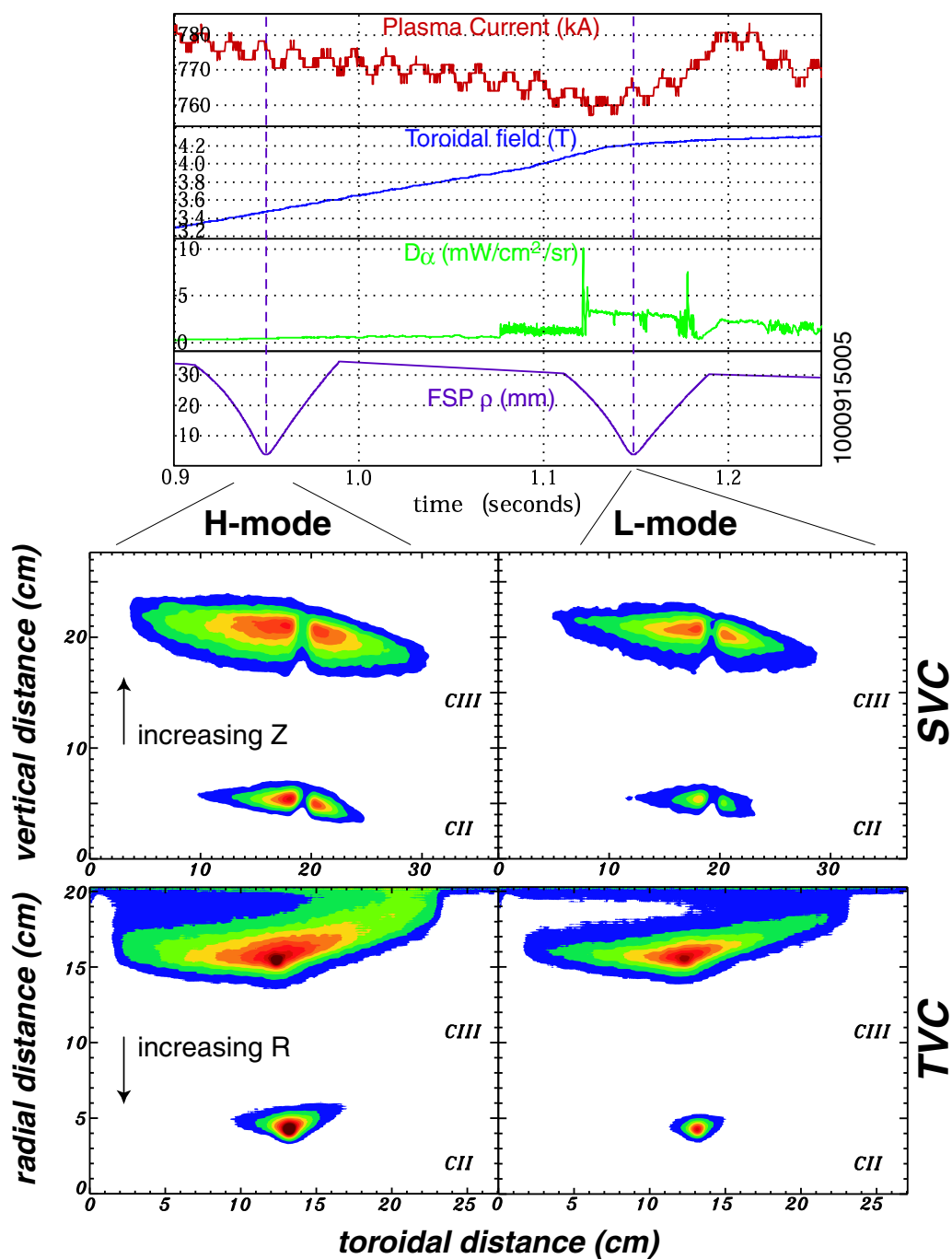


Figure 3-7: Comparison between plumes formed in ohmic L-mode and H-mode. Plumes were formed during the same discharge, at the same SOL depth, this time further out in the SOL ($\rho = 4$ mm). In this case the implied radial electric field is larger in L-mode, again consistent with probe measurements. Combined with results shown in Figure 3-6, this suggests that the radial electric field profile steepens and peaks near (or at) the separatrix during H-mode.

While the plume generated outside the mode layer (top panels) exhibits an emission boomerang consistent with $\mathbf{E}_r > 0$, the plume generated inside the mode layer exhibits a reversed emission boomerang, consistent with $\mathbf{E}_r < 0$. These results suggest that the QC mode exists in a region of negative radial electric field. The presence of the mode makes it extremely difficult for probe data to be used to infer \mathbf{E}_r – in fact, FSP measurements indicate a *positive* radial electric field when this probe is located inside the mode layer. Thus, plumes may provide the only means of estimating the magnitude of \mathbf{E}_r in the QC mode layer.

3.1.3 Two-source model for impurity emission

Impurity emission patterns suggest the presence of two sources: a source due to direct gas injection and one due to sputtering of re-deposited carbon off the probe head. Experimental evidence for a “sputter” source exists in the form of a plume generated *without gas injection*. Images of this CIII plume obtained from the top and side views are shown in Figure 3-9. The plume is generated during the first scan of the probe following a discharge in which C_2D_4 gas was injected through the capillary. The emission brightness in this case is less than but comparable to cases in which plumes are formed with gas injection, indicating that the contribution of the sputtered plume to the overall emission can be significant ($\sim 40\text{-}60\%$) even when gas is injected.

During the discharge in which no gas was injected, the probe was scanned three times, resulting in three separate sputter-generated plumes. Images of the emission for these three probe scans are shown in Figure 3-10 (for the side view, images from only the first two scans are shown – the image from the third scan was saturated due to a problem with the camera exposure gating for that time). The emission is significantly reduced in the second and third scans, implying that most of the re-deposited carbon is sputtered off the probe head in one scan (i.e. the probe “cleans up” in one scan). These results suggest that the rate of sputtering off the probe head is comparable to the gas injection rate ($\sim 10^{19}$ carbon atoms per second) – if it were much faster, there would be very little carbon left on the probe head to generate a plume during the first probe scan without gas injection, and if it were much slower

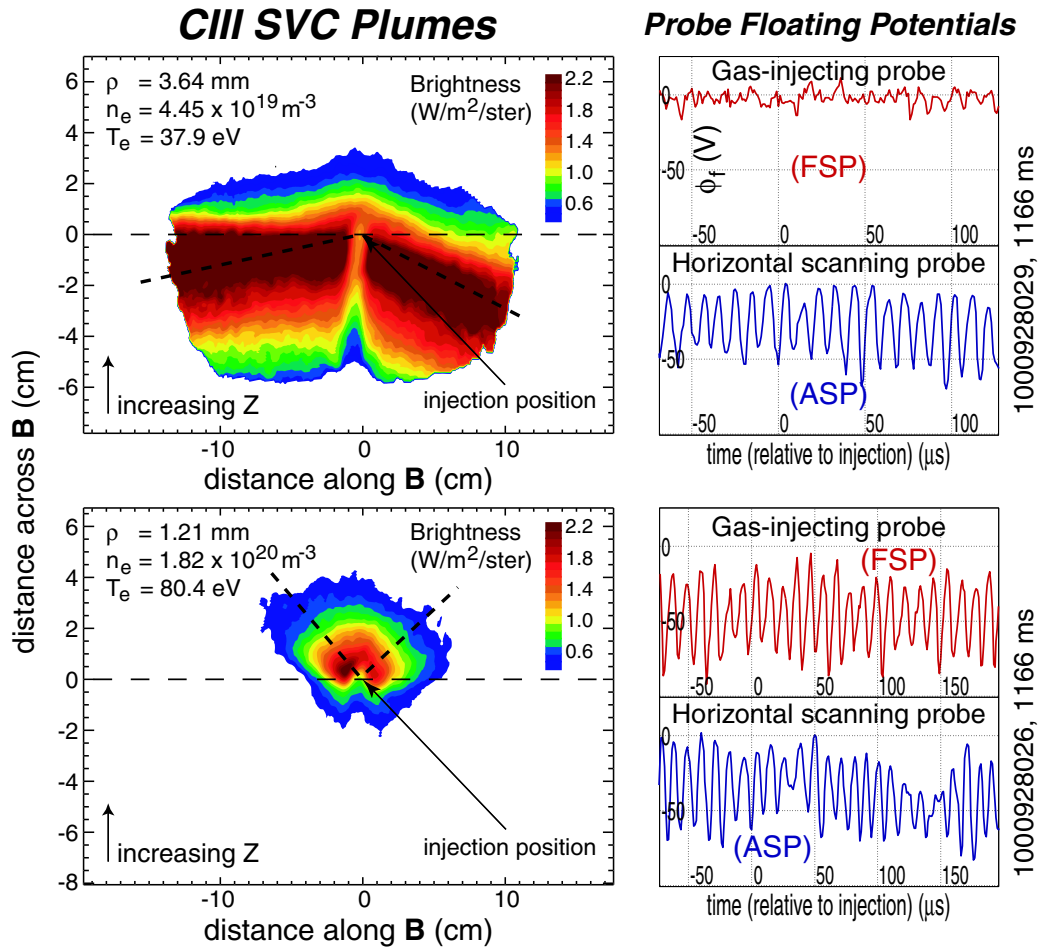


Figure 3-8: Comparison between CIII SVC plumes generated inside and outside of the Quasi-Coherent (QC) mode layer during a pair of Enhanced D_α (EDA) H-mode discharges. Floating potential measurements from the gas-injecting scanning probe (FSP) and a horizontal fast-scanning probe (ASP) located slightly above the outboard midplane in Alcator C-Mod are also shown. Results suggest that the QC mode exists in a region of $\mathbf{E}_r < 0$. Note: Images are 9×9 pixel smoothed, absolutely calibrated, and mapped to field-aligned coordinates.

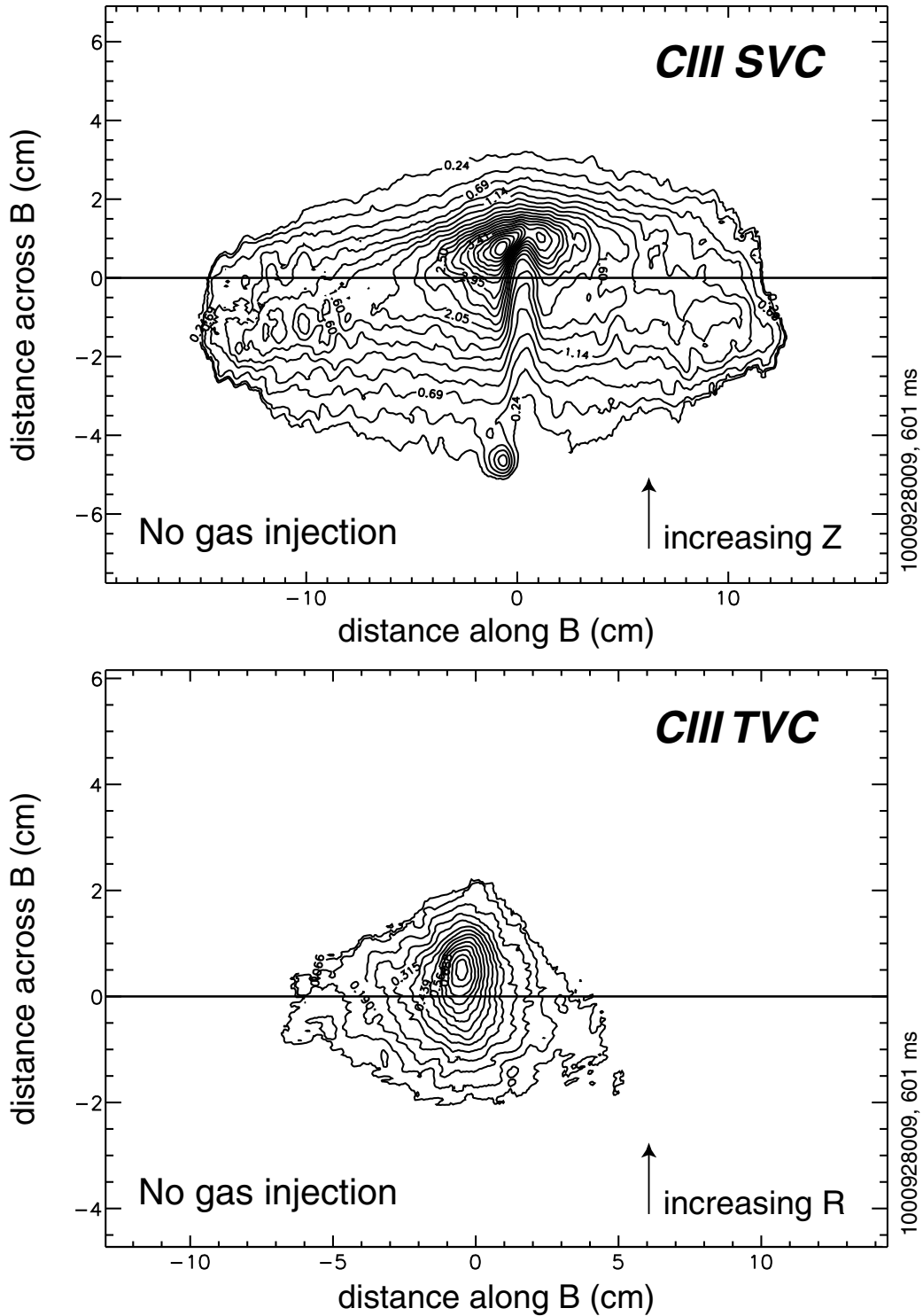
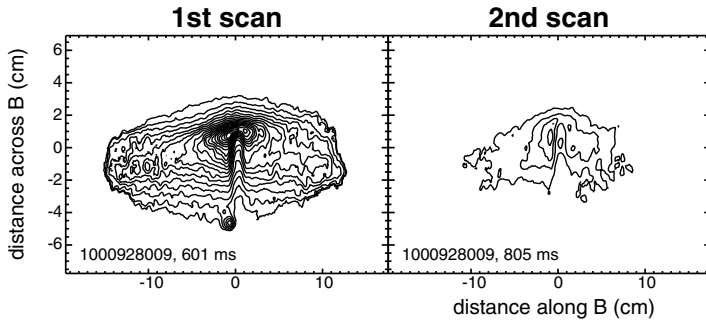


Figure 3-9: Data obtained from plume imaging system for a case with *no gas injection*, side (*top panel*) and top (*bottom panel*) view. The plume is thought to be formed from sputtering of re-deposited carbon off the probe head. Note: Images are 9×9 pixel smoothed, absolutely calibrated, and mapped to field-aligned coordinates.

then the brightness would be both small and of the same magnitude for all three plumes generated from probe scans without gas injection.

CIII SVC



CIII TVC

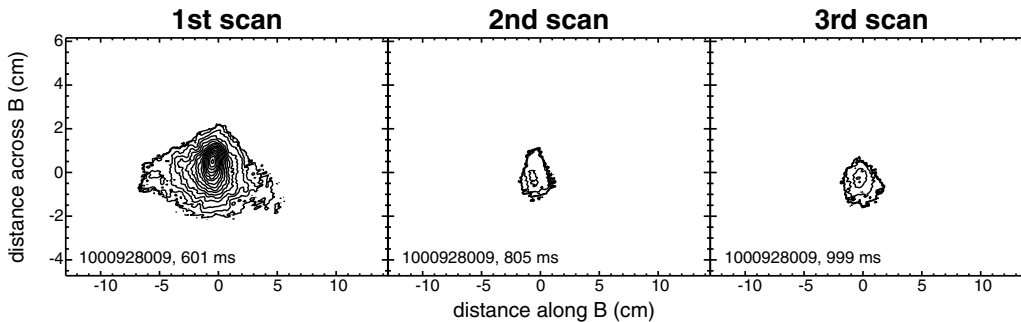


Figure 3-10: Plume images from three consecutive probe scans with no gas injection (only two for the side view, due to a problem with exposure gating for this camera during the third scan). The intensity of emission is significantly reduced in the latter scans, implying that most of the re-deposited carbon is sputtered off of the probe head in one scan. This suggests that the sputtering rate is comparable to the gas injection rate.

An additional characteristic appears in plumes formed in the near SOL which is unrelated to the sputter source. These plumes tend to exhibit a “jet”-like feature near the gas-injection location, leading to non-elliptical emission contours. An example of this behavior for a CIII image taken from the TVC is shown in Figure 3-11. The “jetting” action which occurs in these plumes implies that impurities in the vicinity of the probe (in the cross-field direction) travel with high parallel velocity relative to impurities which are further out. In addition, the parallel extent of the emission is much longer than the ionization mean-free path estimated from local measurements

of n_e and T_e in these cases (see section 3.2.1). This suggests the existence of a mechanism which imparts significant parallel energy to the impurities in the near SOL. Modelling results indicate that a localized density perturbation arising from background ions recycling off the probe head can lead to a strong parallel electric field, which in turn can accelerate impurities away from the probe to a significant parallel velocity (of order $\sqrt{T_e/m_z}$). These results are discussed in more detail in Chapter 5.

CIII TVC plumes which exhibit little (“transition”) or no jet-like behavior are also shown in Figure 3-11 for comparison. For the transition plume, the emission structure suggests that a recycling-induced density perturbation may still be present, but that it is small. Emission contours for the plume with no jet-like structure are nearly elliptical, which is consistent with numerical modelling results from a single-source model of the emission (i.e. plume formation due to sputtering only). These results are discussed further in section 5.2. Finally, qualitative characterization of the plume data into “jet”, “transition” and “no jet” categories is used to explore correlations between plume structure and background plasma conditions – this analysis is presented in section 3.3.

3.1.4 SVC/TVC asymmetry

For the majority of CIII plumes collected, the cross-field extent of the SVC data is found to be larger than the cross-field extent of the TVC data. CIII brightness values are also observed to be somewhat smaller for SVC plume data than for TVC plume data, indicating that the signal on each TVC pixel arises from integration through a larger amount of emission. These results suggest that the C^{+2} emission is vertically elongated (i.e. extends down the probe axis).

An example of CIII plume data which exhibit an asymmetry in cross-field extent is shown in Figure 3-12. For these data, a comparison between the corresponding 1-D cross-field profiles is given in Figure 3-13 (top panel), where the profiles were generated by integrating the 2-D brightness data over a limited extent along \mathbf{B} (i.e.

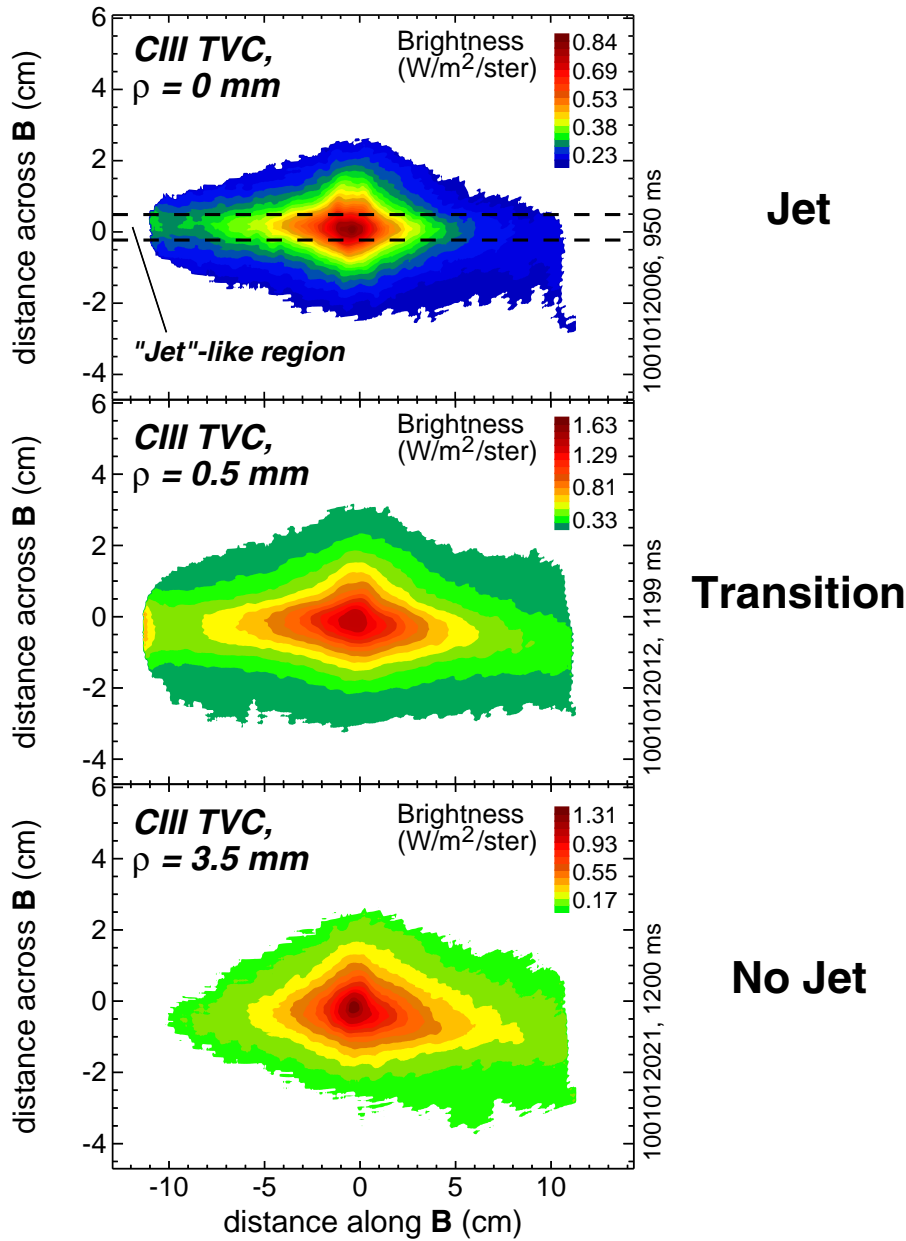


Figure 3-11: *Top panel:* CIII TVC image of a plume generated in the near SOL. The plume exhibits a “jet”-like structure, leading to non-elliptical emission contours. *Middle panel:* Example of a CIII TVC image which exhibits weak jet behavior, and is therefore labeled as a “transition” plume. *Bottom panel:* Example of a CIII TVC image which exhibits no jet-like behavior. The emission contours are nearly elliptical in this case, consistent with results from a single-source model for the plumes (i.e. formation due to sputtering only).

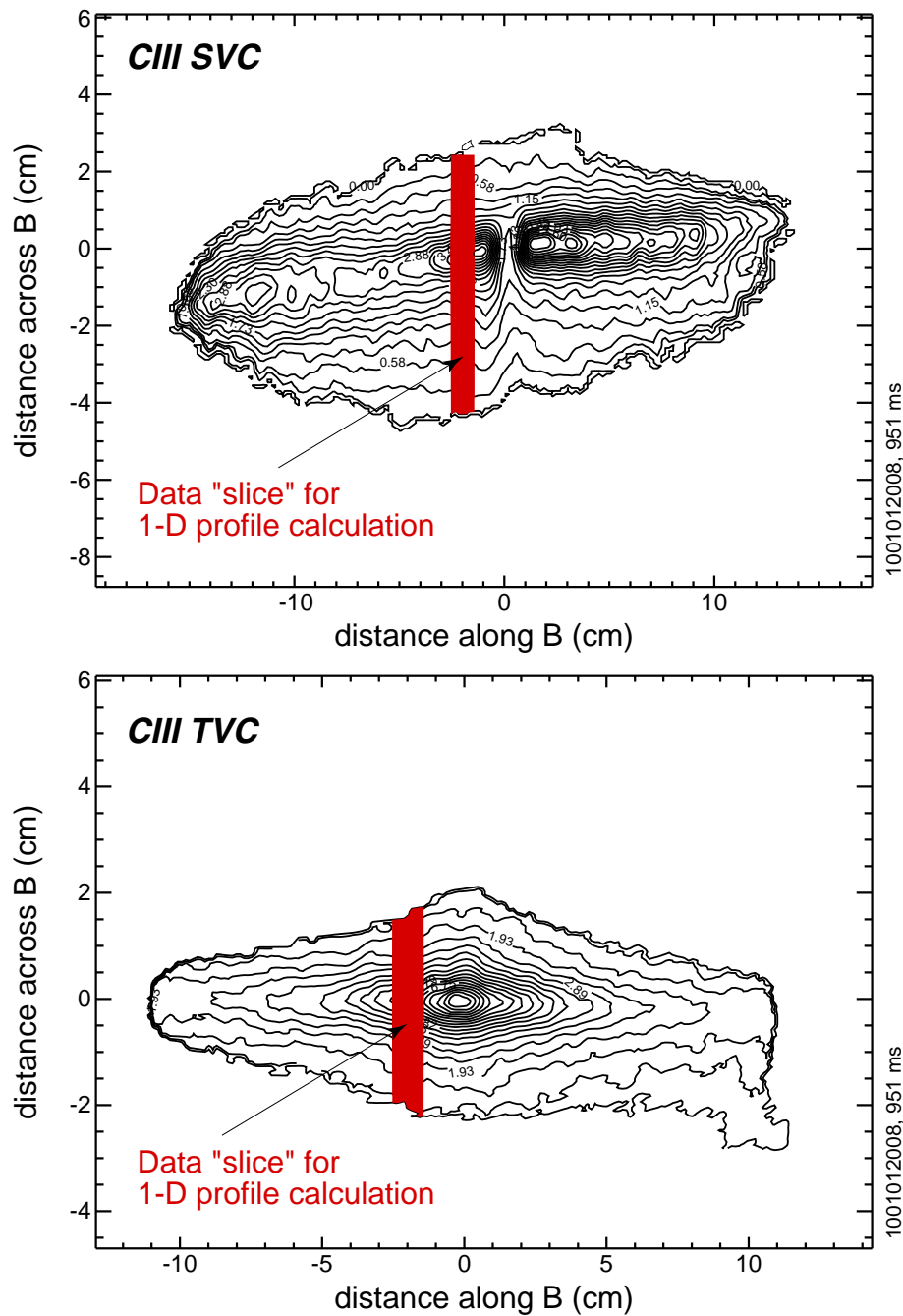


Figure 3-12: SVC and TVC CIII brightness data for a plume generated in the near SOL. The cross-field extent of the SVC data is larger than the extent of the TVC data, suggesting that the impurity emission is vertically elongated. This observation is investigated by comparing 1-D cross-field profiles generated by integrating the 2-D brightness data over a limited extent along \mathbf{B} (i.e. over a given “slice” of the data). The data slice used in the calculation is highlighted for each plume.

over a given “slice” of the data, highlighted in Figure 3-12 for each view). These results indicate that the absolute brightness observed by the TVC is larger than that observed by the SVC in this case. In addition, for cross-field distances greater than $\simeq 2$ cm away from the injection location, the TVC data exhibit unexpected behavior, such as an increase in the brightness with increasing distance towards the core of the plasma (i.e. with decreasing R). This behavior is thought to be caused by the presence of structure in the background emission which results from reflections off invessel component surfaces. However, data at brightness levels which are small relative to the peak ($\lesssim 10\text{-}15\%$) are typically neglected in the moment analysis of the plumes, suggesting that this far-field behavior has little effect on results from such an analysis.

A comparison between the normalized brightness profiles for the two views is shown in the bottom panel of Figure 3-13. Ignoring data in the far field ($\gtrsim 2$ cm away from the injection location across \mathbf{B}), good agreement is observed between the results for the region of plasma towards the core (increasing Z , decreasing R). However, in the region of plasma away from the core, the SVC profile is skewed relative to the TVC profile, indicating that the plume is extended in the vertical direction. This result confirms that CIII emission is elongated along the probe axis.

Finally, neglecting data below a threshold (which is indicated by the dashed line in Figure 3-13, bottom panel), the total power per unit solid angle from the given plume slice was calculated for each view, to provide a cross-calibration between the systems. For the SVC the result is 1.02 mW/ster, while for the TVC the result is 1.29 mW/ster. The level of agreement between these results suggests that the CIII absolute calibration coefficients for these two systems are accurate to within $\simeq 25\%$. This is consistent with results obtained from cross-calibrating the systems using data slices from a number of other plume images (see section 2.3.1).

Possible explanations for the vertical elongation of the CIII plumes are investigated using numerical modelling. The results suggest the presence of a vertical $\mathbf{E} \times \mathbf{B}$ drift for the impurity ions, which is caused by the presence of a local electric field arising from the variation of probe-induced presheath potentials. These results are discussed

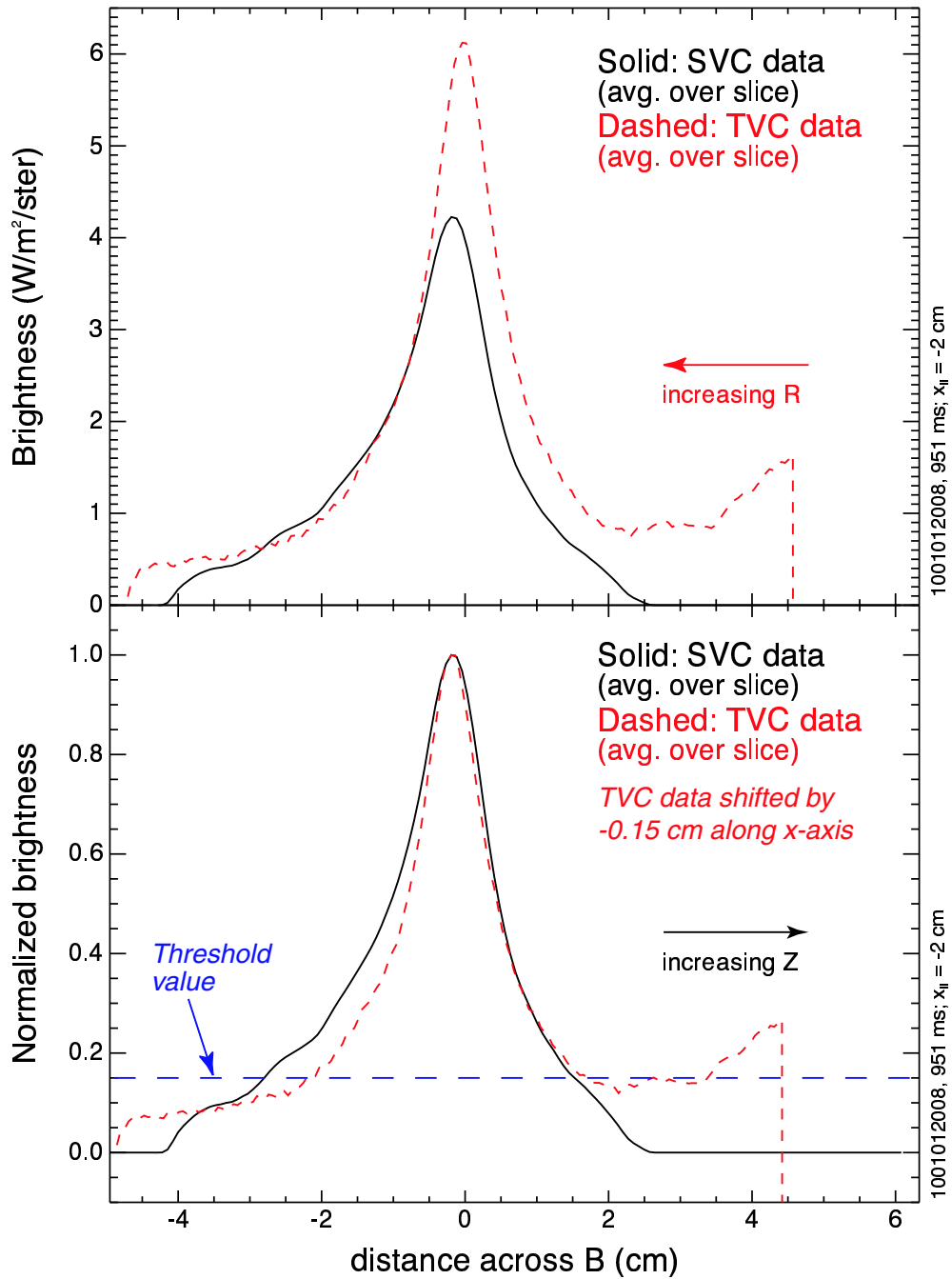


Figure 3-13: Comparisons between 1-D cross-field brightness profiles for CIII SVC and TVC data shown in Figure 3-12. *Top panel:* Absolute brightness profiles calculated from integration of the 2-D brightness data over a limited parallel extent (see highlighted regions in Figure 3-12). *Bottom panel:* Normalized brightness profiles. Neglecting data in the far field, the SVC profile appears skewed relative to the TVC profile, confirming that the plume is vertically elongated.

further in section 5.1.

3.2 Simple plume analysis

3.2.1 Ionization mean-free paths

The parallel mean-free path (λ_{mfp}) of carbon ions in a given background plasma may be estimated as:

$$\lambda_{mfp} = v_{th} \tau_{ion} = \frac{v_{th}}{n_e \langle \sigma v \rangle_{ion}} \quad (3.1)$$

where v_{th} is the thermal velocity of the ions ($=\sqrt{\frac{2T_z}{m_z}}$, where T_z is the impurity ion temperature and m_z is the mass). Assuming that $T_z = T_e$, the mean-free path is simply a function of the electron density and temperature, which are measured directly from the scanning probe.

A plot of λ_{mfp} for C^{+2} vs. electron density for a variety of electron temperatures is shown in Figure 3-14. These curves indicate that typical mean free paths for C^{+2} ions are ~ 5 -30 cm for background plasmas with parameters in the range of $n_e \sim 0.5 - 1.0 \times 10^{20} \text{ m}^{-3}$ and $T_e \sim 20$ -50 eV. These results are generally consistent with experimentally observed values for the parallel extent of the CIII plumes.

In the far SOL, the condition $T_z = T_e$ is likely to be satisfied for C^{+2} ions, since at lower temperatures the thermal equilibration time (τ_{therm}) is generally much shorter than the ionization time. However, in the near SOL $\tau_{therm} \lesssim \tau_{ion}$ for C^{+2} ions, implying that $T_{C^{+2}} < T_e$ in this region. Nonetheless, the parallel extent of the CIII plume emission, which is dominated by the presence of jet-like behavior in this case, tends to be consistent with an ionization mean-free path calculated using the electron temperature. This suggests that there is a mechanism, other than collisional coupling with the background, which provides C^{+2} impurities with temperatures of order T_e or parallel velocities of order $\sqrt{T_e/m_z}$. The presence of a finite \mathbf{E}_{\parallel} at the gas injection location, arising from ion recycling off the probe surface, is thought to be responsible (see sections 5.3 and 5.5).

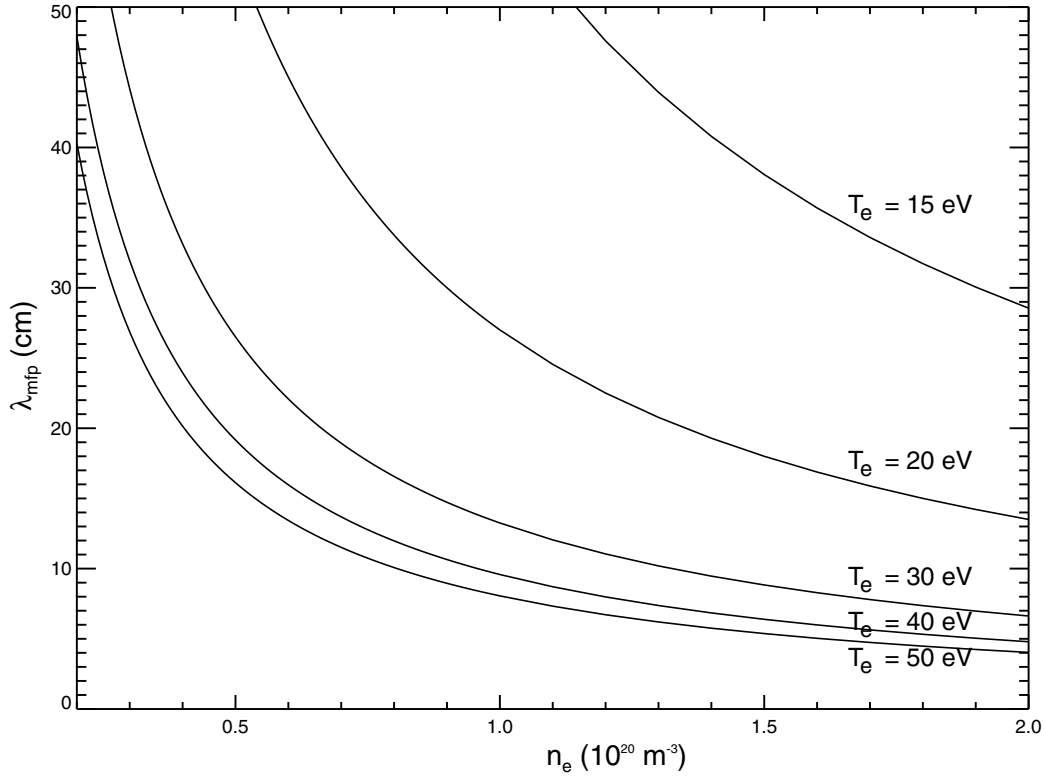


Figure 3-14: Variation of C^{+2} parallel mean-free path (estimated using Equation 3.1) with electron density, for five different values of electron temperature (ranging from 15-50 eV). Values of λ_{mfp} are comparable to the parallel extents observed for experimental CIII plumes, suggesting that in the near SOL there is a collisionless mechanism which results in a parallel velocity for the impurity ions that is comparable to the impurity sound speed, $\sqrt{T_e/m_z}$.

Assuming $T_z = T_e$ for both C^{+1} and C^{+2} , the ratio of the CIII to the CII ionization mean-free paths is equal to the ratio of the respective ionization times (Equation 3.1), which depends only on electron temperature. A plot of this ratio is given in Figure 3-15. Over most of the SOL this ratio is quite large (~ 10 -40), implying that CIII emission should be much more extended along field lines than CII emission. This is confirmed by experiment.

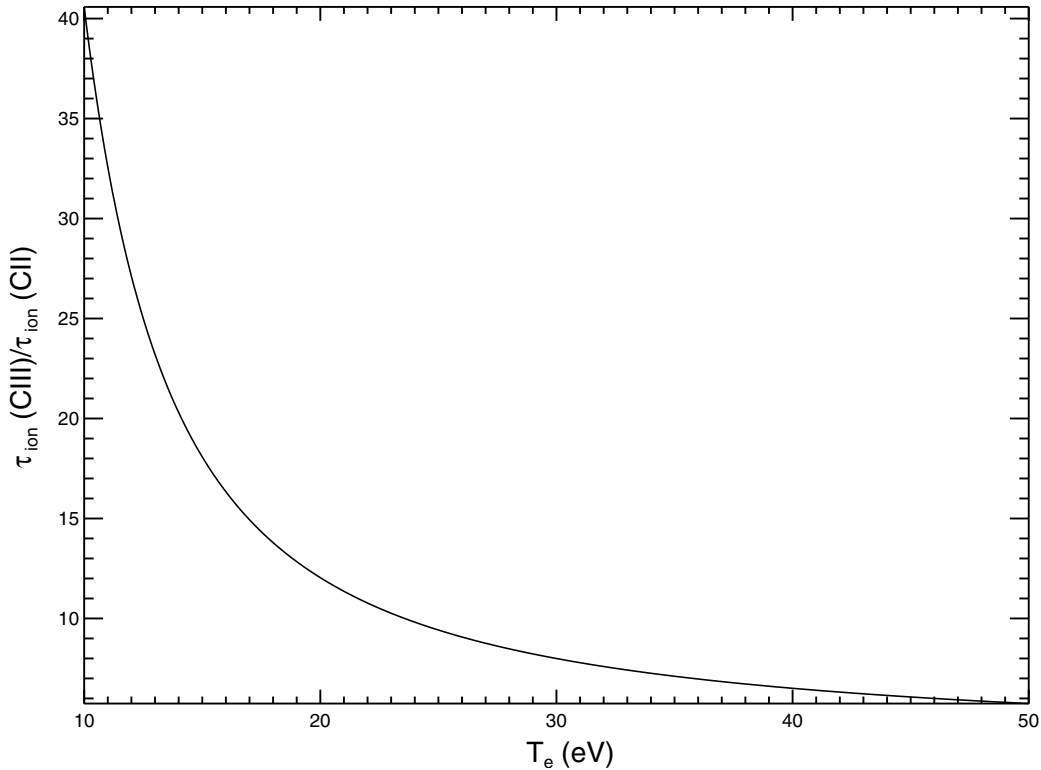


Figure 3-15: Ratio of C^{+2} to C^{+1} ionization times as a function of electron temperature. Over most of the SOL, this ratio is large, suggesting that the parallel extent of CIII emission should be much larger than the parallel extent of CII emission. This is experimentally observed.

3.2.2 Particle & Power balance

For plumes to be useful as a measure of the background plasma, they should not be perturbative (or the perturbation must be readily described). However, in principle, injection of gas in a localized volume in the SOL is expected to affect both the local

particle and power balance. The question is then one of magnitude – how large is the effect?

The magnitude of the local perturbation will depend strongly on the volume into which gas is injected. A significant fraction of injected carbon atoms are simply re-deposited on the probe head – for these atoms the perturbation is thought to be small, since they enter the plasma through sputtering, resulting in a large effective “injection” volume. However, carbon atoms not re-deposited on the probe head can be deposited in a much smaller plasma volume, whose dimension is governed by ionization mean-free paths for the injected species. Comparison with numerical modelling results (section 5.4.3) suggest that in the near SOL the cross-field extent of the injection volume (λ_{cf}) can be characterized by the jet cross-field dimension, which is $\simeq 5$ mm. In the far SOL, where the ionization mean-free path has increased and jet behavior is no longer observed (section 3.3), the cross-field extent of the injection volume is instead comparable to the plume cross-field dimension, which is significantly larger (~ 25 mm).

Density perturbation

To model the gas injection perturbation, the injection volume is taken to be cylindrical, with a diameter λ_{cf} and an extent $L_{\parallel} = 225$ mm (= “typical” parallel extent of the emission). The carbon density at the injection location is determined by particle balance:

$$2\Gamma_{\parallel,0}\left(\frac{\pi\lambda_{cf}^2}{4}\right) = \alpha N_{inj} \quad (3.2)$$

where N_{inj} is the injection rate of C_2D_4 molecules, α is fraction of the injection source which directly ionizes and flows away from the probe (i.e. is *not* re-deposited on the probe head), and $\Gamma_{\parallel,0}$ is the parallel flux of carbon at the injection location. This term can be written as:

$$\Gamma_{\parallel,0} = n_{I,0}v_{\parallel,0} \quad (3.3)$$

where $n_{I,0}$ is the total carbon ion density (all charge states) at the injection location and $v_{\parallel,0}$ is the “average” velocity of carbon impurity ions away from the probe. Simple estimates for the total dissociation energy of C_2D_4 indicate that ~ 1 eV is available for each carbon atom; for a 1 eV carbon atom $v_{\parallel,0} \simeq 4$ km/s. For a typical plume experiment, the injection rate is $\sim 5 \times 10^{18}$ molecules/second = 10^{19} C atoms/second. Assuming that $\simeq 50\%$ of injected molecules are directly ionized, then the carbon density can be written as (using Equations 3.2 and 3.3):

$$n_{I,0} = \frac{2\alpha N_{inj}}{\pi\lambda_{cf}^2 v_{\parallel,0}} = \frac{(2)(0.5)(10^{19} \text{ atoms/second})}{\pi(0.001 \text{ m})^2((\lambda_{cf} \text{ (mm)})^2)(4000 \text{ m/s})} = \frac{8.0 \times 10^{20}}{(\lambda_{cf} \text{ (mm)})^2} m^{-3} \quad (3.4)$$

In the near SOL ($\lambda_{cf} = 5$ mm), the estimated carbon density is $\sim 3.2 \times 10^{19} m^{-3}$. Assuming that within the injection volume the predominant ion charge states are $Z = 1$ and $Z = 2$, the electron density perturbation can be up to a factor of two larger. This is a substantial fraction of the background electron density, and implies that the gas injection is responsible for a local density perturbation at the injection location. However, the magnitude of the recycling-induced density perturbation is found to be much larger in this region (see sections 5.3 and 5.4), indicating that the above perturbation is only a small contribution to the total.

In the far SOL ($\lambda_{cf} \sim 25$ mm), the estimated carbon density is $\sim 1.3 \times 10^{18} m^{-3}$. This is about a factor of 10 times lower than the background electron density, indicating that the density perturbation in this case is small.

Temperature perturbation

The electron temperature perturbation due to the gas injection is assessed from a power balance:

$$\nabla_{\parallel} \cdot q_{\parallel} = \sum (Sources - Sinks) \quad (3.5)$$

$$q_{\parallel} = -\kappa_{\parallel} \nabla_{\parallel} T_e \quad (3.6)$$

Consider a cylindrical flux tube geometry ($z \parallel \mathbf{B}$), where the cross-field dimension in the near and far SOL is determined from the same injection volume model used in the density perturbation calculation. Using a 2-point model [64] to describe parallel heat transport in the injection volume, and assuming a fixed temperature boundary condition at either end of the flux tube, the parallel electron temperature profile is given by:

$$T^{7/2}(z) = T_0^{7/2} + \frac{7P_0L^2}{4\kappa_0} \left(1 - \frac{z^2}{L^2}\right) - \frac{7P_1dL}{2\kappa_0} \left(1 - \frac{|z|}{L}\right) \quad d < |z| \leq L \quad (3.7)$$

$$T^{7/2}(z) = T_0^{7/2} + \frac{7P_0L^2}{4\kappa_0} \left(1 - \frac{z^2}{L^2}\right) - \frac{7P_1dL}{2\kappa_0} + \frac{7P_1d^2}{4\kappa_0} \left(1 + \frac{z^2}{d^2}\right) \quad |z| \leq d \quad (3.8)$$

where $z = 0$ is the parallel coordinate of the injection, $\kappa_{\parallel} = \kappa_0 T_e^{5/2}$ has been used, and:

T_0 = temperature (eV) at flux tube boundary ($z = \pm L$)

P_0 = power (W/m³) into the flux tube – assumed uniform

P_1 = power sink (W/m³) due to gas injection – assumed uniform

L = (1/2) magnetic field line connection length from inner to outer divertor (m)

d = (1/2) parallel plume extent (m)

κ_0 = parallel thermal conductivity = $2.81 \times 10^3 \frac{\text{W}}{\text{m eV}^{7/2}}$ (Spitzer, [61])

P_0 is determined from a power balance without gas injection, i.e. by setting $P_1 = 0$ at $z = 0$ in Equation 3.8. This yields:

$$P_0 = \frac{4\kappa_0}{7L^2} \left[T_{np}^{7/2} - T_0^{7/2} \right] \quad (3.9)$$

where T_{np} is the temperature at the gas injection location in the absence of injection (“no plume”). Typical values of T_0 and L are 10 eV and 12.5 m, respectively. For conditions near the separatrix ($T_{np} \simeq 50$ eV), $P_0 \simeq 10$ MW/m³, while in the far SOL ($T_{np} \simeq 15$ eV), $P_0 \simeq 0.5$ MW/m³.

P_1 is estimated by summing together all possible power sinks due to the gas injection. These include:

- *Electron heating*: Energy required to heat electrons formed during ionization of injected species to the background electron temperature.
- *Dissociation energy*: Energy required to dissociate C_2D_4 molecules. This includes energy to break all necessary bonds as well as energy for excitations that may occur during dissociation.
- *Ionization energy*: Energy required to ionize both deuterons and carbon atoms formed from dissociation of C_2D_4 .
- *Radiation energy*: Energy radiated by both deuterons and carbon impurity ions.

For deuterium, a radiation energy of $\simeq 30$ eV/atom is assumed (based on data from reference [30]). For carbon, reference [7] is used to estimate the amount of radiation energy emitted per atom in a non-coronal equilibrium. This value depends on both electron temperature as well as the product $n_e\tau_{ion}$, and can range from 100 - 1000 eV/atom.

In the near SOL, the total power sink due to the plume is ~ 100 MW/m³. Though this is a factor of 10 greater than the power input P_0 at this location, this is a region where parallel conduction is high (primarily because T_e is high), and consequently the temperature perturbation is small. This is illustrated in Figure 3-16, in which profiles of the unperturbed (dashed) and perturbed (solid) electron temperature for a typical plume formed at the separatrix are shown. In the far SOL the total power sink is ~ 20 MW/m³. Here T_e is smaller, and parallel conduction is not as effective in equilibrating temperature along the field line. Thus, the power sink is large enough ($P_1 \simeq 40 \times P_0$) to induce a perturbation in the electron temperature. Profiles of the unperturbed and perturbed temperature are also shown in Figure 3-16 for this case. Though the perturbation seems to be important in the far SOL, the probes in fact do not measure a temperature perturbation during gas injection. This suggests that either the estimate for the total power sink is too large, or that the perturbation is within the measurement error for the probe.

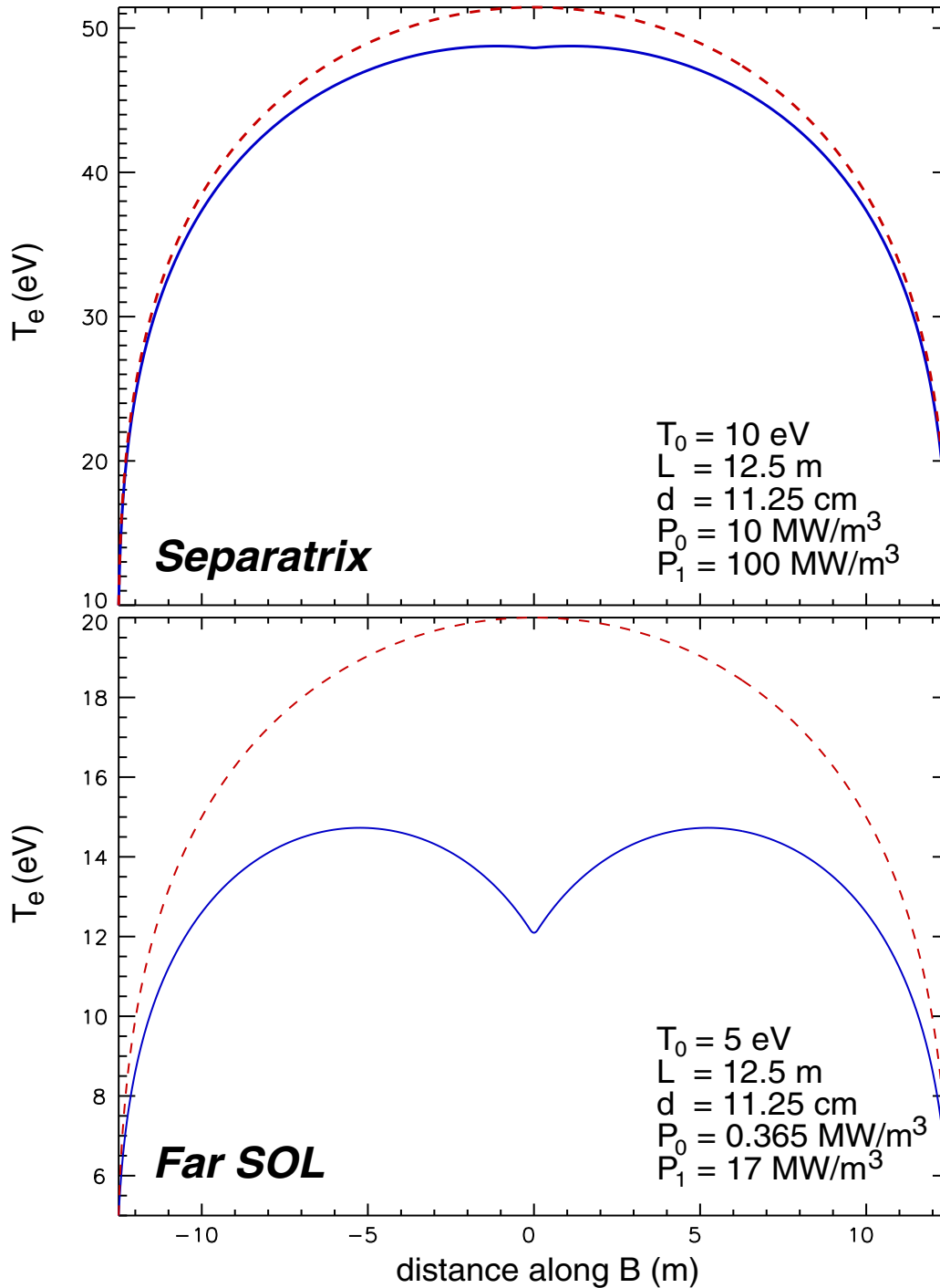


Figure 3-16: Parallel profiles of electron temperature with (solid) and without (dashed) gas injection. *Top*: Conditions typical of the separatrix. In this case the perturbation due to gas injection is small. *Bottom*: Conditions typical of the far SOL. Here the perturbation due to gas injection can be important. However, in most cases the probes measure no temperature perturbation due to gas injection, suggesting that estimates for the power sink are too large in this case or that the perturbation is within the measurement error of the probe.

3.3 Plume database

A database of plume results has been constructed to allow correlations to be explored between emission structure and plasma parameters. In particular, two topics of interest are: (1) **Jet characterization**. Is there a way to quantify jet behavior? Under what background conditions does jet behavior dominate? (2) **Far SOL plume characteristics**. Are results from wall-capillary injection experiments [28] reproduced? How do these plumes differ from those formed in the near SOL?

In this section, the development of the database is presented, as well as results which address the above questions.

3.3.1 Plume characterization

Nearly 300 plumes were generated during the 2000 run campaign. These data (specifically CIII TVC data) have been sorted qualitatively based on observations of the amount of jet behavior exhibited (“Jet; Transition; No Jet”) and on the flow direction implied from observations of the parallel asymmetry (“Flow to the divertor; Flow away from the divertor; No flow”). In addition, scanning probe data have been used to determine correlations between the qualitative observations and local plasma parameters. An example of these results is shown in Figure 3-17, in which electron temperature is plotted against parallel Mach number (computed using Equation 2.1) for discharges in which plumes were generated. Data have also been sorted by toroidal field direction (normal vs. reversed) to determine if observed plume asymmetries depend on this parameter.

A more quantitative approach has also been developed to assess the degree of jet behavior and parallel asymmetry in a given plume. This approach is based on the hypothesis that the component of emission resulting in the jet is spatially localized, i.e. has small cross-field extent. For any given plume, integrated brightnesses and emission centroids are calculated using a moment analysis, resulting in a 1-D parallel emission profile which is used to characterize the parallel extent of the plume and a 1-D parallel centroid profile which is used to determine the plume boomerang angle. Analogous

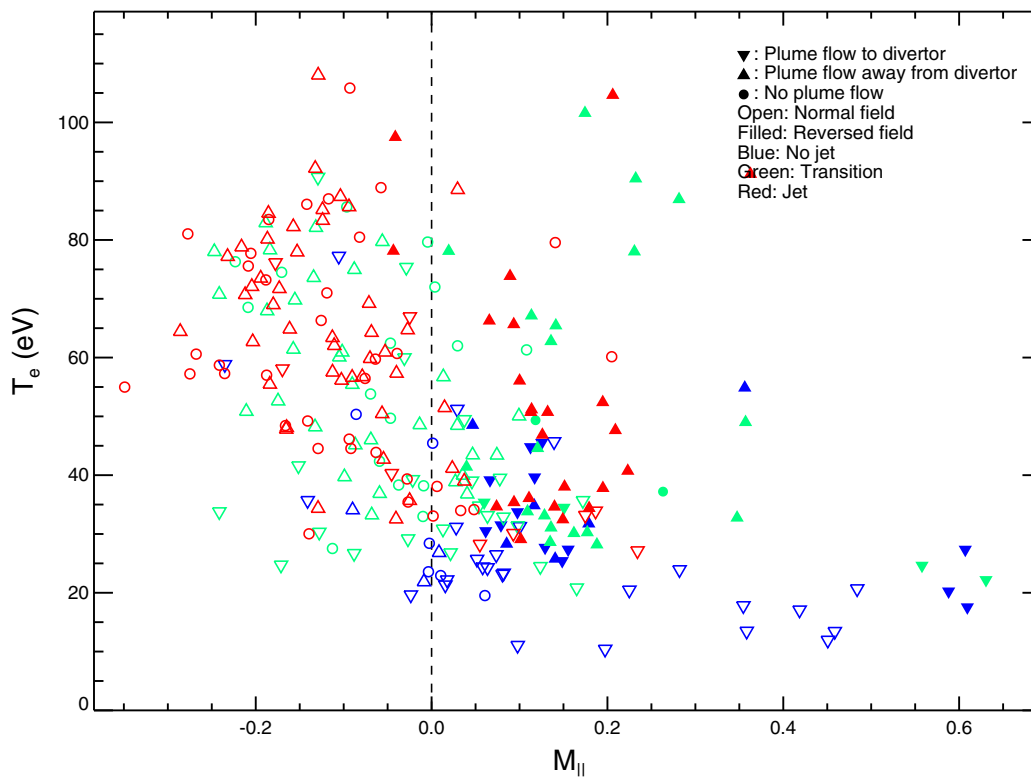


Figure 3-17: Plot of electron temperature vs. parallel Mach number for all points in the plume database. Points are sorted based on a qualitative categorization regarding the degree of “jetting” and parallel asymmetry in the emission. Points are also sorted based on toroidal field direction.

profiles can be determined using a “ridge-line” analysis, in which the centroid at each parallel coordinate is given by the location of the peak in the corresponding 1-D cross-field profile, and the brightness values at these peaks are then used to construct a 1-D parallel emission profile. An example of ridge-line analysis performed for a CIII TVC plume is shown in Figure 3-18. Two conditions are expected for jet-dominated plumes: small cross-field width (\bar{w}), as estimated from the moment analysis, and good agreement between both emission profiles and centroid profiles from moment analysis and ridge-line analysis.

Least-squares differences between emission profiles from moment analysis and ridge-line analysis (Δ_{ep}^2) and between centroid profiles from moment analysis and ridge-line analysis (Δ_{cp}^2) are calculated to quantify the agreement between the two methods. A composite least-squares difference ($\Delta^2 = \Delta_{ep}^2 + \Delta_{cp}^2$) is then constructed to provide an overall figure-of-merit for the agreement. Plume data are sorted by \bar{w} and Δ^2 .

3.3.2 Variation of jet behavior with background conditions

Results from Figure 3-17 indicate that plumes exhibit jet behavior at high temperature ($T_e \gtrsim 30$ eV), and in most cases the parallel asymmetry in these plumes is in the reversed direction (i.e. away from the divertor). This is true irrespective of the parallel flow measured by the Mach probe, suggesting that these plumes are not well-coupled to the background. This is consistent with the observation that at high temperatures the ionization rate for C^{+2} is faster than the collisional coupling rate.

The parallel variation in plasma potential which may be caused by a recycling-induced density perturbation can also affect the degree of jet behavior exhibited by the plumes. In fact, results of numerical simulation (section 5.5.1) indicate that the total potential drop ($\Delta\phi$) along \mathbf{B} is the key parameter in setting the parallel extent of the jet. From a ridge-line analysis of experimental data, an estimate of the potential drop may be obtained. The ionization lifetime of impurities in the jet is first calculated using local values of n_e and T_e (i.e. values measured by the probe *at the injection location*). The average parallel velocity (\bar{v}) of these impurities is then

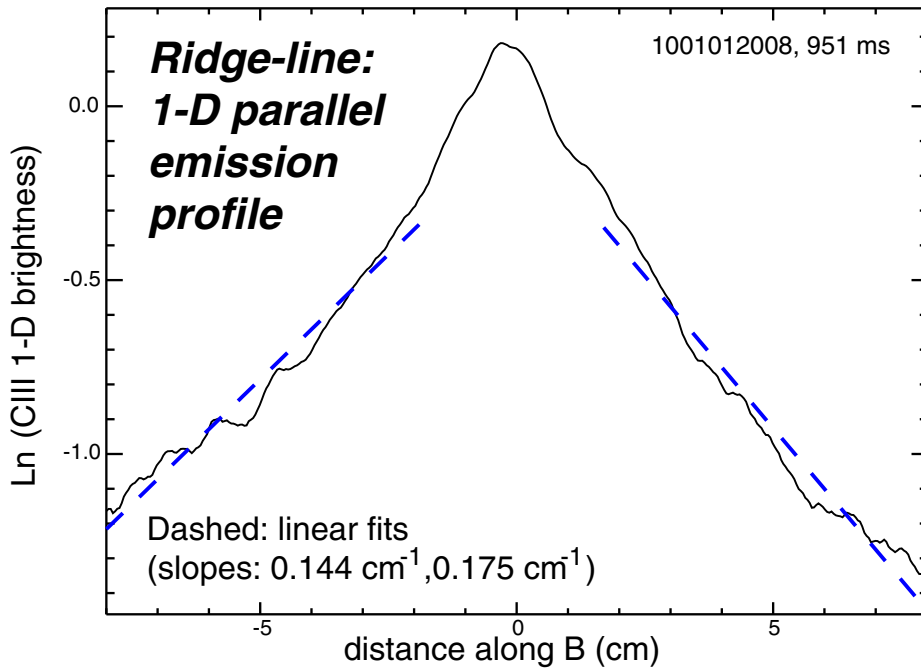
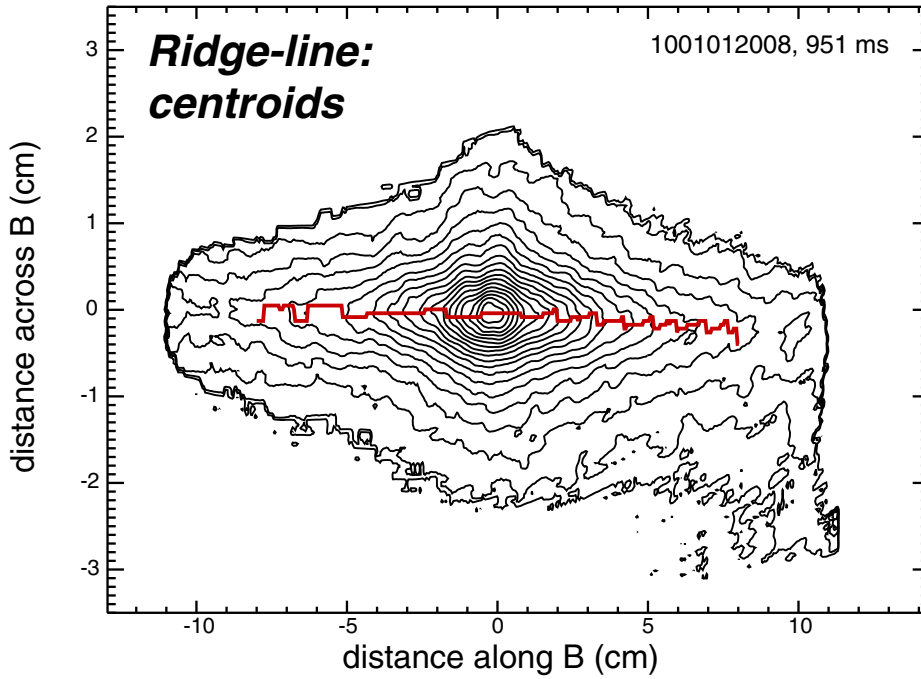


Figure 3-18: An example of “ridge-line” analysis for a CIII TVC plume. Centroids are determined at each parallel coordinate by finding the location of the peak in the corresponding 1-D cross-field profile. The value of the brightness at this peak is then used to fill in the 1-D parallel emission profile array.

calculated by dividing the average parallel decay length of the jet by the ionization lifetime. The potential drop is then determined from an energy balance:

$$\Delta\phi = \left(\frac{1}{e}\right) \left[\frac{1}{2}m\bar{v}^2 - E_0\right] \quad (3.10)$$

where E_0 is the initial energy of the impurity ions, estimated as \sim a few eV based on molecular break-up energies. Using Equation 3.10 (and $E_0 = 3$ eV), $\Delta\phi$ has been calculated for all plumes in the database (even those in which a jet is not exhibited). A plot of $\Delta\phi$ vs. T_e is shown in Figure 3-19. Although there is plenty of scatter in the data, it is clear that the potential drop required to explain the parallel extent of the jet increases with electron temperature.

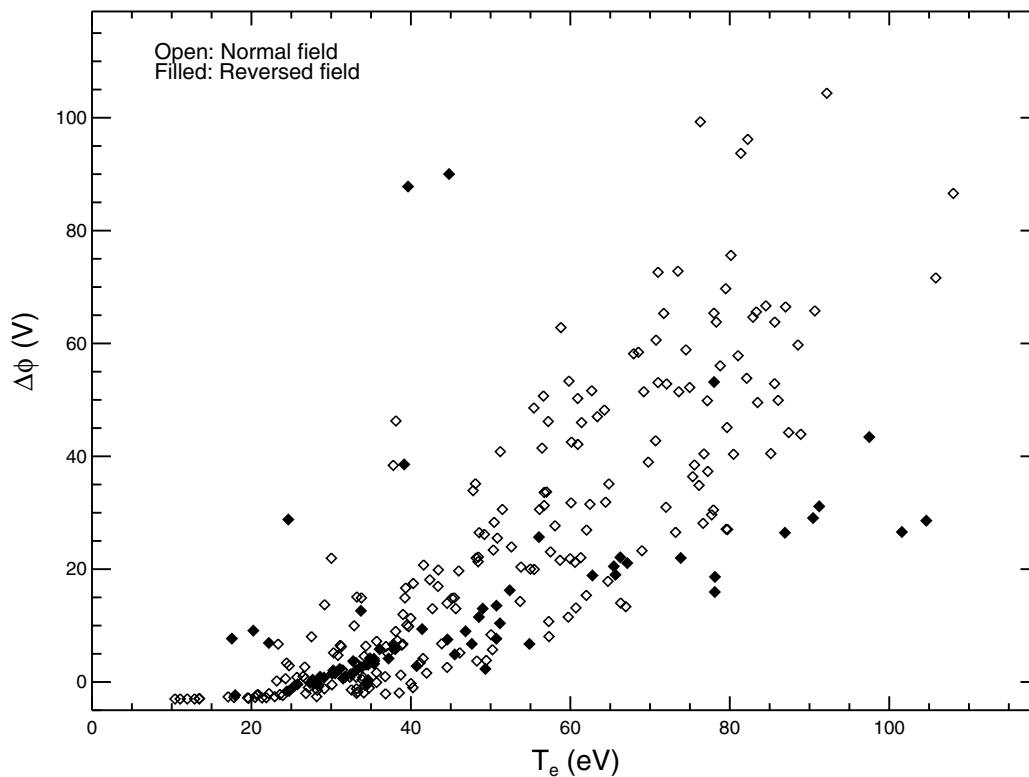


Figure 3-19: A plot of the potential drop calculated using Equation 3.10 vs. electron temperature. These values of potential drop are required to explain the parallel extent of the plume emission. Though there is scatter in the data, the required potential drop increases with T_e .

The recycling-induced perturbation strength is characterized in terms of a normalized potential drop ($\frac{e\Delta\phi}{T_e}$). A plot of $\frac{e\Delta\phi}{T_e}$ vs. atomic deuterium ionization mean-free path (λ_{mfp}, D^0) is shown in Figure 3-20. In the top panel, data points are labeled by plume cross-field width (\bar{w}), while in the bottom panel they are labeled by the composite least-squares difference between moment and ridge-line analysis profiles (Δ^2). In either case, a strong dependence is seen between the normalized potential drop and the ionization mean-free path. The explanation is straightforward: as the mean-free path decreases, ionization of recycling deuterium occurs over a smaller volume, resulting in a larger density perturbation and thus a larger potential drop (assuming that density and potential are related through a Boltzmann relationship: $n_e \propto e^{-e\phi/T_e}$). Though there is scatter in the data, plumes with lower values of \bar{w} and Δ^2 tend to have a larger value of $\frac{e\Delta\phi}{T_e}$, i.e. are more jet-like.

Asymmetries in the plume emission are also quantified using ridge-line analysis. For a given plume, the parallel velocity of impurities in the jet is in general different on one side of the injection location relative to the other. The parameter $\Delta v/\bar{v}$ (where $\Delta v = v(\text{towards divertor}) - v(\text{away from divertor})$) is used as a measure of the plume asymmetry. In Figure 3-21, this parameter is plotted against the parallel Mach number for all plumes in the database. As in Figure 3-20, points are labeled by \bar{w} and Δ^2 .

Plumes with low values of \bar{w} and Δ^2 tend to exist at negative values of $\Delta v/\bar{v}$, implying that the parallel flow of C^{+2} ions present in jet-like plumes is away from the divertor. This is consistent with the qualitative observations shown in Figure 3-17. In addition, plumes which exist at negative values of $\Delta v/\bar{v}$ occur for all values of parallel Mach number, suggesting that there is no direct relationship between background flow and plume asymmetry in these cases. This result seems to be confirmed by the observation that the direction of parallel asymmetry for plumes exhibiting jet-like behavior is insensitive to toroidal field direction, whereas M_{\parallel} measurements made by the probe are strongly dependent on field direction. This is illustrated in Figure 3-22, which shows $\Delta v/\bar{v}$ plotted against the probe-inferred parallel Mach number for plumes with $\bar{w} \leq 1.12$ cm, $\Delta^2 \leq 0.20$, and $\rho \leq 5$ mm.

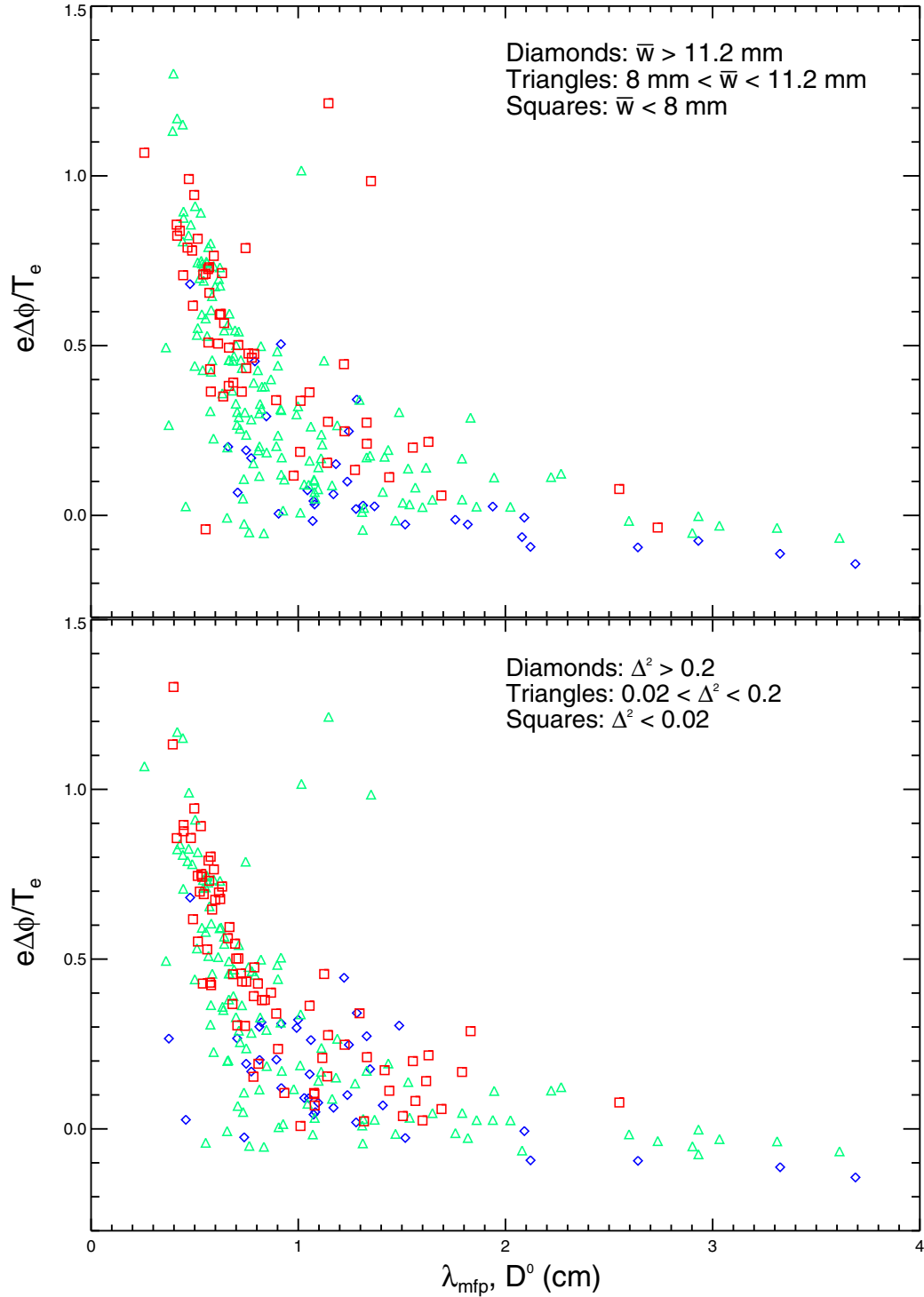


Figure 3-20: A plot of normalized potential drop vs. ionization mean-free path of atomic deuterium for all plumes in the database. *Top:* labeled by cross-field width, \bar{w} . *Bottom:* labeled by least-squares difference parameter Δ^2 . As the ionization mean-free path decreases, so does the volume in which recycling deuterium is ionized, leading to a larger density perturbation and a larger potential drop. Larger potential drops tend to be seen for plumes with smaller \bar{w} and Δ^2 .

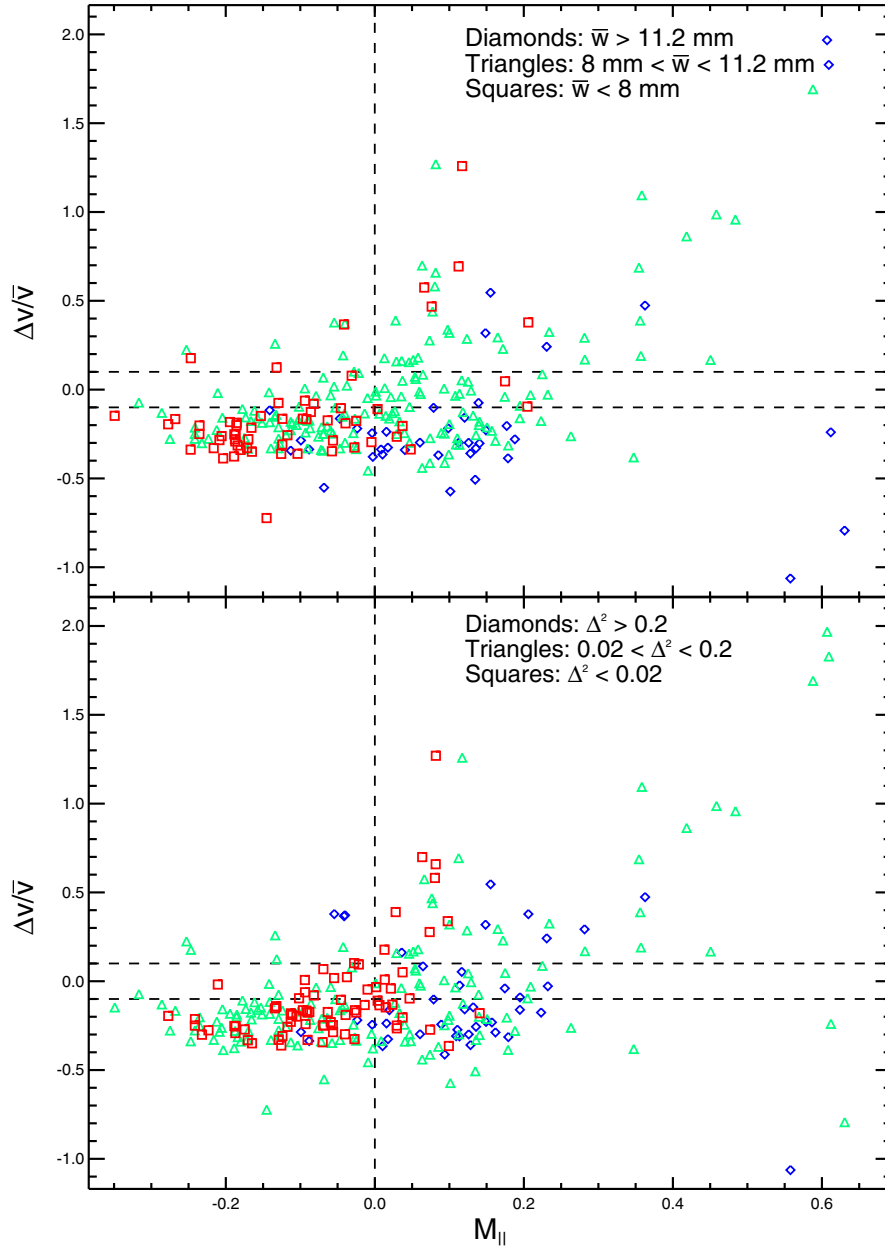


Figure 3-21: Normalized plume asymmetry vs. parallel Mach number inferred from probe measurements. *Top*: labeled by cross-field width, \bar{w} . *Bottom*: labeled by least-squares difference parameter, Δ^2 . For jet-like plumes (i.e. those with low \bar{w} and/or Δ^2), the plume asymmetry generally implies a flow away from the divertor, irrespective of the probe-inferred parallel Mach number. As the plumes become less jet-like, they tend to exist in regions of higher (positive) Mach number, corresponding to locations of larger ρ .

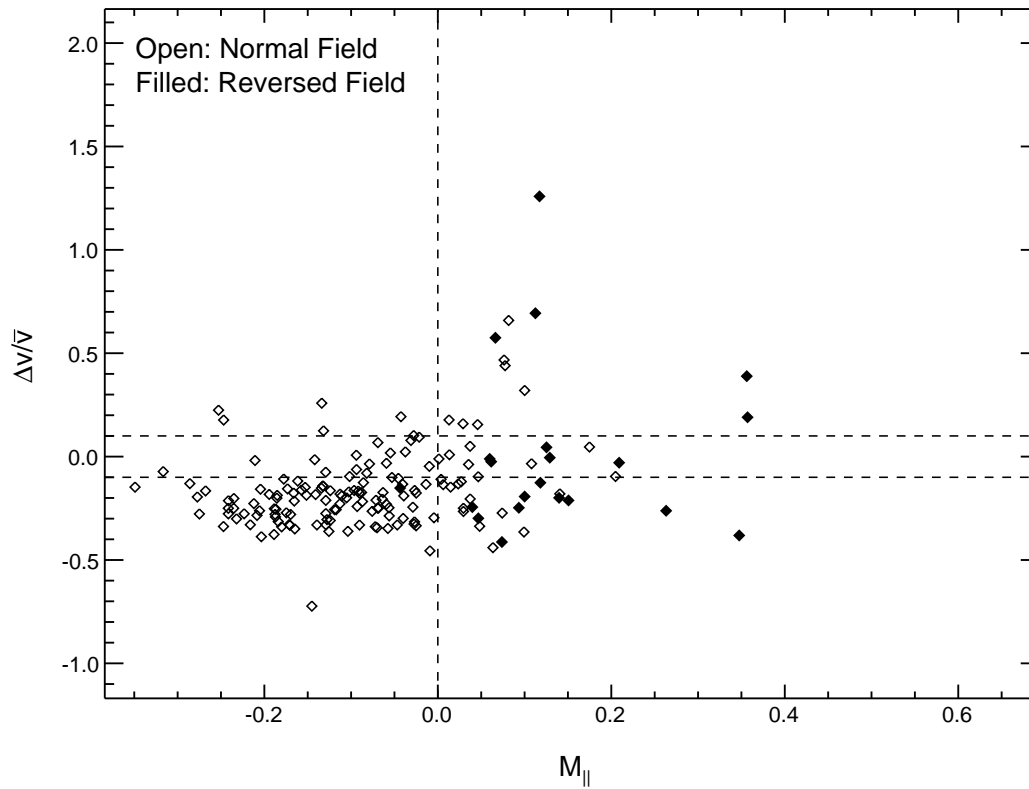


Figure 3-22: Normalized plume asymmetry vs. parallel Mach number inferred from probe measurements, labeled by toroidal field direction. Only plumes which exhibit some level of jet-like behavior are considered ($\bar{w} \leq 1.12$ cm, $\Delta^2 \leq 0.20$, $\rho \leq 5$ mm). The results confirm that no direct relationship exists between background flow and plume asymmetry for cases where jet-like behavior is important.

However, referring back to Figure 3-21, it is observed that as the parallel Mach number increases the plumes tend to become less jet-like, i.e. they have higher values of \bar{w} and/or Δ^2 . Note that there is a tendency for the Mach number (as measured by the probe) to increase with distance from the separatrix, while temperature decreases with ρ . This suggests that plumes in fact are becoming less jet-like at lower temperature, which is consistent with results from the potential drop calculations (Figure 3-19).

3.3.3 Characteristics of plumes without jet

Plumes which do not exhibit a jet tend to be formed in the far SOL, and for these cases the potential drop calculated from Equation 3.10 tends to be small (i.e. $\frac{e\Delta\phi}{T_e} \ll 1$). This is consistent with the model for the jet: in the far SOL the temperature is low, so the ionization mean-free path for recycling deuterium is large, which results in a small recycling-induced density perturbation and therefore no jet. For these cases a ridge-line analysis is an inappropriate means to determine parallel velocities for the impurities, and thus to determine a parallel asymmetry, since no component of the emission is localized. Nonetheless, when this analysis is employed the result is a large, positive value for $\Delta v/\bar{v}$, consistent with the large values of M_{\parallel} measured by the probe (e.g. see Figure 3-21).

Previous plume measurements have been made on Alcator C-Mod using gas injection through wall-mounted capillaries [28]. An example of a CII plume generated by injection through a capillary at the inner wall midplane and viewed from the outer midplane is shown in Figure 3-23. For comparison, an example of a CII SVC plume generated in the far SOL is also shown in this figure. Similarities which exist between these two plumes include the absence of jet-like behavior in the emission structure and the presence of a strong asymmetry implying flow towards the divertor. These results emphasize that far and near SOL plumes differ not only because of differences in the impurity ionization rates at these two locations, but because the physics of ions recycling from the probe head is important in the near SOL. This is discussed further in Chapter 5.

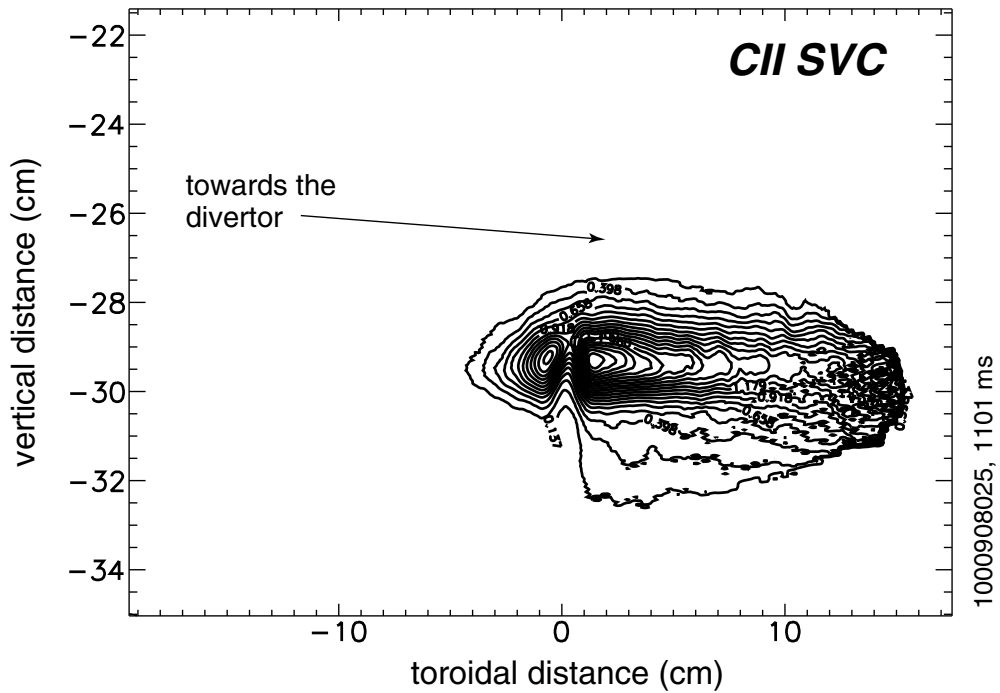
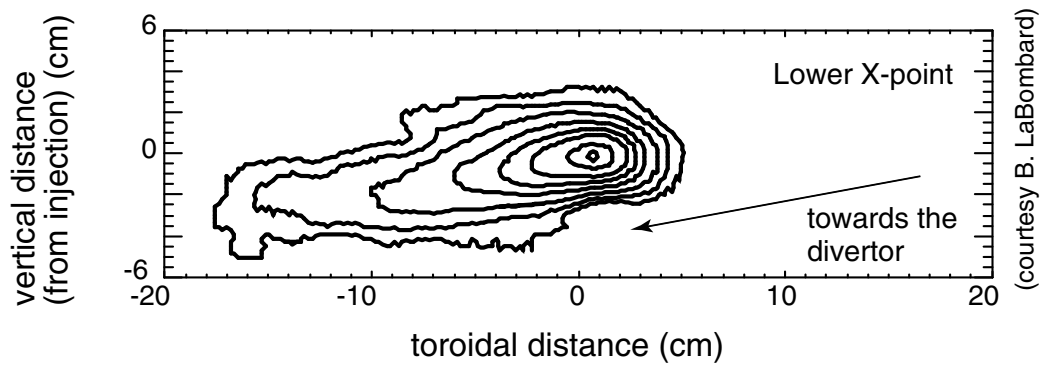


Figure 3-23: Comparison between CII plume generated by injection through a capillary at the inner wall midplane (*top*) and a CII plume generated by injection through the probe in the far SOL (*bottom*). For the inner wall case, the view is from the out-board midplane, while for the probe injection case the view is from the SVC. In both cases plumes exhibit a strong asymmetry towards the divertor, and no jet behavior is observed.

Chapter 4

Plume modelling tools

To assess the utility of the plumes as a diagnostic of SOL flows, a series of modelling tools have been developed for extracting flow information from emission structure. A description of the tools is presented in this chapter, while results obtained from their application to experimental data is given in Chapter 5.

4.1 Analytic fluid modelling

Initial analysis and modelling of the plume emission patterns involved a fluid description of background plasma and impurity transport. Results from this analysis are presented, followed by a discussion of the limitations of analytic modelling.

4.1.1 Development of 1-D & 2-D fluid models

Plume structure is thought to be influenced by the following plasma parameters: v_{\parallel} , \mathbf{E}_r , and D_{\perp} . However, since a significant fraction of the emission results from carbon sputtering off the probe head, the effect of diffusion on the emission structure is thought to be small (for reasonable values of D_{\perp} , e.g. 0.1 - 1.0 m²/s). A 1-D fluid model has been developed to test this assumption, which is based on solution of the continuity equation for impurity species:

$$\nabla \cdot \underline{\Gamma}_j = S_j - n_j n_e \langle \sigma v \rangle_{ion} \quad (4.1)$$

n_j is the impurity density for charge state j , n_e is the electron density, S_j is the volumetric source for impurities in charge state j , $\langle \sigma v \rangle_{ion}$ is the ionization rate coefficient for ionization from state j to state $j + 1$, and $\underline{\Gamma}_j = -D_\perp \nabla n_j + n_j \underline{v}_c$ is the flux of impurity ions in charge state j , accounting for both purely diffusive (D_\perp) and convective (\underline{v}_c) components. Consider a simplified cartesian geometry, where y is the coordinate along which perpendicular diffusion takes place. For finite extent of the plume, Equation 4.1 can be integrated in the other two directions, yielding:

$$\frac{d}{dy}(\bar{n}_j v_c) - \frac{d}{dy} \left(D_\perp \frac{d\bar{n}_j}{dy} \right) = S_0 \pi \lambda_j^2 e^{-y^2/\lambda_j^2} - \bar{n}_j n_e \langle \sigma v \rangle_{ion} \quad (4.2)$$

\bar{n}_j is the integrated 1-D impurity density along y , while v_c and D_\perp are the flow convection and diffusivity in this direction. The following assumptions were made in deriving Equation 4.2: recombination is negligible; S_j is a Gaussian, with a peak of S_0 and a cross-field width of λ_j ; electron density and temperature are constant over the region of the plume. The validity of this last assumption is questionable, and will be addressed in section 4.1.2. Equation 4.2 may be further simplified under the assumption that v_c and D_\perp are also constant over the plume region (again, the validity of this assumption may be argued), allowing an analytic solution to be obtained (using the method of characteristic polynomials and the method of variation of parameters [20]). The solution is given in terms of a normalized 1-D impurity density, η , defined as:

$$\eta = \frac{\bar{n}_j \lambda_j}{S_T \tau_{exp}} \quad (4.3)$$

where S_T is the total integrated source rate for impurities in charge state j ($= S_0 \pi^{3/2} \lambda_j^3$) and τ_{exp} is the exposure time for the camera recording the plume emission. Solutions for η are determined in cases where D_\perp is both finite and zero, to determine the influence of diffusion on the cross-field width. An example is shown in

Figure 4-1. In this case λ_j is set to 8 mm, a typical value for the cross-field width of an experimental CIII plume, and a reasonable value for the source width for the given probe head geometry (see Figure 2-1). The perpendicular diffusion is set to 1.0 m^2/s , and the cross-field flow velocity to ~ 1000 m/s. It is clear that the width of the 1-D density profile cares very little about the value of D_{\perp} , and is being set primarily by the source width. This is consistent with the heuristic arguments presented in section 3.1.1, and suggests that the plumes provide little information on D_{\perp} in the SOL.

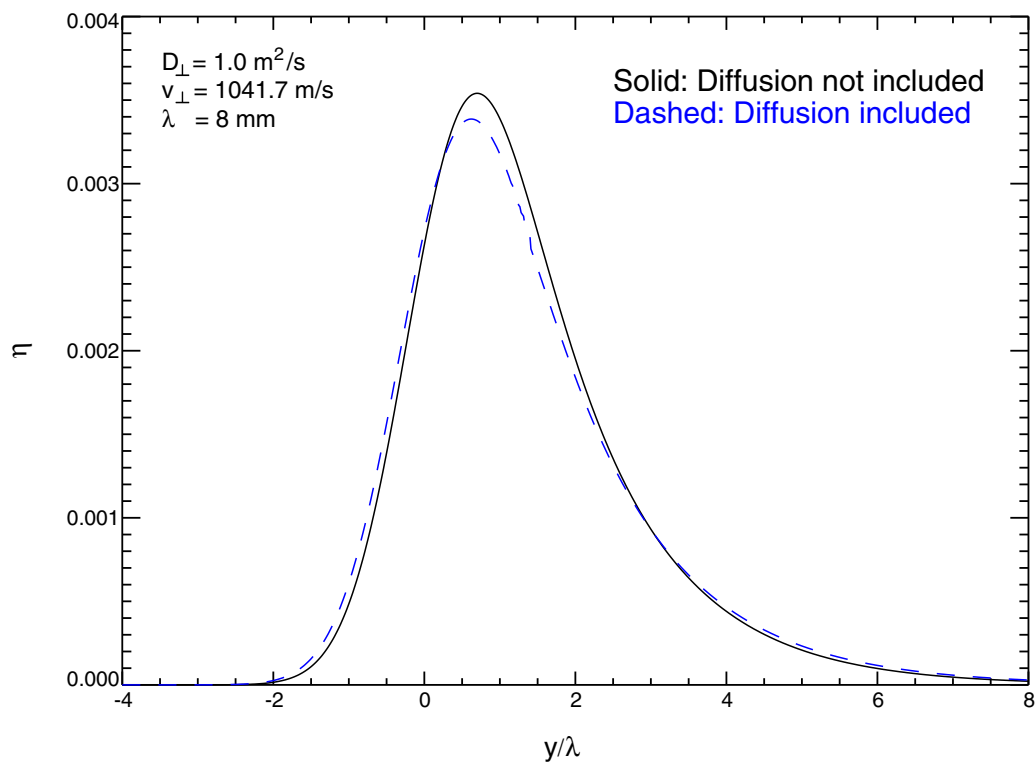


Figure 4-1: Comparison of normalized 1-D impurity density profiles with and without diffusion effects. The source width is set to 8 mm, which is a typical value for the cross-field width of experimental CIII plume emission. For a value of 1.0 m^2/s , the effect of diffusion on the profile width is insignificant. This suggests that the plumes provide little information on D_{\perp} in the SOL.

Given these results, it may be concluded that v_{\parallel} and \mathbf{E}_r are the only important parameters determining the structure of the plumes (in the limit where probe perturbations are negligible). A 2-D fluid model has therefore been constructed to extract

values for these parameters from CIII plume emission. This model is once again based on solution of the continuity equation (Equation 4.1). However, in this case the solution is determined for the region of the plume which is *source-free*, i.e. the region well away from the injection location, meaning that $S_j = 0$. Also, perpendicular diffusion is neglected (based on arguments given above), allowing the ion impurity flux to be written simply as $\Gamma_j = n_j \underline{v}_c = n_j \underline{v}$. In addition, the following assumptions are made: the parallel velocity is a function only of the parallel coordinate (x); the cross-field velocity lying in the flux surface (v_y) is constant over the region of interest; the electron density and temperature are constant over the region of interest. The validity of these latter two assumptions will be discussed in the next section. After integration of Equation 4.1 in the cross-flux surface direction (z) and some algebraic manipulation, the following equation results:

$$\frac{\partial}{\partial x}(\ln \bar{n}_j) + \frac{v_y}{v_x} \frac{\partial}{\partial y}(\ln \bar{n}_j) = -\frac{1}{v_x \tau_{ion}} - \frac{1}{v_x} \frac{d}{dx} v_x \quad (4.4)$$

y represents the cross-field coordinate, \bar{n}_j the integrated 2-D impurity density, and $\tau_{ion} = \frac{1}{n_e \langle \sigma v \rangle_{ion}}$. In order to proceed, a functional form for the parallel flow velocity is required. To simplify the analysis, an exponential dependence is assumed:

$$v_x(x) = v_{x0} \left(a - \exp\left(-\frac{x}{\lambda}\right) \right) \quad [x > x_0] \quad (4.5)$$

x_0 is the parallel coordinate at which plume emission becomes “source-free”; in this model, the upstream and downstream portions of the plume are treated separately. Equation 4.4 can then be solved using the method of characteristics [68], yielding:

$$\bar{n}_j = \bar{n}_{j0} \left(y - \beta \lambda \ln \left[\frac{-1 + a \exp\left(\frac{x}{\lambda}\right)}{-1 + a} \right] \right) \left[\frac{-1 + a}{-1 + a \exp\left(\frac{x}{\lambda}\right)} \right]^\alpha \left[\frac{-1 + a}{a - \exp\left(-\frac{x}{\lambda}\right)} \right] \quad (4.6)$$

where the following definitions have been made: $\alpha = \frac{\lambda}{av_{x0}\tau_{ion}}$, $\beta = \frac{v_y}{av_{x0}}$. Assuming that the impurity density is directly proportional to the measured brightness, Equation 4.6 may be used to fit the plume data for extraction of v_{x0} and v_y , i.e. v_{\parallel} and \mathbf{E}_r . Data

are fitted along each parallel coordinate, and average values of the fitting parameters ($a, \lambda, \alpha, \beta$) are then calculated for the full plume. An example fit for a CIII TVC plume generated in the near SOL is shown in Figure 4-2. The solid line is a line-out of the plume data at a given parallel coordinate ($x = -1.85$ cm), while the diamonds are scaled values of density calculated using Equation 4.6. In this case the fit is quite good; for the full plume the inferred values of v_{\parallel} and \mathbf{E}_r are 10 km/s and -4 kV/m, respectively.

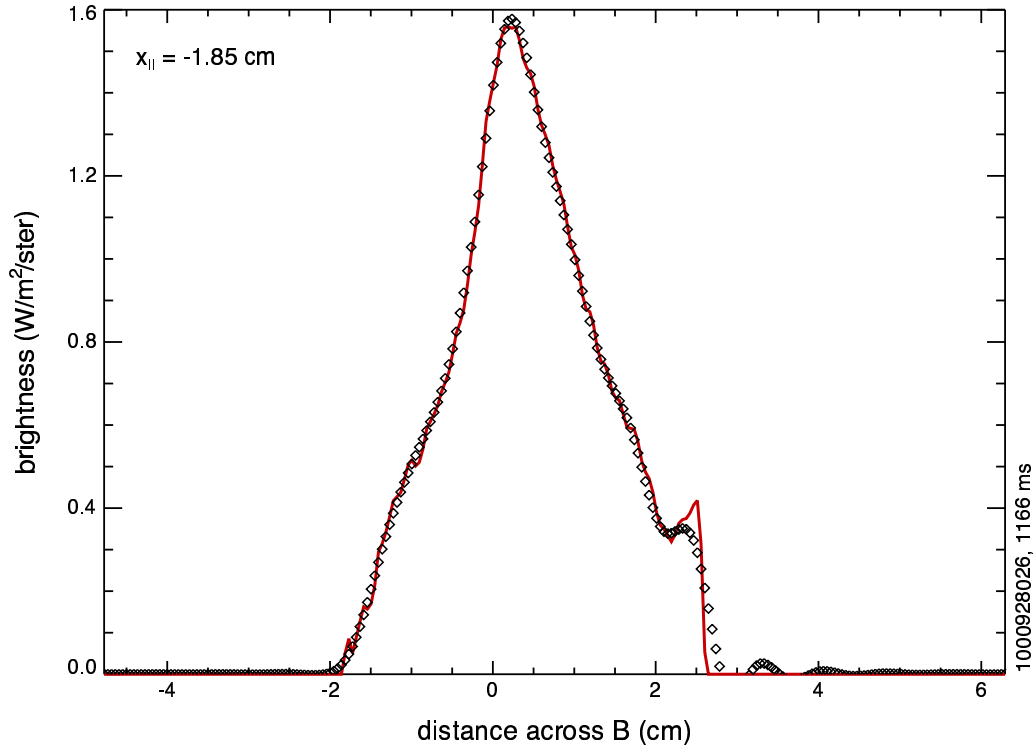


Figure 4-2: Fit to a 1-D cross-field brightness profile from a CIII TVC plume (the full plume is shown in Figure 3-8). The solid line is the experimental data, while the diamonds are scaled values of density calculated using Equation 4.6. The fit is quite good in this case; for the full plume the inferred values of v_{\parallel} and \mathbf{E}_r are $\simeq 10$ km/s and -4 kV/m, respectively.

The estimated parallel velocity is significant fraction of the impurity ion sound speed ($\sqrt{T_e/m_z} \simeq 25$ km/s), suggesting a substantial parallel energy for the impurity ions. This is consistent with the observation that the parallel extent of CIII plume emission generated in the near SOL is comparable to the ionization mean-free path

for C^{+2} ions calculated using the electron temperature. The mechanism thought to be responsible for imparting parallel energy to the impurity ions is a recycling-induced parallel electric field. To model this field, a more appropriate representation of the background plasma is necessary, e.g. one in which electron density is allowed to vary. Variation in the electron density and temperature can also affect the cross-field structure of the emission, which has a direct impact on the estimated value for the radial electric field (see section 5.7.1). These observations suggest that the use of analytic modelling for describing impurity dispersal may be limited (more details in section 4.1.2), and that a more sophisticated description of the impurity emission is necessary.

4.1.2 Limitations of analytic modelling

Although analytic fluid modelling of the plume emission is useful for obtaining estimates of the parallel velocity and radial electric field implied from the emission structure, there exist severe limitations to the results. Primary among these is the assumption of constant density and temperature over the region of the plume. Without this assumption the problem is not analytically tractable. However, it is unlikely that sputtering of deposited carbon off the probe head will occur on a single flux surface. Thus, plumes exist over a finite extent across flux surfaces, over which density and temperature vary. The assumption of constant density and temperature is especially erroneous in the near SOL, where plasma profiles vary strongly with ρ .

For this same reason the assumption of constant perpendicular velocity (and hence \mathbf{E}_r) over the plume region is also likely to be invalid. Probe measurements indicate that the radial electric field profile also varies with ρ in the SOL, and that this variation can be quite strong in the near SOL.

Another deficiency of analytic fluid modelling is that the probe influence on the plume emission structure cannot be taken into account. For example, these models are unable to simulate impurity sputtering or background ion recycling off the probe surface. In addition, they do not include the existence of parallel velocity and electric fields generated in the probe presheath. These presheath fields are responsible for

accelerating impurity ions located on field lines which intersect the probe towards the probe, and may therefore influence the parallel extent of the emission.

This information calls into question modelling efforts performed for plumes generated by gas injection through wall-mounted capillaries [28]. In those calculations, density, temperature, and electric field were all assumed to be constant over the region of the plume; to be more precise, the values extracted were assumed to be “radially-averaged” quantities. However, results of numerical modelling (section 5.7.1) indicate that the radial variation of density and temperature over the plume extent can alter the structure of the plume significantly. In the far SOL, density and temperature profiles are typically observed to flatten out, suggesting there may be some validity to assuming constant density and temperature for plumes generated from injection through the inner wall capillary. Nonetheless, in that case there remains the issue of data mapping from outboard to inboard SOL. For the model presented in [28], plasma parameters are assumed constant along a field line from outer divertor to inboard midplane. However, recent results obtained from a newly installed inner-wall scanning probe suggest that density and temperature may be different at the inner wall and the FSP location [40]. This result highlights the importance of making local measurements of background plasma parameters at the gas injection location.

Simplified 1-D & 2-D fluid modelling provides a basis for intuitive understanding of the plume data, but to realistically simulate the plumes the full set of mass, momentum, and energy equations need to be solved. However, these equations can only be solved analytically for simplified situations (e.g. no background flow, strongly coupled plumes). Rather than invest time in the development of a 3-D numerical fluid code, the decision was made to utilize a resource that was already available for studying impurity transport in SOL plasmas, namely the LIM code [65].

4.2 LIM modelling

The majority of plume modelling undertaken in this work involves the use of LIM. In this section, a brief description of the code will be given, followed by a discussion of

modifications that have been made to the code to allow for a more accurate simulation of the experimental set-up. Finally, results of code benchmarking will be presented.

4.2.1 Code overview

LIM (Limiter Impurity) is a 3-D Monte Carlo impurity transport code. Particles may be “launched” into the plasma as either neutrals or ions (“launch” referring to the specification of the particle position and velocity vectors at its time of origin); they are followed from their point of origin until they exit the plasma by striking a wall or limiter. The coordinate system in LIM is cartesian, where y represents the distance along the magnetic field, x represents the radial cross-field coordinate, and p represents the poloidal (in the flux surface) cross-field coordinate. In this simplified geometry toroidal effects (e.g. curvature drifts) are neglected.

The impurities are launched into a specified background plasma. Although individual particles are followed, they each represent an ensemble of impurity ions with average velocity and temperature. The transport of impurity ions along the field line is assumed classical, and is governed by coulomb collisions with the background plasma according to three characteristic time constants:

$$\tau_S = \frac{m_I T_{iB} (T_{iB}/m_B)^{1/2}}{6.8 \times 10^4 (1 + m_B/m_I) n_B Z_B^2 Z_I^2 \ln(\lambda)} \quad \text{Stopping time} \quad (4.7)$$

$$\tau_T = \frac{(m_I T_{iB} + m_B T_I)^{3/2}}{1.4 \times 10^5 (m_I m_B)^{1/2} n_B Z_B^2 Z_I^2 \ln(\lambda)} \quad \text{Heating time} \quad (4.8)$$

$$\tau_{\parallel} = \frac{m_I T_I (T_{iB}/m_B)^{1/2}}{6.8 \times 10^4 n_B Z_B^2 Z_I^2 \ln(\lambda)} \quad \text{Parallel diffusion time} \quad (4.9)$$

τ_S represents the average time for impurities to acquire the background flow velocity, τ_T the average time for thermalization, and τ_{\parallel} the average time for parallel velocity space diffusion. These parameters depend on local values of the background density (n_B in units of 10^{18} m^{-3}) and ion temperature (T_{iB} in units of eV) which are specified as code inputs, and are allowed to vary with the radial coordinate. m_I and m_B represent the impurity ion and background plasma ion masses (in units of amu), Z_I and Z_B are the impurity ion and background plasma ion charge states, T_I is the

impurity ion temperature (in eV), and $\ln(\lambda)$ is the Coulomb logarithm.

The cross-field transport of impurity ions is modelled as anomalous, and governed by the following transport coefficients, all of which are specified as inputs: D_{pol} , D_{radial} , v_{pol} , v_{radial} . Diffusion coefficients are only allowed to vary along \mathbf{B} , while the radial velocity may be varied with radial coordinate in specific functional forms. The poloidal velocity is allowed to vary with radial coordinate in a general manner (see section 4.2.2).

Other inputs to the code are the parallel flow velocity and the parallel electric field. These may be specified at each individual computational cell, though in general, functional forms are used to generate their values. Further discussion follows in sections 4.2.2 and 5.5.1.

The original purpose of LIM was to model the transport of impurities generated via sputtering from a limiter surface. However, a series of options are now available for specifying various impurity launches in both physical space and velocity space. For example, the impurities may be launched from a fixed point in space or from a surface, with constant energy or a Thompson distribution [5]. More discussion of launch options is given in sections 4.4 – 4.6. Finally, for a given LIM run the number of impurities launched is specified as an input, a typical value being 10,000.

The time step (Δt) for each iteration in the code is also specified as an input. Its value is set by the requirement that Δt be much smaller than any physics time scale present in the problem. For a typical simulation $\Delta t = 50$ ns (more in section 4.2.3).

At each time step, it is first determined whether the charge state of the given impurity ion has changed. The parameter τ_{ch} is defined as [65]:

$$\tau_{ch}^{-1} = [n_B(\langle \sigma v \rangle_{ion} + \langle \sigma v \rangle_{recomb})] \quad (4.10)$$

where $\langle \sigma v \rangle_{ion}$ is the ionization rate coefficient and $\langle \sigma v \rangle_{recomb}$ is the recombination rate coefficient, which are both functions of electron temperature ($T_e = T_{iB}$ is assumed for plume simulation). In the limit of the recombination rate being much smaller than the ionization rate (all cases of interest), $\tau_{ch} = \tau_{ion}$. At each time step, a

random number ξ is drawn (which is uniformly distributed in the domain $[0,1]$), and if $0 < \xi < \frac{\Delta t}{\tau_{ch}}$ then a change of charge state has occurred.

After determining the charge state of the impurity ion being followed, the position, parallel velocity, and temperature of the ion ensemble are calculated. The temperature at each time step is determined from the following:

$$T_{new} = T_{old} + (T_{iB} - T_{old}) \left(\frac{\Delta t}{\tau_T} \right) \quad (4.11)$$

Equations for determining the position and parallel velocity at each time step are presented in later sections. Once the position of the ion has been calculated, indices are determined for the computational cell in which the ion is located. In each cell tallies are kept which indicate the number of times an impurity ion of a given charge state appears in that cell at the end of a time step. For example, if at the end of a time step an impurity ion with $Z_I = 1$ is in a cell with (y, x, p) indices of $(39,34,15)$, then the tally for that cell for that charge state is incremented by one. The number of tallies in each cell is converted to a “normalized cell density” (n_N) at the end of the calculation using the cell dimensions $(\Delta y, \Delta x, \Delta p)$, the numerical time step (Δt) , and the total number of impurities launched. The units of n_N are $(\text{m}^{-3})/(\text{particles/second})$, i.e. the density is normalized to the *impurity injection rate*.

Outputs from the code include 3-D spatial distributions for each charge state, 3-D spatial variations for the total radiated power, and the average ion temperature of each charge state “cloud”. Spatial distributions of each charge state may be converted to number density (m^{-3}) by specifying an injection rate for the impurities. Density in turn may be converted to emissivity using photon emissivity coefficient (PEC) data, and a 2-D brightness at each experimental view location can be calculated from the 3-D emissivity by “virtual imaging” of the emission. In this manner simulated results may be compared directly with experimental data. The details of these algorithms are presented in section 4.3.

4.2.2 Code modifications

A number of modifications have been made to LIM to allow for a more accurate simulation of the gas injection experiments. These include:

Non-symmetric limiter specification

The source of impurities in the experiment is both gas injection through the probe as well as sputtering off the probe head. It is therefore critical that the presence of the probe be included in the simulation. LIM expects a limiter surface to be specified as input, so in simulation of plume experiments this is given by the probe head geometry. In the original version of LIM, the limiter surface was assumed to be poloidally symmetric. However for the plume simulations this assumption is not appropriate, since in the experiment the probe head is generally at an angle with respect to flux surfaces (typically $\simeq 45^\circ$). Modifications have been made in the code to allow for the limiter surface to be rotated with respect to flux surfaces, in order to simulate the probe head. A schematic of the probe head geometry in the LIM coordinate system is shown in Figure 4-3. Also note in this figure that the probe geometry has been simplified. For the “absorbing probe” (i.e. the limiter surface by which impurity ions may exit the plasma) the probe is represented as a pyramid connected to a rectangular parallelepiped (as shown in the figure). For the “recycling probe” (i.e. the surface off which impurity ions may be launched), the probe is more realistically represented as a cone connected to a cylinder. This probe model is discussed further in sections 4.4 and 4.5.

Radial variation of v_{pol}

The poloidal velocity specified in LIM is meant to simulate the effect of $\mathbf{E} \times \mathbf{B}$ drifts resulting from the presence of a radial electric field in the SOL. In the original version of LIM, this velocity was assumed constant over all space. However, experimentally it is observed that \mathbf{E}_r varies with SOL position, and to the extent that

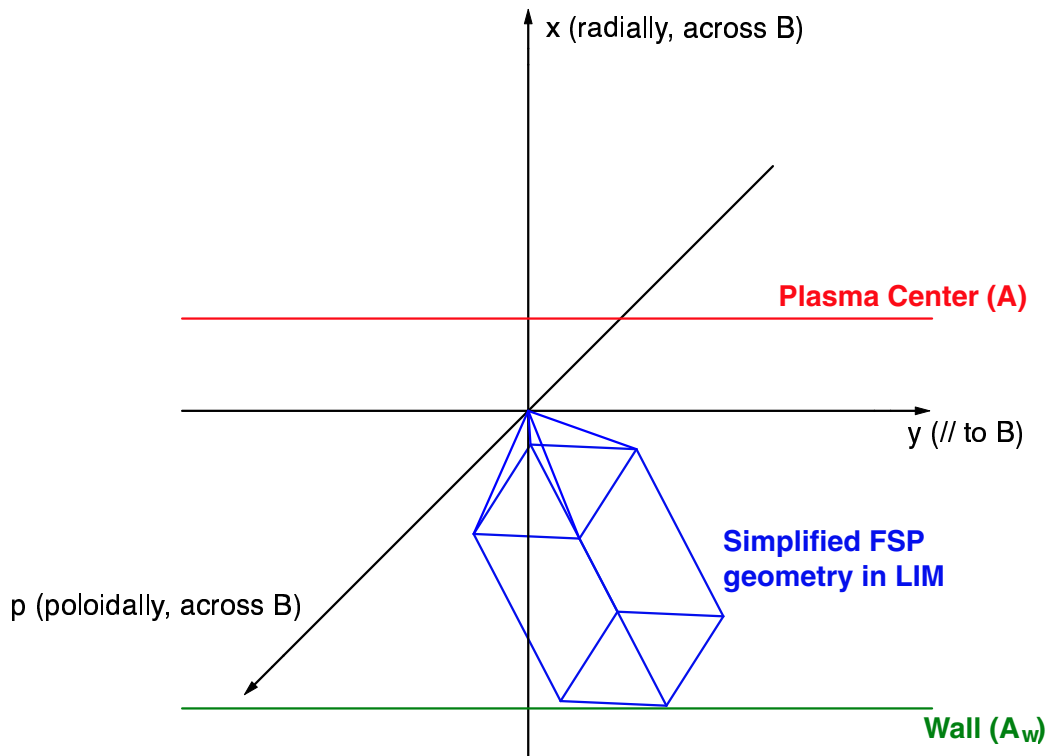


Figure 4-3: Schematic of the FSP probe head geometry implemented in LIM for the case of the “absorbing probe” (pyramid connected to a rectangular parallelepiped). The geometry of the “recycling probe”, that of a cone connected to a cylinder, is a more realistic representation of the probe head, and is used for modelling both the carbon sputter source and the recycling-induced density perturbation. Finally, note the location of radial boundaries in the LIM geometry (A and A_w) – these will be discussed in section 4.2.3.

the plume exists over finite cross-field dimension this effect should be included. A modification was therefore made to allow the poloidal velocity to vary with radial dimension. Values for v_{pol} are required for each radial cell, allowing a general specification of the radial electric field profile to be given.

Inputted n_e, T_e profiles

Time scales that appear in the modelling (e.g. $\tau_{ion}, \tau_{||}$) depend on local values of both the electron density and temperature and ion density and temperature. Experimentally, n_e and T_e values are determined directly at the gas injection location using the probe. For plume simulation it is then assumed that $n_D = n_e$ and $T_D = T_e$. During plume formation, when the probe is at its peak insertion, density and temperature values at radial (cross flux surface) locations other than the probe tip are in principle unknown. However, in the simulation n and T values are required for the full emission volume. Experimental density and temperature data are available for a large extent of the SOL from probe measurements obtained during the full probe scan. The assumption is therefore made that n_e and T_e profiles measured from the full probe scan are the same as the profiles which exist when the probe is at peak insertion, i.e. during plume formation. There is, however, evidence that electron density is in fact approximately constant over the plume extent, for it is otherwise very difficult to explain the vertical elongation observed in the emission. The presence of local $\mathbf{E} \times \mathbf{B}$ drifts induced by probe presheath potentials may be responsible for the transport of plasma down the probe shaft, resulting in a uniform density profile – this is discussed further in section 5.1. Nonetheless, for the plume simulation profile measurements obtained from the full probe scan are used to specify the radial variation of density and temperature.

In the original version of LIM, functional forms for the density and temperature profiles were assumed (e.g. exponential variation). A modification to the code has been made to allow for arbitrary values of density and temperature to be specified in each radial bin. Over the radial range in which probe measurements are available,

these values are then used. Further out radially (relative to the last measurement point) profiles are assumed to decay exponentially, with decay lengths obtained by fitting the last few points in the profiles. Further in radially (relative to the gas injection location) profiles are assumed to increase linearly, with slopes obtained by fitting the first few points in the profiles. Extrapolation of the profiles in this manner results in some error, of course. In the near SOL, this error is expected to be insignificant, since time scales for C^{+1} and C^{+2} ions vary weakly with temperature at high T_e , and since the outward radial extent of the plumes should be covered by the probe measurements and the inward radial extent of the plumes (past the injection location) is small (low ionization lifetime). In the far SOL, where time scales are expected to vary strongly with T_e , errors may be significant. However, results suggest that in this case plume structure is sensitive enough to density and temperature values that the plumes themselves provide information on the profiles. This will be discussed further in Chapter 6.

Presheath model

Background plasma conditions affect the parallel dynamics of the impurity ions, and thus values of v_{\parallel} and \mathbf{E}_r inferred from the plume structure. It is therefore important to include in LIM physics responsible for causing variations in background parameters. For example, at the *same* radial coordinate, values for some background plasma parameters are expected to be different on field lines which are connected to the probe (i.e. field lines in the probe presheath) relative to values on those field lines which do not intersect the probe. This is necessary to satisfy the Bohm criterion [6] for ion flow ($M_{\parallel} = 1$) into the probe sheath. To calculate the presheath fields ($n_e, v_{\parallel}, E_{\parallel}$) in LIM, a modified version [70] of the 2-D fluid model of Hutchinson [23] is employed. This model takes into account effects of perpendicular flow in the presheath analysis. An example of the resulting parallel profiles is shown in Figure 4-4. In this case the background parameters outside of the probe presheath are $n_e = 4.0 \times 10^{19} \text{ m}^{-3}$, $T_e = 30 \text{ eV}$, $v_{\parallel} = 0 \text{ m/s}$, $E_{\parallel} = 0 \text{ V/m}$, and a presheath connection length of 10 m is assumed. The parallel electric field in the presheath is generally weak – however,

values of v_{\parallel} are large and the variation in electron density is significant over the full parallel extent of the plume. In LIM, presheath fields are calculated at each radial coordinate, based on the local values of background parameters at that location. Results from simulation studies indicate that the inclusion of presheath fields causes a slight reduction in the parallel extent of the plumes and an increased boomerang angle.

Finally, a series of new launch options have been added to the code, to simulate the plume sputter-source as well as to investigate causes for jet behavior in the plume emission. These will be described in detail in the following sections.

4.2.3 Benchmarking

To proceed with analysis of experimental data using LIM, it must first be demonstrated that the code output is trustworthy. This is verified by conducting a series of tests to benchmark the code.

Diffusion model

At each time step the radial and poloidal position of the impurity ion being followed is incremented in the following manner:

$$x_{new} = x_{old} \pm (2D_{radial}\Delta t)^{1/2} + v_{radial}\Delta t \quad (4.12)$$

$$p_{new} = p_{old} \pm (2D_{pol}\Delta t)^{1/2} + v_{pol}\Delta t \quad (4.13)$$

where the sign in front of the diffusive terms is chosen using a uniformly distributed (on $[0,1]$) random number, such that there is a 50% probability of either sign being chosen in either case. To test that the diffusive transport model is correctly implemented, a simulation was run for a simplified case in which an analytic solution could also be found. The case is one with constant density and temperature, constant diffusivity, no flows, and no probe influence (i.e. no limiter absorption, no presheath fields). The problem is solved in a cylindrical geometry, with r representing the cross-field coordinate and $z \parallel \mathbf{B}$. Assuming that the impurity ion source is uniformly distributed

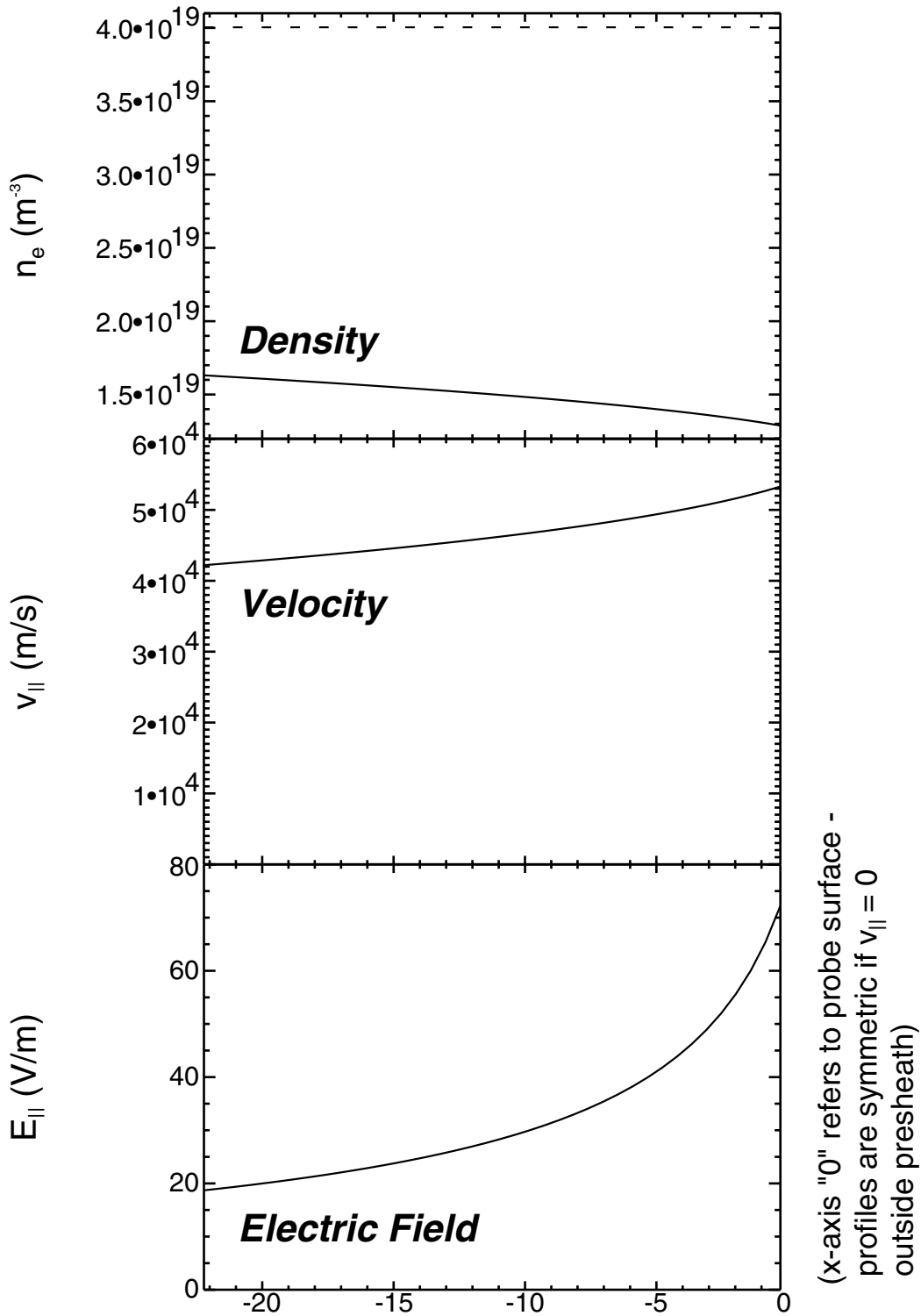


Figure 4-4: Parallel profiles of n_e , $v_{||}$, and $E_{||}$ in the probe presheath. In this case values for background parameters outside the presheath are $n_e = 4.0 \times 10^{19} \text{ m}^{-3}$, $T_e = 30 \text{ eV}$, $v_{||} = 0 \text{ m/s}$, $E_{||} = 0 \text{ V/m}$, and a presheath connection length of 10 m is assumed. While the parallel electric field in the presheath is weak, $v_{||}$ is large and the variation in electron density is significant over the full extent of the plume.

over some region $r \leq \Delta$, and that ionization is only allowed to occur in the region $r > \Delta$, the continuity equation for this system may be written as:

$$\frac{1}{r} \frac{d}{dr} \left(r \frac{dn}{dr} \right) - H(r - \Delta) \alpha^2 n = -H(\Delta - r) \left(\frac{S_1}{D_\perp} \right) \quad (4.14)$$

where n is the C^{+1} ion density (assumed to be a function of r only, i.e. $n = n(r, \theta, z) = n(r)$), S_1 is the volumetric source rate (neutrals/m³/s), α is defined as $\frac{1}{\sqrt{D_\perp \tau_{ion}}}$, and H is the Heaviside step function [60], given by:

$$\begin{aligned} H(t - a) &= 0 & t \leq a \\ H(t - a) &= 1 & t > a \end{aligned}$$

Since D_\perp and τ_{ion} are constants, α is also a constant, allowing Equation 4.14 to be solved in the region $r > \Delta$. A solution may also be found in the region $r \leq \Delta$ since S_1 is assumed constant. Taking \bar{n} to represent the integral of the C^{+1} ion density in the z direction, in the limit of $\Delta \rightarrow 0$ (i.e. a point source) \bar{n} is given by:

$$\bar{n} = \frac{S_0 K_0(\alpha r)}{2\pi D_\perp} \quad (4.15)$$

where S_0 is the integrated source rate (neutrals/s) and K_0 is the modified Bessel function of the second kind of order zero [74]. This solution is compared to a LIM run in which the density and temperature are set constant ($n_e = 4 \times 10^{19} \text{ m}^{-3}$, $T_e = 30 \text{ eV}$), and the poloidal and radial diffusivities are set equal ($D_{radial} = D_{pol} = 10 \text{ m}^2/\text{s}$). S_0 is set equal to 1 neutral/s for this comparison, because the source rate (i.e. the injection rate) in LIM is also 1 neutral/s (more details in section 4.3.1). The results of the comparison between Equation 4.15 and the LIM output are shown in Figure 4-5. There is generally good agreement between the simulation (diamonds) and the analytic solution (solid), indicating that the diffusion model in LIM is correctly implemented.

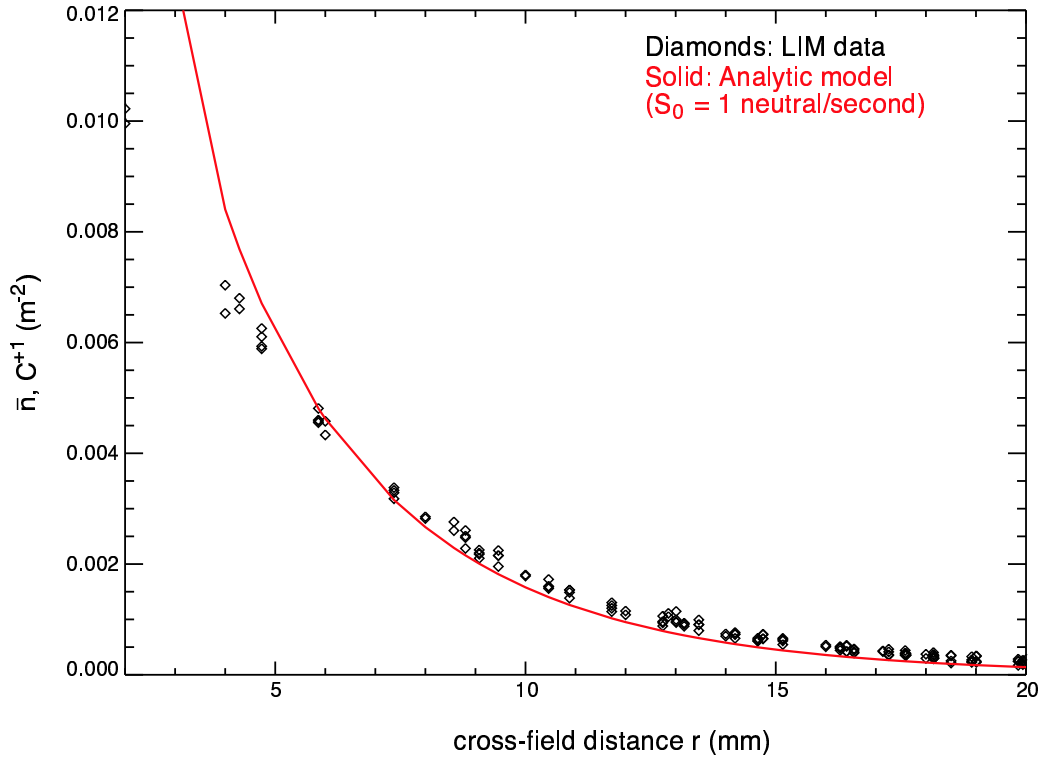


Figure 4-5: Comparison between analytic (solid) and simulation (diamonds) results of a simple diffusion model test. In this case all background parameters are constant: $n_e = 4.0 \times 10^{19} \text{ m}^{-3}$, $T_e = 30 \text{ eV}$, $D_{radial} = D_{pol} = 10 \text{ m}^2/\text{s}$, $v_{radial} = v_{pol} = v_{\parallel} = 0 \text{ m/s}$. In addition, there is no probe influence, due either to absorption of impurity ions or creation of presheath fields. In this simplified case results from the simulation and analytic modelling exhibit generally good agreement, indicating that the diffusive transport model in LIM is correctly implemented.

Grid size & time step

Tests have also been conducted to determine the effect of computational cell size and time step on the code output. Virtually no dependence on Δt is observed, as long as it is much less than any other time scale in the simulation. The smallest values for ionization and equilibration times (Equations 4.7 – 4.9) are on the order of μs for typical SOL conditions. Thus for most cases a time step of 50 ns is used.

The effect of the cell size is related to the boundary definitions in LIM. In the parallel direction the computational volume is assumed to be periodic in $2L_c$, where this represents the distance from the injection location to the edge of the domain along \mathbf{B} . However, background plasma parameters which vary with parallel coordinate (e.g. n_e and v_{\parallel} in the probe presheath) are assumed to be periodic in L_c . This is a remnant of the original version of the code, in which the impurity source was sputtering from a limiter, and toroidal periodicity was assumed. L_c is specified as a code input – as long as this value is sufficiently large relative to the plume parallel extent, the density of impurities will be small in regions near the periodic boundary for the background plasma, and the effects of periodicity will be negligible. The parallel bin size is given by the ratio of $4L_c$ (since the computation volume for impurity ions extends to $\pm 2L_c$ in the parallel direction) to the number of parallel bins (limited to 80 by computational resources). Since this size (~ 6 mm) is smaller than the typical parallel mean-free paths for C^{+1} and C^{+2} ions, the bin size does not result in poor computational resolution.

In the poloidal direction, the boundaries are at $\pm\infty$, i.e. the boundary bins are infinitely large in the poloidal direction. The choice for bin size over the remainder of the grid is determined by maximizing the poloidal view while maintaining good poloidal resolution, and minimizing the number of impurity ion tallies in the boundary bins. Results indicate that the presence of a significant number of impurity ion tallies in the poloidal boundary bins can affect the structure of the simulated 2-D plumes. This is because data present in these bins are not included in the imaging – since the bins extend to $\pm\infty$ the bin density is in principle zero, but in reality it is ill-

defined since the actual poloidal extent of the plume is not recorded in the code. Neglecting this data also limits the values of \mathbf{E}_r that can be inferred from the plume emission, since high poloidal velocity also results in a significant impurity population in the poloidal boundary bins (at least the bin that is in the direction of the flow). A typical value for the bin size in the poloidal direction is ~ 4 mm.

Finally, in the radial direction the boundaries are defined by the plasma center and plasma wall coordinates, which are also specified as code inputs (see Figure 4-3). Impurities which make it to the plasma center are reflected – however, by specifying this coordinate to be a significant distance away from the injection location (e.g. ~ 10 cm), it is ensured that very few impurity ions make it this far, since the ionization lifetime is decreasing in this direction. Conversely, impurity ions which make it to the plasma wall are absorbed. It was originally thought that this interaction should also be minimized, so the plasma wall coordinate was placed far away from the injection location. However, this leads to the formation of an extremely large ($\gtrsim 17$ cm) radial bin at this boundary, in which tallying statistics are significantly poorer than in the rest of the grid. Therefore, the plasma wall coordinate is instead positioned so that this boundary bin is equal in size to the adjacent radial bin. Simulations were then run in which the radial bin size was changed from 1 to 2 mm. Results are shown in Figure 4-6, in which CIII 1-D parallel profiles (obtained by integrating the 3-D tally data in the cross-field directions) are compared for the two cases. The parallel profiles are found to be nearly identical, indicating that radial bin size does not affect the code output. The radial bin size used for plume simulation is determined by maximizing the radial view while maintaining good radial resolution, and is typically 2 mm.

Parallel velocity model

For LIM to be a useful tool for extracting v_{\parallel} and \mathbf{E}_r from plume emission structure, the parallel dynamics of impurity ions must be correctly modelled in the code. Calculations for the impurity ion parallel velocity are therefore checked for consistency with well-documented [22] results for parallel transport in classical (i.e. coulomb-collision dominated) systems.

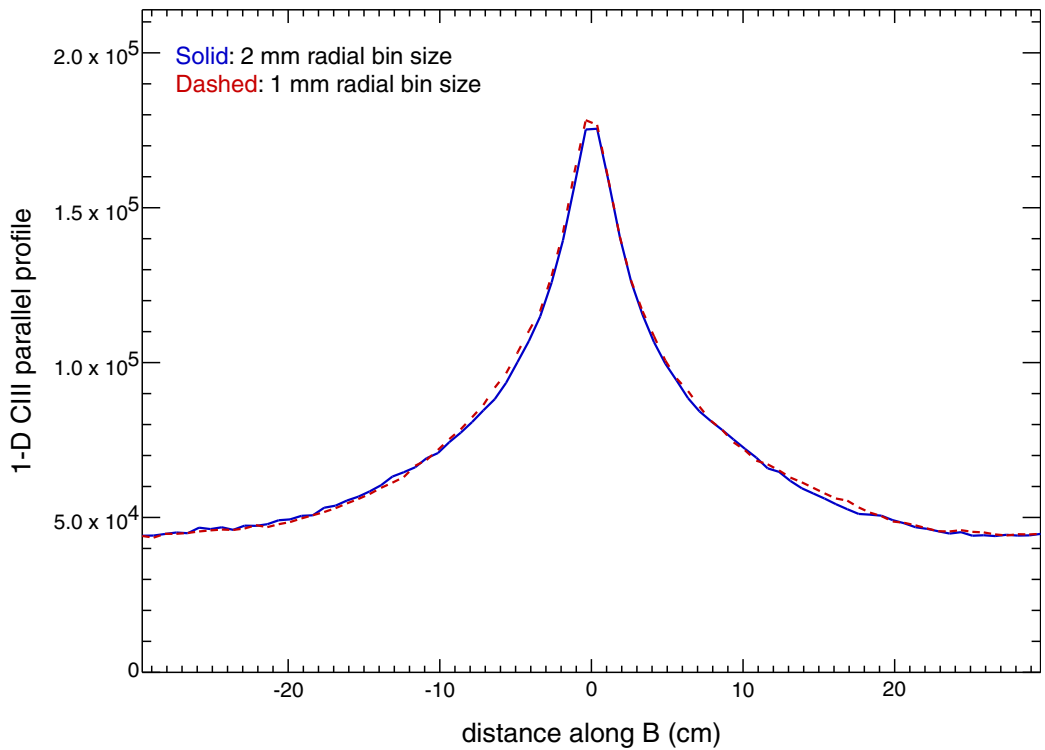


Figure 4-6: Comparison of CIII 1-D parallel profiles for two different radial bin sizes (1 mm vs. 2 mm). The profiles are nearly identical, suggesting that bin size has a negligible effect on code output.

In LIM, the effects of interaction between an individual impurity ion and the background plasma are determined by treating the impurity ion as a representation of an ensemble of ions or a “fluid packet”. This packet is characterized using a Maxwellian ion velocity distribution function with temperature T_I and parallel velocity v_I . Thus, an interaction between an impurity ion and the background plasma is in fact an ensemble-averaged quantity, representing the full set of interactions between all “micro-particles” in the distribution function and the background. This treatment of the impurity ions is used to determine both the ion parallel dynamics as well as the ion temperature (Equation 4.11). Two relaxation processes arising from the interaction of the fluid packet with the background may act to alter the parallel velocity of the packet: slowing down (i.e. background drag) and parallel diffusion (i.e. pitch-angle scattering). The influence of drag on the impurity ion parallel velocity is given by:

$$v_{new} = v_B + (v_{old} - v_B) e^{-\Delta t/\tau_S} \quad (4.16)$$

where v_B is the background parallel flow velocity. The impurity ion parallel velocity approaches v_B on a time scale equal to τ_S , as expected. Parallel diffusion alters the parallel ion velocity in the following manner:

$$v_{new} = v_{old} + v_{th,I} \left(\frac{\Delta t}{\tau_{\parallel}} \right)^{1/2} \left(1 + \frac{m_B}{m_I} \right)^{1/2} \sqrt{-2 \ln(\xi_1)} \cos(2\pi\xi_2) \quad (4.17)$$

where $v_{th,I}$ is the impurity ion thermal velocity ($= \sqrt{\frac{2T_I}{m_I}}$), and ξ_1 and ξ_2 are uniformly distributed (on $[0,1]$) random numbers. To understand the origin of this equation, start with the assumption of a Maxwellian distribution for ions in the fluid packet. Since this distribution is isotropic in velocity space, pitch-angle scattering collisions only affect the speed (v) of the packet-averaged impurity ion. In addition, the probability that the speed is changed an amount Δv by a collision is given by a Gaussian distribution:

$$P(\Delta v) = \frac{1}{\sqrt{2\pi}\Delta v_0} e^{-\Delta v^2/2\Delta v_0^2} \quad (4.18)$$

Δv_0 represents the root-mean square (RMS) change in speed of an impurity ion ($\Delta v_0^2 \equiv \int_{-\infty}^{\infty} \Delta v^2 P(\Delta v) d(\Delta v)$). A velocity diffusivity (D_v) may be defined from this value, analogous to the definition of D_{\perp} in physical space (e.g. Equation 4.12):

$$\Delta v_0^2 = 2D_v\Delta t \quad (4.19)$$

In Equation 4.17, ξ_1 is used to pick out a normalized value of Δv with probability distributed according to a normalized version of Equation 4.18 (i.e. $P(\frac{\Delta v}{\Delta v_0})$). The actual value of Δv is obtained by multiplying this normalized value by Δv_0 . From Equation 4.17, we find that in LIM $\Delta v_0 = v_{th,I} \left(\frac{\Delta t}{\tau_{\parallel}}\right)^{1/2} \left(1 + \frac{m_B}{m_I}\right)^{1/2}$. Finally, ξ_2 is used to determine the component of the velocity change along \mathbf{B} . For an isotropic distribution, the parallel component is given by the cosine of the angle (θ) between the impurity ion velocity vector and the parallel axis, with the probability distribution for θ being uniform (on $[0,2\pi]$).

To verify that LIM is correctly modelling parallel diffusion, the value of D_v implied by Equations 4.17 and 4.19 is checked against results from the NRL Plasma Formulary [22]. The LIM value is given by the expression:

$$D_v \text{ (LIM)} = \frac{1}{2} \left(\frac{v_{th,I}^2}{\tau_{\parallel}}\right) \left(1 + \frac{m_B}{m_I}\right) \quad (4.20)$$

This expression may be simplified further by substituting for $v_{th,I}$ and τ_{\parallel} (Equation 4.9), leading to:

$$D_v \text{ (LIM)} = \frac{1}{6} \left(\frac{A_D}{\sqrt{\pi}}\right) \sqrt{\gamma} \left(1 + \frac{m_B}{m_I}\right) \quad (4.21)$$

where $A_D \equiv 16\pi Z_B^2 Z_I^2 m_I^{-2} \left(\frac{e^2}{4\pi\epsilon_0}\right)^2 n_B \ln(\lambda)$ and $\gamma \equiv \frac{m_B}{2T_{iB}}$. These parameters are only a function of background conditions and impurity ion charge state. In the Plasma

Formulary, the velocity diffusivity is more generally defined for a test particle with velocity \mathbf{v} streaming through a stationary background of field particles (p. 31 in [22]):

$$D_v (\text{NRL}) = \frac{1}{2} \nu_{\parallel} v^2 \quad (4.22)$$

where it has been assumed that $\frac{d}{dt}(\mathbf{v} - \bar{\mathbf{v}})_{\parallel}^2$ may be represented by $\Delta v_0^2 / \Delta t$, and Equation 4.19 has again been used to define D_v . ν_{\parallel} is the parallel diffusion frequency, defined by $\nu_{\parallel}(x) = \nu_0[\psi(x)/x]$, with $\nu_0 = \frac{1}{2}A_D$ (converting between cgs and SI units), $x = \gamma v^2$ and $\psi(x) = \frac{2}{\sqrt{\pi}} \int_0^x \sqrt{t} e^{-t} dt$. Using a variable substitution, $y = \sqrt{x}$, ν_{\parallel} may be rewritten as:

$$\nu_{\parallel} = \frac{1}{2} A_D \gamma^{3/2} \frac{\zeta(y)}{y^3} \quad (4.23)$$

where $\zeta(y)$ is defined in terms of error functions ($\phi(y)$):

$$\zeta(y) = \frac{\phi(y) - \frac{2y}{\sqrt{\pi}} e^{-y^2}}{2y^2}$$

$$\phi(y) = \frac{2}{\sqrt{\pi}} \int_0^y e^{-t^2} dt$$

The decision to use the parallel (and not the transverse) diffusion rate in the following calculations is arbitrary, since the test particle represents an ensemble of particles with an isotropic distribution in velocity space.

Combining expressions for ν_{\parallel} and D_v , the velocity diffusivity for a test particle may be written as $D_v (\text{NRL}) = 0.25v^{-1} A_D \zeta(v\sqrt{\gamma})$. Treating this particle as a fluid packet, its distribution function is given by $f_I = \left(\frac{\beta}{\pi}\right)^{3/2} e^{-\beta v^2}$, where $\beta \equiv \frac{m_I}{2T_I}$. Integrating D_v (NRL) over this distribution function yields:

$$\bar{D}_v = \int d^3\mathbf{v} f_I D_v (\text{NRL}) = \frac{A_D}{\sqrt{\pi}} \sqrt{\gamma} I_v$$

$$I_v = \left(\frac{\beta}{\gamma}\right)^{3/2} \int_0^{\infty} dy y e^{-\frac{\beta}{\gamma} y^2} \zeta(y) \quad (4.24)$$

Using Equations 4.21 and 4.24, the ratio of \bar{D}_v to D_v (LIM) is found to be

$6 I_v \left(1 + \frac{m_B}{m_I}\right)^{-1}$. I_v is evaluated numerically as a function of β/γ , and a plot of $6 I_v$ vs. β/γ ($= m_I T_{iB}/m_B T_I$) is shown in Figure 4-7. As β/γ increases, the product $6 I_v$ approaches unity, indicating that in LIM the large mass-ratio limit ($m_I/m_B \gg 1$) is assumed. For carbon-deuterium interactions, β/γ has a minimum value of 6 (assuming $T_I \leq T_{iB}$), suggesting that errors in parallel diffusion modelling arising from approximations used in the code will be $\lesssim 25\%$ for plume simulations.

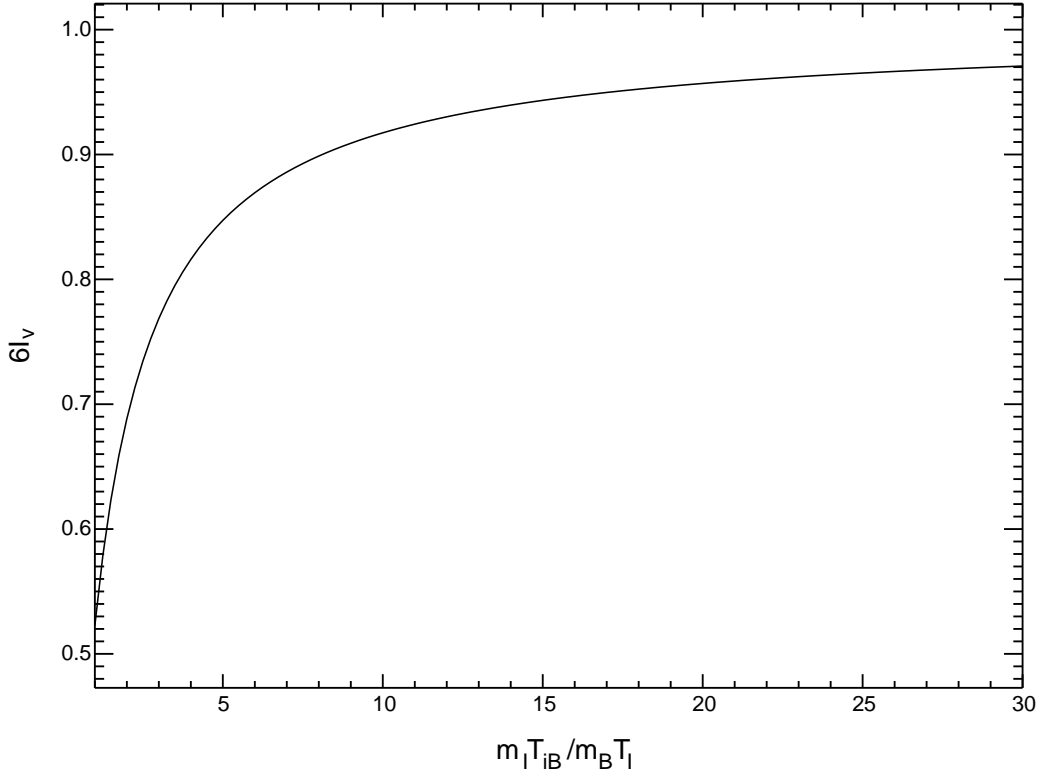


Figure 4-7: Plot of $6 I_v$ vs. β/γ , where I_v is given in Equation 4.24. β/γ is the product of m_I/m_B and T_{iB}/T_I , while $6 I_v$ is the approximate ratio of the velocity diffusivity calculated from the NRL Plasma Formulary to the value calculated in LIM. These results indicate that in LIM the large mass-ratio limit ($m_I/m_B \gg 1$) is assumed. For carbon-deuterium interactions, this approximation results in $\lesssim 25\%$ error in the parallel diffusion model.

Finally, calculations are also performed to determine the effect of allowing the impurity ions to have a bulk parallel velocity with respect to the background. In this case the impurity ion distribution function is described by a drifting Maxwellian:

$f_{I,d} = \left(\frac{\beta}{\pi}\right)^{3/2} e^{-\beta((v_{\parallel}-v_{\parallel,0})^2+v_{\perp}^2)}$. An integral expression for \bar{D}_v , similar to Equation 4.24, is constructed for this distribution function, which depends on T_I , T_{iB} , and $v_{\parallel,0}$. A plot of \bar{D}_v vs. $v_{\parallel,0}$ for fixed impurity ion and background temperature ($T_I = T_{iB} = 25$ eV) is given in Figure 4-8, where the diffusivity has been normalized to its value at $v_{\parallel,0} = 0$. The effect of a parallel impurity drift is observed to be small over a large range of drift velocities, up to $v_{\parallel,0} = v_{th,I}$. Thus, little error is introduced by neglecting parallel drifts for the impurity ions in the parallel diffusion model in LIM.

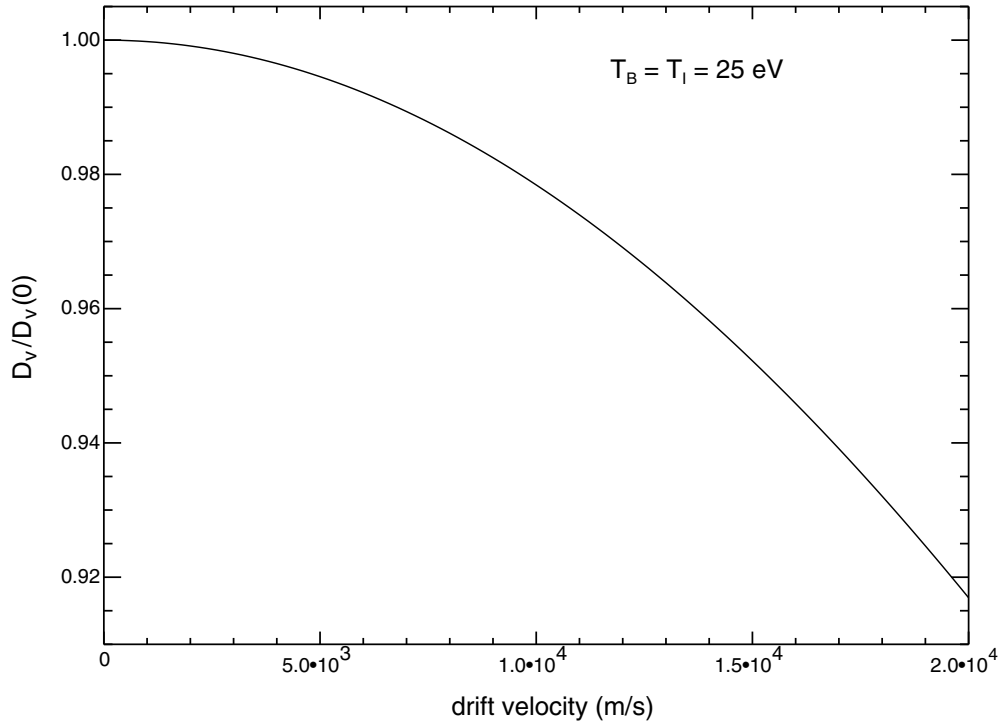


Figure 4-8: Plot of the velocity diffusivity calculated from the NRL Plasma Formulary including parallel drifts vs. parallel drift velocity. Results indicate that parallel drift effects are small, even for values of $v_{\parallel,0} = v_{th,I}$. Thus, there is little error in neglecting parallel drifts for the impurity ions.

4.3 Generating impurity plume images in LIM

To facilitate comparison between experimental and simulation results, 3-D charge state distribution data outputted from LIM are converted into 2-D simulated plumes using “virtual imaging”. Two steps are necessary to generate simulated 2-D images: the calculation of 3-D plume emissivity from LIM output, and conversion of this emissivity to brightness. In this section algorithms developed to complete each step are described.

4.3.1 Emissivity Calculation

Normalized densities (n_N) recorded in LIM correspond to an injection rate of 1 particle/second. The normalization was verified by running a simple case in which density and temperature were constant throughout the simulation volume ($n_e = 1.14 \times 10^{20} \text{ m}^{-3}$, $T_e = 59.6 \text{ eV}$), all flows and electric fields were set equal to zero, and the influence of the limiter was neglected (i.e. no absorption, no presheath fields). In this case the ionization lifetime for each charge state is constant over the simulation volume. For each charge state, it was found that the result of integrating the normalized density over the volume ($= I_z$) is equal in value to the ionization lifetime (τ_{ion}) to within a high degree of approximation. For example, for C^{+1} $I_z = 4.19 \times 10^{-7}$, whereas for the given background conditions $\tau_{ion}(C^{+1}) = 4.18 \times 10^{-7}$ seconds. Since I_z represents the total number of particles of a given charge state in the volume, it may also be determined by multiplying the injection rate by τ_{ion} . However, since in all cases $I_z \approx \tau_{ion}$, the implied injection rate is 1 particle/second.

Thus, to convert LIM output to units of absolute density, results simply need to be multiplied by the experimental injection rate. For a given plume, this quantity may be estimated using the relationship between plenum pressure and the number of injected molecules (see Figure 2-5) and the approximate time scale for gas injection (8-10 ms; see Figure 2-3). For a typical plume the carbon injection rate is $\sim 10^{19}$ atoms/second.

To calculate brightness, density must be converted to units of emissivity (W/m^3).

The plume emissivity at any given location is simply the amount of radiated power per unit volume at that location. In particular, only power radiated from a specific transition in the ion is of interest, since bandpass interference filters are used in the experiment to view emission from a narrow spectral region. In this case the relationship between emissivity and density is given by:

$$\epsilon = nn_e \Delta E_{jk} (PEC)_{j \rightarrow k} \quad (4.25)$$

where n is the impurity ion density for the charge state of interest, ΔE_{jk} is the energy released per photon for the $j \rightarrow k$ transition in the ion ($= \frac{hc}{\lambda_{jk}}$), and $(PEC)_{j \rightarrow k}$ is the photon emissivity coefficient (photons $\text{m}^3 \text{s}^{-1}$) for radiation from the $j \rightarrow k$ transition in the ion. PEC data are typically a function of both electron density and temperature.

Photon emissivity data have been tabulated for a number of transitions in a number of elements. For the simulated plumes the source for these data is the ADAS database [69]. Using ADAS, matrices of PEC data were generated for both carbon lines (i.e. both transitions) of interest at a variety of electron densities and temperatures, ranging from 5.0×10^{18} to $5.0 \times 10^{20} \text{ m}^{-3}$ and from 1 to 100 eV. Spline-fits to the data allow PEC values to be calculated for either carbon line at arbitrary density and temperature within this range. Finally, for simulation of plume experiments it is assumed that the dominant mechanism for population of the upper level in the transition (j) is electron impact excitation. Population of level j due to radiative recombination, charge exchange recombination, and electron impact ionization was also considered, but over most conditions typical of the SOL the emissivity coefficients for these processes are much smaller than that for excitation.

In each computational cell in LIM, values of electron density and temperature are known, allowing photon emissivities to be calculated. Impurity ion density may also be calculated in each cell by multiplying LIM results by the gas injection rate. With these data, Equation 4.25 may then be used to determine the plume emissivity at each cell in the simulation volume.

4.3.2 Determining brightness

Once the emissivity in each cell is calculated, the 2-D simulated plume brightness may be determined using virtual imaging. The concept behind this calculation is straightforward. Consider an imaging system composed of a set of detectors on a 2-D plane located outside of the emission volume. The signal on each detector will depend its view of the emission volume, which is determined from the view aperture of the system. However, generally speaking, the brightness on any given detector can be related to the emission inside the volume by:

$$b_i = \sum_j A_{ij} \epsilon_j \quad (4.26)$$

where b_i is the brightness at detector i ($\text{W}/\text{m}^2/\text{ster}$), ϵ_j is the emissivity in volume element j , and A_{ij} represents the contribution of emission from volume element j to the total signal at detector i . The 2-D matrix \mathbf{A} is commonly referred to as the **geometry matrix**, since the value in each element is determined by a geometric relationship between the positions i and j . In other words, for given emission volume geometry, imaging plane location, and view aperture, \mathbf{A} is fixed. Strictly speaking, the relationship between b_i and ϵ_j given by Equation 4.26 is valid only in the limit of optically thin emission.

The calculation of geometry matrix elements for the simulated plume system is based on an algorithm developed by Dr. C. MacLatchy [45]. In this algorithm the coordinate system for the virtual emission volume is cartesian. Axes are located along \mathbf{B} (y) and in the vertical (Z) and radial (R) directions, where Z and R correspond to the vertical and major radial axes of the tokamak. The y and R centers of the virtual emission volume are given by the probe location – however, since the Z coordinate of the probe may vary for different plumes, the Z center of the virtual emission volume is instead given by the vertical position of the side view camera system. Virtual imaging planes corresponding to the SVC and TVC are then positioned outside of the emission volume. The locations of these planes relative to the virtual emission volume are

identical to the locations of the actual camera systems relative to the experimental emission volume. Finally, the position of detector i on an imaging plane corresponds to the location of a virtual imaging fiber, where the spacing between fibers is identical to that for the coherent fiber bundles used in the experiment.

The value of any geometry matrix element A_{ij} is determined from a series of calculations in which each element in the virtual emission volume is “lit-up” individually, with a constant emissivity of 1 W/m^3 (the emissivity in the rest of the volume being zero). From Equation 4.26, the brightness at detector i for this case is:

$$b_i = A_{ij_0} \quad (4.27)$$

where j_0 is the index for the illuminated volume element. In this case the geometry matrix element A_{ij_0} for a given imaging system is simply given by the brightness at detector i in that system due to emission from volume element j_0 .

Emission from a volume element j_0 will in general result in signal on multiple virtual fibers. To deal with this effect, each emission cell is divided into 1000 sub-elements, where emission from each sub-element is assigned to signal on only one virtual fiber. The corresponding fiber is determined using a *pinhole camera* approximation for the imaging system view aperture, which allows simple ray-tracing calculations to be performed to relate the position of the volume sub-element to detector position on the imaging plane. The relationship between brightness and emissivity in this system is determined by modelling the emission as a Lambert source [32]:

$$b_i = \frac{P_{sv}}{4\pi A_s \cos \phi} \quad (4.28)$$

where P_{sv} is the power emitted by the sub-element ($= 1 \text{ W/m}^3 \times$ the sub-element volume), A_s is the projected area of the volume sub-element in the direction perpendicular to the view, and ϕ is the angle between the viewing chord and the surface normal of the imaging plane.

The full contribution of emission from the volume element j_0 to signal at the imaging plane is determined by adding up the contributions from each of the sub-

elements. After each sub-element calculation is completed, the algorithm proceeds to the next volume element, until all geometry matrix elements have been determined.

The size of the virtual emission volume is determined by optimizing the overlap between the LIM and geometry matrix emission volumes, taking into account that the emission volume in LIM is rotated $\simeq 45^\circ$ with respect to the emission volume used in the geometry matrix calculation. This rotation is a result of coordinate axes being aligned with the probe axis in the geometry matrix coordinate system, while being aligned with flux surfaces in the LIM coordinate system. Emissivity values in each LIM cell are mapped to values in each geometry matrix cell using a simple interpolation algorithm. The interpolation is a function of the displacement (ΔZ) between the probe Z coordinate at gas injection (which represents the origin for the LIM emission volume) and the SVC Z coordinate (which is the origin for the geometry matrix emission volume). To compensate for ΔZ effects and ensure an optimal mapping between LIM and geometry matrix emission volumes for each plume, the radial (cross-flux surface) bin coordinates in LIM may be shifted to provide slightly different radial ranges. Once the emissivity in each cell of the geometry matrix volume is determined, the brightness may be calculated at each imaging plane using Equation 4.26.

4.4 Sputter source model in LIM

A sputter source model has been developed in LIM to investigate the effect that sputtering of carbon from the probe head has on the plume emission structure.

The ability to define an arbitrary limiter surface for purposes of interaction with the background impurities, namely for impurity ions to be absorbed upon, is somewhat constrained in LIM. This is because LIM requires this surface to be stored as 3-D array in its cartesian coordinate system, resulting in a surface that has well-defined, sharp boundaries (as in Figure 4-3). It is therefore impossible to specify the “absorbing” limiter surface with a cylindrical geometry, which is more representative of probe. However, modifications were made to the code to allow neutrals to be

launched from such a surface, simulating sputtering.

The probe model for the neutral launch is one of a cone attached to a cylinder (where the tip of the cone coincides with the gas capillary exit). This probe has the same orientation in the LIM coordinate system as “absorbing” probe surface shown in Figure 4-3. Any position on the probe surface is characterized by a distance down the probe axis (d_p) and by an azimuthal angle about the probe axis (ϕ_p). For a given neutral launch, these positions are determined using uniformly distributed random numbers. The probability distribution for the azimuthal angle is assumed to be uniform, while the probability of a neutral being launched a distance d_p down the probe axis is assumed to decay exponentially with distance, with a typical decay length being $\simeq 1$ cm (more details in section 5.2). Finally, d_c represents the distance down the probe axis at which the cone and cylinder are joined – this is a fixed number in the probe model ($\simeq 1.3$ cm). For $d_p \geq d_c$, the probe radius is also fixed ($r_p = r_{FSP} = 8$ mm), while for $d_p < d_c$ the probe radius varies linearly with distance: $r_p = r_{FSP} \left(\frac{d_p}{d_c} \right)$.

The velocity space distribution is based on the Thompson distribution for sputtered atoms [5]:

$$\frac{d^3Y}{dE d^2\Omega} = \frac{2U_0 E}{(E + U_0)^3} \frac{\cos\beta}{\cos\alpha} \frac{Q}{\pi} S_n(\varepsilon) g(\varepsilon') \quad (4.29)$$

where Y is the sputtering yield, E is the sputtered particle energy, Ω is the solid angle of emission ($d^2\Omega = \sin\beta d\beta d\chi$), α and β are angles with respect to the surface normal of the incident ion and sputtered particle trajectories, respectively, U_0 is the binding energy of the surface atoms, E_0 is the incident ion energy, and Q is the yield factor. S_n is function representing the nuclear stopping potential, which varies with $\varepsilon = \frac{E_0}{E_{TF}}$, where E_{TF} is the energy in the center-of-mass system for a head-on collision between incident ion and sputtered particle with the screening radius as the nearest approach. Finally, g is a function representing the correction factor for low incident ion energy, which varies with $\varepsilon' = \frac{E_0}{E_{th}}$, where E_{th} is the threshold energy for sputtering for the specific incident ion-sputtered particle pair. Q , E_{TF} , and E_{th} are parameters

characterizing the interaction for a given incident ion-sputtered particle pair, and are therefore fixed quantities for a given incident ion-sputtered particle pair.

For the Thompson distribution, the sputtered particle yield varies as the cosine of the emission angle with respect to the surface normal. Surface normals (\hat{n}) for any position on the probe are found to be functions only of d_p , ϕ_p , and d_c , and are thus easily calculated for any launch position. Two uniformly distributed (on $[0,1]$) random numbers are then used to determine the orientation of the velocity vector (\hat{v}) for the sputtered particle relative to \hat{n} – one for the azimuthal angle χ and the other for β . A simple schematic illustrating the definition of these two angles is shown in Figure 4-9. The probability distribution for χ is uniform, while the probability distribution for β varies as $\cos \beta$, reflecting the variation of yield with emission angle.

The energy distribution for sputtered particles is given by the first term in Equation 4.29, namely $P(E) = \frac{2U_0 E}{(E+U_0)^3}$. The energy for a given launched particle is determined from this distribution using a uniformly distributed (on $[0,1]$) random number ξ_E . For this case, there is a maximum value of ξ_E which can be used, since there is a maximum amount of energy that the sputtered particle can have:

$$E_{max} = \gamma_E(1 - \gamma_E)E_0 - U_0$$

$$\gamma_E = \frac{4m_B m_I}{(m_B + m_I)^2}$$

For incident deuterium ions causing sputtering of carbon atoms, the product $\gamma_E(1 - \gamma_E) \simeq \frac{1}{4}$. In this case, the maximum value of ξ_E is given by the expression $\left(1 - \frac{4U_0}{E_0}\right)^2$. Based on energetics there is also a minimum value of incident ion energy required for sputtering – for the $D^+ - C$ system, it is $\simeq 4U_0$. The incident ion energy is determined by the local values of ion and electron temperature and physics of the probe sheath, and is given by the expression $E_0 = 2T_{iB} + e\Delta V_s$. ΔV_s is the potential drop through the sheath, calculated by subtracting the floating potential from the plasma potential (i.e. $\Delta V_s = V_p - V_f$). Experimental results [39] indicate that at the probe tip $eV_p \simeq T_e$ and $e\Delta V_s \simeq 3T_e$, suggesting that $eV_f \simeq -2T_e$. Assuming that the floating potential for the probe body is a single value, set by the floating potential

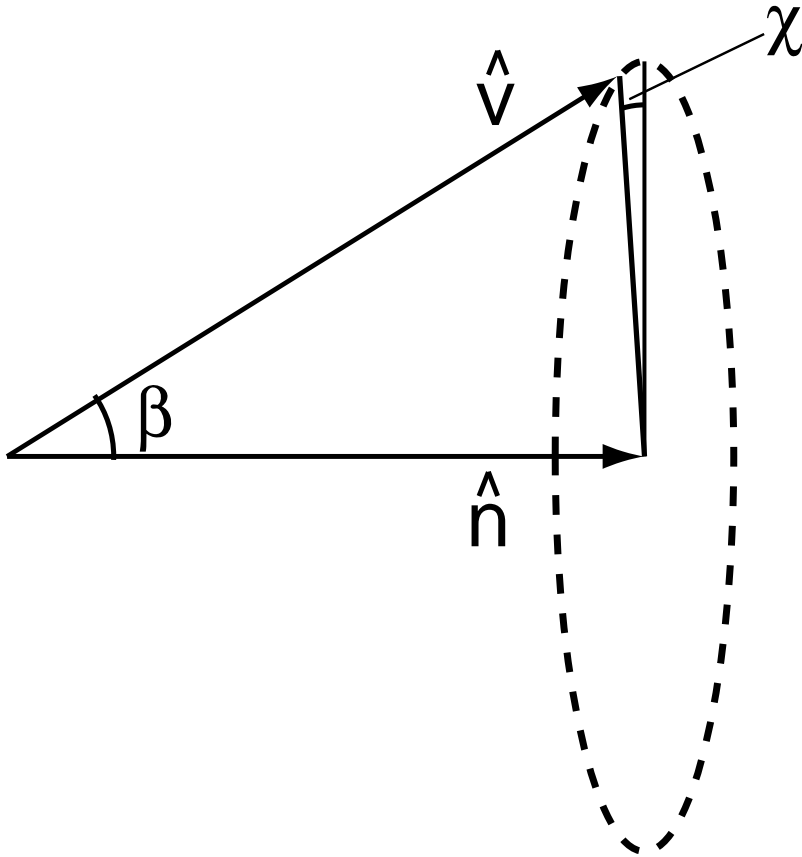


Figure 4-9: Simple schematic illustrating the definition of the angles χ and β , used to determine the orientation of the velocity vector (\hat{v}) for a sputtered particle relative to the surface normal (\hat{n}) for a Thompson distribution.

at the probe tip, and using the experimental result that $eV_p \simeq T_e$ over most of the SOL [39], the sheath potential drop at locations other than the probe tip may be estimated as $e\Delta V_s \simeq T_e + 2T_{e,tip}$. This results in the total energy per incident ion being $E_0 = 2T_{iB} + T_e + 2T_{e,tip} = 3T_e + 2T_{e,tip}$ (since $T_{iB} = T_e$ is assumed).

Finally, the surface binding energy U_0 is specified as an input parameter. Estimates are based on values for sputtering of carbon atoms from graphite, for which the binding energy is 7.4 eV [56]. The dependence of plume structure on U_0 is discussed in section 5.2.

4.5 Recycling D₂ plume simulation using LIM

LIM has been configured to determine the magnitude of the parallel electric field which is generated as a result of deuterium recycling from the probe surface.

Plasma recycling from the probe head results in the formation of D₂ molecules, which subsequently dissociate into deuterium atoms which each have an energy of $\simeq 3$ eV (Frank-Condon dissociation model [29]). The recycling model implemented in LIM does not treat the dissociation step – instead, it is assumed that recycling results directly in the production of 3 eV deuterium atoms. This assumption is justified for cases where the D₂ dissociation mean-free path is much smaller than the D⁰ ionization mean-free path, which is true for most SOL conditions.

In LIM, deuterium recycling is modelled using a launch of deuterium neutral atoms from the surface of the probe into a fixed plasma background (i.e. a perturbative analysis is employed). The physical space launch distribution used to simulate recycling is the same as the distribution used to model carbon sputtering off the probe head, i.e. the location from which a deuterium neutral is launched is characterized in terms of a distance (d_p) down the probe axis and an azimuthal angle (ϕ_p) about the probe axis. Since the amount of deuterium recycling is proportional to the incident plasma flux on the probe, the distribution for d_p is again taken to be exponential. However, a modification was made to allow the distribution in ϕ_p to be non-uniform, for simulation of asymmetric recycling off the probe head. A $\cos \theta_n$ distribution is assumed,

where θ_n is the angle between the surface normal (\hat{n}) and the parallel (to \mathbf{B}) axis – the ratio of launches on the upstream and downstream sides of the probe is then determined from an inputted asymmetry factor A_R . Finally, for this case the velocity space distribution is not appropriately described with a Thompson model. Instead, the velocity vector is aligned with the surface normal ($\hat{v} = \hat{n}$) at each launch position (i.e. there is no $\cos \beta$ weighting), while the energy of each launched neutral is taken to be 3 eV.

Another important effect included in the neutral launch is charge exchange. For typical SOL conditions, the charge exchange cross section for deuterium is of the same magnitude as the ionization cross section, indicating that charge exchange and ionization rates are approximately equal. In LIM, the following dimensionless parameters are defined to characterize neutral “event” probabilities:

$$P_{ne} = \Delta t \left[\frac{1}{\tau_{ion}} + \frac{1}{\tau_{cx}} \right]$$

$$P_{cx} = \frac{\tau_{ion}}{\tau_{ion} + \tau_{cx}}$$

where $\tau_{cx} \equiv \frac{1}{n_e \langle \sigma v \rangle_{cx}}$. For the given neutral being followed, at each time step a uniformly distributed (on $[0,1]$) random number is drawn – if this number is less than P_{ne} , then *either* an ionization or charge exchange event has occurred. In that case another uniformly distributed random number is drawn – if this number is less than P_{cx} , then the event is a charge exchange.

The LIM code is split into two different sections – one which follows all launched neutrals until ionization (NEUT), and then a second which follows all ions until they are lost from the system (LIM3). Once the ion section of the code has begun, any ions which convert to neutrals (i.e. by charge exchange recombination) are not subsequently tracked – instead they are treated as being ions which are lost from the system, and LIM3 moves on to the next ion. Thus a completely self-consistent charge exchange model cannot be implemented in LIM. Instead, charge exchange is treated entirely in the neutral section of the code. When a neutral deuterium atom undergoes charge exchange, NEUT continues to follow the newly-formed neutral. Since

this neutral is “born” from an ion, its properties are determined using local values of background plasma parameters. For example, the neutral velocity is calculated by assuming an isotropic Maxwellian distribution for the ions at the local ion temperature, and by including local values for the parallel and poloidal ion velocity in the final determination of the velocity vector. NEUT continues to follow this neutral until it is ionized – if it undergoes charge exchange, the newly-formed neutral will again be followed. The effect of charge exchange in LIM is therefore to increase the neutral mean-free path, which in turn increases the volume over which ionization of the recycling deuterium atoms takes place. This volume plays a role in determining the magnitude of the density perturbation and thus the effect of recycling on the injected impurity ions, justifying the need to include charge exchange in the model.

There are a few practical modifications which need to be made in order to use LIM for D₂ “plume” simulation. The result desired from the simulation is the equilibrium density distribution arising from a constant injection rate of deuterium neutral atoms off the probe surface. However, unconstrained, the code could in principle run for an extremely long time even after this equilibrium is reached, since the only ion sinks in the simulation for this case are absorption on a limiter surface or wall. Therefore, an arbitrary specification has been included in the simulation to limit the amount of time that each deuterium ion is followed in LIM3. Results indicate that over the range of times tested there is little effect of this cut-off time on the code output. A typical cut-off is 10 seconds of CPU time per ion. In addition, the parallel mean-free path of the deuterium ions is extremely long in most cases, and if the same parallel bin size used for carbon plume simulation were used for deuterium plume simulation then the periodicity boundary condition would introduce an artifact in the code output (section 4.2.3). In fact, tests have been conducted which indicate that the periodicity boundary condition can serve to symmetrize the parallel emission profile in cases where asymmetric recycling is assumed. However, increasing the parallel bin size uniformly reduces the resolution in the region of interest, i.e. over the parallel extent of the impurity plumes. Instead, only the parallel bin at the boundary is increased in size, and by a large amount ($> \times 20$) to ensure that the number of deuterium ions

which reach the parallel boundary is small.

Finally, D^+ densities resulting from the D_2 plume simulation are again normalized to an injection rate of 1 particle/second. In order to assess the level of recycling-induced density perturbation, these results need to be multiplied by the true injection rate. In steady-state, the injection rate of deuterium atoms is equal to the collection rate by the probe, which in turn may be calculated from saturation current measurements. The probe measures current density at the probe tip (j_0), while the current density along the probe axis is expected to vary as a result of variations in the background density and temperature. Assuming an exponential variation for the density and temperature, the current density variation will also be exponential, characterized by a decay length of $\lambda_j = \frac{2\lambda_T\lambda_n}{2\lambda_T+\lambda_n}$, where λ_T and λ_n are the decay lengths for electron temperature and density profiles, respectively. The total current to the probe is simply the integral of the current density over the probe area:

$$I = \int_{A_p} j dA_p = 2 \int_0^\infty \int_{-\frac{\pi}{2}}^{\frac{\pi}{2}} j_0 e^{-d_p/\lambda_j} \cos \theta_n r_p(d_p) d\theta_n dd_p \quad (4.30)$$

Recall that for the probe model of a cone connected to a cylinder, the probe radius (r_p) is a function of d_p :

$$\begin{aligned} r_p &= r_{FSP} \frac{d_p}{d_c} & d_p < d_c \\ r_p &= r_{FSP} & d_p \geq d_c \end{aligned}$$

where d_c is the distance at which the cone and cylinder meet ($\simeq 1.3$ cm) and r_{FSP} is the full radius of the probe (8 mm). Finally, in Equation 4.30 the factor of 2 takes into account current received by the probe from the upstream and downstream side (symmetric recycling has been assumed, though in the asymmetric case the recycling rate will be approximately the same). This equation is easily integrated, yielding:

$$I = 4j_0 r_{FSP} \lambda_j \left[\frac{1 - e^{-d_c/\lambda_j}}{d_c/\lambda_j} \right] \quad (4.31)$$

Assuming a current density of 1 A/mm^2 at the probe tip (typical experimental value), a plot of the total probe current vs. current density decay length is shown in Figure 4-10. For a decay length of $\sim 5 \text{ mm}$, the total current is $\sim 50 \text{ A}$, corresponding to a collection rate of $\sim 3 \times 10^{20}$ atoms/second. For a given set of background plasma conditions (e.g. those present during formation of a plume of interest), values for λ_j and j_0 may be obtained from probe data, allowing a recycling rate to be estimated. This value can then be used to scale deuterium plume simulation data obtained when running LIM with the same set of background conditions.

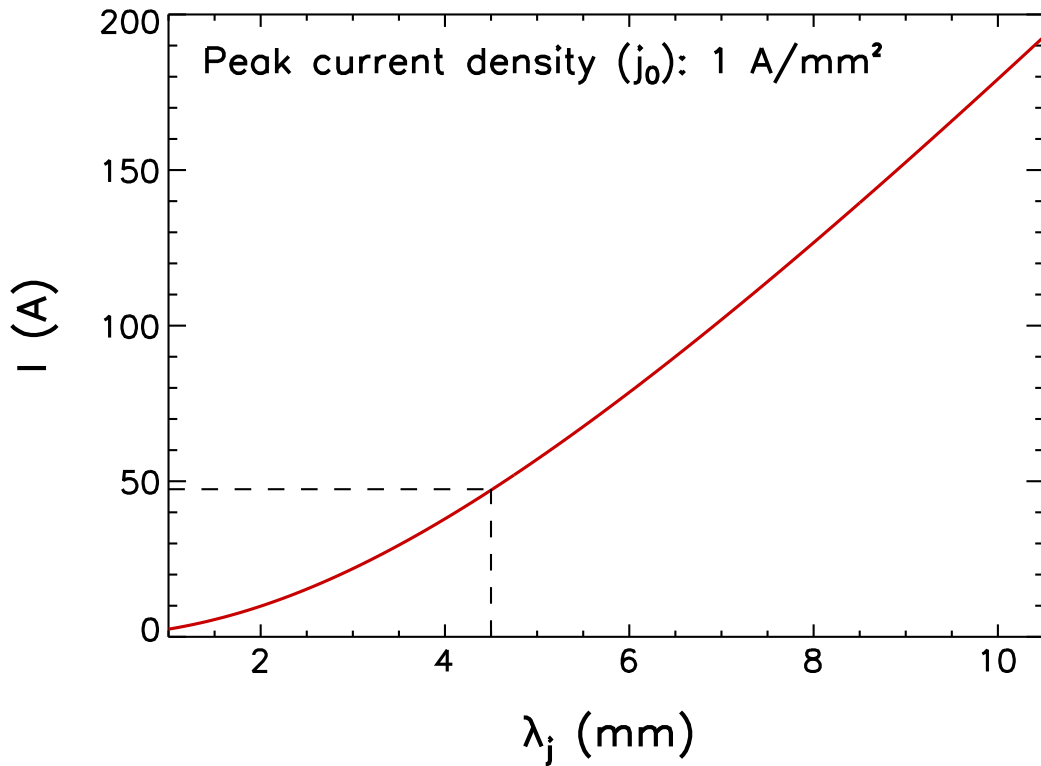


Figure 4-10: Plot of the total current collected by the probe vs. the current density decay length. A current density of 1 A/mm^2 at the probe tip is assumed. For a typical decay length of 5 mm , the total current is $\sim 50 \text{ A}$, corresponding to a collection (and thus recycling) rate of $\sim 3 \times 10^{20}$ atoms/second.

4.6 Injected D plume simulation using LIM

Parallel electric fields may also be generated as a result of the density perturbation arising from gas injection. Estimates for the contribution due to carbon injection are given in section 3.2.2, which indicate that the resultant perturbation can be significant in the near SOL, where the ionization volume is small. LIM has been configured to study the density perturbation which arises from injection of deuterium.

The injection model in LIM is rather simple. Molecular break-up and ionization of deuterium injected in the form of C_2D_4 is assumed to occur over a very small distance relative to the capillary diameter. Therefore the model does not treat these steps – instead it is assumed that deuterium is injected directly in the form of ions (with injection taking place at the probe tip). The distribution of these ions in both physical and velocity space is Gaussian. The width of the physical space distribution is 1 mm, corresponding to the capillary diameter, while the width in velocity space is characterized by an energy of 3 eV (based on available energy from molecular dissociation).

The same modifications required for the recycling deuterium simulation (cut-off time limit, extended parallel boundary bin) are necessary in this case as well. D^+ normalized density results are then scaled to absolute density using the known gas injection rate through the capillary, allowing for a quantitative analysis of the perturbation.

Chapter 5

Plume analysis & simulation

A number of tools have been developed for modelling the plume emission data, and the application of these tools will be presented in this chapter. Simulation results are based on the use of two separate models to describe the background plasma conditions (“jet background” & “non-jet background”) and two separate models to describe the impurity launch conditions (“point source” & “sputter source”). In the “jet background” model, the presence of parallel electric field and density variations are included to account for the effects of the density perturbation arising from both background ion recycling off the probe surface and from the gas injection (see sections 5.4 and 5.5). In the “non-jet background” model, effects resulting from this density perturbation are neglected. In the “point source” model, impurities are launched as neutrals from the probe tip, with a Gaussian distribution in both physical space (characterized by a width of 1 mm, corresponding to the gas injection nozzle diameter) and in velocity space (characterized by an energy of 3 eV, estimated from molecular break-up energies for C_2D_4). Finally, in the “sputter source” model, impurities are launched as neutrals from the probe surface, with an exponentially decaying spatial distribution along the probe axis (characterized by a decay length λ) and Thompson energy distribution (characterized by a surface binding U_0). Values for λ and U_0 are specified as code inputs (see section 5.2). For the majority of simulation results, either the “jet background” and “point source” models were specified in tandem, or the “non-jet background” and “sputter source” models were specified in

tandem. This is because simple analysis suggests the use of the “point source” model with the “non-jet background” model is insufficient to reproduce both the cross-field extent of the plumes as well as the parallel plume extent in the near SOL, whereas errors would arise from using the “jet background” model with the “sputter source” model as a result of computational limitations which constrain the specification of the parallel electric field in the simulation (see section 5.5.1).

5.1 SVC/TVC plume width investigation

Experimental results indicate that there is a difference in the cross-field widths inferred from the SVC and TVC plume data. A comparison between 1-D cross-field profiles for the two views suggests that the impurity density distribution is elongated along the vertical axis, implying a mechanism exists to transport impurity ions down the probe axis. A number of possible explanations for this phenomenon were investigated using LIM. These include effects of carbon recycling off the probe surface and the presence of a vertical ion drift velocity. Results are discussed in the following sections.

5.1.1 Carbon recycling model

Gas injection through the scanning probe results in the formation of carbon layer over an unknown fraction of the probe surface. However, a rapid removal of this deposited layer is observed when the probe is scanned into the plasma without gas injection. This indicates that the carbon layer results from a dynamic balance between deposition and sputter erosion. Therefore, it may be appropriate to consider a situation in which the carbon concentration on the probe surface is approximately constant in time, i.e. that during gas injection a steady-state is reached. In such a case, for each carbon ion which is absorbed onto the probe surface a carbon neutral is released. This “100% recycling” model is expected to significantly increase the effective lifetime of a given carbon atom, which may allow diffusion to play a significant role in transporting impurity ions down the probe axis.

A recycling model for carbon impurity ions was implemented in LIM based on a steady-state assumption. In this model a carbon ion which is absorbed onto the probe surface is re-launched as a neutral, with an energy given by a Thompson distribution (i.e. using the velocity-space component of the sputter source model). The only mechanisms by which this ion may be lost from the system are absorption by the boundary wall (see Figure 4-3) and ionization.

A comparison between simulated 2-D CIII SVC plumes from runs with and without carbon recycling is shown in Figure 5-1. In both cases the point source model is used to specify the initial launch of carbon neutrals. Also for both cases the cross-field diffusivity is set equal to $1.0 \text{ m}^2/\text{s}$, inputted density and temperature profiles are characteristic of the near SOL, and the non-jet background model is employed. The primary difference between the results is that the parallel extent of the emission is increased when recycling is included, due to a 40% increase in the effective carbon lifetime. However, the cross-field width of the emission exhibits little change between these two cases, i.e. the vertical extent of the emission is not affected by recycling under these conditions.

The effect of cross-field diffusivity in the recycling model was then investigated. For a factor of 10 increase in the diffusivity (i.e. $D_{\perp} = 10 \text{ m}^2/\text{s}$) with otherwise similar background conditions, the corresponding increase in the cross-field extent of the impurity emission was only $\simeq 20\%$. In addition, the CIII SVC simulated plume width in this case is still $\simeq 70\%$ smaller than the experimentally observed value. Based on these results, the value of D_{\perp} necessary in the model to explain the vertical extent of the experimental emission is expected to be quite large, which is unjustified. A recycling model with diffusion only is therefore insufficient to simulate the experimental results.

5.1.2 Probe-induced $\mathbf{E} \times \mathbf{B}$ drifts

Another possible mechanism for transporting carbon ions down the probe axis is a vertical ion drift, which may be induced by the presence of the probe. Specifically, near the probe surface large gradients in the plasma potential exist due to the presence

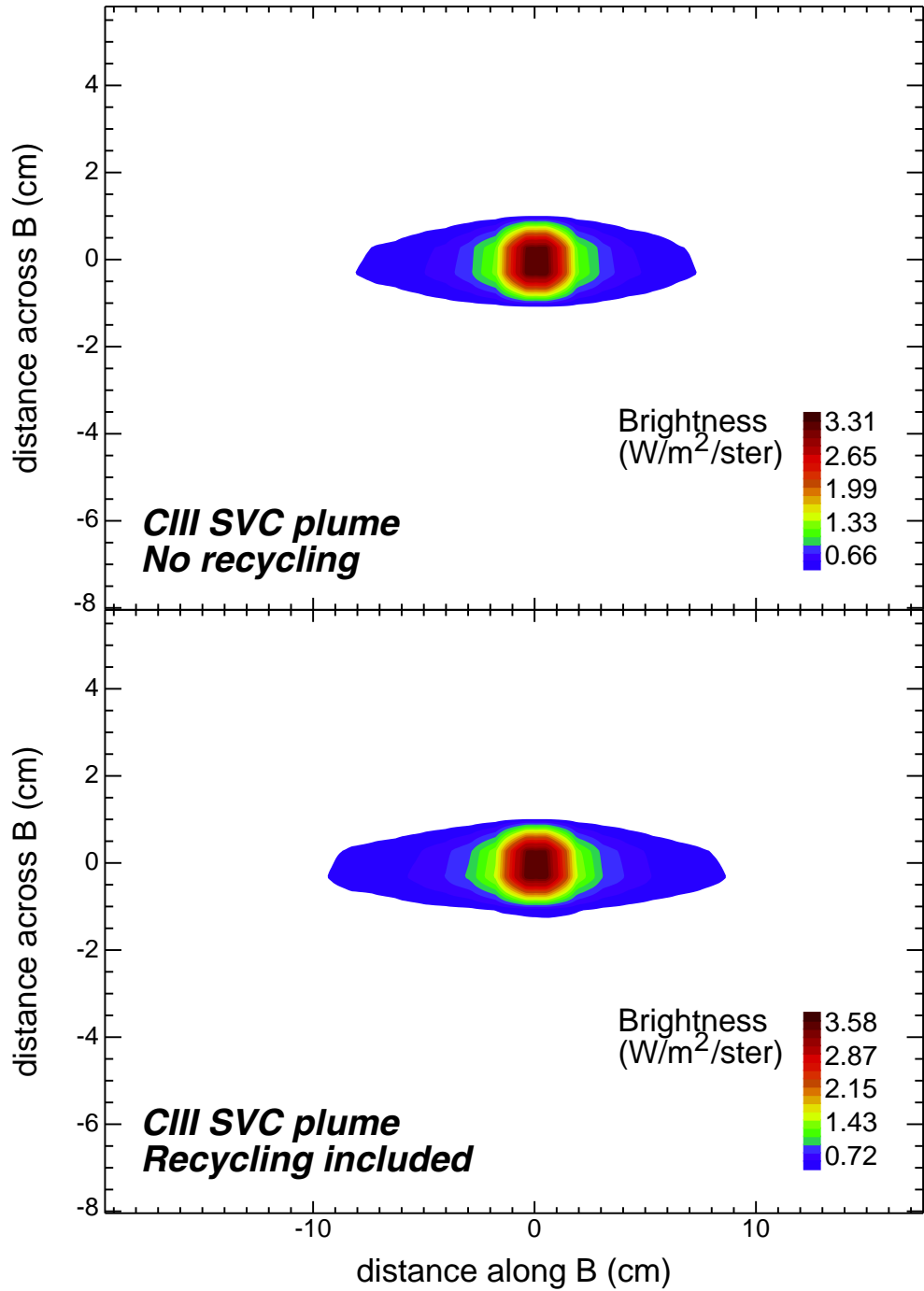
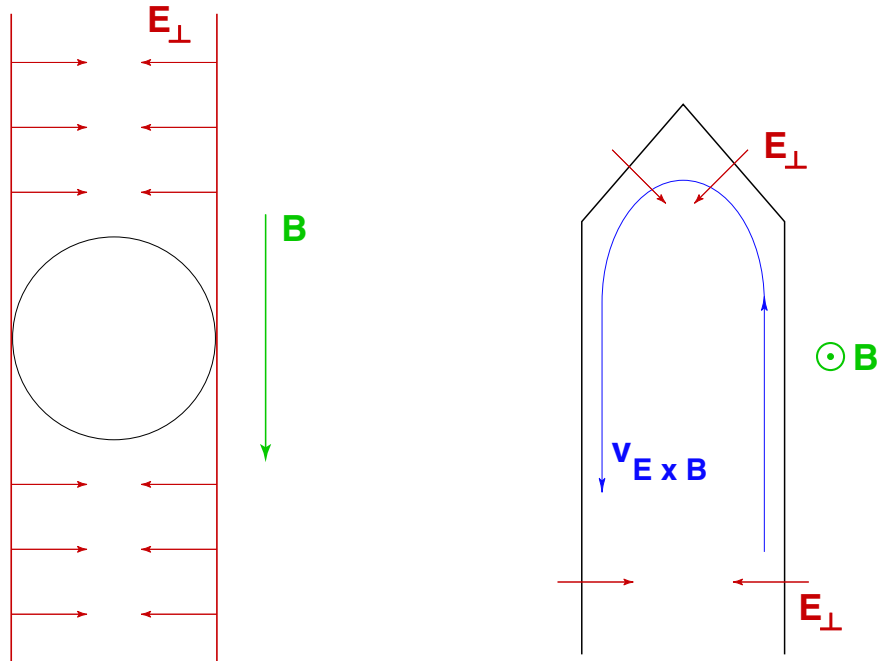


Figure 5-1: Comparison between simulated CIII SVC 2-D plume emission for cases with (*bottom panel*) and without (*top panel*) carbon recycling off the probe surface. In both cases $D_{\perp} = 1.0 \text{ m}^2/\text{s}$, inputted density and temperature profiles are characteristic of the near SOL, and the non-jet background/point source model is used. There is very little difference in the cross-field extent of the emission for these two cases, suggesting that the vertical extent of the plumes is not affected by recycling under these conditions.



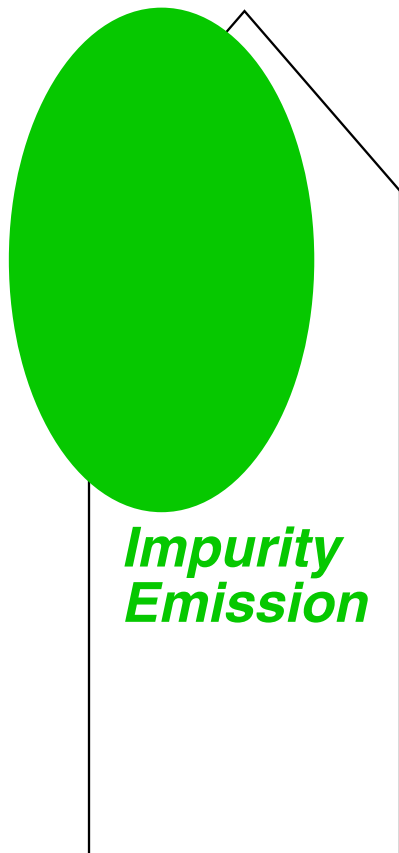
Probe Head - Top View

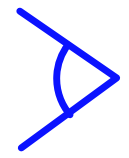
Probe Head - Side View

Figure 5-2: Schematic of the probe geometry indicating the direction of the electric field which results from variations in the plasma potential near the probe surface. These variations are due to probe-induced presheath effects. In the near SOL this field can be $\simeq 3\text{-}4$ kV/m, leading to an $\mathbf{E} \times \mathbf{B}$ drift of $\simeq 750\text{-}1000$ m/s.

of the probe-induced presheath. Estimates derived from presheath modelling suggest that the potential can vary by $T_e/2$ over a cross-field distance corresponding to the probe radius. In the near SOL ($T_e \simeq 50$ eV) this leads to a local electric field of $\simeq 3\text{-}4$ kV/m. The field is directed towards the region of presheath density depression caused by the probe, resulting in an $\mathbf{E} \times \mathbf{B}$ drift which circulates around the probe (see Figure 5-2). For typical values of the magnetic field strength at the probe location ($\simeq 4$ T), the $\mathbf{E} \times \mathbf{B}$ velocity is $\simeq 750\text{-}1000$ m/s, which is quite substantial. A schematic illustrating the possible effect of such a velocity field on the impurity ion distribution is shown in Figure 5-3.

TVC 




SVC

Probe Head

Figure 5-3: Schematic which illustrates the possible effect of a circulating $\mathbf{E} \times \mathbf{B}$ drift on the impurity ion distribution. This drift is thought to be caused by the presence of the probe-induced presheath (see Figure 5-2).

LIM has been configured to include a constant drift down the axis of the probe in the region of the plasma below the injection nozzle. Although this velocity field does not have the circulating pattern shown in Figure 5-2, it can be used to investigate the possible influence of probe-induced $\mathbf{E} \times \mathbf{B}$ drifts on the impurity ion distribution. Simulated 2-D CIII SVC and TVC plumes are shown in Figure 5-4 for a case in which the drift velocity down the axis of the probe is 1000 m/s, $D_{\perp} = 1.0 \text{ m}^2/\text{s}$, inputted density and temperature profiles are characteristic of the near SOL, carbon recycling off the probe surface is included, and the jet background/point source model is used. A comparison between simulated and experimental 1-D cross-field profiles of normalized brightness is given for both the SVC and TVC in Figure 5-5 (experimental data are the same as in Figure 3-13), in which relatively good agreement between simulation and experiment is observed. However, in order to get the simulated SVC plume to have a skewness which is similar to the experimental data, it is necessary to postulate a relatively constant electron density profile in computing the CIII excitation rate.

Although the presence of a drift velocity in LIM results in a vertical elongation in the carbon density distribution, the local carbon emissivity (which is related to brightness using Equation 4.26) also depends on the local value of the electron density (see Equation 4.25). Measurements from the probe imply that n_e varies strongly with distance down the probe axis in the absence of the probe. For such a density profile, the resulting simulated carbon emissivity would be peaked near the injection location, and the 2-D simulated plume would *not* be vertically elongated. To generate a closer match to the experimental results, the electron density has instead been *assumed constant* in the calculation of the emission excitation rate (i.e. the product $n_e(PEC)_{j \rightarrow k}$ in Equation 4.25), fixed at the value of n_e measured at the injection nozzle. This assumption has been used to produce the simulated results shown in Figures 5-4 and 5-5. The comparison between simulation and experiment suggests that this assumption is appropriate, i.e. that the electron density is approximately uniform over the emission volume which is in the vicinity of the probe body. For comparison, simulation results in which the measured electron density profile was used to calculate the emission excitation rate are shown in Figure 5-6 (all other simulation

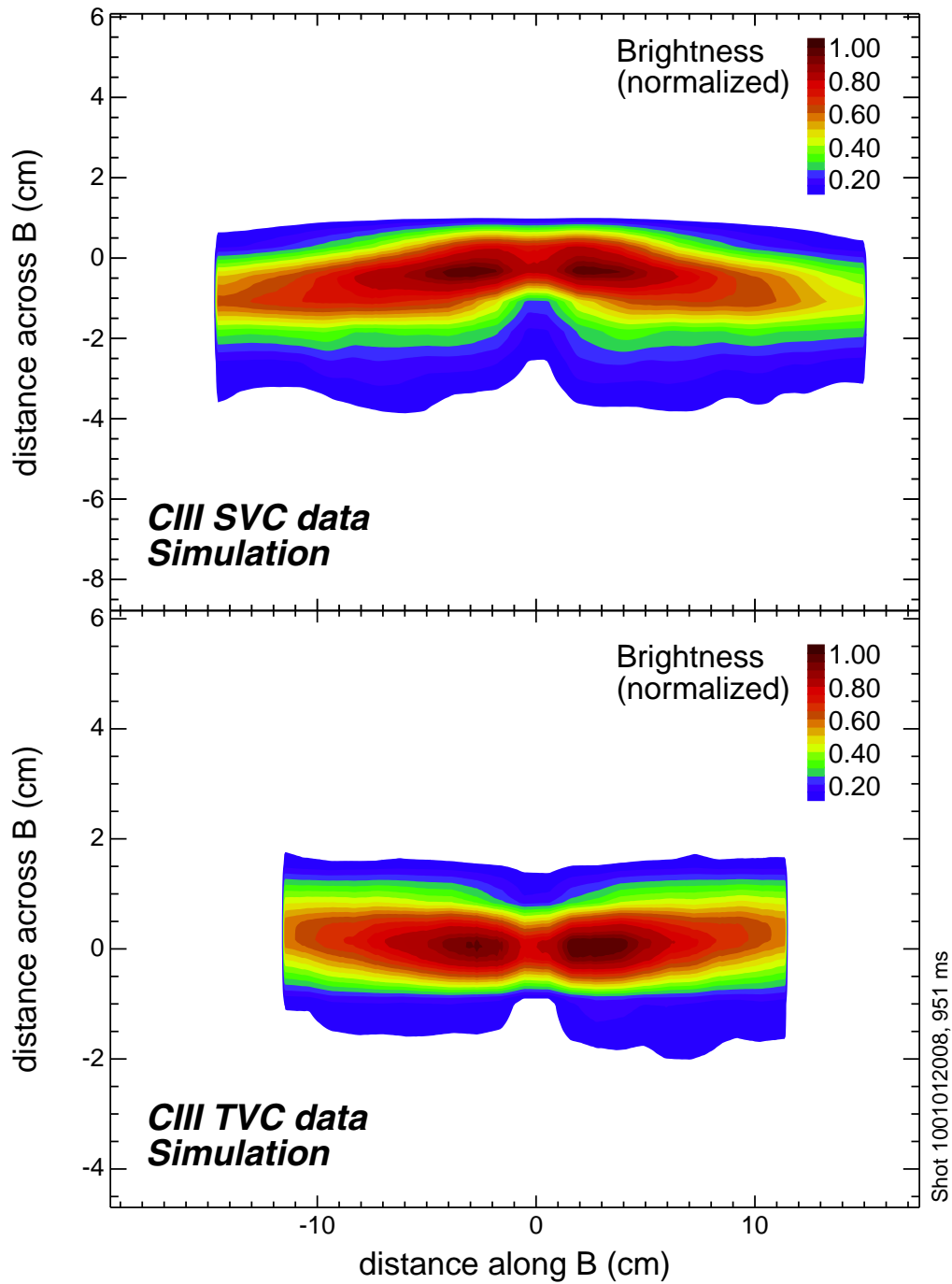


Figure 5-4: CIII SVC (top panel) and TVC (bottom panel) plumes for a simulation in which a vertical impurity ion drift of 1000 m/s has been included. The electron density has also been assumed constant in the calculation of the emission excitation rate, which is required if the simulated SVC plume is to match the skewness of the experimental emission (see Figure 5-5).

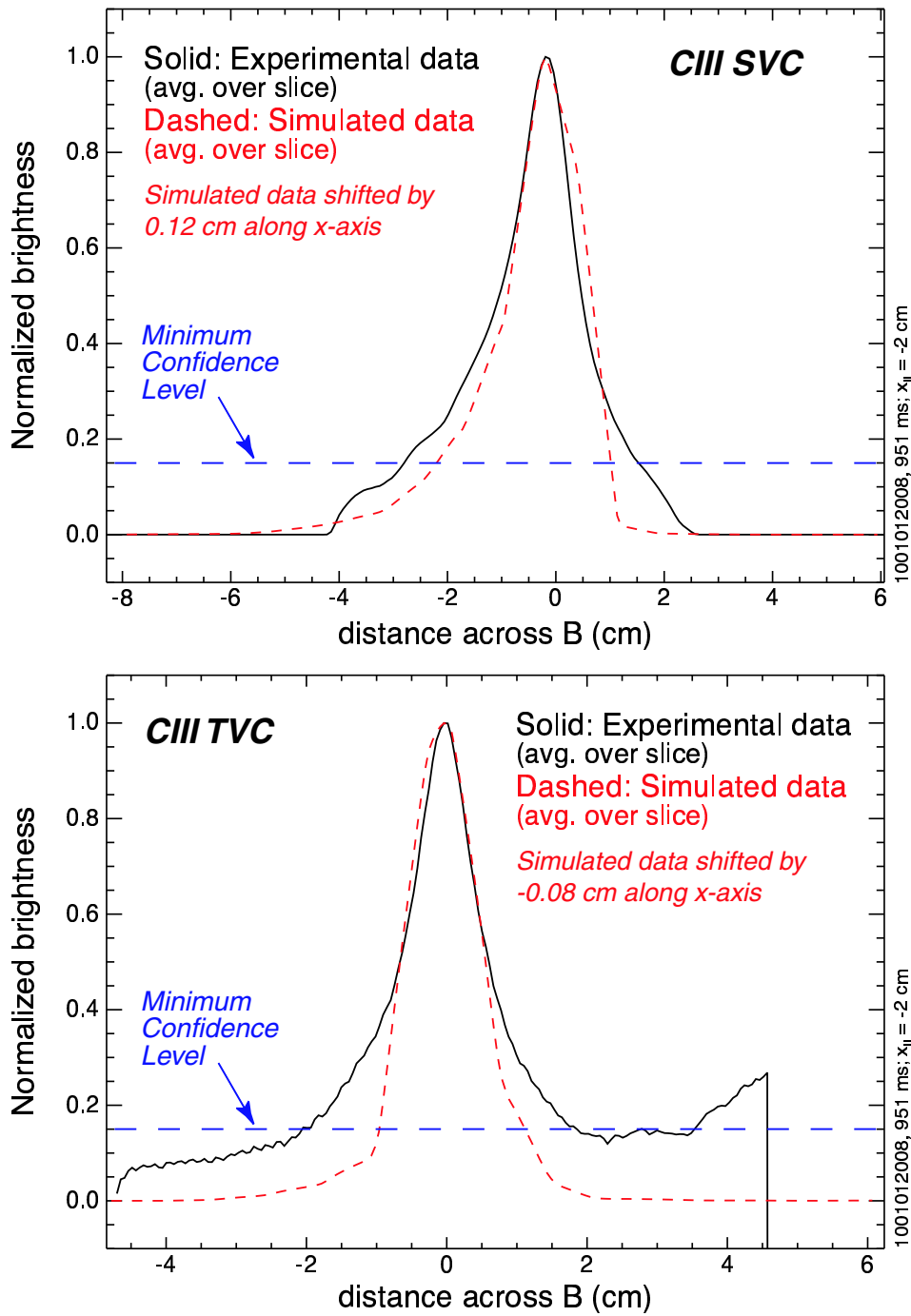


Figure 5-5: Comparison between simulated and experimental 1-D cross-field profiles of normalized brightness for the SVC (top panel) and TVC (bottom panel). The corresponding 2-D plumes are shown in Figure 5-4 (simulation) and Figure 3-12 (experiment). Relatively good agreement is observed between simulation and experiment for both the profile width and profile skewness in this case (when considering data above a minimum confidence level).

parameters are identical). In this case the simulation is unable to reproduce the experimentally-observed skewness of the SVC plume data.

These results are not necessarily inconsistent with the probe measurements. At each location in the SOL, the probe in fact measures the value of electron density at its tip, while values of n_e further down the axis are unknown. If a large $\mathbf{E} \times \mathbf{B}$ drift is responsible for transporting impurity ions formed near the probe tip down the probe axis, this drift will also result in the transport of bulk plasma ions down the probe axis, since $\mathbf{E} \times \mathbf{B}$ drifts are the same for all ion species. This drift affects the electron density along the probe axis, and can result in a uniform distribution.

The $\mathbf{E} \times \mathbf{B}$ drift model implemented in LIM is rather basic, and by no means is it complete. There are a number of refinements which may be made to improve the calculation, such as allowing for a spatially-varying drift velocity, or computing a fully self-consistent solution which accounts for the effect of the drift velocity on the electron density and temperature profiles (such that the profiles used in LIM are consistent with those used in the emission excitation rate calculation). However, the goal of this investigation was to construct a plausibility argument for a mechanism which may be used to explain the asymmetry in the experimental plume emission between SVC and TVC, i.e. the vertical elongation of the plumes. Results suggest that an $\mathbf{E} \times \mathbf{B}$ drift resulting from probe presheath effects provides such an explanation.

Modifications to the electron density profile which are caused by the probe-induced $\mathbf{E} \times \mathbf{B}$ drift are thought to have a much larger affect on the SVC results than on the TVC results (e.g. see Figures 5-5 and 5-6). In fact, the experimental SVC data cannot be reproduced without including these modifications in the simulation. However, the development of an appropriate model for describing the effect of $\mathbf{E} \times \mathbf{B}$ drifts on the electron density is beyond the scope of this work. Thus, analysis presented in the remainder of this chapter focuses on the simulation of TVC data.

In the near SOL, carbon recycling and vertical $\mathbf{E} \times \mathbf{B}$ drifts are expected to primarily affect the cross-field dimension of the simulated TVC results, and not the parallel extent since this is dominated by the presence of the recycling-induced density perturbation. In the far SOL this perturbation is weak, and effects of carbon recycling

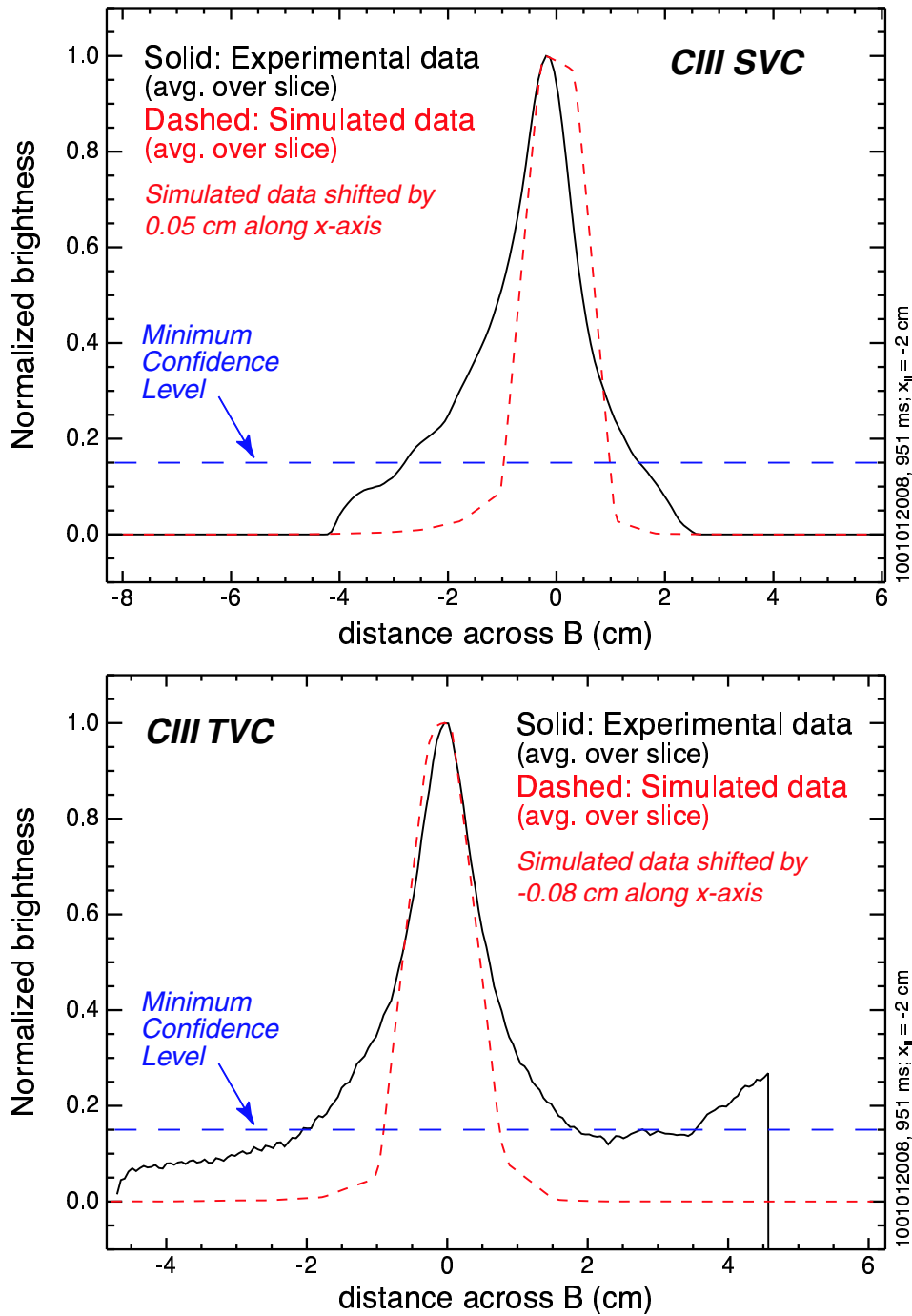


Figure 5-6: Comparison between simulated and experimental 1-D cross-field profiles of normalized brightness for the SVC (bottom panel) and TVC (top panel). Simulation parameters are identical to those used in generating Figure 5-5. However, in this case the measured electron density profile has been used to calculate the emission excitation rate. Results indicate that the simulation is unable to reproduce the experimentally-observed skewness of the SVC plume.

and vertical ion drifts may also influence the parallel extent of the emission in this region. However, rather than attempt to simulate the $\mathbf{E} \times \mathbf{B}$ flow pattern in the probe presheath and the resultant carbon deposition profile on the probe, a simple sputter source model has been developed to investigate the contribution to the plumes of emission resulting from carbon deposited on the probe surface. Results indicate that the model is sufficient to explain the cross-field extent of the experimental emission (see section 5.2). In addition, this model is able to provide an explanation for the parallel extent of emission generated in the far SOL. Therefore, the carbon recycling and $\mathbf{E} \times \mathbf{B}$ models presented in this section will not be used in further analysis of the impurity plume dispersal.

5.2 Results from Sputter Source Model

A model has been developed in LIM (section 4.4) to investigate the effect of sputtering on the plume results. In this model, the probability of a carbon neutral being sputtered from a location some distance down the probe axis is assumed to decay exponentially with distance from the probe tip, while the energy distribution for the sputtered neutrals is given by a Thompson distribution [5]. Two input parameters are therefore used in LIM to characterize the sputter source: λ , which represents the exponential decay length down the probe axis for the sputter distribution, and U_0 , which represents the surface binding energy of the carbon atoms.

The physical space distribution for sputtering will depend on both the carbon deposition profile on the probe surface and the flux of background plasma ions to the probe ($\propto n_e \sqrt{T_e}$). For a uniform surface distribution of carbon, λ may be estimated as the decay length of the saturation current density measured by the probe (since this current is a measure of the ion flux to the probe), which is of order ~ 5 mm for conditions typical of the near SOL. However, carbon recycling off the probe surface and probe-induced $\mathbf{E} \times \mathbf{B}$ drifts down the probe axis may significantly affect the carbon deposition profile. In addition, vertical $\mathbf{E} \times \mathbf{B}$ drifts may increase the ion flux to the probe, since these drifts are thought to be responsible for transporting bulk

plasma ions down the probe axis. Values for λ are therefore expected to be larger than the current density decay length. For a given plume simulation, λ is simply specified to provide the best fit to the experimental data.

Values for U_0 are also difficult to determine, because very little information exists on the surface chemistry for carbon atoms deposited on molybdenum. However, for sputtering of carbon from a graphite surface, $U_0 = 7.4$ eV [56]. Binding energies in the range of a few eV are therefore expected.

A brief sensitivity study was performed to determine the effect of varying λ on the simulation output. An example of these results is given in Figure 5-7, in which simulated CIII TVC plumes are shown for two values of λ (3, 12 mm). In both cases $U_0 = 20$ eV, $M_{\parallel} = -0.46$ (constant over the emission volume), and density and temperature profiles typical of near SOL conditions were used (the non-physical high value of U_0 is required to match the parallel extent of the experimental plume data – more discussion below). Also note that for both cases, as for all simulation results presented in this section, the non-jet background model was used to specify the background plasma conditions. At larger λ , both the cross-field width of the simulated plume and its parallel asymmetry are observed to increase. Recall that the probe geometry in the sputter source model is a cone connected to a cylinder, with the distance down the probe axis at which the connection occurs given by $d_c \simeq 13$ mm. For cases where λ is smaller than d_c , increasing λ increases the cross-field source size. This is because the radius of the probe surface is proportional to distance down the probe axis in this region, and therefore as λ increases the average radius from which sputtered neutrals are launched also increases. In addition, as λ increases a larger fraction of neutrals are launched from regions of colder and less dense plasma, where ionization rates are smaller. The average effective lifetime of the impurity ions subsequently increases, allowing these ions more opportunity to cross-field diffuse. The combination of these effects (larger source, longer lifetime) leads to a larger cross-field plume width. Finally, in regions of colder and less dense plasma coulomb momentum transfer rates also increase, increasing the collisional coupling between impurity ions and the background plasma. Therefore as λ increases a larger fraction

of impurity ions have an opportunity to acquire the background parallel flow velocity, resulting in a larger parallel asymmetry for the plume.

In general, use of the non-jet background/sputter source model involves choosing values for the decay length, binding energy, and parallel Mach number which provide the best match between simulation and experiment. The primary effect of U_0 in the simulation is to increase the parallel extent of the emission (characterized in terms of decay lengths), while the effect of M_{\parallel} is to increase the parallel plume asymmetry (for cases when the impurity ions are well-coupled to the background flow). The effect of λ in the simulation has been discussed above. An example of an experimental CIII TVC plume generated in the near SOL and simulated using this model is shown in Figure 5-8 (top panel). In attempting to simulate this plume, λ was varied between 6 mm and 15 mm, U_0 was varied between 5 eV and 25 eV, and M_{\parallel} was varied between -0.26 and -0.53. The simulated CIII TVC plume which provides the best match to the experimental data is shown in Figure 5-8 (bottom panel) – for this simulation $\lambda = 12$ mm, $U_0 = 20$ eV and $M_{\parallel} = -0.46$. This result is considered to provide the best match to the experiment based on the agreement between simulated and experimental values for the parallel decay length on either side of the injection location, which are within $\simeq 8\%$ in this case, and the agreement between the simulated and experimental values for the cross-field plume width, which are within $\simeq 16\%$ in this case.

The cross-field extent of the emission is comparable for both simulation and experimental results, indicating that the non-jet background/sputter source model provides a good explanation for this feature of the plumes. This result is independent of the value of D_{\perp} chosen (1 m²/s in this case), consistent with conclusions reached from simulation parameter studies (section 5.7.4). However, this model is unable to recreate the “jet” seen in the experimental data, the presence of which leads to a broad parallel emission profile. To generate the same parallel extent in the simulation results without creating a jet, a large value for the binding energy is required ($U_0 = 20$ eV), resulting in the average speed of impurity ions away from the injection location being large. Subsequently, a large background flow is necessary to generate the same parallel asymmetry in the simulated plume as observed experimentally. This

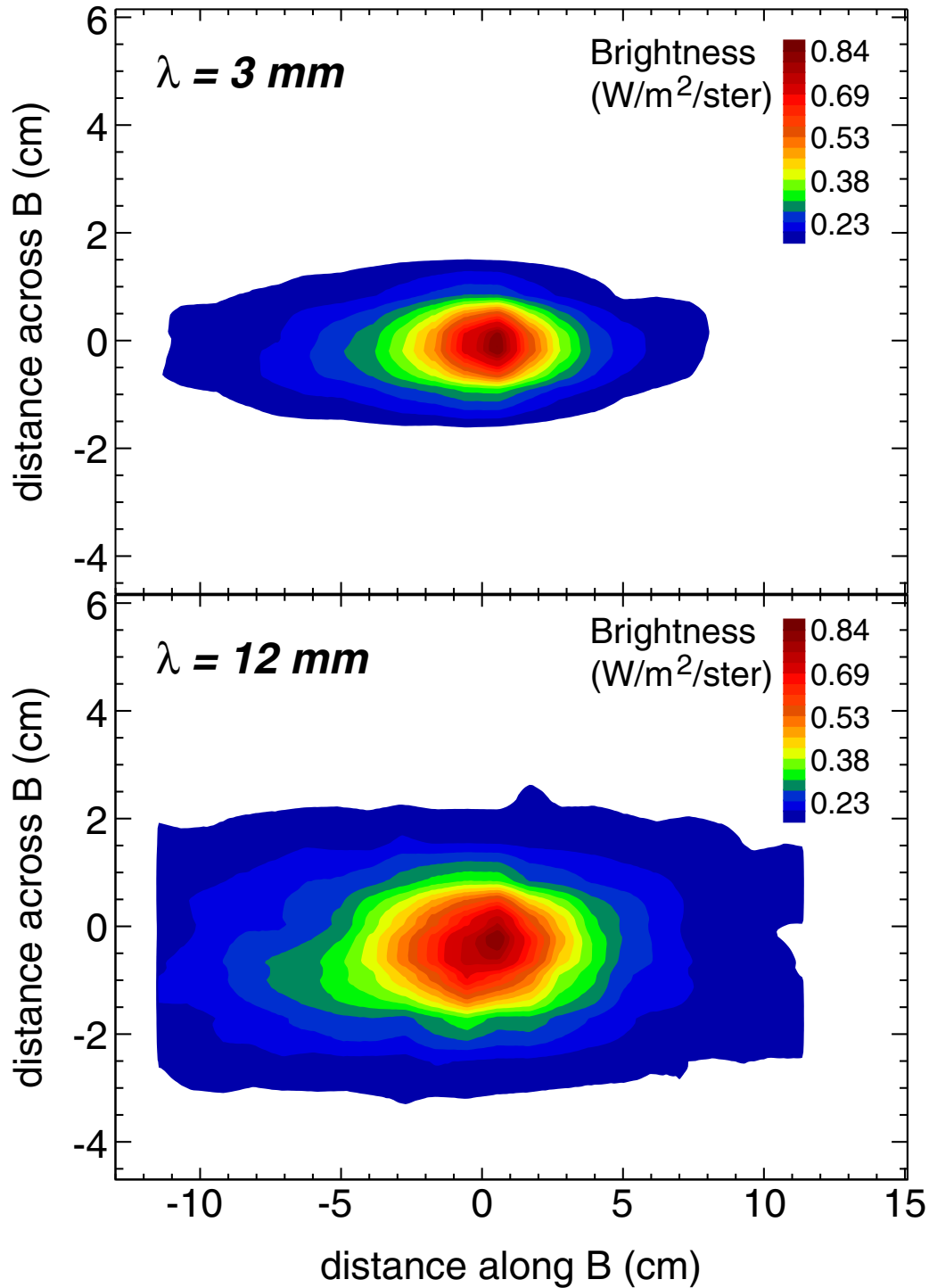


Figure 5-7: Comparison of simulated CIII TVC plumes for two values of λ (*top panel*: $\lambda = 3 \text{ mm}$; *bottom panel*: $\lambda = 12 \text{ mm}$). In both cases the binding energy was set equal to 20 eV, the parallel Mach number (assumed constant over the plume volume) was set equal to -0.46, and density and temperature profiles characteristic of conditions near the separatrix were used. Two main differences are apparent: as λ increases, both the cross-field width and the parallel asymmetry increase.

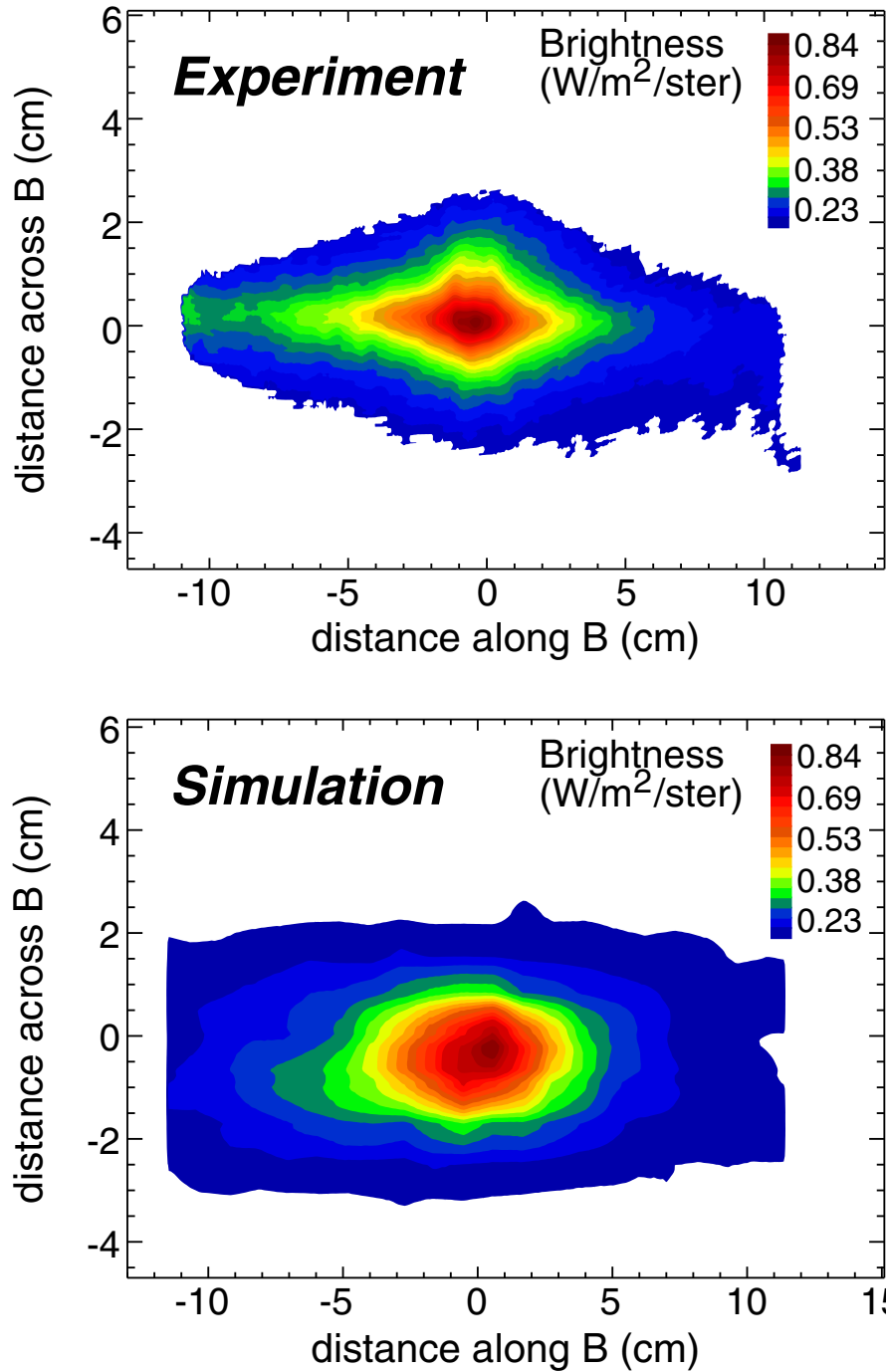


Figure 5-8: Comparison between experimental and simulated CHH TVC plumes. *Top panel:* Experimental plume generated in the near SOL ($n_e = 1.14 \times 10^{20} \text{ m}^{-3}$, $T_e = 60 \text{ eV}$). Emission has been absolutely calibrated and mapped to field-aligned coordinates. *Bottom panel:* Simulated plume. Code inputs are: $M_{\parallel} = -0.46$ (constant over plume volume); $v_{\perp} = 2.2 \text{ km/s}$ (towards the divertor) at the injection location, corresponding to $\mathbf{E}_r = 11 \text{ kV/m}$ for this discharge; $\lambda = 12 \text{ mm}$; $U_0 = 20 \text{ eV}$; $D_{\perp} = 1 \text{ m}^2/\text{s}$.

results in a large discrepancy between the parallel Mach number used in the simulation ($M_{\parallel} = -0.46$) and the value measured by the Mach probe ($= -0.20$; calculated using Equation 2.1) for this scan.

In general, parallel asymmetries of experimental plumes formed in the near SOL tend to be unrelated to measurements made by the Mach probe (e.g. see Figures 3-21 and 3-22). LIM sensitivity studies (section 5.7.3) also suggest that in the near SOL parallel plume structure is unrelated to the background plasma flow (see Figure 5-30). It is therefore not surprising that the parallel Mach number necessary to simulate plume emission in the near SOL is very different from the probe-measured value. The absence of “density perturbation physics” in the non-jet background/sputter source model also explains why a large value of U_0 was necessary for the simulation. This value of U_0 is unreasonable, given the value for the surface binding energy of carbon on graphite.

A study was conducted to investigate whether the parallel extent of the emission could be explained by inaccurate background plasma measurements rather than an unrealistic value of U_0 . In other words, are the density and temperature values measured by the scanning probe (and subsequently inputted into the simulation) too large? In the near SOL, the sensitivity of CIII plume emission to electron temperature is weak, since the ionization cross-section profile is rather flat in this region. For example, if the probe measurement of $T_e = 50$ eV is in error by ± 10 eV, the resulting variation in the ionization cross section is only $\simeq 27\%$. However, the ionization lifetime is inversely proportional to the electron density, so errors in density correspond directly to errors in the parallel mean-free path of the impurity ions. To determine the effect of such errors, a pair of simulations were run in which the electron density was varied.

A comparison between the CIII TVC 1-D parallel emission profiles for these two simulations is shown in Figure 5-9. In the first case (solid curve), density and temperature profiles characteristic of the near SOL were inputted, and a value of $U_0 = 5$ eV was used. This value is assumed to be representative of the actual value of the surface binding energy for sputtering carbon off molybdenum. Inputs to the simulation in the

second case (dashed) were identical to those in the first, with the exception that the density everywhere was lowered by a factor of two. The results given in Figure 5-9 suggest that in the near SOL the parallel extent of the simulated emission is insensitive to the value of electron density. This is thought to result from the variation of the thermalization time (τ_{therm}) with density. For low (and appropriate) values of U_0 , the parallel velocity of the impurity ions is primarily a function of the impurity ion temperature. As density is reduced, coulomb collision frequencies are also reduced, resulting in lower ion temperature, and therefore smaller ion velocity. So although the ionization lifetime is increasing as well in this case, the parallel mean-free path is relatively unchanged. These results indicate that probe measurement errors are not responsible for the inability of the non-jet background/sputter source model to simulate the parallel extent of plume emission generated in the near SOL.

However, this model has been demonstrated to provide a reasonable simulation of plume emission in the far SOL. An example of this is shown in Figure 5-10. For this case $\lambda = 10$ mm, $U_0 = 5$ eV and $M_{\parallel} = -0.18$ (constant over the emission volume). In the top panel a comparison between experimental and numerically generated 2-D CIII TVC plumes is given, while in the bottom panel a comparison between the corresponding 1-D parallel emission profiles is shown. The main difference is the emission structure in the near field (close to the injection location), where reflections off the probe head result in the experimental emission being peaked. In the far field ($\gtrsim 2$ cm away from the injection location along \mathbf{B}) the decay lengths are approximately equal, indicating good agreement between simulation and experiment. These results suggest that “density perturbation physics” are not important for plumes generated in the far SOL plasma, and that a sputtering launch-energy distribution is an appropriate model in these cases.

5.3 Possible causes for jet behavior

The non-jet background/sputter source model is not able to simulate plumes in the near SOL unless an unrealistic value for the surface binding energy is used. The

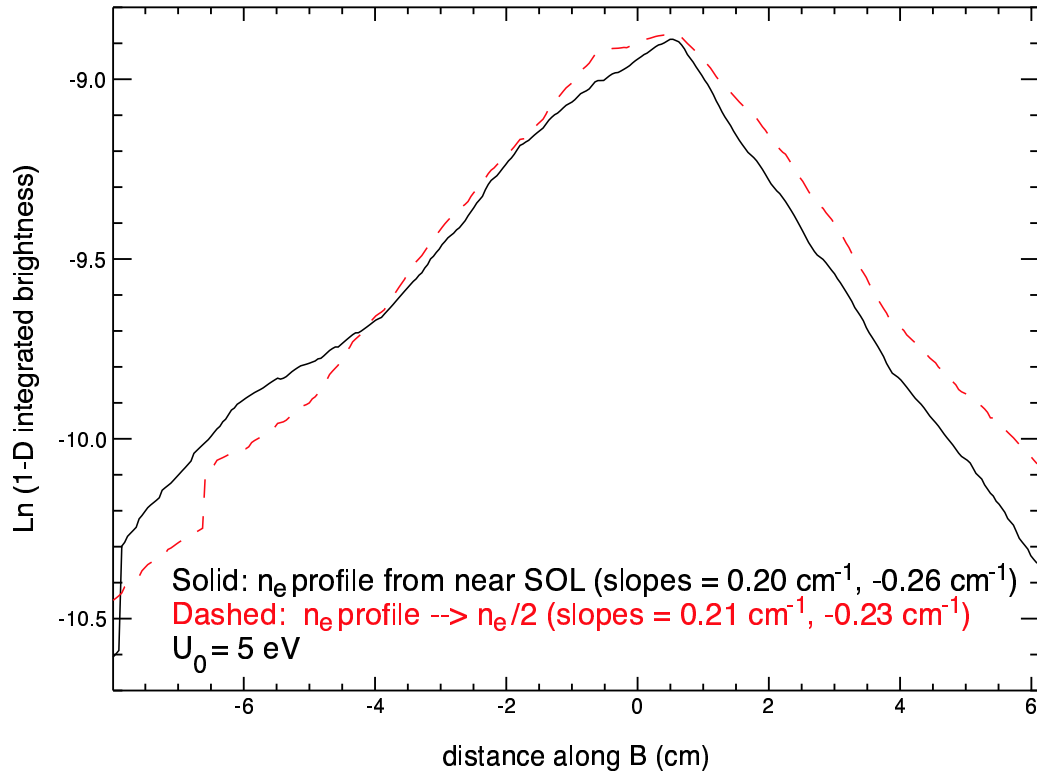


Figure 5-9: Comparison of 1-D CIII TVC parallel emission profiles for a pair of simulation runs in which the electron density was varied. In the first case (solid curve), density and temperature profiles characteristic of the near SOL were inputted, and a value of $U_0 = 5 \text{ eV}$ was used. In the second case (dashed) the density everywhere was lowered by a factor of 2. The results indicate that in the near SOL the parallel extent of the simulated emission is relatively insensitive to the value of electron density.

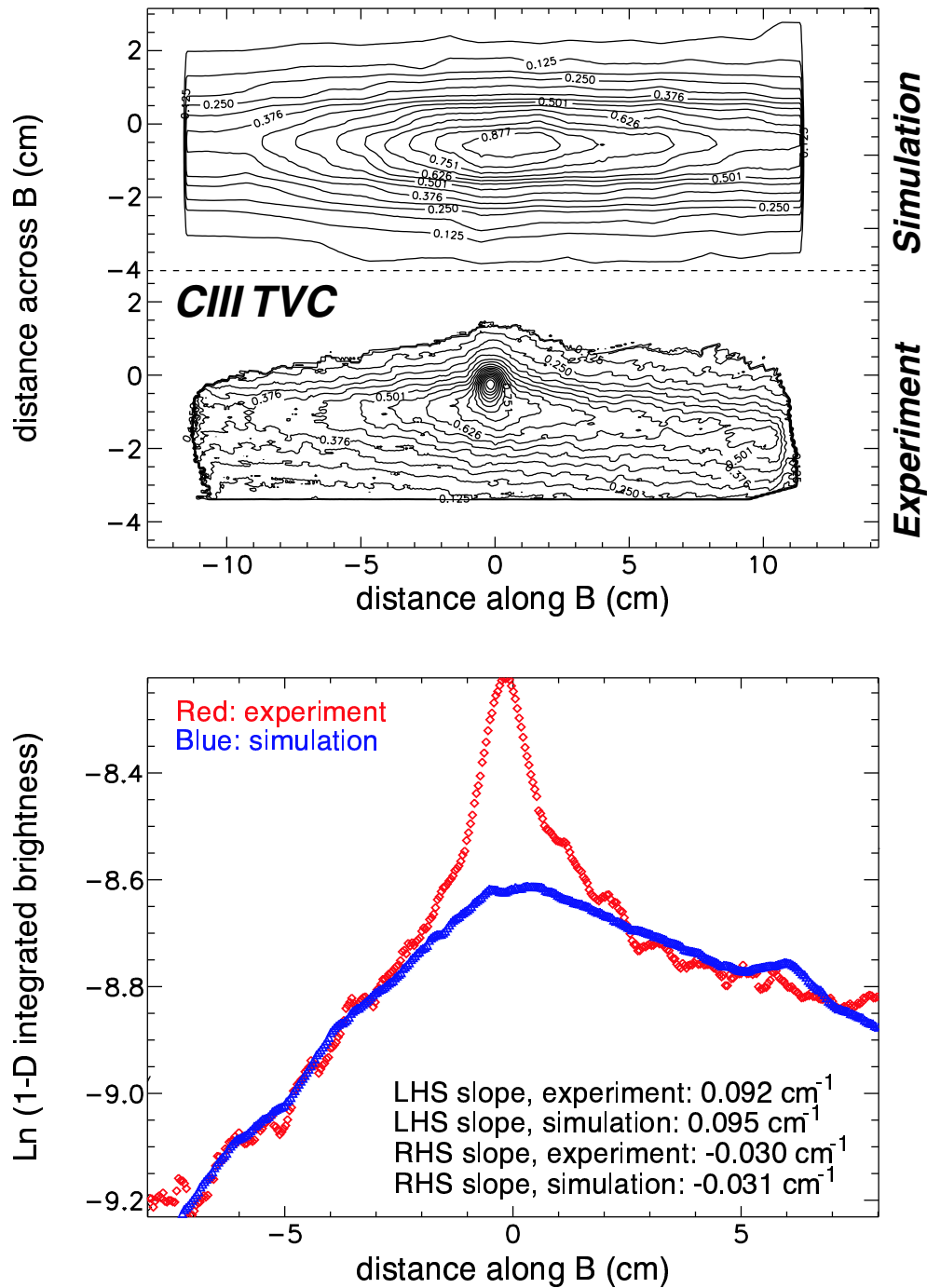


Figure 5-10: *Top panel:* Comparison between experimental and numerically generated 2-D CIII TVC plumes in the far SOL plasma. *Bottom panel:* Comparison between 1-D parallel emission profiles for plumes shown above. Near the injection location, the experimental emission is peaked as a result of reflections off the probe head. In the far field, however, the decay lengths are approximately equal, suggesting that “density perturbation physics” are not important for plumes generated in the far SOL.

general conclusion is that the parallel velocity of impurity ions away from the probe must be large in order to explain the parallel extent of the emission. A mechanism other than sputtering must therefore exist to provide “directed” parallel energy to the impurity ions. In addition, it must be a collisionless mechanism, since coulomb momentum transfer rates are small for C^{+2} ions present in conditions typical of the near SOL. Finally, since the impurity ions must have a directed flow away from the probe, it is reasonable to assume that this energy-transfer mechanism does not exist in the background plasma in the absence of the probe. Thus perturbations resulting from plume formation, either due to gas injection or to the probe itself, are investigated as possible mechanisms which might give rise to the jet.

Analysis indicates that a significant density perturbation can arise as a result of impurity gas injection into the near SOL plasma. For example, for a carbon injection rate of 10^{19} atoms/second the resulting electron density perturbation can be as large as $\sim 6.5 \times 10^{19} \text{ m}^{-3}$, which is a significant fraction of the background density. The density perturbation resulting from ions recycling off the probe surface is estimated to be even larger.

As a result of the pyramidal probe head geometry, one expects the recycling flux of neutrals from the probe surface to appear predominantly on field lines which do not intersect the probe. Ionization of neutrals on these field lines might cause the formation of a localized density perturbation. This process is illustrated schematically in Figure 5-11. Estimates for the density perturbation may be obtained using Equation 3.4. The important parameters for characterizing the perturbation are found to be the injection rate (N_{inj}), the average parallel velocity away from the probe ($v_{\parallel,0}$), and the cross-field ionization width (λ_{cf}). In section 4.5, the effective injection rate of deuterium atoms due to recycling is estimated to be \sim a few 10^{20} per second (which is equal to the collection rate onto the probe, i.e. a 100% recycling model is assumed). The parallel velocity for the resulting deuterium ions is calculated assuming the ions have an average energy of $\simeq 3$ eV (i.e. that the ion energy equals the neutral atom energy, which in turn is given by the Frank-Condon dissociation energy [29]), resulting in $v_{\parallel,0} \simeq 30$ km/s. Finally, the cross-field ionization width for deuterium in the

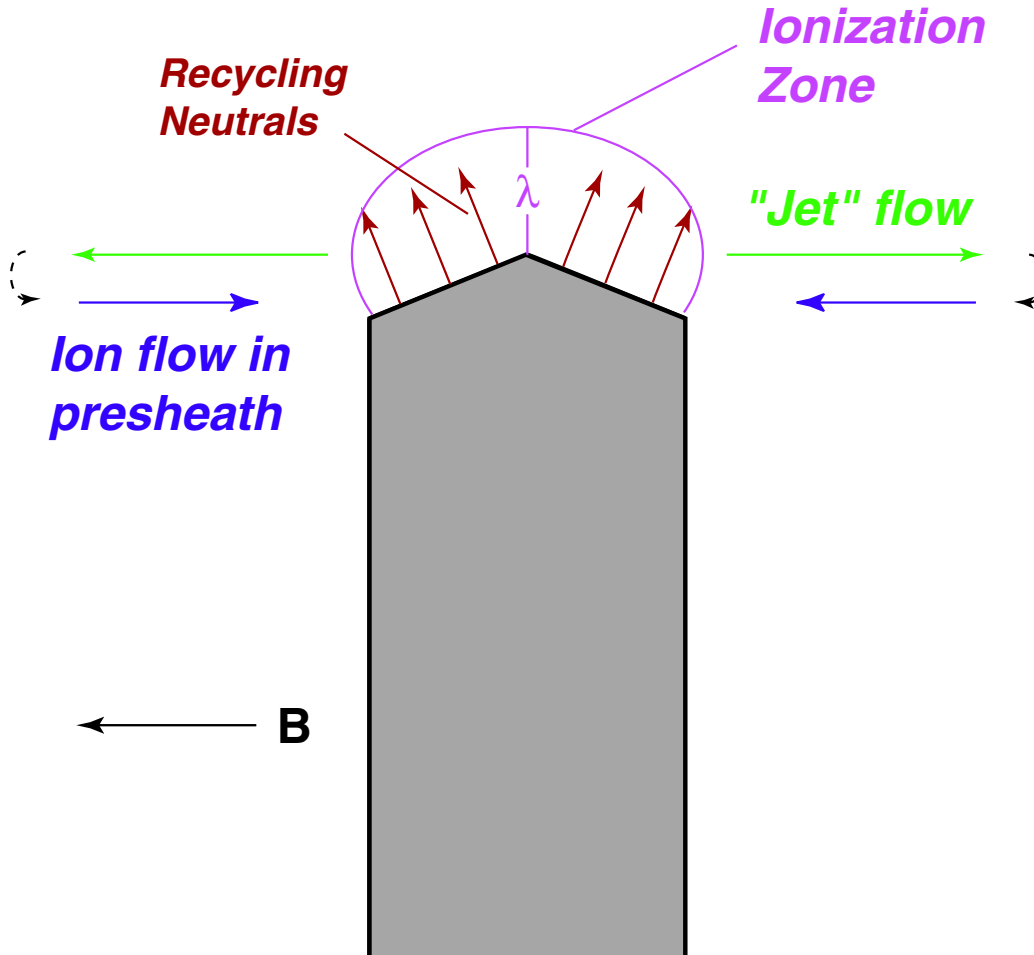


Figure 5-11: Schematic illustrating the process of background ion recycling off the probe surface. Neutrals formed by recycling appear predominantly on field lines outside the presheath, and ionize in a volume determined by local plasma conditions (n_e , T_e). This local ionization results in the formation of a density perturbation, which is thought to be responsible for causing the impurity ion jet.

near SOL is $\simeq 5$ mm, which is comparable to the estimate of λ_{cf} used for the injected carbon atoms (section 3.2.2). Plugging these values into Equation 3.4, the result is a density perturbation which can be a factor of 4 or more larger for recycling than for gas injection.

However, for both gas injection and recycling, the resultant ionization source is localized near the probe, implying that in the far field (i.e. well away from the injection location along \mathbf{B}) the density might be considerably lower. A variation of density along \mathbf{B} would lead to a variation in the plasma potential, assuming that density and potential are related by a Boltzmann relationship: $n_e \propto e^{-e\phi/T_e}$. This

variation would result in the generation of a parallel electric field ($E_{\parallel} = -\nabla_{\parallel}\phi$), present on field lines that do not intersect the probe (see Figure 5-11) and directed away from the probe. This mechanism could provide impurity ions present near the probe tip with “directed” parallel energy away from the probe. The parallel velocity of these ions would therefore primarily be determined by E_{\parallel} and not thermalization with the background plasma. For a sufficiently large parallel electric field, the plume would be extended in the parallel direction.

LIM was configured to investigate the magnitude of the density perturbation caused by local recycling (section 4.5) and whether the resultant parallel electric field is sufficient to explain the parallel extent of experimental plumes formed in the near SOL. Results from this analysis are discussed below.

5.4 Results from density perturbation model

5.4.1 D^+ plume arising from D_2 recycling

A typical result from the deuterium recycling simulations is shown in Figure 5-12, in which surface plots of the total electron density (background plus recycling-induced) are shown for two radial coordinates: $x = 0$ mm and $x = -2$ mm. The location of these surfaces with respect to the probe geometry is also illustrated schematically in this figure. Background density and temperature profiles characteristic of the near SOL were used as inputs to the simulation for this case. LIM output were scaled to absolute units (m^{-3}) using a typical experimental value for the recycling rate, taken to be 2.6×10^{20} atoms/second. Effects arising from density variation in the presheath have also been included. The observation of strong density peaking in the poloidal coordinate (p) suggests that the recycling perturbation occurs predominantly on field lines near (but not connected to) the probe surface. The poloidal density asymmetry observed on the $x = -2$ mm flux surface results from the variation in recycling flux with distance down the probe axis. Finally, for the flux surface at $x = 0$ mm the density perturbation is highly localized to the field line which passes above the probe

tip.

A plot of the parallel electron density variation on this field line is given in Figure 5-13, in which only the portion of the total density resulting from recycling is shown. In this case the peak density due to ion recycling is found to be comparable to the background electron density at this location ($1.14 \times 10^{20} \text{ m}^{-3}$). In addition, the density profile is rather broad relative to the parallel extent of the probe ($= 1.6 \text{ cm}$), and a finite level of perturbation is found to exist over a parallel extent which is typical for experimental CIII emission ($\simeq 22.5 \text{ cm}$).

These results are based on the assumption that ion recycling may be treated with a perturbative analysis, i.e. that the background conditions are not affected by recycling. This is shown to be invalid by the level of the observed perturbation. Nonetheless, proceeding with this assumption, the full density profile at the gas injection location may be estimated by summing together values given in Figure 5-13 with the background density at this location. The result is a density profile which varies by \sim a factor of 2 over a parallel extent typical for experimental CIII plumes. The parallel variation in plasma potential may be determined by assuming a Boltzmann relationship between density and potential:

$$\phi = -\frac{T_e}{e} \ln \left(\frac{n_e}{n_{e0}} \right) \quad (5.1)$$

where n_{e0} is the peak electron density. For results given in Figure 5-13, the corresponding potential profile is shown in Figure 5-14.

The parallel variation in plasma potential is similar to that in electron density, as expected from Equation 5.1. More importantly, in this case the total potential drop on either side of the injection location is a significant fraction of the local electron temperature (59.6 eV), implying that impurity ions present near the probe tip may be accelerated by this potential drop to a significant fraction of the impurity ion sound speed ($\sqrt{T_e/m_z}$). This result is consistent with the requirement for the impurity ion parallel velocity necessary to explain the parallel extent of experimental CIII emission in the near SOL. The resulting parallel electric field is determined from the gradient

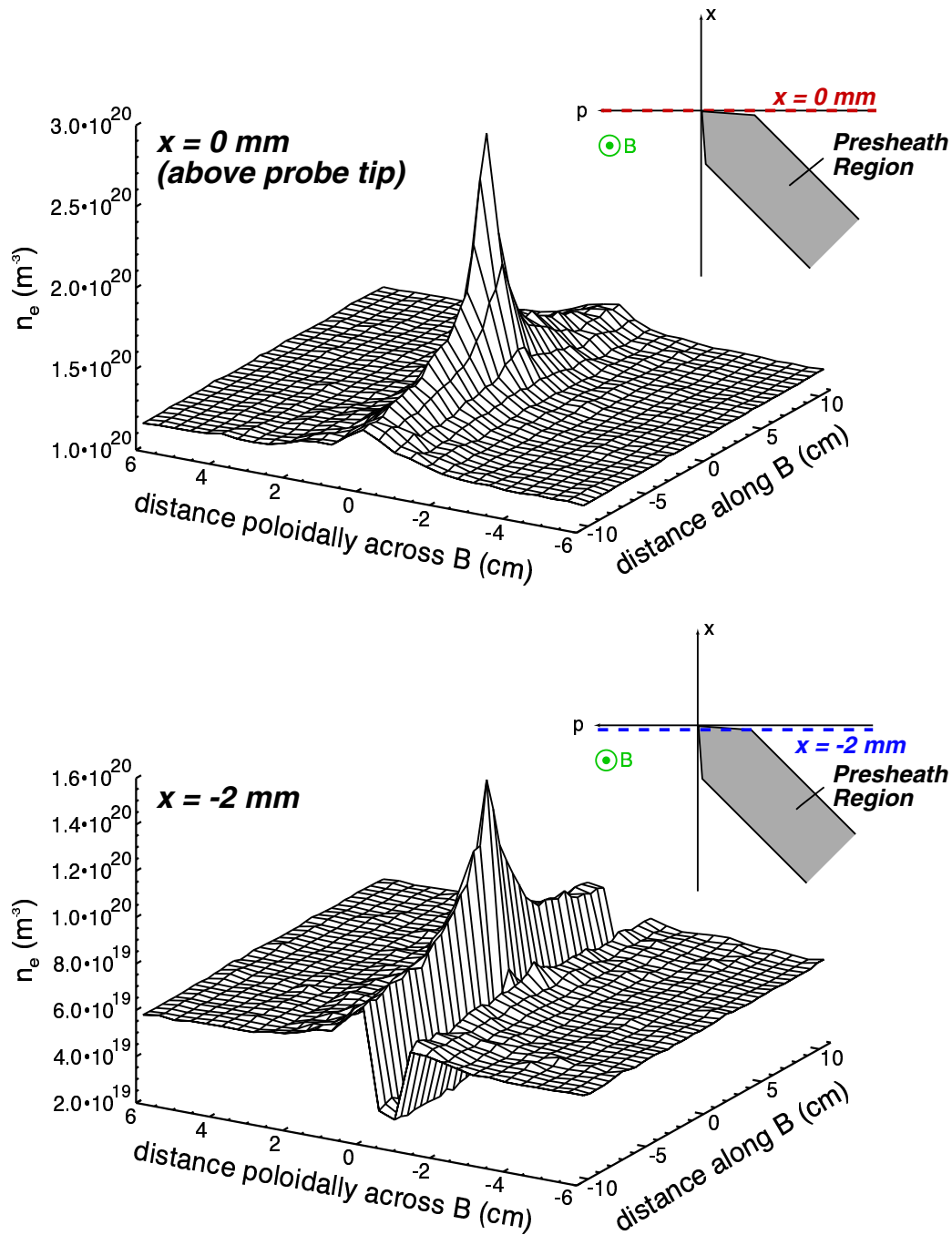


Figure 5-12: Surface plots of the total electron density (background plus recycling-induced) at two radial coordinates: $x = 0 \text{ mm}$ (top panel) and $x = -2 \text{ mm}$ (bottom panel). Background density and temperature profiles typical of the near SOL were used as inputs, and a recycling rate of 2.6×10^{20} atoms/second is assumed. Effects arising from density variation in the presheath have also been included. The density is peaked in the poloidal coordinate, suggesting that the recycling perturbation occurs predominantly on field lines near (but not connected to) the probe surface.

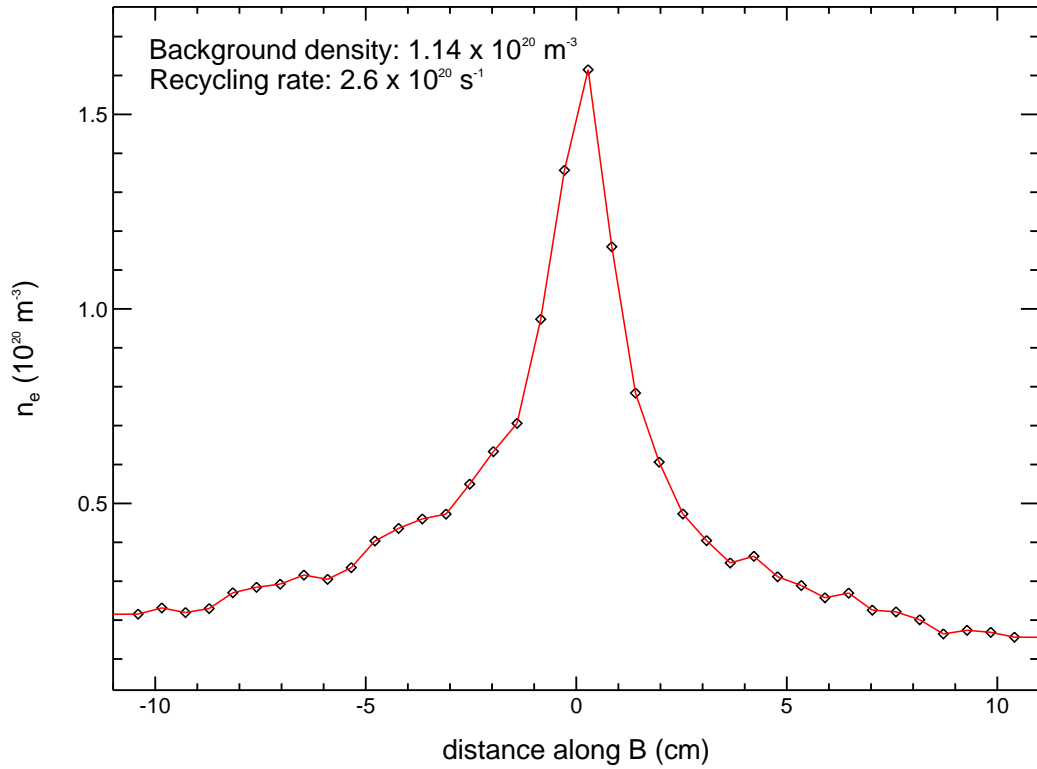


Figure 5-13: Plot of the electron density resulting from deuterium recycling vs. parallel coordinate for the field line passing above the probe tip (the corresponding 2-D surface plot with background density included is shown in the top panel of Figure 5-12). In this case the peak density which results from recycling is comparable to the background electron density at this location ($1.14 \times 10^{20} \text{ m}^{-3}$).

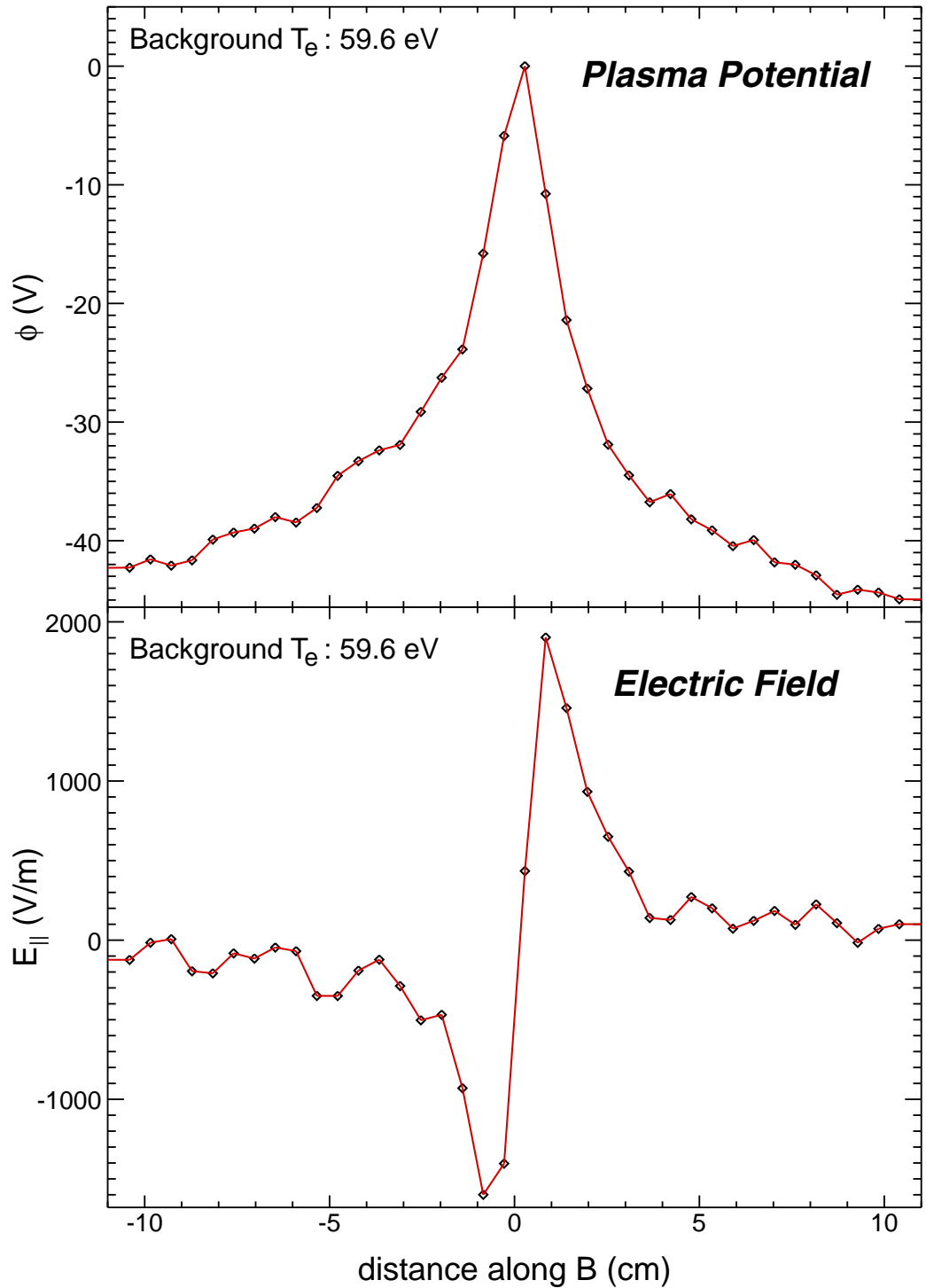


Figure 5-14: *Top panel:* Parallel variation of the plasma potential on the field line passing above the probe tip. Values are calculated using Equation 5.1 and the density profile results shown in Figure 5-13. The potential drop is a significant fraction of the local electron temperature (59.6 eV) in this case. *Bottom panel:* Parallel variation of the electric field, determined from the gradient of the plasma potential shown above. The peak electric field is ≈ 2 kV/m.

of the potential, and is also shown in Figure 5-14. The peak electric field is $\simeq 2$ kV/m in this case.

A test was then conducted in which the parallel electric field shown in Figure 5-14 was included in the recycling simulation, to estimate the effects of this field on the resulting density distribution. A plot of the parallel density variation on the field line passing above the probe tip is shown in Figure 5-15. For this case E_{\parallel} was incorporated into the simulation using a simple fitted analytic function (more discussion in section 5.5). Results from this analysis indicate that the peak density is reduced relative to the case with no electric field (Figure 5-13), implying that the potential drop, and therefore the resulting parallel impurity ion velocity, are also reduced. However, the perturbation is still significant in this case (the relative reduction is $\simeq 50\%$). In a fully self-consistent calculation, the parallel electric field determined from the parallel density variation (using Equation 5.1) and the electric field inputted to the simulation would converge to the same solution after some number of iterations. Results from the “zeroth” (no electric field, Figure 5-13) and “first” (Figure 5-15) iteration provide bounds for the final solution, and suggest that effects due to ion recycling would persist, and remain important, in the final calculation.

However, based on the emission structure for plumes generated in the far SOL, recycling perturbations in this region of the plasma are thought to be small. This observation has been investigated by conducting a simulation with inputted n_e and T_e profiles characteristic of the far SOL. For this simulation, a plot of the parallel density variation on the field line passing above the probe tip is shown in Figure 5-16. A recycling rate of 4.4×10^{19} atoms/second has been assumed, consistent with the total current collected by the probe under these conditions, while the observed parallel asymmetry in the profile results from the presence of a background parallel flow in the simulation. The resulting peak density is smaller than the background electron density at this location ($3.36 \times 10^{19} \text{ m}^{-3}$), suggesting that the perturbation is indeed weaker in this case.

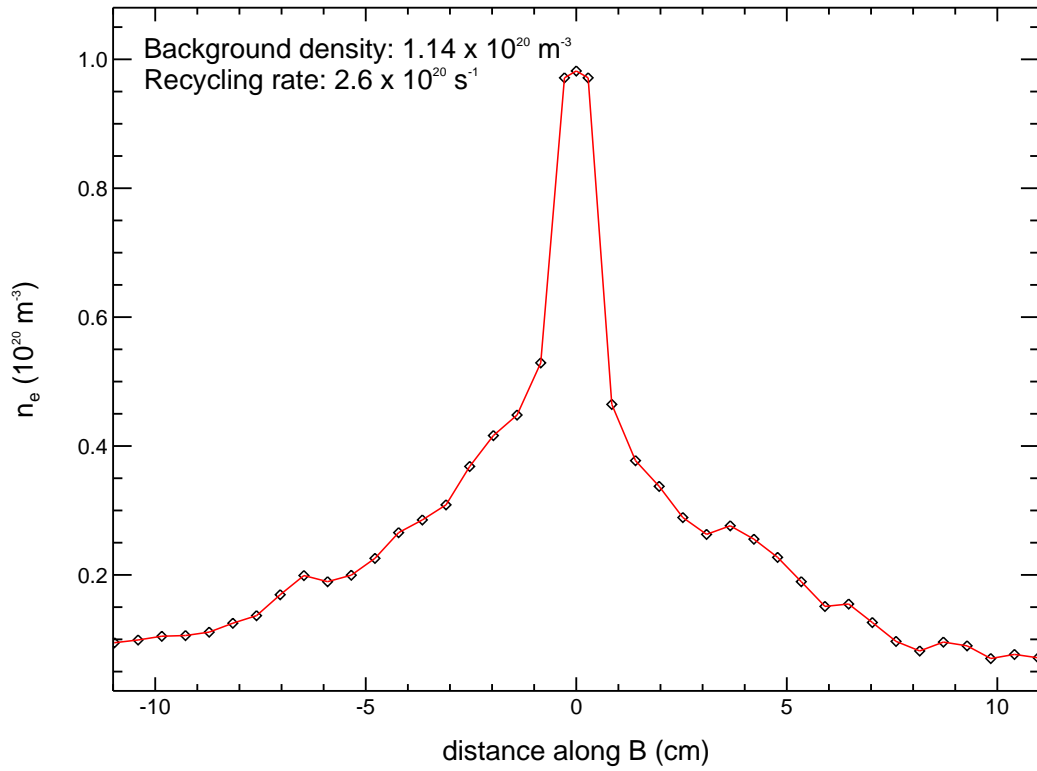


Figure 5-15: Plot of the electron density resulting from deuterium recycling vs. parallel coordinate for the field line passing above the probe tip. For this case, the parallel electric field shown in Figure 5-14 is included in the simulation (using a simple fitted analytic function) to estimate its effect on the resulting density distribution. Results indicate that the density perturbation is still significant, suggesting that the effects due to ion recycling would persist, and remain important, in a fully self-consistent calculation.

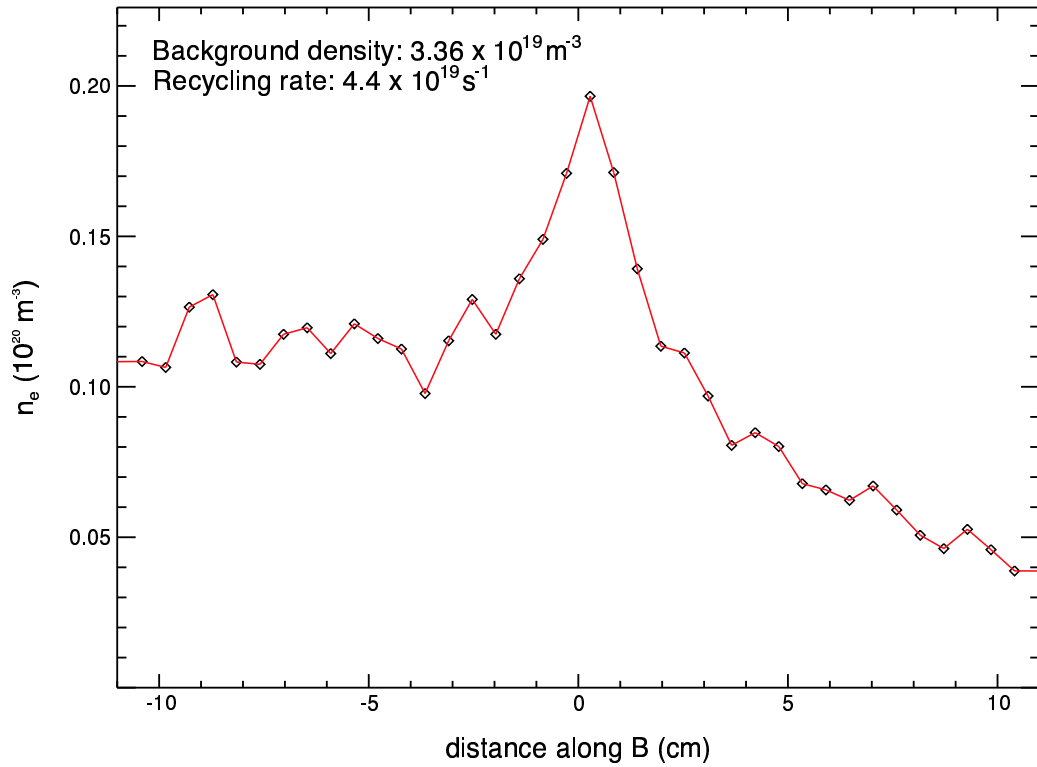


Figure 5-16: Plot of the electron density resulting from deuterium recycling vs. parallel coordinate for the field line passing above the probe tip. In this case, n_e and T_e profiles typical of the far SOL were used as inputs, and a recycling rate of 4.4×10^{19} atoms/second is assumed. The resulting peak density is smaller than the background electron density at this location ($3.36 \times 10^{19} \text{ m}^{-3}$), suggesting that the recycling perturbation is weak in the far SOL.

Finally, the effect of the density perturbation on the experimental results is found to depend strongly on the value for the ionization mean-free path of the recycling deuterium neutrals. This result, plotted in the form of normalized potential drop vs. mean-free path, is shown in Figure 5-17 (identical to Figure 3-20, but the data points are not sorted in this case). Also plotted in this figure are three simulation data points corresponding to LIM runs with input conditions typical of the near, intermediate, and far SOL. In the near SOL, i.e. at small values for the ionization mean-free path, there is good agreement between the simulation and experiment. However, the dependence of potential drop on the ionization mean-free path is found to be weaker in the simulation than in the experiment. The explanation for this is unknown. Nonetheless, the general trends between experiment and simulation are similar, suggesting that a recycling perturbation is a likely cause for the jet-like behavior of plumes generated in the near SOL.

5.4.2 D^+ plume arising from C_2D_4 injection

Simulations have also been conducted to investigate the effect injected deuterium (resulting from C_2D_4 injection) has on the local electron density. A plot of the resulting parallel density variation at the gas injection location is shown in Figure 5-18. In this case, inputted density and temperature profiles were identical to those used for simulating deuterium recycling off the probe surface in the near SOL. LIM output have been scaled to absolute units (m^{-3}) using a typical experimental value for the gas injection rate, taken to be 5×10^{18} molecules/second ($= 2 \times 10^{19}$ D^+ ions/second). For these conditions, the peak density due to deuterium injection is \sim a factor of 2 smaller than the background electron density at this location ($1.14 \times 10^{20} m^{-3}$). The profile width is also found to be smaller than but comparable to the parallel extent of the probe, and the perturbation is observed to exist over a reduced parallel extent relative to the recycling-induced perturbation. This last observation may be understood in terms of two separate effects. First, the cross-field source size for the D^+ plume arising from C_2D_4 injection is smaller than the cross-field source size for the plume resulting from D_2 recycling – in the first case, the source size is

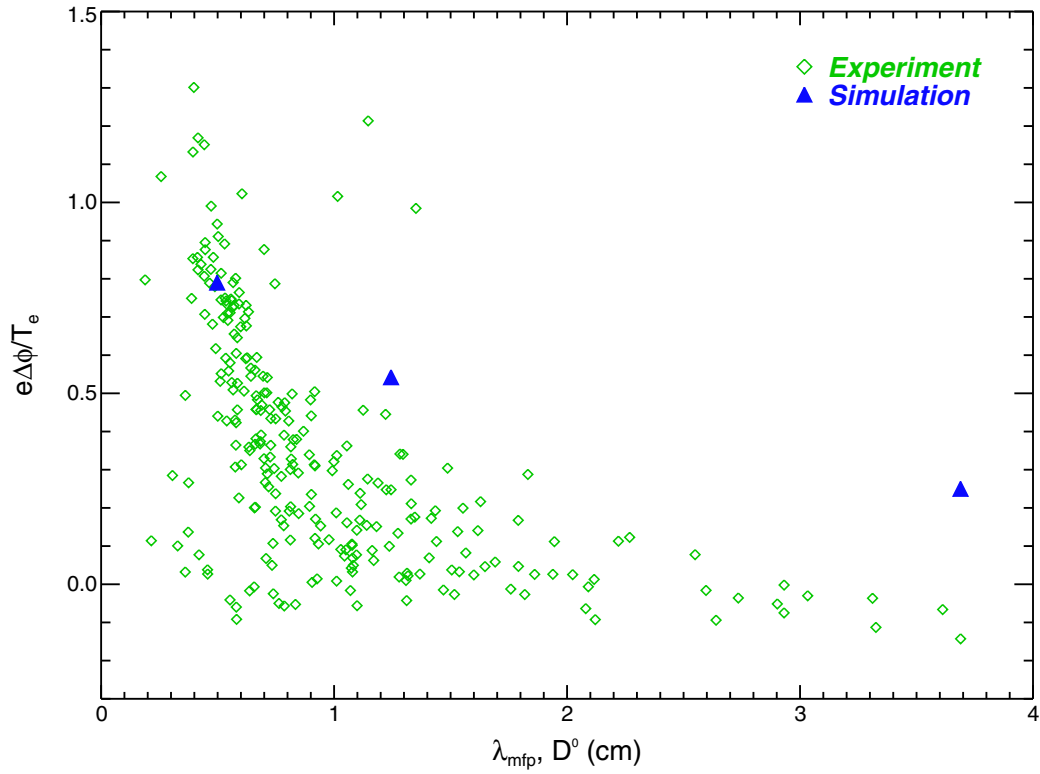


Figure 5-17: Plot of the normalized potential drop vs. ionization mean-free path for deuterium neutrals recycling from the probe surface. The experimental results (*diamonds*) suggest a strong relationship between potential drop and mean-free path, whereas simulation results (*triangles*) indicate a weaker dependence. Nonetheless, the general trends are similar, and there is good agreement for results in the near SOL (i.e. at small λ_{mfp}).

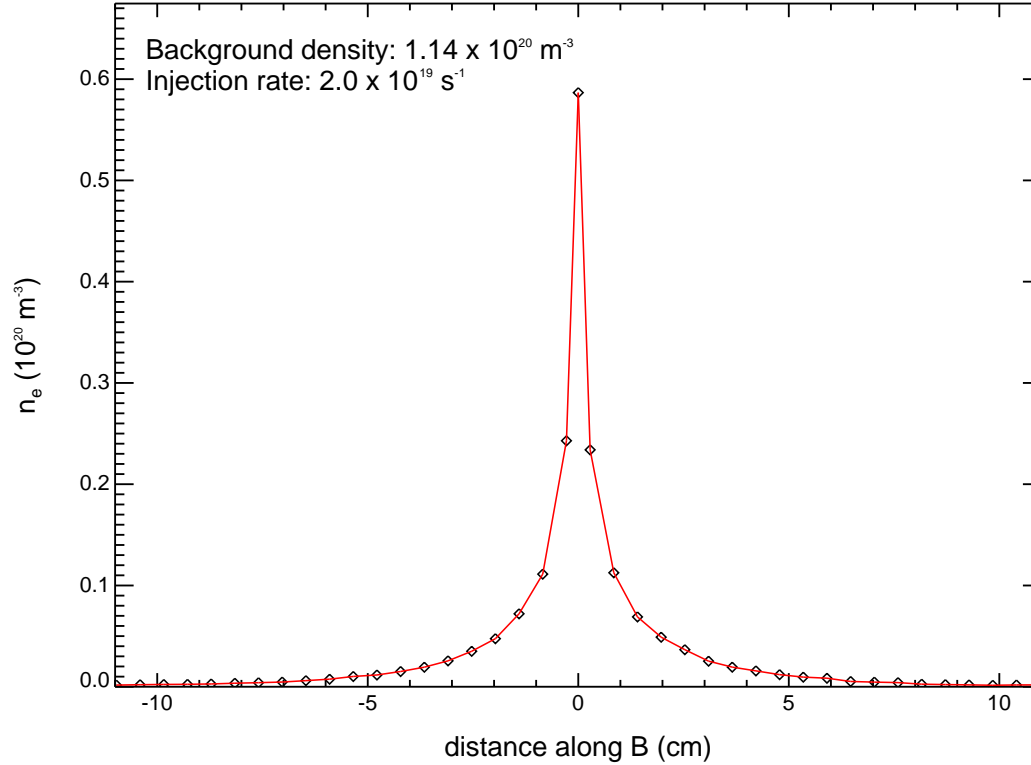


Figure 5-18: Plot of the electron density resulting from C_2D_4 injection vs. parallel coordinate for the field line passing through the gas injection location (i.e. above the probe tip). An injection rate of $2.0 \times 10^{19} \text{ D}^+$ ions/second is assumed. In this case, the peak density is \sim a factor of 2 smaller than the background electron density at this location ($1.14 \times 10^{20} \text{ m}^{-3}$).

the gas injection capillary diameter (1 mm) while in the second case the source size is determined by the probe head geometry. Second, neutral deuterium atoms which result from D_2 recycling can undergo charge exchange, which effectively increases the neutral mean-free path and therefore the parallel extent of the ionization source distribution. Both of these effects are consistent with a smaller parallel extent for the density perturbation arising from C_2D_4 injection relative to the perturbation resulting from D_2 recycling.

The peak density perturbation resulting from deuterium recycling is approximately three times larger than that for deuterium injection under similar background conditions (i.e. those representative of the near SOL). Therefore, the effect of deuterium injection is only to provide a minor increase in the total potential drop experienced by the impurity ions over a distance typical of the parallel CIII plume extent.

However, since the injection perturbation is localized near the probe tip, this suggests that it may be important in establishing the initial acceleration felt by the injected impurity ions.

5.4.3 Density perturbation arising from injected carbon

The perturbation which results from carbon injection may also affect the local electron density in the near SOL. This perturbation is estimated in LIM by calculating the total electron density at the gas injection location due to carbon ions:

$$n_{C,tot} = \sum_Z Z n_Z \quad (5.2)$$

where Z is the charge state of the carbon impurity ion and n_Z is the density of that charge state in the computation cell centered at the gas injection location. Results from simulations conducted with inputted profiles characteristic of the near SOL indicate that $n_{C,tot} \simeq 3\text{-}4 \times 10^{19} \text{ m}^{-3}$ when summing from $Z = 1$ to $Z = 3$. This result is consistent with the estimate obtained from analytic modelling (i.e. using Equation 3.4), justifying the value chosen for the cross-field extent of the injection volume in that model. This density perturbation is also comparable to the peak value resulting from the deuterium component of the injection, suggesting that both components of injected gas (C,D) play a similar role in determining the parallel electric field at the gas injection location. Perturbations due to background ion recycling are nonetheless the dominant effect in establishing the potential variation responsible for accelerating injected impurity ions to parallel velocities near the impurity ion sound speed.

5.5 Jet modelling in LIM

A model has been developed in LIM to include the effects of density perturbations discussed in section 5.4 in the plume simulations. The basic components of the model, as well as results derived from its implementation, are presented in this section.

5.5.1 Parallel electric field

Parallel electric fields inputted into LIM are the result of recycling and gas injection perturbations ($E_{\parallel,pert}$) as well as probe-induced presheath effects ($E_{\parallel,ps}$). While $E_{\parallel,ps}$ exists on field lines which are connected to the probe, $E_{\parallel,pert}$ is present only on those field lines outside the presheath.

Surface plots of the parallel electric field are shown in Figure 5-19 for two radial coordinates: $x = 0$ mm and $x = -2$ mm. In this case the electric field in regions outside of the presheath is determined from the Boltzmann relationship using the electron density structure given in Figure 5-12, while the electric field on field lines which intersect the probe is calculated using a standard presheath model.

One would like to study the influence of the parallel electric fields shown in Figure 5-19 on impurities injected from the probe tip (point source model). However, due to computational limitations which constraint the number and size of additional inputs to the code, the full 3-D structure cannot be used in LIM. Therefore, the approximation is made that the parallel electric field in the jet (i.e. $E_{\parallel,pert}$) has no cross-field variation over the extent of the impurity source. The inputted 1-D $E_{\parallel,pert}$ profile is taken to be the profile on the field line passing above the probe tip.

To increase the parallel resolution of the inputted electric field and to smooth out statistical fluctuations, an analytic function is used to fit $E_{\parallel,pert}$:

$$\begin{aligned}
 E_{\parallel,pert} &= -E_{lhs} e^{(x_{\parallel}+a_0)/\lambda_{lhs}} & -L_c \leq x_{\parallel} < -a_0 \\
 E_{\parallel,pert} &= \frac{E_{lhs}}{a_0 + x_0} (x_{\parallel} - x_0) & -a_0 \leq x_{\parallel} < x_0 \\
 E_{\parallel,pert} &= \frac{E_{rhs}}{b_0 - x_0} (x_{\parallel} - x_0) & x_0 \leq x_{\parallel} < b_0 \\
 E_{\parallel,pert} &= E_{rhs} e^{-(x_{\parallel}-b_0)/\lambda_{rhs}} & b_0 \leq x_{\parallel} < L_c
 \end{aligned} \tag{5.3}$$

The parallel electric field is taken to be periodic in L_c , where $2L_c$ represents the distance from the injection location to the edge of the domain along \mathbf{B} . This periodicity condition is the same for all background plasma profiles specified in LIM.

An example of a typical $E_{\parallel,pert}$ profile (solid) and its analytic fit (dashed) are shown

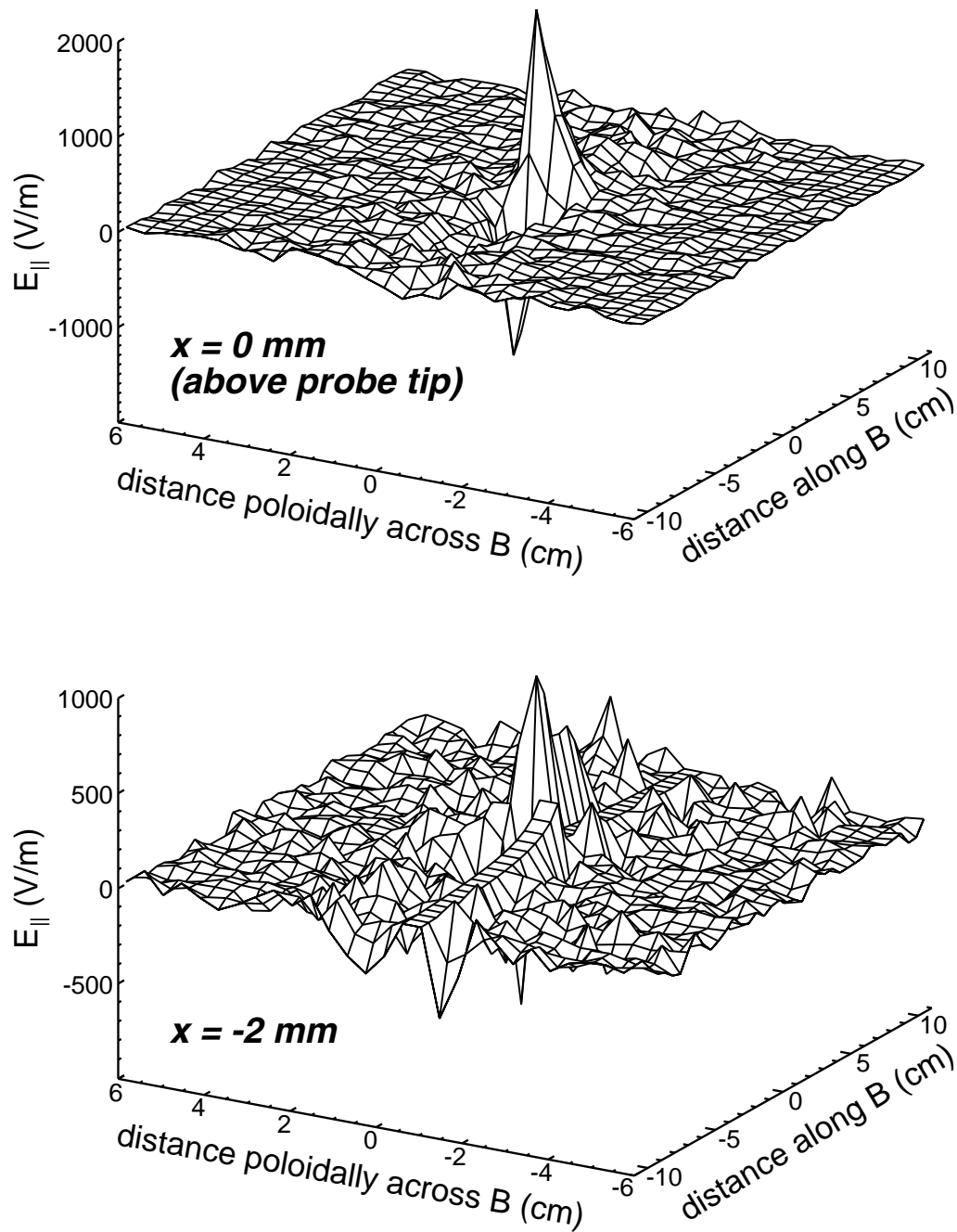


Figure 5-19: Surface plots of the parallel electric field at two radial coordinates: $x = 0 \text{ mm}$ (top panel) and $x = -2 \text{ mm}$ (bottom panel). The electric field in regions outside of the presheath is determined from the Boltzmann relationship using the electron density structure shown in Figure 5-12.

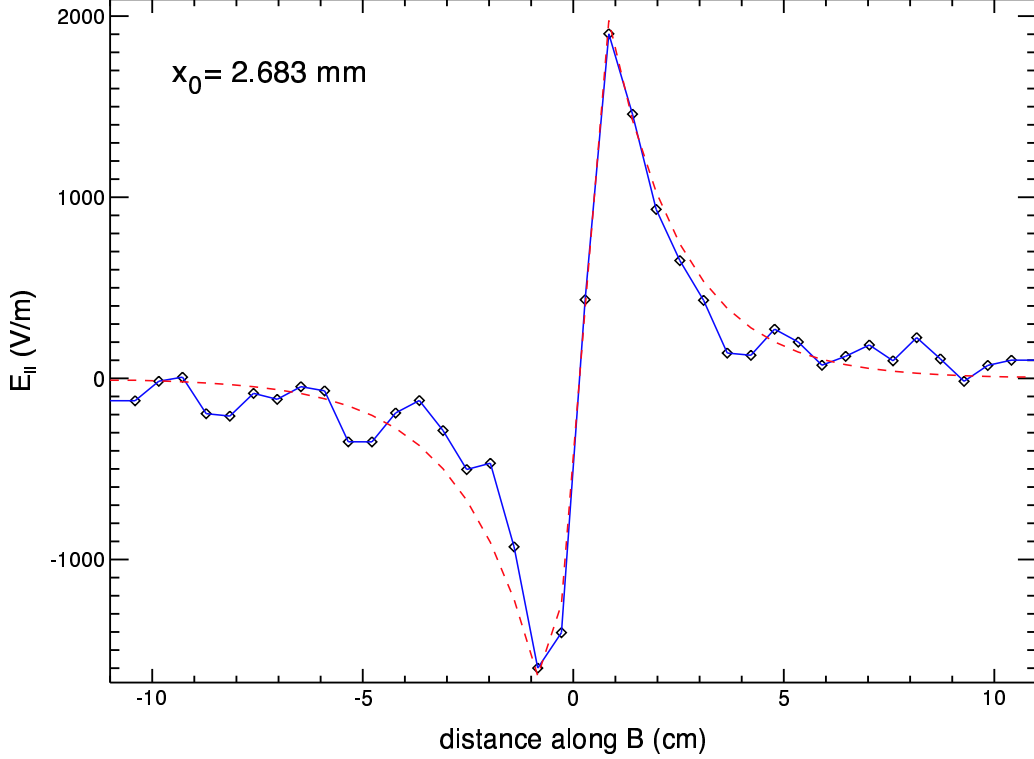


Figure 5-20: Example of a typical $E_{\parallel, pert}$ profile (solid) and its analytic fit (dashed), with the analytic function used for the fit given in Equation 5.3. The fit indicates that the electric field is described with different near-field linear slopes ($S_{lhs} = E_{lhs}/(a_0 + x_0)$, $S_{rhs} = E_{rhs}/(b_0 - x_0)$) and far-field exponential decay lengths (λ_{lhs} , λ_{rhs}) on either side of the zero-crossing location (x_0). Nonetheless, the total potential drop on either side of x_0 ($= - \int E_{\parallel} dx_{\parallel}$) is the same, approximately 43 V in this case.

in Figure 5-20. The fit indicates that the electric field is described with different near-field linear slopes ($S_{lhs} = E_{lhs}/(a_0 + x_0)$, $S_{rhs} = E_{rhs}/(b_0 - x_0)$) and far-field exponential decay lengths (λ_{lhs} , λ_{rhs}) on either side of the zero-crossing location (x_0). However, the total potential drop on either side of x_0 ($= - \int E_{\parallel} dx_{\parallel}$) is the same, approximately 43 V in this case.

Non-zero values of x_0 imply a non-zero parallel electric field at the injection location, which may be responsible for causing parallel asymmetries in jet-dominated plumes. Although results from deuterium plume modelling suggest that $x_0 \neq 0$, including this in the impurity plume simulations results in the appearance of a double-slope feature in the the simulated 1-D CIII TVC parallel emission profiles (e.g. see Figure 5-21, bottom panel, dashed curve) which is not observed in the experimental

data (the cause of this feature is discussed below). Therefore, for all simulations of experimental data x_0 is set equal to zero, i.e. the parallel electric field is assumed to be symmetric about the probe tip.

Tests have been conducted which indicate that the far-field behavior of the C^{+2} impurity ions is relatively insensitive to the structure of $E_{\parallel,pert}$, but is instead primarily dependent on the total potential drop experienced. This is illustrated in Figure 5-21, in which a comparison is given between results from two simulation runs where the total potential drop is the same but the structure of the electric field is quite different. In both runs $E_{lhs} = E_{rhs}$, $a_0 = b_0$, $\lambda_{lhs} = \lambda_{rhs}$, and $x_0 = 0$. Shown in the top panel are $E_{\parallel,pert}$ profiles for the two runs – in the first case (solid curve) the near-field linear slopes are twice as large as for the second case (dashed) and the far-field exponential decay lengths are twice as short. The resulting potential profiles are shown in the middle panel ($\Delta\phi_{tot} = 45$ V), while the 1-D CIII TVC parallel emission profiles are shown in the bottom panel. In the far field ($\gtrsim 2$ cm away from the injection location along \mathbf{B}), profiles from the two cases agree quite well over the full parallel extent of the plume. However, in the near field, the plume generated with a broader electric field profile (dashed) exhibits strong peaking, leading to the appearance of a double-slope feature in the emission profile.

The cause of the strong peaking, and thus the double-slope feature, is related to the structure of the C^{+2} parallel velocity profile. To understand why this is the case, consider the parallel transport of C^{+2} ions on the field line passing above the probe tip. For strong peaking of the parallel electric field, the electron density and C^{+2} parallel velocity are approximately constant on this field line (equal to their far-field values) as a result of the full potential drop occurring over very short distance. In general, the only sink for C^{+2} ions on this field line is ionization (neglecting effects of cross-field transport), and in this case the ionization lifetime is constant (since T_e is also constant on this field line). As a result of this constant sink, the parallel ion density (and therefore the parallel emission) decays with distance away from the injection location in a smooth fashion over the full parallel extent of the plume. This behavior occurs on all field lines in the emission volume over which $E_{\parallel,pert}$ exists, resulting in

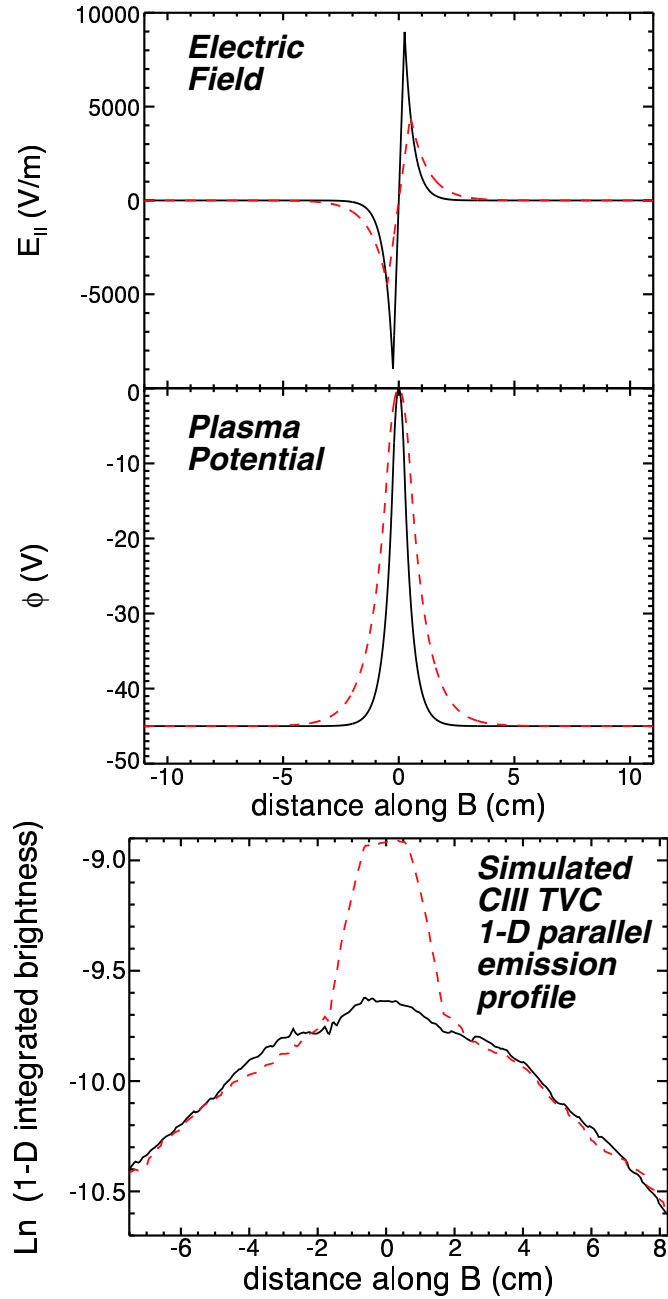


Figure 5-21: Comparison between simulation runs in which the total potential drop experienced by the impurity ions is the same but the parallel electric field structure is different. *Top panel:* $E_{||,pert}$ profiles for the two runs. In the first case (solid curve) the slopes are twice as large as for the second case (dashed) and the decay lengths are twice as short. *Middle panel:* Plasma potential profiles. $\Delta\phi_{tot} = 45$ V in both cases. *Bottom panel:* Simulated 1-D CIII TVC parallel emission profiles. Profiles from the two cases agree quite well in the far field ($\gtrsim 2$ cm away from the injection location along \mathbf{B}), indicating that the far-field emission structure is primarily determined by $\Delta\phi_{tot}$.

a smooth 1-D parallel emission profile. However, for a broad parallel electric field profile the results differ. In the far field, after the impurity ions have experienced the full available potential drop, the electron density and C^{+2} parallel velocity are again constant, resulting in a smooth decay of the parallel ion density. Conversely, in the near field, both the electron density and the parallel velocity vary with distance from the injection location (decreasing n_e , increasing v_{\parallel}). The combination of a sharper decrease in the parallel ion flux (relative to the case where $E_{\parallel,pert}$ is peaked) and an increasing parallel ion velocity with distance from the injection location results in a sharp decrease in the parallel ion density with distance in this region. Again, this behavior occurs on all field lines in the emission volume over which $E_{\parallel,pert}$ exists, leading to the appearance of a double-slope feature in the 1-D emission profile.

Simulation results also indicate that the presence of a finite parallel electric field (and thus a finite parallel ion velocity) at the injection location causes a strong peaking of the parallel ion density in the near field. The explanation is similar to the one presented above – for finite $E_{\parallel,pert}$ at the injection location, in the region $-a_0 \lesssim x_{\parallel} \leq x_0$ the electron density and parallel ion velocity exhibit strong variation, resulting in a sharp variation in the parallel ion density in the near field. Again, since near-field peaking is not observed experimentally, x_0 is taken to be zero in all simulations of experimental data. In addition, for experimental plume simulation only the total potential drop implied by deuterium plume modelling is used to determine the parallel electric field, since the structure of the field is found to have no impact on the far-field impurity ion behavior. In the simulation the field structure is then specified to ensure that near-field peaking is not observed in the resulting parallel emission profiles.

5.5.2 Jet plume results

Using the parallel electric field model described in section 5.5.1, simulations of the impurity ion jet have been conducted. An example of a typical CIII TVC jet plume is shown in Figure 5-22 (bottom panel). For this case, density and temperature profiles typical of the near SOL were inputted, and the electric field was specified such that $\Delta\phi_{tot} = 45$ V. In addition, the jet background/point source model was employed.

The experimental data which the numerical plume is meant to simulate is shown in the top panel of Figure 5-22. Recall that in this case the numerical plume is only simulating the jet component of the emission, whereas the experimental results contain both jet and sputter components (a full simulation is shown in Figure 5-25 – see section 5.6). Nonetheless, these results suggest that the simulation is able to approximately reproduce both the parallel and cross-field extent of the jet portion of the measured CIII emission.

A comparison between 1-D parallel emission profiles for the experimental data and the jet plume simulation is shown in Figure 5-23. The primary difference occurs in the near field, where the experimental data exhibit a more peaked structure due to the contribution of sputtering (and perhaps reflection off the probe head) to the emission. In the far field the simulation profile is broader than the experimental results, implying that the total potential drop used in the simulation is too large in this case. However, the contribution due to sputtering needs to also be included in the simulation before a full assessment can be made.

5.5.3 Unresolved issues for the jet model

There remain two unresolved questions regarding jet modelling in LIM. The first is related to the appearance of a double-slope feature in simulated 1-D CIII TVC emission profiles, which occurs when the inputted parallel electric field has a broad structure (e.g. see Figure 5-21). This feature is not observed in the experimental data, which suggests that the parallel electric field profile is peaked, and a peaked profile has therefore been used in the impurity plume simulations. However, results from D_2 recycling simulations suggest that the electric field profile arising from background ion recycling off the probe surface is in fact broad. This leads to an inconsistency in the jet model. Simulation studies indicate that the far-field behavior of the impurity ions is unaffected by this discrepancy, i.e. that only the total potential drop experienced by the impurity ions is important. In addition, since the experimental camera view of the near-field emission is corrupted by the presence of the probe, any difficulties which may be encountered in an attempt to simulate emission from this region are

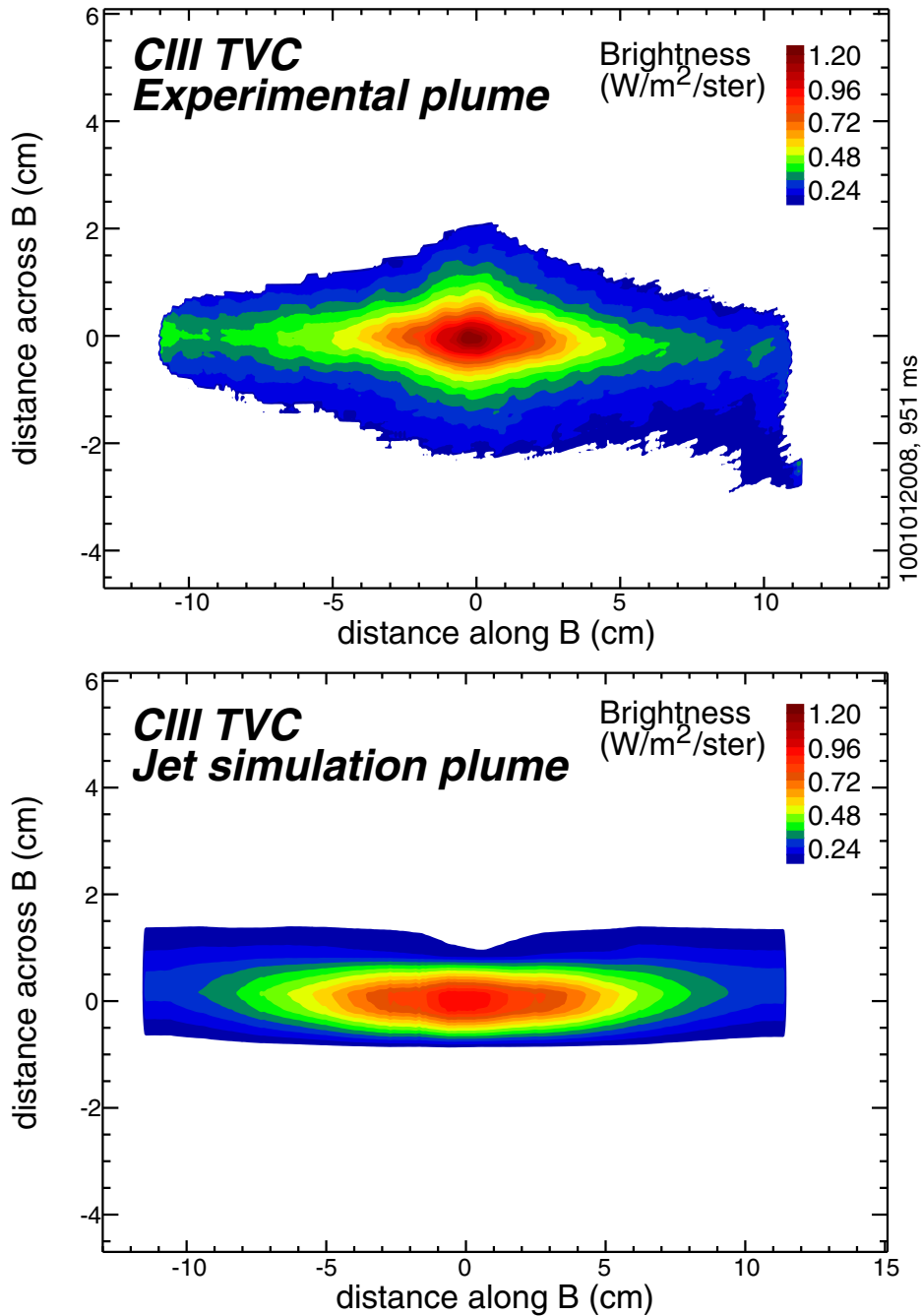


Figure 5-22: Comparison between an experimental CIII TVC plume generated in the near SOL and a simulation of the jet component of that plume. Density and temperature profiles typical of the near SOL were inputted to the simulation, and the electric field was specified such that $\Delta\phi_{tot} = 45$ V. The jet background/point source model was also employed. The results suggest that the simulation is able to approximately reproduce both the parallel and cross-field extent of the jet portion of the measured CIII emission.

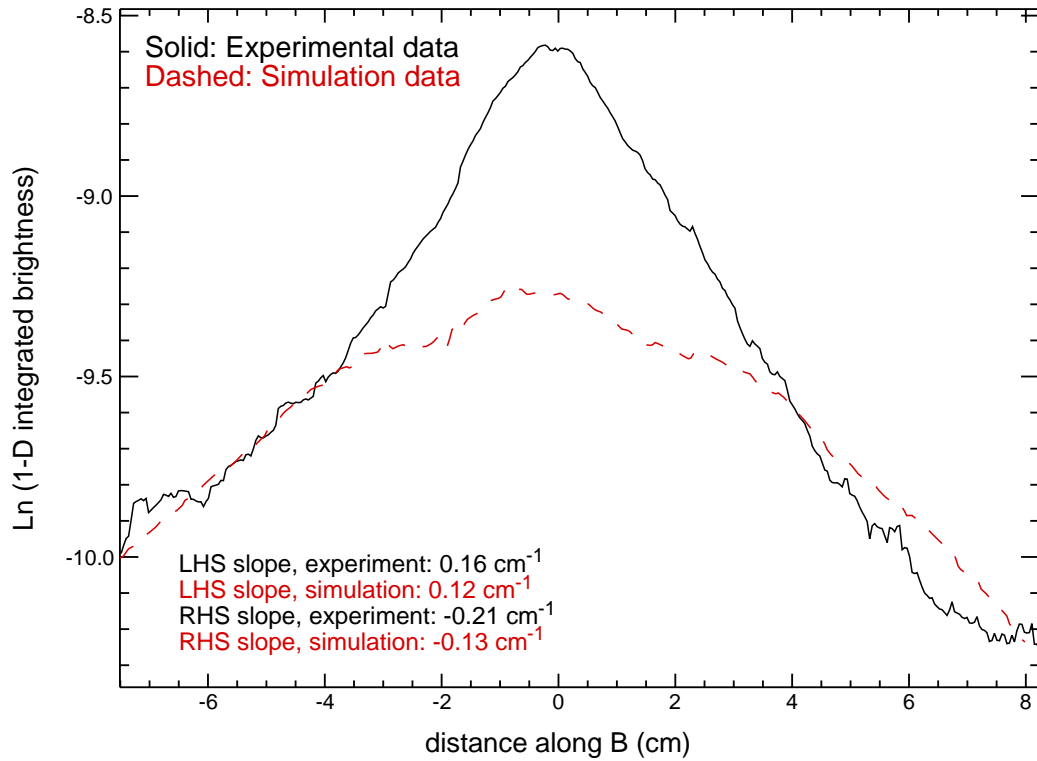


Figure 5-23: Comparison between 1-D CIII TVC parallel emission profiles for experimental and numerical plumes shown in Figure 5-22. Although the simulation profile is broader than the experimental results in the far field, the contribution due to sputtering needs to be included in the simulation before a full assessment can be made.

somewhat irrelevant, since simulated data are never compared to experimental data in the near field. Nonetheless, the discrepancy between the E_{\parallel} profile necessary for impurity plume simulation and the profile inferred from a D₂ recycling model suggests that the development of the jet model is incomplete.

The second unresolved issue is the cause of parallel asymmetries in experimental CIII TVC plumes generated in the near SOL. These asymmetries are generally in a direction consistent with impurity ions travelling *away* from the divertor (i.e. $\Delta v/\bar{v} < 0$, see Figure 3-21). One possible explanation is the presence of a parallel temperature gradient on the field lines on which the impurity ions are located. The force on an impurity ion due to this gradient is given by [62]:

$$F_{\nabla T} = \alpha_e \frac{dT_e}{dx_{\parallel}} + \beta_i \frac{dT_i}{dx_{\parallel}} \quad (5.4)$$

where α_e and β_i are constants which are a function of the impurity ion charge state and the impurity and background plasma ion masses, and T_i is the background plasma ion temperature. Since parallel thermal conduction for background ions is smaller than for electrons, it is expected that $|\nabla_{\parallel} T_i| \leq |\nabla_{\parallel} T_e|$. Assuming that $|\nabla_{\parallel} T_i| = |\nabla_{\parallel} T_e|$, for C⁺² ions the effective parallel electric field due to the thermal gradient force ($E_{\nabla T} = F_{\nabla T}/q$) is given by:

$$E_{\nabla T} \simeq 5.5 \frac{dT_e}{dx_{\parallel}} \quad (5.5)$$

Parallel gradients in the electron temperature also lead to parallel plasma potential variations and thus the formation of a parallel electric field. However, the resulting field is small relative to the effective field given by Equation 5.5, and thus provides only a minor correction ($\simeq 25\%$). For typical conditions in the near SOL, estimates obtained from a 2-point model for the flux tube power balance (section 3.2.2) suggest that the maximum value for $\frac{dT_e}{dx_{\parallel}} \lesssim 10$ eV/m, implying that the maximum parallel electric field felt by impurity ions due to the temperature gradient is ~ 50 V/m. This field is small compared to the values of E_{\parallel} necessary to explain the plume jet (~ 5 -10

kV/m). Therefore parallel temperature gradients are unlikely to be responsible for parallel asymmetries observed in the plume emission.

Systematic errors in the calibration vignetting field may also contribute to apparent asymmetries in the parallel plume emission. As indicated in Figure 2-13, TVC calibration factors for CIII emission decrease in value across the chip, since for a uniform input there is systematic increase in the camera response across the chip. However, if the vignetting field was in error such that the camera response to a uniform input is actually uniform across the chip, then such a systematic variation would lead to an asymmetry in the resulting calibrated emission. This asymmetry would be in a direction consistent with the observed asymmetry in typical plumes formed in the near SOL. To investigate the influence of such an error, the vignetting field was modified to represent a uniform response to a uniform input. An experimental CIII TVC plume generated in the near SOL was then re-calibrated using this field. A comparison of the 1-D CIII TVC parallel emission profiles for cases using the original and modified vignetting fields is shown in Figure 5-24. Although only a $\sim 20\%$ modification to the original vignetting field was necessary, the parallel asymmetry in the plume is noticeably affected. These results suggest that errors in the vignetting field may also play a role in determining the parallel asymmetry of plumes formed in the near SOL. However, based on calibration results there is no reason to believe that such a systematic error is present.

5.6 Plume modelling results

To simulate an experimental plume formed in the near SOL, components of the emission arising from a point source launch into a jet background and a sputter source launch into a non-jet background were summed together. An example of a simulated CIII TVC plume generated in this fashion is shown in Figure 5-25 (top panel). In this case the two components were added together with equal weight, i.e. it was assumed that the plumes which result from the point source launch and sputter source launch

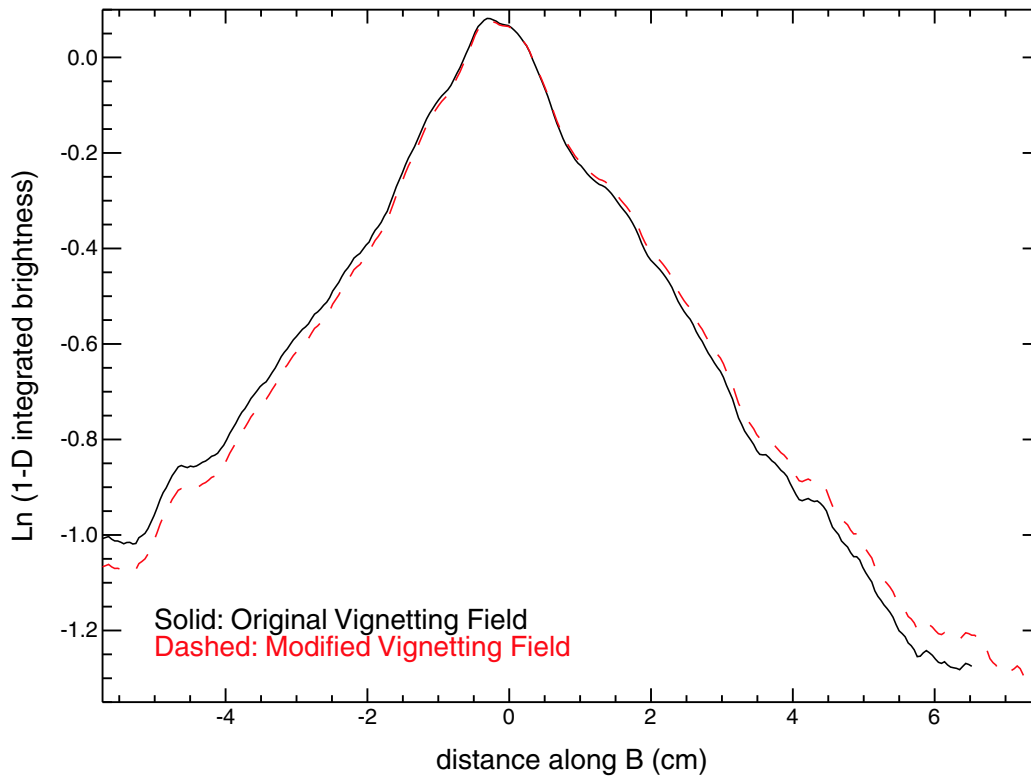


Figure 5-24: Comparison between 1-D parallel emission profiles for an experimental CIII TVC plume in which two sets of calibration factors were applied. In the first case (solid curve), the original vignetting field for this system was used, while in the second case (dashed) a modified field was used, in which the response of the system to a uniform input was made to be uniform. The results indicate that errors in the vignetting field may contribute to the observed parallel asymmetry in plumes formed in the near SOL.

contribute equally to the overall emission. The experimental data which this plume is meant to simulate is shown in Figure 5-22 (top panel).

There remains structure in the near field which has not been reproduced, i.e. the non-elliptical shape of the emission contours. This may be due to the inability of the numerical modelling to simulate the effect of reflections off the probe head. It may also be a result of errors introduced from neglecting the 3-D structure of the perturbation-induced parallel electric field. For example, a more accurate simulation of the experimental data would require that emission arising from a sputter source launch into a jet background be included – however, this emission component can only be correctly determined if the full 3-D structure of the parallel electric field (e.g. see Figure 5-19) is employed in the simulation, rather than a 1-D approximation for this field (Figure 5-20). While the 1-D approximation may be reasonable for use with the point source launch, it would clearly be unreasonable for use with the sputter source launch, since this launch has a wide cross-field extent. The influence of the true 3-D parallel electric field on sputter-launched impurities might be to stretch the plume emission contours along field lines passing near the probe tip while leaving emission contours on field lines away from the probe tip unaffected – a process that might generate the non-elliptical emission contours which are observed experimentally.

Nonetheless, both the cross-field width and the parallel extent of the simulated emission compare reasonably well with the experimental results. This is confirmed by comparing inverse decay lengths for the simulated 1-D parallel emission profile against the corresponding values for the experimental parallel emission profile (both profiles are shown in Figure 5-25, bottom panel), which are found to agree within $\simeq 10\%$, and by comparing values for the average cross-field width of the experimental and simulated plumes, which are found to agree within $\simeq 20\%$. These results suggest that the sputter and jet models for the plume emission provide appropriate descriptions for the physics of impurity ions injected into SOL plasmas via the FSP.

The majority of analysis presented in this chapter pertains to simulation of CIII emission. However, to further test the plume emission model, the variation of CII emission for cases in the near and far SOL is also investigated. Simulated 2-D CII

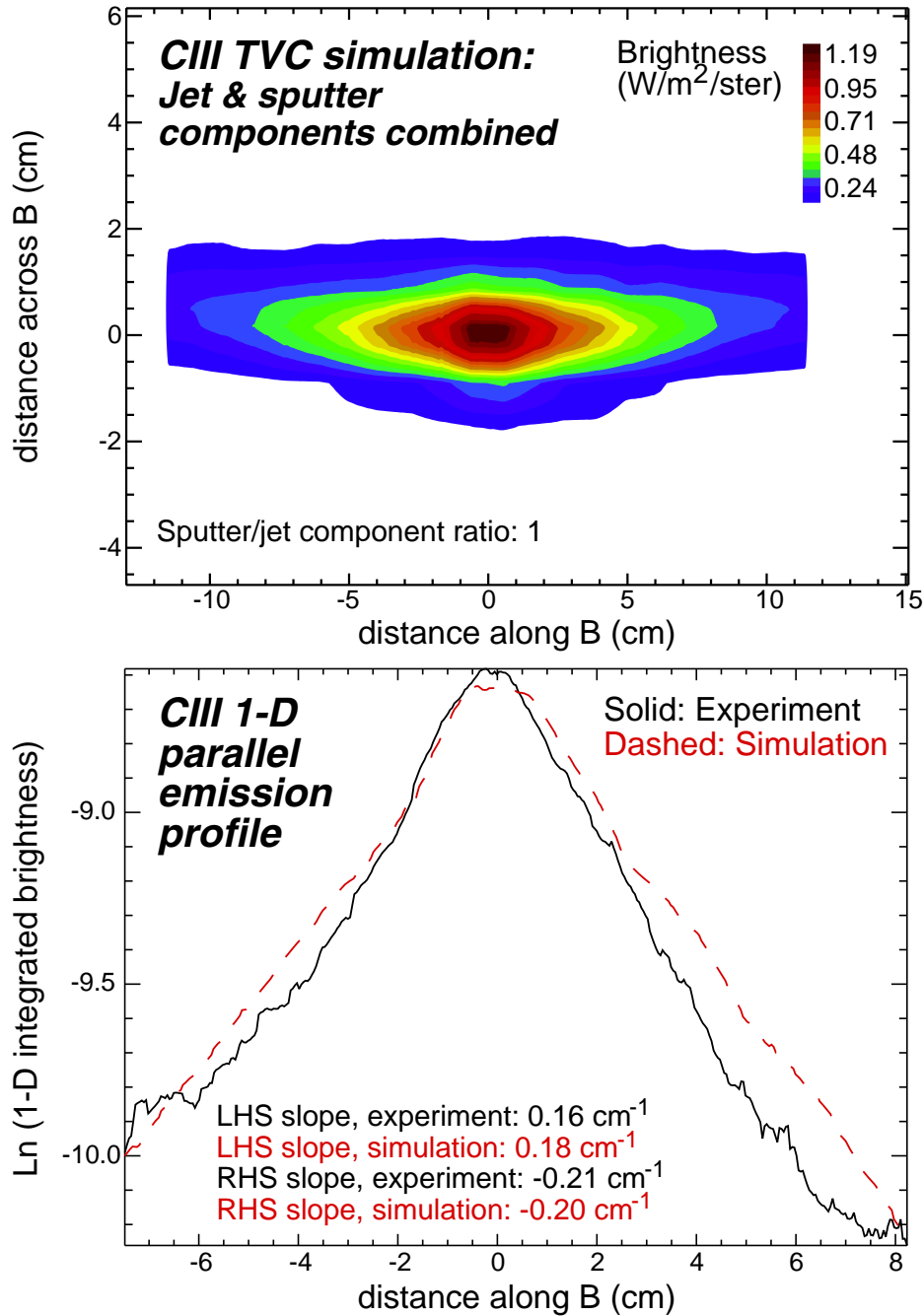


Figure 5-25: *Top panel:* Composite CIII TVC simulation plume, generated by summing together components arising from a point source launch into a jet background and a sputter source launch into a non-jet background with equal weight. In this case both the cross-field width and the parallel extent of the emission compare reasonably well with the experimental results (shown in Figure 5-22, top panel). *Bottom panel:* Comparison between experimental and simulated 1-D parallel emission profiles for the experimental plume shown in Figure 5-22 (top panel) and the simulated plume shown above. Values for the inverse decay lengths are found to agree within $\simeq 10\%$.

TVC plumes for both cases are shown in Figure 5-26. For the plume generated under conditions characteristic of the near SOL, a jet background/point source model was used, while for the plume generated under conditions typical of the far SOL a non-jet background/sputter source model was employed. The variation in plume size between these two cases is found to be consistent with experimental observations (e.g. see Figure 3-3). This confirms that LIM is accurately modelling both the parallel and cross-field dynamics of impurity ions injected into near and far SOL plasmas.

5.7 Plume variation with plasma conditions

To examine what other physics may be important for defining the spatial structure of the plumes, a number of sensitivity studies have been conducted to determine the effect of various background plasma parameters on the simulated emission structure. Results from this analysis are presented in this section.

5.7.1 Background profile variation

The effect of background profile variation (n_e, T_e) on the plume structure was investigated for plumes generated in conditions typical of the near SOL. A comparison between 2-D simulated CIII TVC plumes generated with and without radial density and temperature variation is shown in Figure 5-27. In both cases the poloidal drift is set to zero (i.e. $\mathbf{E}_r = 0$) and the jet background/point source model was used. Two major differences are apparent between these plumes: at constant density and temperature the plume exhibits a double-peaked structure and very little boomerang angle, while for varying background conditions the emission tends to peak at the injection location and exhibit a negative boomerang angle, which might be mistaken for a poloidal drift with $\mathbf{E}_r < 0$.

Emission centroids calculated from moment analysis of these simulated plumes are given in Figure 5-28. In the far field, the variation of emission centroid with distance is roughly linear for the plume formed under conditions of varying density

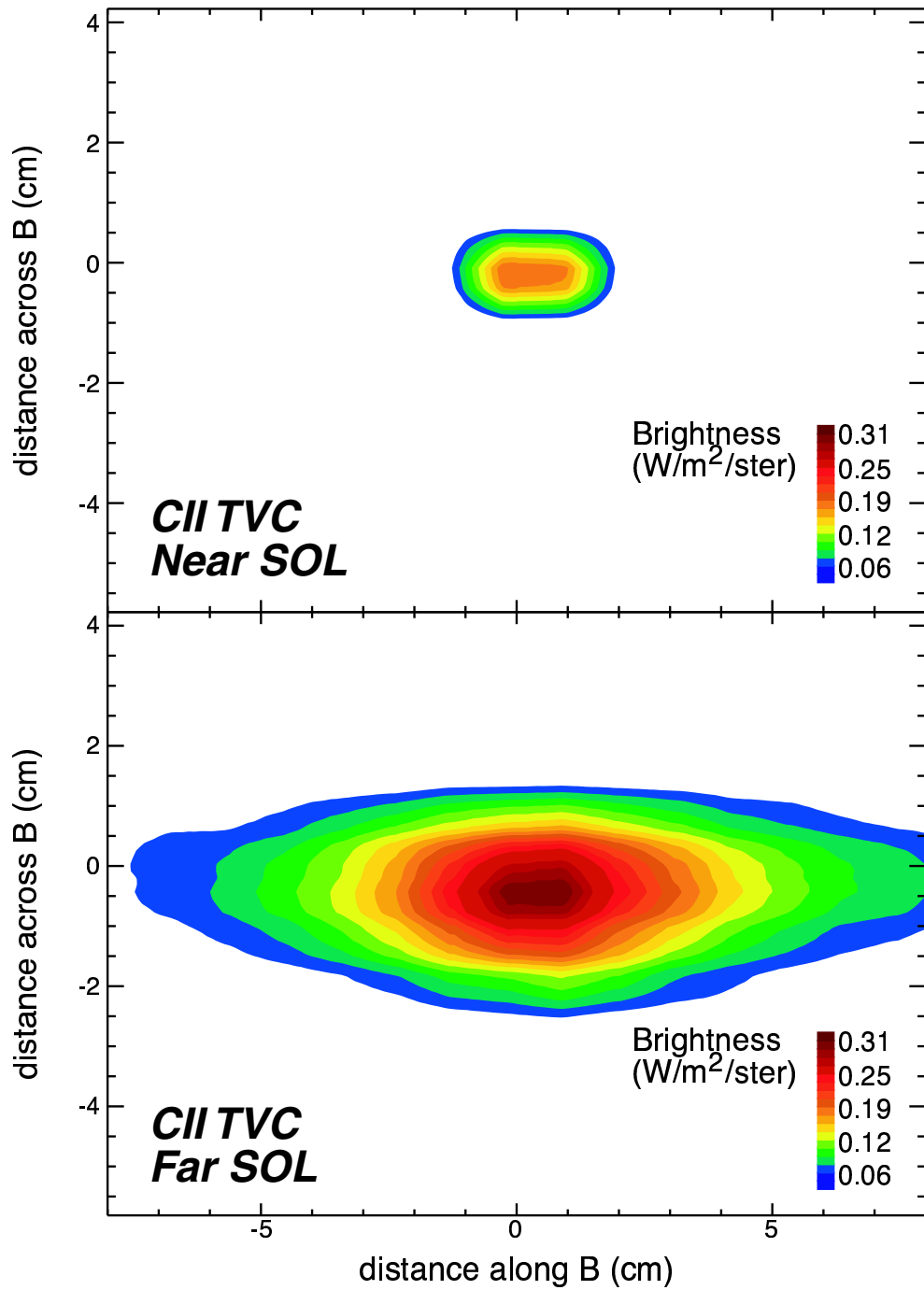


Figure 5-26: Comparison between simulated 2-D CII TVC plumes for cases in the near (*top panel*) and far (*bottom panel*) SOL. For the near SOL plume a jet background/point source model was used, while for the far SOL plume a non-jet background/sputter source model was employed. The variation in plume size is consistent with experimental observations (e.g. see Figure 3-3).

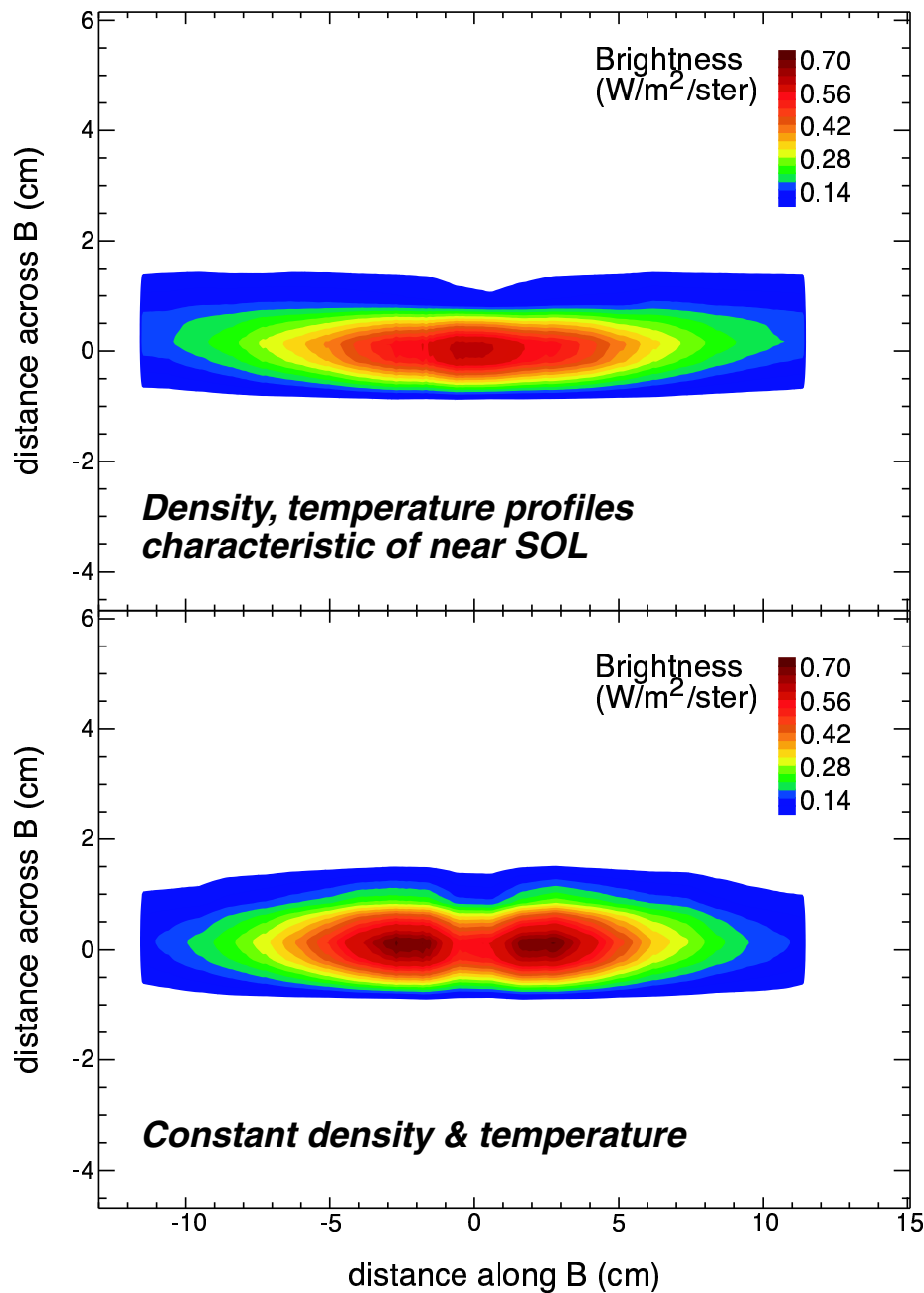


Figure 5-27: Comparison between 2-D simulated CIII TVC plumes generated in conditions typical of the near SOL. In both cases a jet background/point source model is employed. *Top panel:* Plume formed in a background plasma containing radial variation in the density and temperature profiles and $\mathbf{E}_r = 0$. *Bottom panel:* Plume formed in a background plasma with constant conditions and $\mathbf{E}_r = 0$. The plume formed under varying conditions exhibits a negative boomerang angle, which might be mistaken for a poloidal drift with $\mathbf{E}_r < 0$.

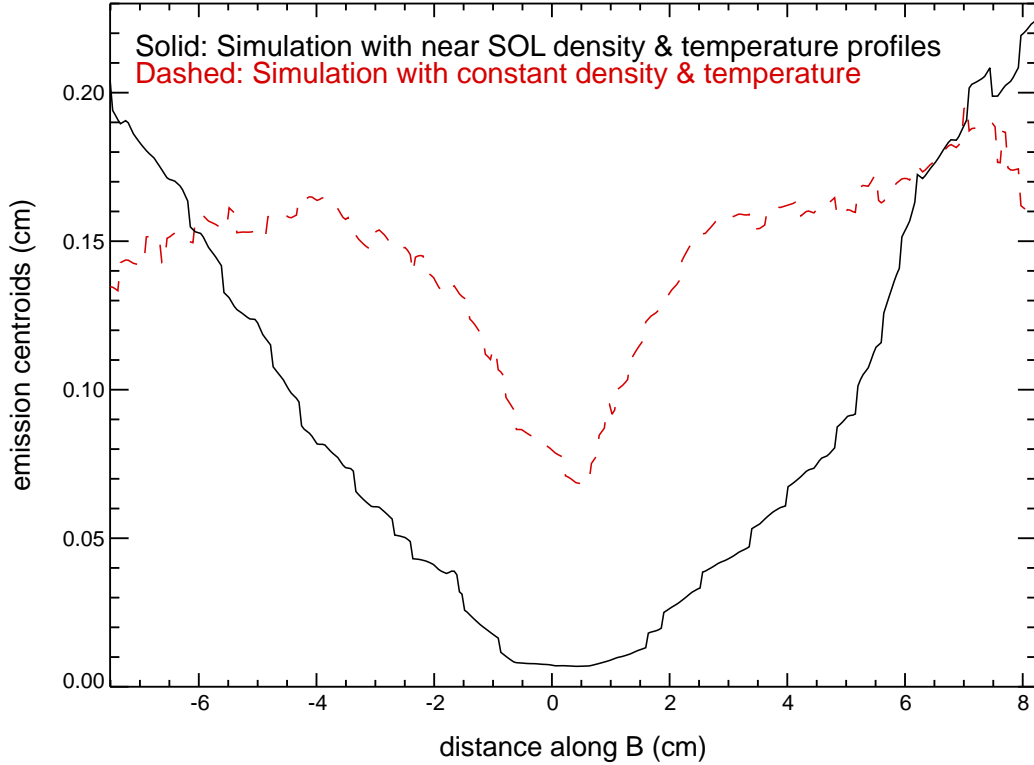


Figure 5-28: Emission centroid comparison between simulated CIII TVC plumes shown in Figure 5-27. In the far field, the variation of emission centroid with distance is roughly linear for the plume formed under conditions of varying density and temperature (solid curve), and roughly constant for the plume generated under conditions of constant density and temperature (dashed).

and temperature (solid curve), and roughly constant for the plume generated under conditions of constant density and temperature (dashed).

The double-peak structure observed in the constant density and temperature simulation is caused by the presence of the parallel electric field in the jet background model. In this case, the peaks in the impurity ion distribution occur at locations given approximately by the product of the ion velocity and the C^{+1} ionization lifetime, which itself is constant over the emission volume. Radial variation of the density and temperature results in a variation of the parallel mean-free path of impurity ions over the emission volume, effectively “smoothing out” peaks in the parallel distribution.

The boomerang angle observed for the plume generated under varying background conditions results from the radial skewness of impurity ion density. To understand

the cause of this skewness, consider a case in which impurity ions are born on a single flux surface, i.e. at a single radial coordinate. For constant D_{\perp} , these ions have an equal probability of diffusing onto flux surfaces in either radial direction. However, the ionization lifetime decreases for ions which diffuse to regions of hotter and denser plasma, and increases for ions which diffuse in the opposite direction. The result is a radial impurity density profile which is weighted towards regions of colder and less dense plasma, i.e. radially outward. In both the experiment and simulation the imaging system views are not orthogonal to flux surfaces (e.g. see Figure 2-6) – therefore the skewness appears as an emission boomerang in each view. For positive \mathbf{E}_r and normal field operation, the boomerang angle resulting from poloidal impurity ion flow is in the same direction as the angle resulting from ionization lifetime variations for the SVC, and in the opposite direction for the TVC.

5.7.2 Poloidal flow effects

The presence of poloidal flow in the simulation (i.e. resulting from $\mathbf{E} \times \mathbf{B}$ drifts) also leads to the formation of an emission boomerang, due to the poloidal skewness in impurity ion density which results from the flow. Since in both the experiment and simulation the imaging system views are not orthogonal to flux surfaces, the skewness appears as an emission boomerang in each view.

A comparison between CIII TVC emission centroids for simulation runs with and without poloidal flow is shown in Figure 5-29. In both cases a jet background/point source model was employed, and density and temperature profiles characteristic of the near SOL were used. With no poloidal flow (dashed curve) the boomerang angle is negative, as a result of radial variations in the ionization lifetime. When a poloidal flow profile (whose value is 2250 m/s at the injection location) is included (solid), the boomerang angle changes direction (a flow profile, rather than a constant flow, is necessary to ensure that the simulated plume is generated with a minimum number of tallies present in the poloidal boundary bins). For any given plume, the total boomerang angle therefore depends on both the density and temperature profile scale lengths and the magnitude of the poloidal flow. Assuming that ionization lifetime

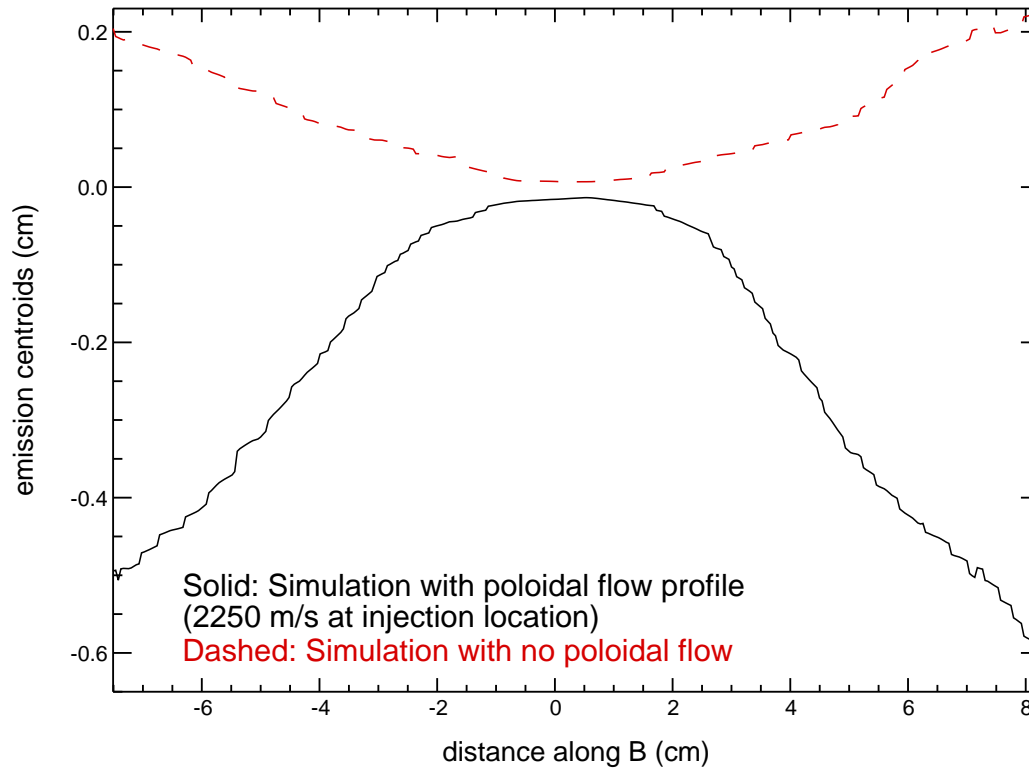


Figure 5-29: Emission centroid comparison between simulated CIII TVC plumes formed with and without poloidal flow. In both cases a jet background/point source model is employed. With no flow, the boomerang angle is negative, due to radial variation of the ionization lifetime. Including a poloidal flow profile, the boomerang angle changes direction. For any given plume, the total boomerang angle therefore depends on both the density and temperature profile scale lengths and the magnitude of the poloidal flow.

effects are properly taken into account, the plume boomerang angle may be directly related to radial electric field. Such analysis is discussed further in Chapter 6.

5.7.3 Parallel flow effects

A comparison between simulated CIII TVC 1-D parallel emission profiles for plumes generated under conditions typical of the near SOL is shown in Figure 5-30. In both simulations a jet background/point source model is employed. However, in one case (solid curve) no parallel flow is included in the simulation, while in the other case (dashed) a parallel Mach number of -0.18 (constant over the emission volume) is specified. Nonetheless, in both cases the parallel profiles are very similar, and very

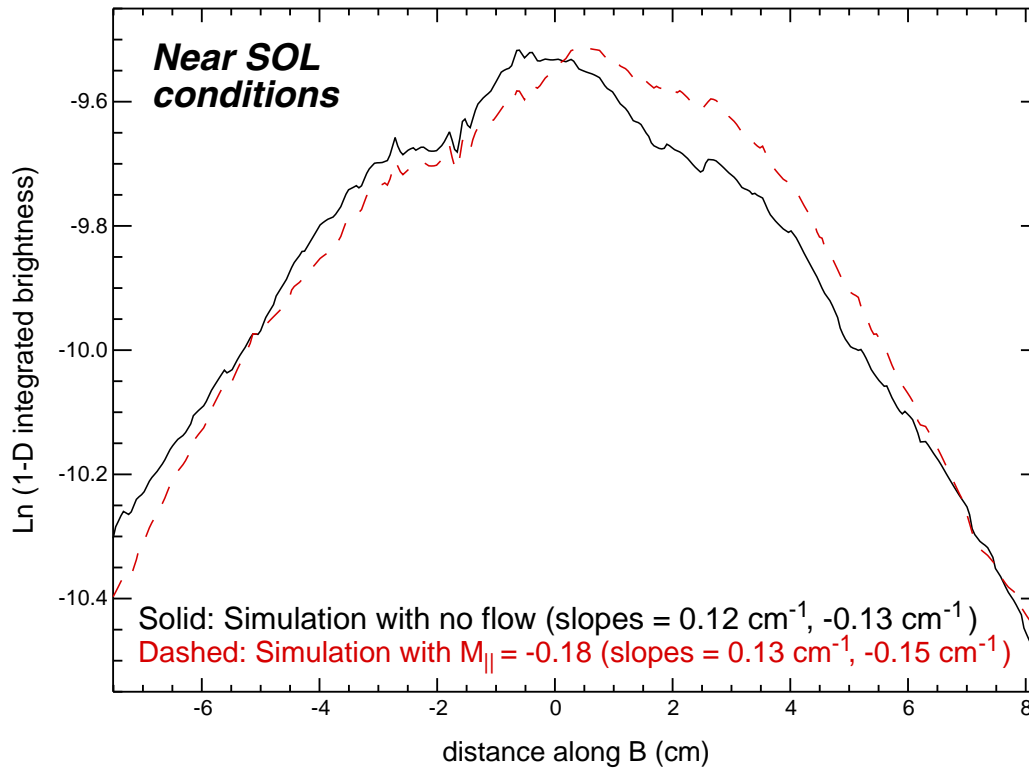


Figure 5-30: Comparison between simulated CIII TVC 1-D parallel emission profiles for cases with (dashed curve) and without (solid) background plasma flow. In both cases a jet background/point source model is employed, and density and temperature profiles characteristic of the near SOL are used. Profiles are similar for both cases, and very symmetric, indicating that background plasma flows have very little influence on the parallel structure of plumes formed in the near SOL.

symmetric. These results confirm that in the near SOL background plasma flows have very little influence on the parallel emission structure. This is consistent with results given in sections 3.1.2 and 3.3 (e.g. see Figure 3-21).

The results are quite different for simulations conducted with input conditions typical of the far SOL. A comparison between CIII TVC 1-D parallel emission profiles for plumes generated under such conditions is shown in Figure 5-31. For both cases a non-jet background/sputter source model was employed. Again, the solid curve represents the case with no parallel flow, and the dashed curve a case with $M_{\parallel} = -0.16$ (constant over the emission volume). The parallel emission profile is very symmetric when no flow is included, but a significant parallel asymmetry appears in the plume formed under conditions of background plasma flow. These results are consistent

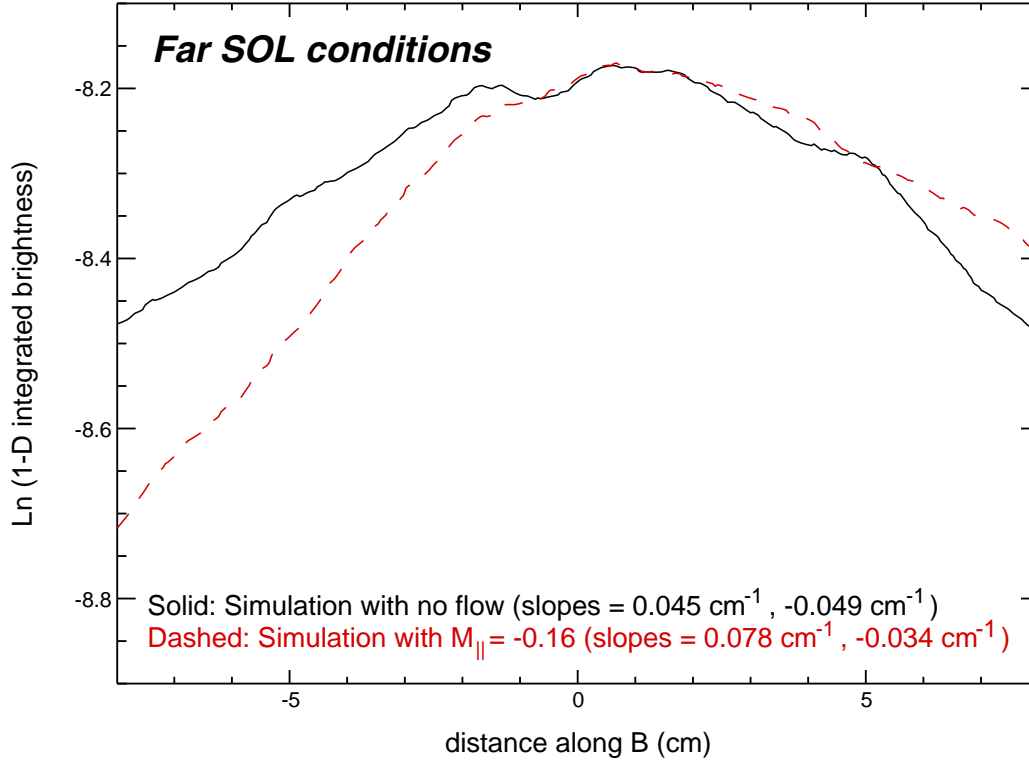


Figure 5-31: Comparison between simulated CIII TVC 1-D parallel emission profiles for cases with (dashed curve) and without (solid) background plasma flow. In both cases a non-jet background/sputter source model is employed, and density and temperature profiles characteristic of the far SOL are used. The profiles are very different for the two cases: with no flow, the profile is very symmetric, while with flow included the profile exhibits a strong asymmetry. These results are consistent with the experimental observations for plumes generated in the far SOL.

with the experimental observations for plumes generated in the far SOL. They also indicate that only in the far SOL can plume emission structure be used to infer the local parallel flow velocity. Analysis to extract v_{\parallel} from far SOL plume data is presented in Chapter 6.

5.7.4 Diffusion effects

In cases where sputtering may be weak and jet-like behavior dominates, diffusion effects may play an important role in setting the cross-field width of the plumes. The effect of cross-field diffusion on simulated jet-like plumes is therefore investigated in LIM.

A comparison between CIII TVC 1-D cross-field width profiles for simulation runs with different cross-field diffusivities is shown in Figure 5-32. D_{\perp} was set equal to 0.2 (dashed curve) and 1.0 (solid) m^2/s , while for both cases background density and temperature profiles characteristic of the near SOL were used as inputs and a jet background/point source model was employed. The profiles are found to be similar over the full parallel extent of the emission for both cases, as are the average values for the cross-field width ($D_{\perp} = 0.2 \text{ m}^2/\text{s}$, $\bar{w} = 4.1 \text{ mm}$; $D_{\perp} = 1.0 \text{ m}^2/\text{s}$, $\bar{w} = 4.2 \text{ mm}$). These results confirm that the value of diffusivity is unimportant in determining the cross-field plume structure even in cases where jet-like behavior dominates. For cases where sputtering is dominant diffusion is expected to play an even less important role – therefore the final results are insensitive to the choice of D_{\perp} used in the simulation.

5.8 Conclusions from plume analysis & simulation

From analysis presented in this chapter, a number of conclusions may be reached regarding the physics of impurity plume dispersal in the SOL of Alcator C-Mod. A summary of these results is given in this section.

An asymmetry exists between experimental plume emission seen from the side and top camera views which suggests that the impurity emissivity is extended along the probe axis. LIM has been used to investigate possible causes for this behavior, and results indicate that a substantial $\mathbf{E} \times \mathbf{B}$ drift of impurity ions down the probe axis is necessary to explain the experimental observations. It is also necessary to postulate that this drift transports bulk plasma down the probe axis. The effect is consistent with the formation of a carbon layer over a finite extent of the probe surface. However, the drift and surface layer formation models implemented in LIM are rather basic, and are not capable of exploring the influence of such $\mathbf{E} \times \mathbf{B}$ flow patterns on impurity and bulk plasma transport in a self-consistent way. Instead, a model has been developed to account for the contribution from sputtering of carbon deposited on the probe surface to the overall plume emission, where the e-folding

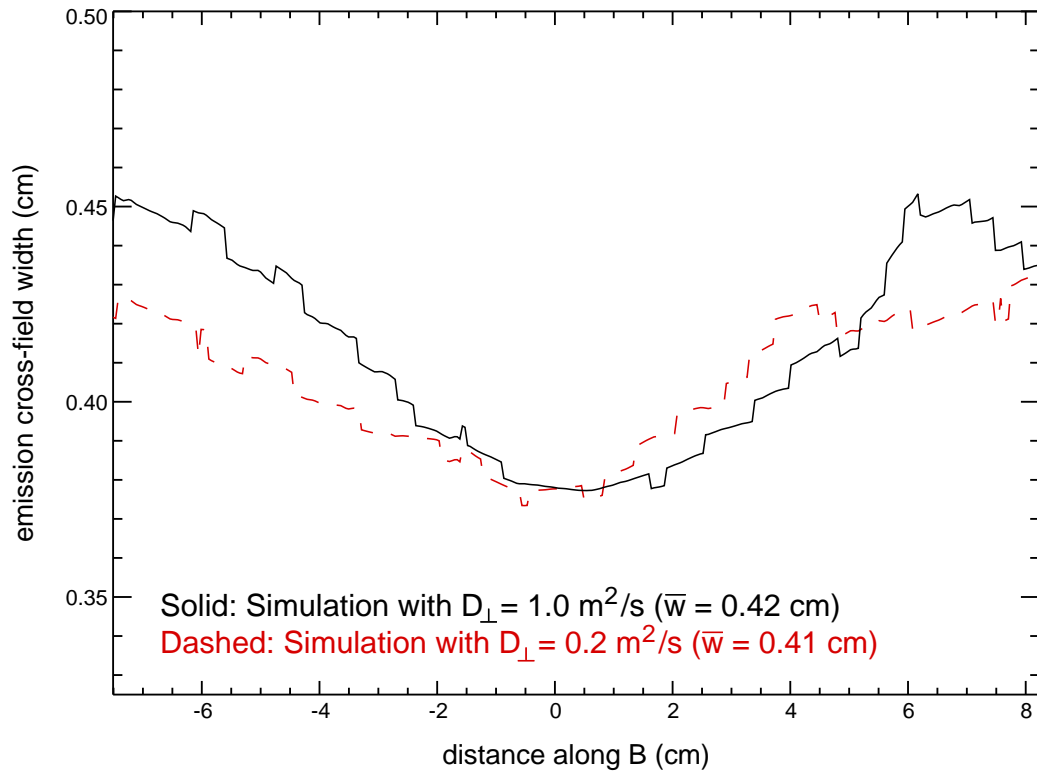


Figure 5-32: Comparison between simulated CIII TVC 1-D cross-field width profiles for cases with different cross-field diffusivities. D_{\perp} was set equal to 0.2 (dashed curve) and 1.0 (solid) m^2/s , while for both cases background density and temperature profiles characteristic of the near SOL were used as inputs and a jet background/point source model was employed. Results indicate that diffusion plays a small role in setting the cross-field width of the emission ($D_{\perp} = 0.2 \text{ m}^2/\text{s}$, $\bar{w} = 4.1 \text{ mm}$; $D_{\perp} = 1.0 \text{ m}^2/\text{s}$, $\bar{w} = 4.2 \text{ mm}$).

length (down the probe axis) for carbon sputtering is specified to provide the best match between simulation and experiment.

Results from sputter source modelling indicate that the cross-field extent of the experimental plumes can be explained in terms of carbon sputtering off the probe surface. For plumes generated in the far SOL, the launch energy distribution for carbon neutrals which is given by this model is also sufficient to describe the parallel transport of impurity ions. However, for plumes formed in the near SOL, unrealistic values for the surface binding energy are necessary to simulate the parallel extent of the experimental emission. In addition, emission contours exhibit a non-elliptical shape, indicative of strong parallel transport near the injection location (i.e. a “jet”). Simulation studies indicate that measurement errors in electron density and temperature are insufficient to resolve the discrepancies, suggesting the presence of a mechanism which provides parallel energy to impurity ions formed near the probe tip in the near SOL.

LIM has been configured to investigate if density perturbations arising from deuterium ion recycling off the probe surface may be responsible for the impurity plume jet. For conditions typical of the near SOL, the density at the probe tip resulting from ion recycling is found to be larger than the background electron density at this location. This result implies that impurity ions formed near the probe tip experience a potential drop of order the electron temperature over a distance corresponding to the parallel plume extent. This is consistent with potential drop estimates obtained from a ridge-line analysis of the experimental results (see Figure 3-19). A parallel electric field model has been implemented in LIM to confirm that the jet-like feature of the experimental plumes may be explained by this perturbation.

However, for conditions typical of the far SOL, simulation results indicate that the density at the probe tip arising from ion recycling off the probe surface is smaller than the background electron density at this location (see Figure 5-16). Thus, recycling perturbations are small in the far SOL, consistent with the observation of weak jet-like behavior for experimental plumes generated in this region.

In general, the effect of a density perturbation on the experimental plume results

is found to depend strongly on the value for the ionization mean-free path of the recycling deuterium neutrals. Simulations of the recycling perturbation were conducted for conditions typical of the near, intermediate, and far SOL in an attempt to reproduce this result (see Figure 5-17). While the dependence of the perturbation strength on the ionization mean-free path was found to be weaker in the simulation than in the experiment, the general trends between experiment and simulation are similar, suggesting that a recycling perturbation is a likely cause for the jet-like behavior of plumes generated in the near SOL.

The variation of impurity plume dispersal with background plasma parameters has also been investigated in LIM to determine the effect of various inputs on the simulated emission structure. For example, in the absence of background poloidal drifts (i.e. for $\mathbf{E}_r = 0$), variations in the background electron density and temperature over the emission volume result in the appearance of a boomerang angle in the emission structure. This is caused by the variation of the ionization rate, which results in a radial skewness in the impurity ion density distribution. At constant density and temperature and finite \mathbf{E}_r , a boomerang angle also appears in the emission structure as a result of the poloidal skewness in the impurity ion density distribution which is caused by impurity ion $\mathbf{E} \times \mathbf{B}$ drifts. For $\mathbf{E}_r > 0$ and normal field operation, the boomerang angles caused by ionization rate variations and by $\mathbf{E} \times \mathbf{B}$ drifts are in the same direction for the SVC and in the opposite direction for the TVC. Therefore, it is necessary to include effects arising from the spatial variation of the ionization rate when relating the emission boomerang angle to the radial electric field.

Sensitivity studies also suggest that the parallel asymmetries of simulated CIII plumes are unrelated to background plasma flows in the near SOL, but strongly dependent on these flows in the far SOL. These results are consistent with experimental observations. Finally, the effect of anomalous diffusion on the cross-field width of simulated CIII TVC plumes is found to be small, which suggests that the final results of experimental plume simulation are insensitive to the choice of D_{\perp} used in the simulation.

The results presented in this chapter allow for an assessment of impurity plume

dispersal as an edge plasma flow diagnostic in Alcator C-Mod. They suggest that in the near SOL CII and CIII plumes provide little information on background parallel flows, due to the poor collisional coupling between the background plasma and impurity ions in these charge states under these conditions. However, the localization of impurity ions in the jet does allow for a local measurement of the radial electric field. This is assuming that the parallel transport of impurity ions in the jet is correctly modelled in LIM – in this case the cross-field deviation of these impurities (determined from a ridge-line analysis) may be directly related to \mathbf{E}_r . Analysis used to obtain radial electric field estimates from plume emission ridge-line centroids is presented in Chapter 6.

In the far SOL, where jet-like behavior is weak, values for the local radial electric field cannot be inferred from plume emission structure (the plume boomerang angle is related to a volume-averaged \mathbf{E}_r in this case). However, collisional coupling between C^{+2} ions and the background plasma is strong in this region, suggesting that parallel asymmetries in the CIII plumes are directly related to background parallel flows. These asymmetries are modelled in LIM to determine plume emission volume-averaged values for v_{\parallel} . This analysis is also presented in Chapter 6.

Chapter 6

Plasma flows inferred from Impurity Plumes

From the development of a plume emission model, conditions under which the emission structure may be used to infer values for the parallel and cross-field plasma flow have been determined. Analysis conducted to obtain estimates of v_{\parallel} and \mathbf{E}_r from the plume data is presented in this chapter.

6.1 Jet-inferred $\mathbf{E} \times \mathbf{B}$ flows

Ridge-line analysis has been employed to estimate the average parallel velocity (\bar{v}) of impurity ions in the jet. The use of this analysis is based on the assumption that the peak brightness at each parallel coordinate in the 2-D plume image is dominated by emission from the jet. This is of course an approximation – for example, for the TVC imaging system the signal on each pixel results from integration through an emission volume which is vertically elongated, and thus emission from regions outside of the jet is expected to contribute. However, in the limit where the plumes are dominated by jet-like behavior, this approximation is valid. An example of ridge-line analysis conducted for an experimental CIII TVC plume is shown in Figure 3-18.

Estimates for the jet boomerang angle (θ_b) may also be determined from a ridge-line analysis. The average cross-field velocity of impurity ions in the jet is then

calculated using $v_{\perp} = \bar{v} \tan(\theta_b)$. Assuming that the cross-field impurity ion velocity is related to the radial electric field, values for \mathbf{E}_r are given by the product $v_{\perp} B$ (where B is the magnetic field strength at the injection location). Using this analysis, estimates for the radial electric field have been obtained from the jet emission structure of impurity plumes generated in the near SOL. Results from numerical modelling indicate that the density perturbation thought to be responsible for the impurity ion jet is spatially localized (see Figure 5-12), suggesting that the inferred values of \mathbf{E}_r are also localized. Thus, these results may be directly compared with local radial electric field measurements obtained from scanning probe data.

However, radial variations in the local ionization rate need to be considered when relating the boomerang angle to \mathbf{E}_r , since these variations may also contribute to the measured angle (e.g. see Figure 5-28). Although measurements obtained from the impurity ion jet are localized, gradient scale lengths for the electron density and temperature in the near SOL are small enough to suggest that ionization rate variations may still be important. To assess their effect, a simple 1-D Monte Carlo code has been developed in IDL which approximates the 1-D integrated radial density distribution resulting from the existence of finite n_e and T_e gradients at the gas injection location (in this case it is unnecessary to follow the transport of impurity ions in the flux surface, since n_e and T_e are constant in the flux surface). In this code, C^{+2} ions are launched with a Gaussian distribution (characterized by a 1 mm width) from the probe tip, under the assumption that the ionization mean-free paths for C^0 and C^{+1} are much smaller than the injection nozzle diameter for conditions typical of the near SOL. At each time step a random number is drawn to determine whether the ion which is being followed is ionized to the next charge state – if so, it is lost from the system (and the next ion is launched), but if not its position is incremented by a constant step size, with another random number being drawn to determine the direction of motion (radially inward vs. radially outward). Tallies kept in each computational cell record the number of times that an impurity ion is present in that cell at the end of each time step, and represent the ion distribution. For a typical case the time step is 5 ns, the cell size is 0.5 mm, the cross-field step size is

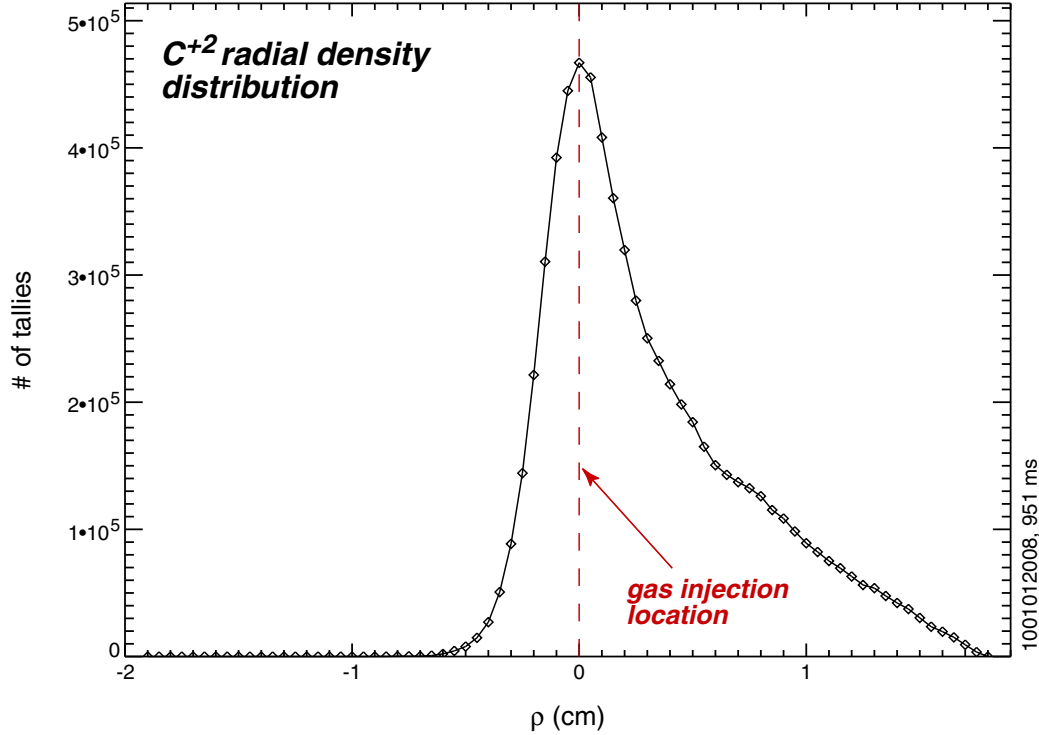


Figure 6-1: Plot of the 1-D integrated radial C^{+2} density distribution resulting from the presence of finite n_e and T_e gradients at the gas injection location. The ion distribution is obtained using a simple Monte Carlo code developed in IDL. The distribution is skewed towards regions of lower density and temperature (i.e. larger ρ) as a result of variations in the ionization rate.

0.1 mm, and 10,000 ions are launched. An example of resulting 1-D distribution is shown in Figure 6-1.

The boomerang angle which results from this distribution is determined by including effects of parallel ion transport. In this case, the ion density variation along field lines is assumed to be exponential, with the exponential decay length at each radial coordinate being equal to the local mean-free path. The mean-free path is in turn calculated from the product of the parallel ion velocity and the local ionization time, with the parallel velocity equal to the velocity of impurity ions in the jet (\bar{v}), determined from a ridge-line analysis of the experimental data. A 2-D contour plot of the C^{+2} density distribution (in (x_{\parallel}, ρ) space) constructed using the radial profile given in Figure 6-1 and the above approximations for the parallel distribution is shown in Figure 6-2. Results indicate that the boomerang angle correction due to effects of ionization rate variation is small ($\simeq 1^\circ$). Nonetheless, these corrections are

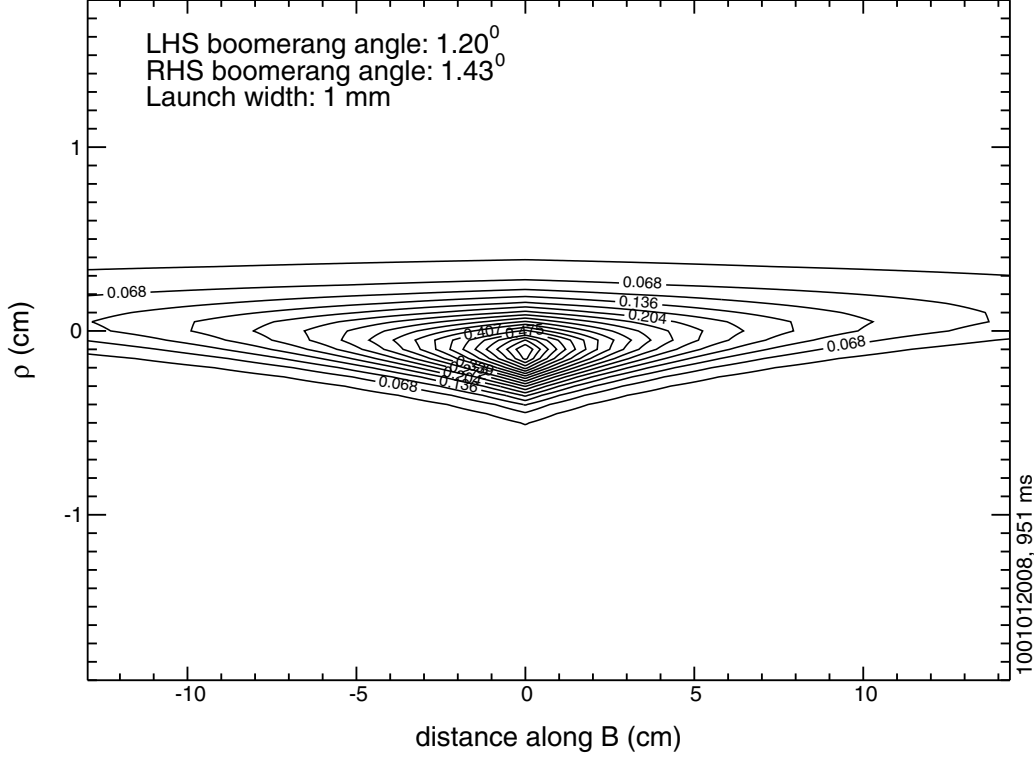


Figure 6-2: 2-D contour plot of the C^{+2} density distribution resulting from the presence of finite n_e and T_e gradients at the gas injection location. This plot is constructed using the radial ion distribution shown in Figure 6-1, and a parallel ion distribution determined by assuming an exponential variation for the ion density along \mathbf{B} . The results indicate that corrections to the ridge-line boomerang angle due to effects of ionization rate variation are small.

accounted for in the calculation of the cross-field impurity ion velocity, resulting in more accurate estimates for \mathbf{E}_r .

6.1.1 Comparison with probe-inferred $\mathbf{E} \times \mathbf{B}$ flows

Using ridge-line analysis to determine the plume boomerang angle (and correcting for effects of ionization rate variation), plume-inferred values of the radial electric field ($\mathbf{E}_{r,plume}$) have been obtained for a number of discharges. These values are compared to probe measurements in order to assess the accuracy of both the plume and probe results. Following analysis presented in reference [36], probe-inferred values for the radial electric field are obtained from two separate calculations: one from the radial gradient in the inferred plasma potential profile ($\mathbf{E}_{r,ps}$), and one from the poloidal propagation of plasma fluctuations ($\mathbf{E}_{r,pf}$).

The plasma potential is calculated from floating potential and electron temperature measurements using a standard model for the probe sheath:

$$V_{p,s} = V_f + \alpha T_e \quad (6.1)$$

$$\alpha = -0.5 \ln \left[\frac{2\pi m_e}{m_D} \frac{2}{1 - \delta^2} \right] \quad (6.2)$$

where V_f is the floating potential, m_e and m_D are the electron and deuteron masses, respectively, and δ is the coefficient for electron-induced secondary electron emission from the probe surface. For typical SOL conditions values of α are $\simeq 2.5$ - 2.8 . The radial electric field is then determined from the radial gradient of the plasma potential, i.e. $\mathbf{E}_{r,ps} = -\nabla_\rho V_{p,s}$.

The radial electric field may also be determined from a measurement of the poloidal propagation velocity (v_{ph}) of edge plasma fluctuations. These fluctuations are expected to propagate with a superposition of $\mathbf{E} \times \mathbf{B}$ ($v_{\mathbf{E} \times \mathbf{B}}$) and drift-wave (v_d) velocities [73]:

$$v_{ph} = v_{\mathbf{E} \times \mathbf{B}} + v_d \quad (6.3)$$

$$v_d \approx \frac{T_e}{B} \frac{\nabla_\rho n_e}{n_e} + \beta \frac{\nabla_\rho T_e}{B} \quad (6.4)$$

where β is a constant accounting for the contribution of finite electron temperature fluctuations to the drift-wave velocity, and is of order $\sim \tilde{T}_e n_e / \tilde{n}_e T_e$. For typical SOL conditions, the contributions of v_d and $v_{\mathbf{E} \times \mathbf{B}}$ to v_{ph} are comparable. In addition, both experiments [50],[4] and modelling [76] indicate that β is near unity in the edge plasma. However, to investigate the sensitivity of the results to this parameter, calculations are performed for both $\beta = 0$ and $\beta = 1$.

From probe measurements of the fluctuation propagation velocity and of local gradients in the electron density and temperature, values for the $\mathbf{E} \times \mathbf{B}$ velocity ($v_{\mathbf{E} \times \mathbf{B},pf}$) may be inferred using Equations 6.3 and 6.4. In this case, the comparison between plume-inferred results and probe measurements is made by converting plume-inferred values of \mathbf{E}_r to $\mathbf{E} \times \mathbf{B}$ velocities ($v_{\mathbf{E} \times \mathbf{B},plume}$) using the local value of the

magnetic field strength.

A comparison between $\mathbf{E}_{r,plume}$ and $\mathbf{E}_{r,ps}$ is shown in Figure 6-3 for a number of ohmic L-mode discharges. Probe measurements from both the gas-injecting scanning probe (FSP) and a horizontal fast-scanning probe (ASP) located above the midplane of Alcator C-Mod are given. The discharge conditions span the range of line-average densities from $0.8 \times 10^{20} \text{ m}^{-3} < \bar{n}_e < 2.4 \times 10^{20} \text{ m}^{-3}$, plasma currents from $0.5 \text{ MA} < \mathbf{I}_p < 1.0 \text{ MA}$, and toroidal magnetic fields from $4 \text{ T} < \mathbf{B}_\phi < 6 \text{ T}$. For each discharge considered, $\mathbf{E}_{r,ps}$ data are plotted from *each full probe scan* in ρ -space, whereas $\mathbf{E}_{r,plume}$ values are generated only at the peak insertion of the FSP (i.e. during plume formation). Some of the variation in \mathbf{E}_r values obtained from the probe measurements can be related to the different discharge conditions [36]. Overall, the results indicate that values of radial electric field inferred from the two measurements are of the same magnitude, but that the radial variation of the inferred \mathbf{E}_r profiles is different. For example, while values for $\mathbf{E}_{r,plume}$ are observed to be positive over the full SOL ($\rho > 0$), indicating that \mathbf{E}_r only changes sign inside the separatrix, data from both the FSP and the ASP suggest that the radial electric field changes sign in the SOL, near $\rho \sim 1\text{-}3 \text{ mm}$. In addition, \mathbf{E}_r profiles measured by the probes exhibit a steeper gradient near the separatrix relative to the plume-inferred results. However, this apparent discrepancy may be a result of the lack of plume data near the separatrix. Nonetheless, the comparison between $\mathbf{E}_{r,plume}$ and $\mathbf{E}_{r,ps}$ suggests the possibility of an error in either the plume or probe measurements.

Comparisons between $v_{\mathbf{E} \times \mathbf{B},plume}$ and $v_{\mathbf{E} \times \mathbf{B},pf}$ for the same set of discharges are shown in Figures 6-4 and 6-5. Again, data from both the FSP and ASP are given. For each discharge considered, $v_{\mathbf{E} \times \mathbf{B},pf}$ data are plotted from *each full probe scan* in ρ -space, whereas $v_{\mathbf{E} \times \mathbf{B},plume}$ values are generated only at the peak insertion of the FSP (i.e. during plume formation). For $\beta = 0$ (Figure 6-4), plume results appear to be in better agreement with the ASP data, while for $\beta = 1$ (Figure 6-5) $v_{\mathbf{E} \times \mathbf{B},plume}$ values agree more favorably with the FSP results. The best level of agreement between plume-inferred and probe-inferred values for $v_{\mathbf{E} \times \mathbf{B}}$ is observed for FSP data with $\beta = 1$ (Figure 6-5, top panel). This is not surprising, since the plumes are generated

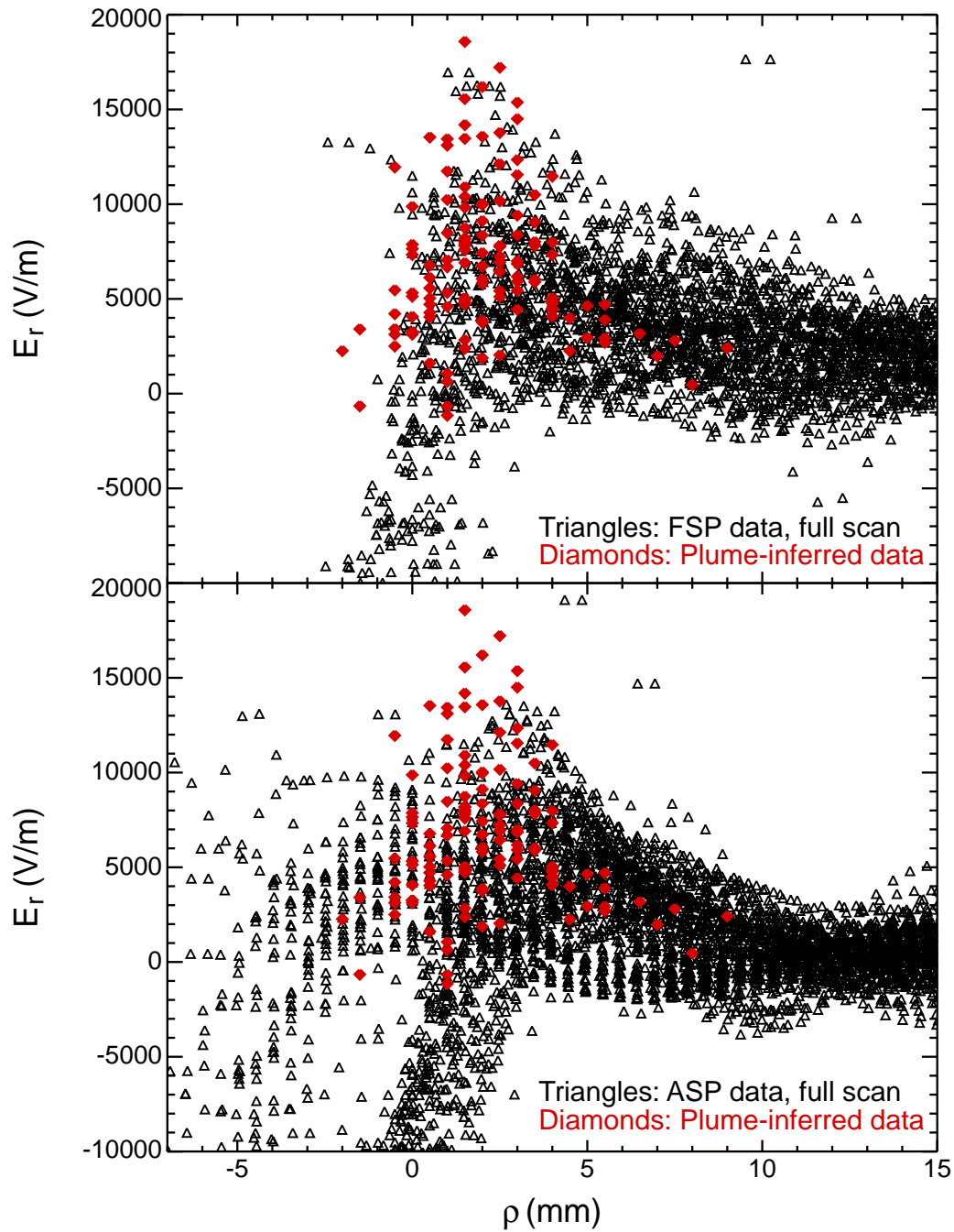


Figure 6-3: Comparison between radial electric field values obtained from plume data and probe data for a number of ohmic L-mode discharges. The latter values are calculated from the radial gradient of the inferred plasma potential (Equation 6.1). Results indicate that values of \mathbf{E}_r inferred from the two measurements are of the same magnitude, but that the radial variation of the inferred \mathbf{E}_r profiles is different. This suggests the possibility of an error in either the plume or probe measurement.

at the same location as the FSP measurements, and (as already noted) since relative electron density fluctuations (\tilde{n}_e/n_e) and relative electron temperature fluctuations (\tilde{T}_e/T_e) are thought to be approximately equal in the edge plasma. Nonetheless, in all cases, the radial variation of the $\mathbf{E} \times \mathbf{B}$ velocity profile is similar for both plume and probe measurements – for instance, each profile exhibits a peak in the velocity near $\rho = 2$ mm, and remains relatively broad near the separatrix. These results suggest an error in the measurement of \mathbf{E}_r calculated from a probe-sheath model ($\mathbf{E}_{r,ps}$).

However, there are discrepancies between the plume-inferred and probe-inferred values for the $\mathbf{E} \times \mathbf{B}$ velocity. For example, values for $v_{\mathbf{E} \times \mathbf{B},pf}$ exhibit a strong variation with collisionality [36], which is not detected in the plume results. Unfortunately, $v_{\mathbf{E} \times \mathbf{B},plume}$ measurements are also concentrated in a narrow region of ρ -space, due to both the difficulty in generating plumes inside the separatrix, and because plumes formed further out in the scrape-off layer cannot be used to infer local values of \mathbf{E}_r . As a result, a systematic comparison of $\mathbf{E} \times \mathbf{B}$ velocity profiles inferred from the two measurements (plume & probe) cannot be made at either smaller or larger values of ρ . Nonetheless, the plume results suggest that measurement of the poloidal propagation velocity of edge plasma fluctuations may be a reliable means of determining the local value of radial electric field in the SOL.

Estimates for the radial electric field have also been made for plumes formed during Enhanced D_α (EDA) H-mode. Plume emission has been generated both inside and outside of the Quasi-Coherent (QC) mode layer, and results for the plume boomerang angle suggest that the radial electric field changes sign inside the mode layer (e.g. see Figure 3-8). Using ridge-line analysis, the values of \mathbf{E}_r are estimated to be 4.3 kV/m outside of the mode layer ($\rho = 3.64$ mm) and -3.3 kV/m inside of the mode layer ($\rho = 1.21$ mm). In this case, radial electric field values inferred from a probe-sheath model are 5.1 kV/m and 5.4 kV/m outside and inside of the QC mode layer, respectively. These results indicate that probe measurements do not get the sign of \mathbf{E}_r correct in the mode layer, suggesting that plumes may provide the only means of measuring radial electric field in this region. In addition, the plume results suggest a strong radial electric field gradient in the vicinity of the QC mode, of order ~ 3.1 V/mm².

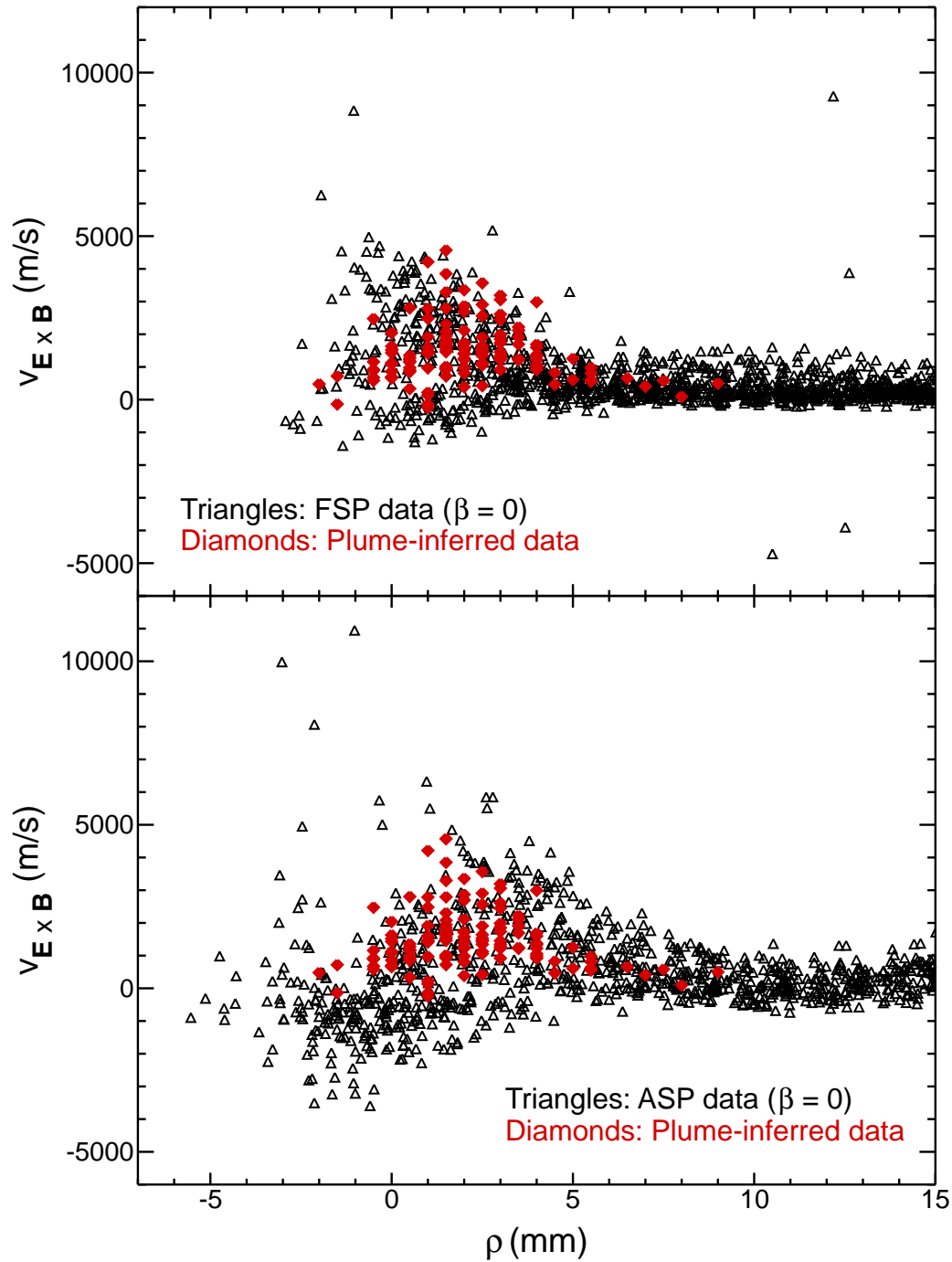


Figure 6-4: Comparison between $\mathbf{E} \times \mathbf{B}$ velocities obtained from plume and probe data (both FSP and ASP) for a number of ohmic L-mode discharges. The latter values are calculated by subtracting the drift-wave velocity (v_d) from the poloidal propagation velocity of edge plasma fluctuations (v_{ph}). In this case effects of finite temperature fluctuations are neglected (i.e. $\beta = 0$ in Equation 6.4). The results suggest better agreement between plume-inferred values and the ASP data, although the velocity profile comparison is similar for both ASP and FSP results.

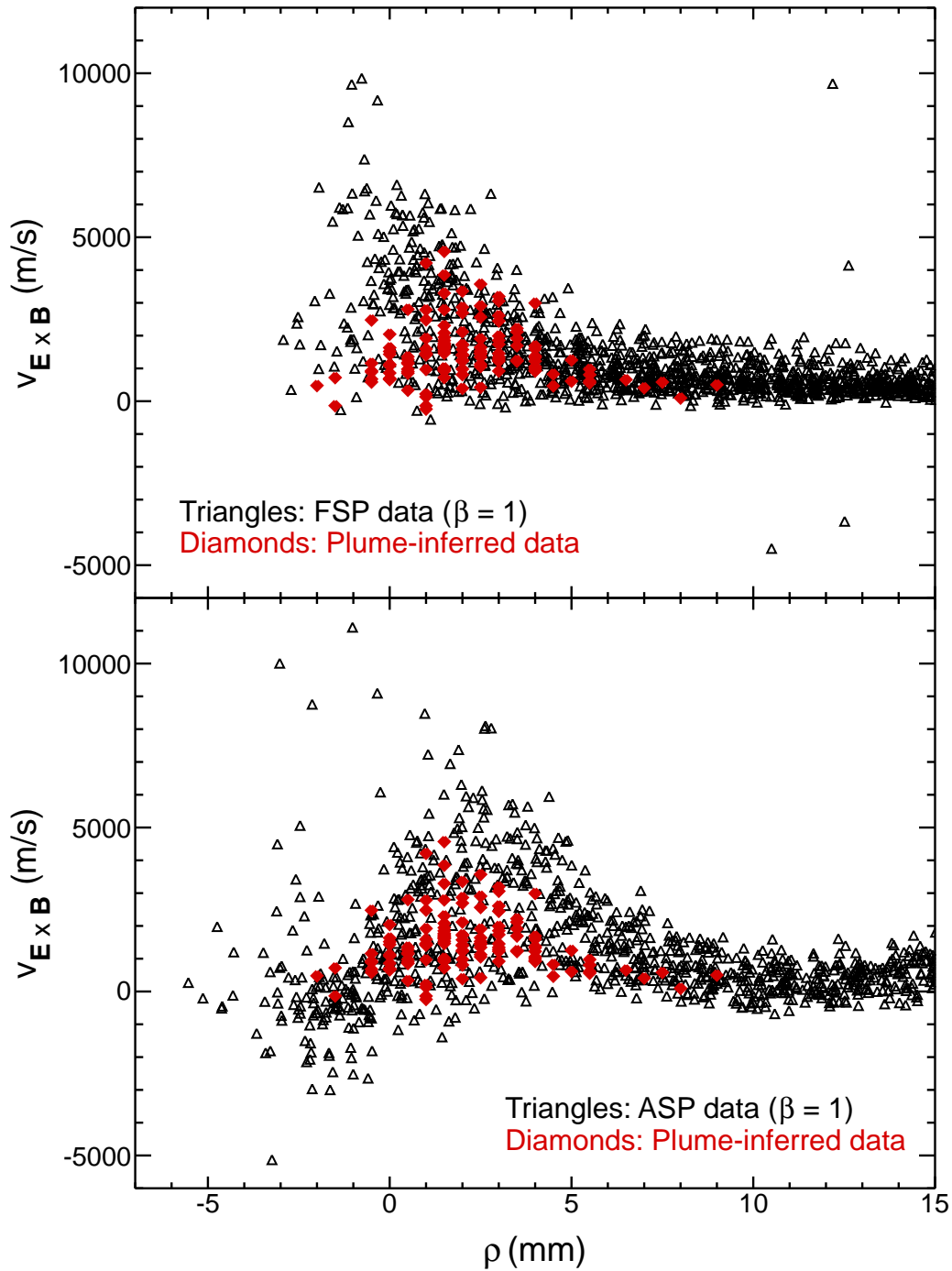


Figure 6-5: Comparison between $\mathbf{E} \times \mathbf{B}$ velocities obtained from plume and probe data (both FSP and ASP) for a number of ohmic L-mode discharges. The latter values are calculated by subtracting the drift-wave velocity (v_d) from the poloidal propagation velocity of edge plasma fluctuations (v_{ph}). In this case effects of finite temperature fluctuations are included (using $\beta = 1$ in Equation 6.4). For $\beta = 1$ the results suggest better agreement between plume-inferred values and the FSP data. Nonetheless, the velocity profile comparison is similar for both ASP and FSP data.

6.2 Parallel flows in the far SOL

LIM has been used to simulate CIII plume emission generated in the far SOL. The non-jet background/sputter source model is employed for these cases, since in this region the recycling-induced density perturbation is expected to be small (see Figure 5-16). In addition, the parallel Mach number (M_{\parallel}) is assumed to be constant over the emission volume (on field lines outside of the probe presheath). The value of M_{\parallel} inferred from simulation of the parallel plume asymmetry is therefore a volume-averaged quantity.

For conditions typical of the far SOL, the simulated CIII parallel plume extent is found to be quite sensitive to inputted values for the electron temperature. This is primarily a result of the sharp variation in the C^{+2} ionization lifetime with T_e under these conditions. Simulation studies indicate that an increase in the temperature profile of 25% can result in a reduction of the simulated CIII parallel plume extent by $\sim 50\%$. This sensitivity suggests that simulation of the CIII parallel plume extent may provide a cross-calibration for electron temperature measurements made by the scanning probe.

Asymmetries in the parallel plume extent are expected to be sensitive to parallel asymmetries of electron density and temperature in the presheath zones under conditions typical of the far SOL. n_e and T_e asymmetries in the far SOL are thought to result from the shorter connection length for field lines on the downstream side of the probe (i.e. field lines connected to the outer divertor) relative to the upstream side. As a result of the shorter connection length, cross-field particle and thermal diffusion onto these field lines cannot make up for convective particle and heat losses occurring on these field lines (which result from ion flow towards the probe), causing a reduced electron density and temperature on the downstream side of the probe. Probe measurements which illustrate the upstream/downstream temperature asymmetry are shown in Figure 6-6 – for this case the electron temperature is $\simeq 65\%$ lower on the downstream side relative to the upstream side. In principle, the parallel mean-free path of impurity ions will differ on either side of the probe due to n_e and

T_e asymmetries (since the ionization lifetime will differ), which can lead to a parallel asymmetry in the impurity emission even in the absence of a background parallel flow. However, results arising from these effects are thought to be small, since the asymmetries only occur on field lines in the probe presheath (i.e. the fraction of the emission volume over which the asymmetries exist is small). Nonetheless, parallel n_e and T_e asymmetries are included in the simulation of far SOL plume emission. Results from simulation studies indicate that the effect of including these asymmetries is a modification in the parallel plume asymmetry by $\sim 10\text{-}15\%$ (for typical values of the asymmetry, e.g. $n_{e,up}/n_{e,down} = T_{e,up}/T_{e,down} = 1.8$). This suggests that uncertainties in the plume-inferred values of M_{\parallel} resulting from the presence of parallel density and temperature asymmetries are of the same order (i.e. $\sim 10\text{-}15\%$).

Using the non-jet background/sputter source model (with $U_0 = 5$ eV and $\lambda = 1$ cm), and taking into account effects due to parallel n_e and T_e asymmetries in the probe presheath, LIM has been used to simulate a pair of experimental CIII TVC plumes generated in the far SOL plasma. These results are shown in Figures 6-7 and 6-8 (note that Figure 6-7 is the same as Figure 5-10). In the first case (Figure 6-7) the experimental plume was generated during normal field operation, while in the second case (Figure 6-8) the experimental plume was generated during reversed field operation. In both cases the main difference between experiment and simulation is the structure of the emission close to the injection, where reflections off the probe head result in the experimental emission being peaked. However, in the far field, inverse decay lengths obtained from a fit to the 1-D parallel emission profile are approximately equal for both experiment and simulation in both cases.

To obtain a match between simulation and experiment for the normal field discharge, it was necessary to increase the electron temperature profile inputted into the simulation uniformly by 25% relative to measurements from the scanning probe. In addition, for this simulation parallel n_e and T_e asymmetries in the probe presheath were both taken to be 40% (i.e. $n_{e,up}/n_{e,down} = T_{e,up}/T_{e,down} = 1.4$). For these conditions, the inferred Mach number was found to be $M_{\parallel} = 0.18$. This is significantly

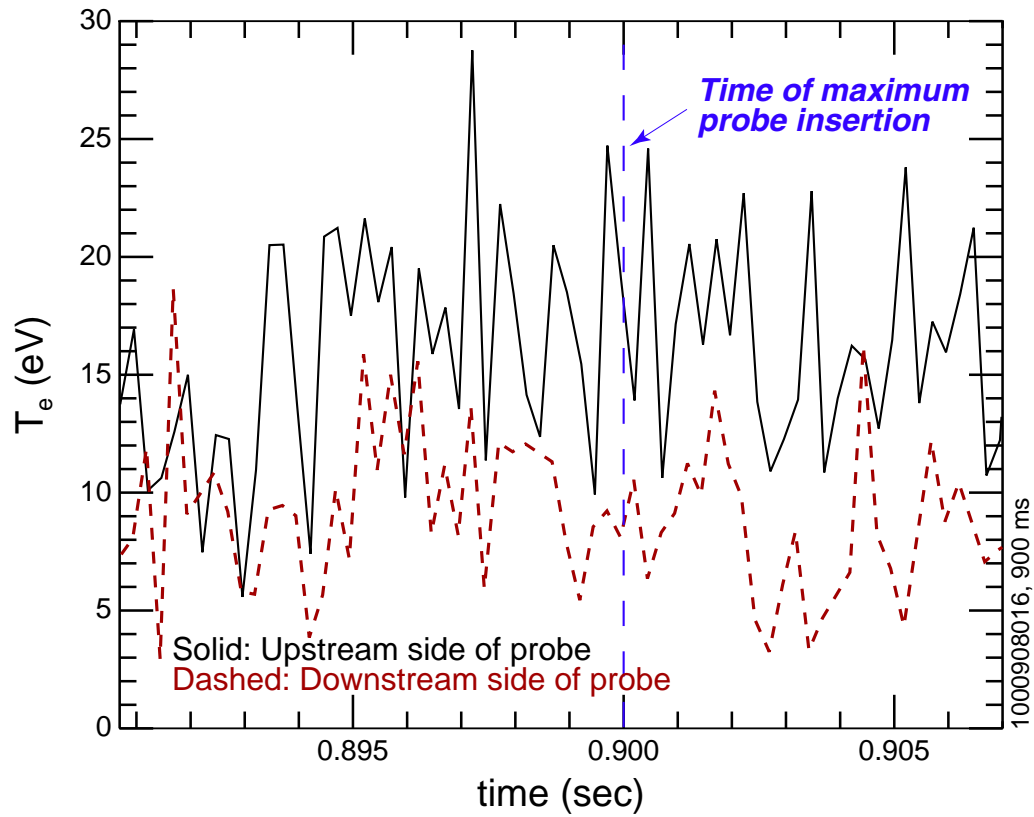


Figure 6-6: Comparison between electron temperature measurements made by the scanning probe on the upstream and downstream side of the probe head for conditions typical of the far SOL. These results indicate an asymmetry in the electron temperature along \mathbf{B} , which is due to the shorter connection length for field lines on the downstream side of the probe. This asymmetry can lead to an asymmetry in the parallel extent of the impurity emission even in the absence of a background parallel flow, and is therefore accounted for in the simulation.

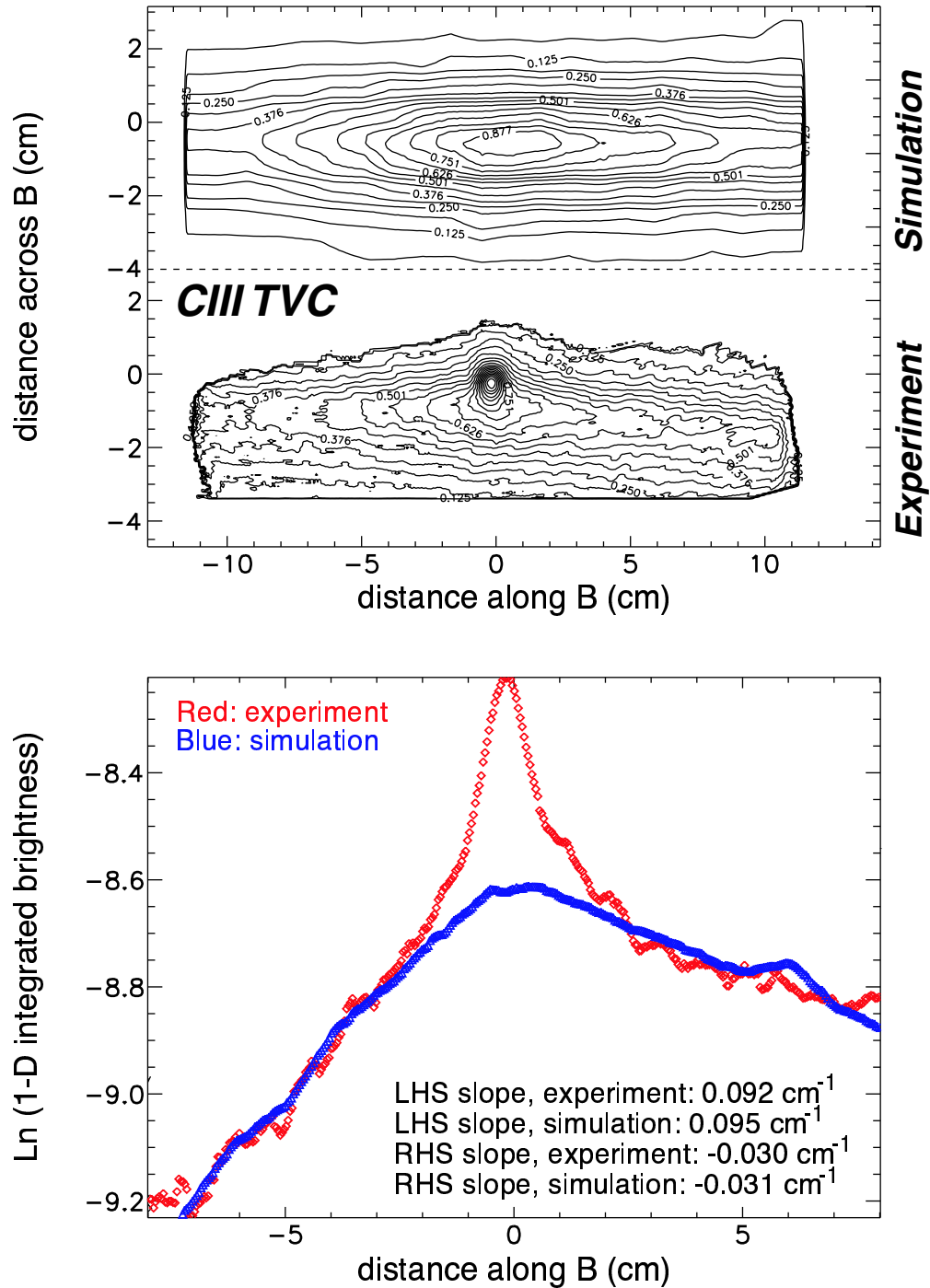


Figure 6-7: *Top panel:* Comparison between experimental and simulated 2-D CIII TVC plumes in the far SOL plasma, for normal field operation. *Bottom panel:* Comparison between 1-D parallel emission profiles for plumes shown above. Close to the injection, reflections off the probe head result in the experimental emission being peaked. However in the far field inverse decay lengths are approximately equal for experiment and simulation. The parallel Mach number inferred from the plume simulation in this case is $M_{\parallel} = 0.18$.

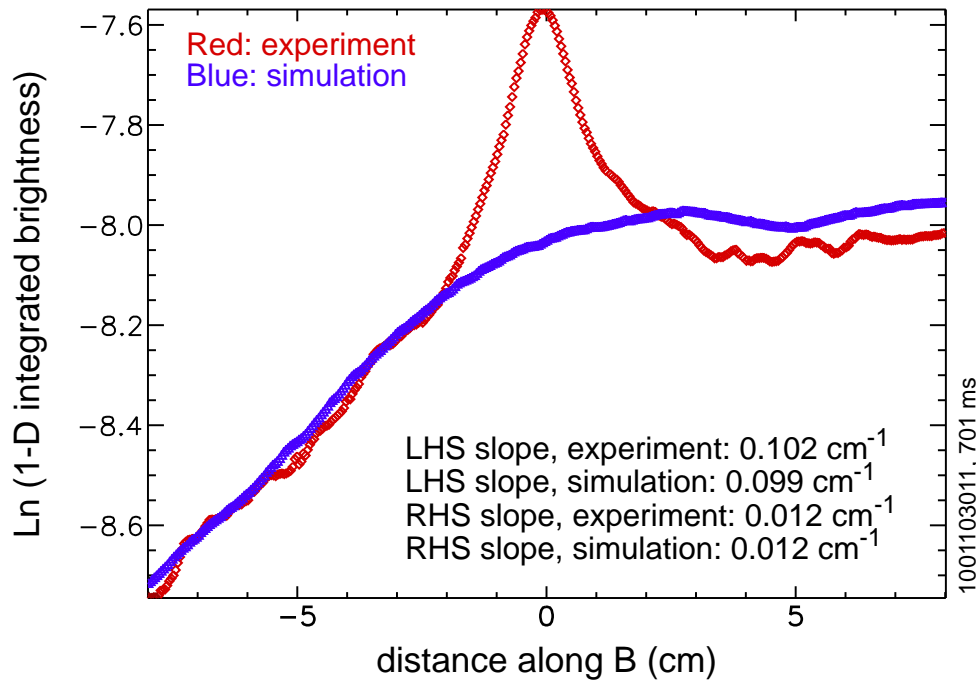
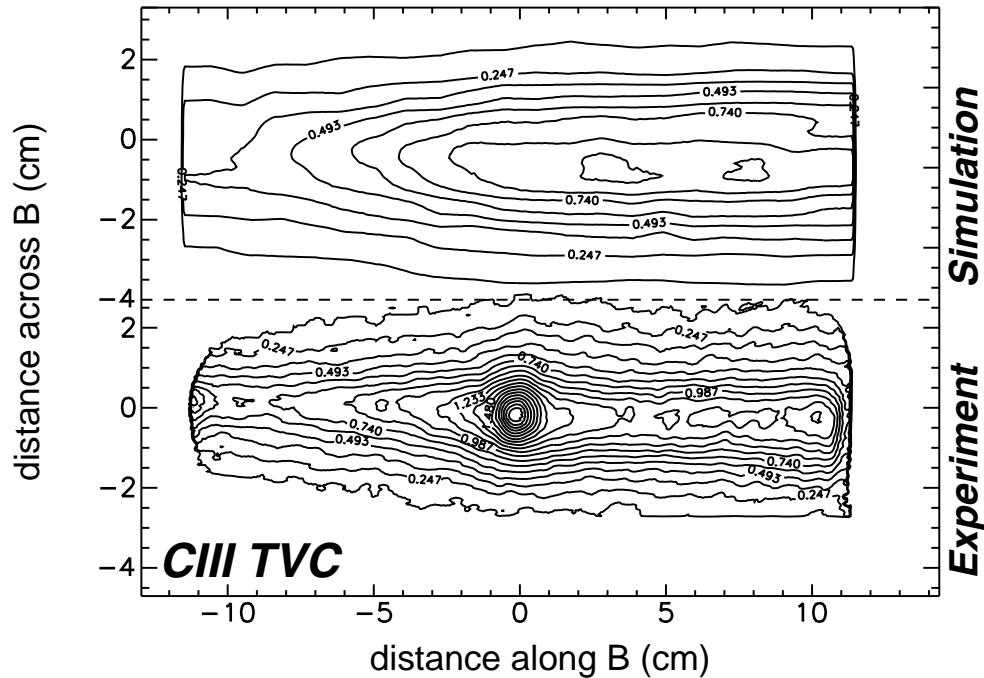


Figure 6-8: *Top panel:* Comparison between experimental and simulated 2-D CIII TVC plumes in the far SOL plasma, for reversed field operation. *Bottom panel:* Comparison between 1-D parallel emission profiles for plumes shown above. Close to the injection, reflections off the probe head result in the experimental emission being peaked. However in the far field inverse decay lengths are approximately equal for experiment and simulation. The parallel Mach number inferred from the plume simulation in this case is $M_{\parallel} = 0.21$.

lower than the value measured by the scanning probe for this discharge ($= 0.46$; calculated using Equation 2.1).

To simulate the experimental plume generated during reversed field operation, it was necessary to decrease the electron temperature profile inputted into the simulation uniformly by 25% relative to measurements from the scanning probe. In addition, for this simulation parallel n_e and T_e asymmetries in the probe presheath were both taken to be 100% (i.e. $n_{e,up}/n_{e,down} = T_{e,up}/T_{e,down} = 2$). The larger parallel asymmetry required in this case relative to the normal field simulation is consistent with the larger parallel asymmetry measured by the scanning probe in the reversed field discharge relative to the normal field discharge. For these conditions, the inferred Mach number was found to be $M_{\parallel} = 0.21$. This is again significantly lower than the value measured by the scanning probe for this discharge ($= 0.59$; calculated using Equation 2.1).

One possible explanation for the discrepancy between plume-inferred and probe-inferred values of M_{\parallel} is the small field line connection length on the downstream side of the scanning probe. Equation 2.1 is based on a probe presheath model in which the field line connection lengths upstream and downstream are both much larger than the presheath connection length (i.e. the parallel distance over which cross-field diffusion into the flux tube balances parallel transport to the probe surface). On the upstream side of the probe this criterion is always met, whereas on the downstream side of the probe this criterion is not satisfied in the far SOL. A consequence of this result is lower electron density on the downstream side, which leads to a larger value for the probe-inferred Mach number (since this quantity is related to the upstream/downstream density ratio – see Equation 2.1). Thus, it is possible that low density on the downstream side of the probe, and not a strong parallel flow, is responsible for the large values of M_{\parallel} inferred from the probe measurements. This suggests that it may be necessary to use a more sophisticated Mach probe theory, i.e. one which corrects for effects of small field line connection length relative to presheath connection length (such as [24]), in the analysis of probe data from far SOL plasmas.

Another possible explanation for the discrepancy is that the plume-inferred results for M_{\parallel} are volume-averaged while the probe-inferred results are localized. However,

the plumes exist over a volume which is further out in the SOL than the probe measurements. Therefore, if the values of M_{\parallel} inferred from the plumes are smaller than the values inferred from the probe, then for these results to be consistent the parallel Mach number must decrease with SOL depth. This is inconsistent with general probe results (e.g. see Figure 3-21), which indicate that the Mach number inferred from Equation 2.1 increases further out in the SOL. Differences between plume and probe results cannot be explained as the result of volume-averaging.

The observations presented thus far suggest that effects arising from small field line connection length on the downstream side of the probe result in a corruption of the probe measurements. However, these effects are expected to be similar in both the normal and reversed field discharges. Thus the measured difference in parallel Mach number (ΔM_{\parallel}) inferred from both the plume and probe results might be in better agreement. Unfortunately, the ΔM_{\parallel} value measured by the probe is also larger than that measured by the plume ($\Delta M_{\parallel} = 0.13$ and 0.03 for the probe and plume, respectively). Therefore, either the assumption that this value is independent of connection length effects is incorrect, or there is another cause for the discrepancy between plume and probe results. The latter may be a result of measurement errors by the probe and/or the use of an inappropriate model for calculating M_{\parallel} from the probe data, again suggesting that a more sophisticated Mach probe theory (such as [24]) may be necessary. Discrepancies may also result from using an inappropriate parallel flow model in the simulation, which suggests that a more sophisticated model of background plasma flows in the far SOL may be necessary in LIM.

Nonetheless, the value for the plume-inferred parallel Mach number is found to be larger in the reversed field discharge relative to the normal field discharge, which is consistent with general probe results. In addition, the plume results suggest that probe data obtained in the far SOL may be corrupted, indicating that plumes have the potential to serve as a useful diagnostic for cross-calibrating Mach probe measurements in this region. These results also imply that, if anything, the (FSP) Mach probe over-estimates the flow towards the divertor in the far SOL, which strengthens the argument for the main-chamber recycling view of scrape-off layer particle flow in

Alcator C-Mod [38].

Chapter 7

Summary

This chapter provides a summary of results from the gas injection plume experiments. This includes a brief description of the emission structure dependencies on background plasma conditions, the characterization of effects arising from probe insertion into the scrape-off layer plasma, and an assessment of the utility of the impurity dispersal plumes as an edge flow diagnostic. A discussion of possible improvements to the data collection system and of further work which is necessary for development of the plume physics model are also presented.

7.1 Results

7.1.1 Diagnostics

A unique system has been developed for studying impurity transport in the scrape-off layer (SOL) of the Alcator C-Mod tokamak, in which impurity gas is injected through the end of a reciprocating fast-scanning probe. More precisely, gas is injected through the end of a capillary located in the center of the probe body and connected to a nearby gas plenum. An inertial valve present inside the capillary provides localization of the gas deposition near the probe's end-of-stroke, while the amount of gas injected is determined primarily by the plenum pressure. For typical impurity plume experiments, gas deposition occurs over a period of 8-10 ms, with \simeq

5×10^{16} molecules of deuterated ethylene (C_2D_4) injected per probe scan.

The resultant impurity emission is imaged from two near-perpendicular views, one from the top of the machine (TVC) and one from the side (SVC). These views are obtained using coherent fiber bundles optically coupled to gated, intensified CCD cameras through beam-splitters, allowing C^{+1} (CII) and C^{+2} (CIII) emission to be captured simultaneously at each view location. In addition, the timing between the cameras is synchronized, allowing images from each view location to be captured simultaneously using a single video frame-grabber board.

A series of calibrations and alignments have been performed to convert the image data to units of brightness and to map this data to field-aligned coordinates. These transformations make it easier to differentiate between parallel and cross-field asymmetries in the emission structure (which may be related to parallel and cross-field transport coefficients), as well as allow a more direct comparison of experimental data with simulation results, generated using a modified version of the LIM impurity transport code.

7.1.2 Overview of impurity dispersal results

Impurity plume data have been collected from a variety of plasma discharges, over a variety of background plasma conditions. In general both CII and CIII emission exhibit an elongation along \mathbf{B} , which is expected since ion transport is unconstrained in this direction. However, the aspect ratio of the plumes is smaller than expected as a result of the cross-field plume widths being larger than expected – expected values for the cross-field widths being $\lesssim 2$ mm for CII emission and $\lesssim 5$ mm for CIII emission, estimated using the dimensions of the gas injection capillary and typical values for the cross-field diffusivity in the SOL. In most cases both the CII and CIII cross-field plume widths are comparable to the cross-field probe size, suggesting that emission resulting from sputtering of deposited carbon off the probe surface may contribute significantly to the overall plume structure. Direct evidence for the existence of a sputter source for the plumes is given in the form of a plume generated without gas injection (following a probe scan with gas injection). The measured brightness of the resultant emission

suggests that the contribution from sputtering can be important even during gas injection. Based on these findings, a sputter source model for the impurity dispersal has been developed in LIM. Simulation results indicate that the cross-field extent of the plume emission is indeed determined by the probe head geometry, consistent with the experimental observations (more discussion in section 7.1.3).

Plume emission structure is observed to depend on local values for the electron density and temperature, as well as the location of plume formation in the scrape-off layer. For example, the majority of CIII plumes generated in the near SOL exhibit a parallel asymmetry indicative of flow away from the divertor (i.e. *reversed flow*), while the majority of CII and CIII plumes generated in the far SOL exhibit a parallel asymmetry indicative of flow towards the divertor. However, the direction of CIII plume asymmetry in the near SOL is found to be uncorrelated with the direction of background plasma flow measured by the scanning probe, suggesting that these plume asymmetries may be caused by other physics.

Plume structure is also found to be sensitive to the plasma confinement mode, as a result of the variation in radial electric field between L-mode and H-mode. In general, the presence of a finite radial electric field at the gas injection location produces a gull-wing or boomerang in the emission structure, indicating that the magnitude of the emission boomerang angle may be related to the local value of \mathbf{E}_r . More generally, the direction of the emission boomerang may be used to determine the sign of the local radial electric field. For example, the direction of the boomerang angles for CIII plumes generated inside and outside of the Quasi-Coherent (QC) mode layer during Enhanced D_α (EDA) H-mode suggests that the QC mode exists in a region of negative radial electric field, but that outside of the mode layer $\mathbf{E}_r > 0$.

In the near SOL, CIII plumes also exhibit a jet-like feature, indicated by non-elliptical emission contours and large parallel extent relative to the ionization mean-free path. A ridge-line analysis has been employed to determine the average parallel velocity for C^{+2} ions present in the jet, and the results suggest that this velocity is comparable to the impurity ion sound speed. A possible cause for this large parallel velocity is the presence of a localized parallel electric field (E_{\parallel}) near the probe tip,

which provides directed parallel energy (away from the probe) to impurity ions formed in this region. Plausibility arguments for the existence of such an electric field have been investigated using numerical modelling (i.e. LIM – see section 7.1.3).

Finally, for CII and CIII plumes generated in both the near and far SOL, emission viewed from the SVC is observed to have a larger cross-field width than emission viewed from the TVC. From a comparison between 1-D cross-field emission profiles for the two views, the existence of a strong impurity ion drift down the probe axis is implied. A possible cause for this drift is the presence of a vertical $\mathbf{E} \times \mathbf{B}$ drift near the probe surface. This has also been investigated using LIM (see section 7.1.3).

7.1.3 Probe-induced perturbations

Differences observed between the SVC and TVC cross-field plume widths are thought to result from the existence of an $\mathbf{E} \times \mathbf{B}$ drift down the probe axis, where the electric field is caused by the presence of large gradients in the probe-induced presheath potential near the probe surface. LIM has been used to estimate the magnitude of the drift velocity necessary to explain the observed plume width differences, and results indicate that in the near SOL this velocity can be as large as 1000 m/s. However, to get the simulated plume to have a spatial extent down the probe axis which is similar to the experimental data, it is also necessary to postulate that the $\mathbf{E} \times \mathbf{B}$ drift transports bulk plasma down the probe axis. This is of course possible since $\mathbf{E} \times \mathbf{B}$ drifts affect all ion species equally. The effect is consistent with the formation of a carbon layer over a finite extent of the probe surface. However, the drift and surface layer formation models implemented in LIM are rather basic, and are not capable of exploring the influence of the resultant $\mathbf{E} \times \mathbf{B}$ flow patterns on impurity and bulk plasma transport in a self-consistent way. Instead, a simple model has been developed to account for the contribution from sputtering of carbon deposited on the probe surface to the overall plume emission, where the e-folding length (down the probe axis) for carbon sputtering is specified to provide the best match between simulation and experiment. Results indicate that this model is able to reproduce the cross-field extent of the experimental plumes in all cases. In addition, the model provides

an accurate simulation for the parallel extent of experimental emission generated in the far SOL, suggesting that in this region of the plasma a sputtering launch-energy distribution is appropriate for the carbon neutrals.

The parallel extent of experimental CIII plumes generated in the near SOL suggests the existence of a mechanism which provides directed parallel energy to impurity ions formed near the probe tip. Since coulomb collision rates between background plasma and C^{+2} ions are small in this region, this mechanism must also be collisionless. The presence of a localized parallel electric field above the probe tip, generated as a result of a localized density perturbation which arises from background ion recycling off the probe surface, is thought to be responsible. LIM has been used to investigate the magnitude of the electric field that could be generated as a result of ion recycling. Results from a perturbative analysis suggest that in the near SOL the recycling perturbation is large, leading to a parallel variation in the plasma potential which is of order the electron temperature. This variation is consistent with the requirement that C^{+2} ions must be accelerated up to the impurity ion sound speed by the electric field in order to explain the parallel extent of the jet. However, in the far SOL the perturbation is weak, consistent with the observation of little or no jet-like behavior for plumes formed in this region. In general, since E_{\parallel} is a result of a localized density perturbation, the magnitude of the parallel electric field is thought to be related to the ionization volume for the recycling deuterium neutrals, which depends on the ionization mean-free path for these neutrals. Experimentally, the variation of the recycling perturbation strength with the ionization mean-free path is found to be strong. However, in LIM the trend is observed to be weaker, and suggests that a finite level of perturbation exists even in the far SOL. Nonetheless, the general trends are similar for experiment and simulation, indicating that the recycling perturbation is indeed a likely cause for the jet-like behavior of impurity plumes formed in the near SOL.

Results from density perturbation modelling have been incorporated back into LIM for simulation of impurity plume dispersal in the near SOL. Using parallel electric fields consistent with the magnitude of the recycling perturbation, the simulation

is able to reproduce the parallel extent of experimental CIII TVC plume emission. However there remain two unresolved issues regarding the impurity jet model. First, the structure of the parallel electric field necessary in the impurity plume simulation is peaked relative to the structure of the field implied from the recycling perturbation analysis, although for impurity ions in the far field (i.e. $\gtrsim 2$ cm away from the injection location along \mathbf{B}) the total potential variation experienced is the same for both cases. The peaked profile is necessary because the use of a broad parallel electric field in the simulation leads to the appearance of a double-slope feature in the simulated 1-D parallel emission profiles, which is not observed experimentally. Second, no mechanism has been produced which explains the parallel asymmetry observed in experimental CIII plume emission generated in the near SOL. Possible causes for this asymmetry include the existence of an asymmetric parallel electric field or a systematic error in the imaging system calibration. However, these explanations are again inconsistent with experimental observations – for example, the presence of an asymmetric E_{\parallel} in LIM also results in the appearance of a double-slope feature in the simulated 1-D parallel emission profiles. Nonetheless, unresolved issues aside, results from the impurity jet model suggest that the presence of a localized parallel electric field arising from ion recycling off the probe surface is responsible for explaining the parallel extent of CIII emission generated in the near scrape-off layer plasma.

7.1.4 Application of plumes as an edge flow diagnostic

For plumes generated in the near SOL, the localization of the recycling-induced density perturbation allows a ridge-line analysis to be used to relate the cross-field deviation of impurity ions present in the jet to the local radial electric field. Measurements of \mathbf{E}_r based on analysis of CIII TVC plume data in the near SOL have been performed for a number of ohmic L-mode discharges. These results were then compared to estimates obtained from the scanning probe from two separate calculations: the radial gradient of the inferred plasma potential profile, and the poloidal propagation velocity of edge plasma fluctuations. While the magnitude of the radial electric field inferred from the plume data is comparable to that calculated from the radial gra-

dient of the inferred plasma potential profile, there exists better agreement for both the magnitude and profile structure of \mathbf{E}_r between plume-inferred results and probe measurements of the poloidal propagation velocity of edge plasma fluctuations. This suggests that the latter technique may be a more reliable means of estimating the radial electric field from probe data.

In addition, a ridge-line analysis has been used to relate CIII plume structure to the radial electric field inside of and outside of the QC mode layer during EDA H-mode. Results confirm that the QC mode exists in a region of negative \mathbf{E}_r ($\mathbf{E}_r = -3.3$ kV/m). However, results derived from probe estimates of the inferred plasma potential profile indicate the opposite sign for the radial electric field in this case, suggesting that plumes may provide the only means of estimating \mathbf{E}_r in the QC mode layer. The plume results also indicate that the radial electric field gradient near the mode layer is large, of order 3 MV/m².

In the far SOL, collisional coupling between background plasma and C⁺² ions is strong, suggesting that parallel asymmetries in the CIII plume emission can be used to estimate values for the parallel flow velocity. Numerical modelling has been used to extract volume-averaged values of the parallel Mach number (M_{\parallel}) from plume emission data generated in the far SOL for both a normal and reversed field discharge, and these values have been compared to the scanning probe measurements. Plume results indicate that the Mach number is larger in reversed field than in normal field, which is consistent with the probe measurements. However, in both normal and reversed field the values of M_{\parallel} inferred from the plume structure are much smaller than values inferred from the probe data. Part of this discrepancy results from a corruption of the probe data in the far SOL, caused by short field line connection length on the downstream side of the probe. However, there are additional difference between the measurements which remain unexplained. Nonetheless, the results suggest that plumes may have the potential to serve as a useful diagnostic for cross-calibrating scanning probe measurements of M_{\parallel} in the far scrape-off layer.

7.2 Future Work

Although impurity dispersal plumes have been used to gain an understanding of a variety of interesting phenomena, there remains a great deal of work that could be done to improve the diagnostic capabilities of the plumes. These include upgrades to both the data collection system and the numerical modelling tools. Each of these items is discussed below.

7.2.1 Diagnostic upgrades

Using data from the top view of the probe, the parallel extent of experimental CIII emission generated in the near SOL has been simulated by including the presence of a localized parallel electric field in the modelling. However, to determine the cross-field transport of the impurity ions in this case (e.g. resulting from the presence of a background radial electric field), it was necessary to assume that the contribution of emission from impurity ions in the jet dominates the total image signal. From a toroidal view of the probe (i.e. a view in the R - Z plane), this information could in principle be obtained more directly. For example, using this view it would be simple to determine if impurity ions in the jet were drifting poloidally in the flux surface, as a result of a local radial electric field, or if these ions were simply rotating toroidally. The latter motion is thought to occur for background plasma ions in the near SOL, for which the poloidal components of the $\mathbf{E} \times \mathbf{B}$ drift velocity and the parallel velocity are found to approximately cancel [36]. From this view the distribution of impurity ions inside and outside of the jet emission region could also be readily determined.

A toroidal view would also provide information on the extent of the vertical drift of the impurity ions down the probe axis (i.e. the magnitude of the probe-induced $\mathbf{E} \times \mathbf{B}$ drift). To determine the extent to which this drift is responsible for transporting bulk plasma ions down the probe axis, it would be ideal to have an additional Langmuir probe located at a position further down the probe body.

7.2.2 Plume physics modelling

A self-consistent calculation of the probe recycling perturbation is necessary to determine more accurately the effect of this perturbation on the impurity plume emission. This involves determining the converged solution for the parallel density and electric field variation on all field lines outside of the probe presheath, and the ability to implement this full 3-D solution in the numerical simulation. A more accurate representation of the probe head geometry may also be useful for this analysis.

A self-consistent model for carbon deposition on the probe surface is also necessary to develop a better understanding of the overall plume structure. In this analysis, the 3-D structure of the circulating $\mathbf{E} \times \mathbf{B}$ flow pattern which results from the structure of the probe-induced presheath potential fields would also be included, as would the effects of this flow on background plasma conditions. This model would have the potential to provide an accurate simulation of the observed differences between experimental SVC and TVC cross-field plume widths. This model would also provide constraints for the contributions of gas injection and sputtering to the overall plume emission, allowing for a direct calculation of the jet and non-jet emission component fractions, and possibly producing a more accurate simulation of the 2-D emission structure of experimental CIII plumes generated in the near SOL.

Finally, it is also necessary to develop models which provide more accurate explanations for parallel asymmetries present in the experimental CIII emission. For example, the implementation of a more sophisticated parallel flow model in LIM may produce better agreement between the probe and plume results in the far SOL (assuming that corruption of the probe data may also be accounted for), and therefore the development of such a model should be undertaken. Conversely, there is currently no explanation for the appearance of parallel asymmetries in experimental CIII plumes generated in the near SOL. Some effort therefore needs to be spent developing modelling tools which can be used to investigate possible causes.

Bibliography

- [1] International Energy Agency. *World Energy Outlook 2002*. OECD, Paris, France, 2002.
- [2] Andover Corporation, 4 Commercial Drive, Salem, NH 03079.
- [3] N. Asakura, S. Sakurai, N. Hosogane, M. Shimada, K. Itami, Y. Koide, and O. Naito. Heat and particle transport of sol and divertor plasmas in the w shaped divertor on jt-60u. *Nuclear Fusion*, 39(11Y):1983–1994, 1999.
- [4] J.A. Boedo, D. Rudakov, R. Moyer, S. Krasheninnikov, D. Whyte, G. McKee, G. Tynan, M. Schaffer, P. Stangeby, P. West, S. Allen, T. Evans, R. Fonck, E. Hollmann, A. Leonard, A. Mahdavi, G. Porter, M. Tillack, and G. Antar. Transport by intermittent convection in the boundary of the diii-d tokamak. *Physics of Plasmas*, 8(11):4826–4833, 2001.
- [5] J. Bohdansky. Sputtering. In R.A. Langley et al., editors, *Data Compendium for Plasma-Surface Interactions*, Nuclear Fusion Special Issue, pages 61–72. IAEA, Vienna, 1984.
- [6] D. Bohm. Minimum ionic kinetic energy for a stable sheath. In A. Guthrie and R.K. Wakerling, editors, *The Characteristics of Electrical Discharges in Magnetic Fields*, chapter 3. McGraw-Hill, Inc., New York, NY, 1949.
- [7] P.G. Carolan and V.A. Piotrowicz. The behaviour of impurities out of coronal equilibrium. *Plasma Physics*, 25(10):1065–1086, 1983.
- [8] Cat I Manufacturing, P.O. Box 208, 840 Schneider Drive, South Elgin, IL 60177.

- [9] J.P. Coad, N. Bekris, J.D. Elder, S.K. Erents, D.E. Hole, K.D. Lawson, G.F. Matthews, R.-D. Penzhorn, and P.C. Stangeby. Erosion/deposition issues at jet. *Journal of Nuclear Materials*, 290–293:224–230, 2001.
- [10] T.J. Dolan. *Fusion Research: Volume III - Technology*. Permagon Press, New York, NY, 1982.
- [11] Edmund Industrial Optics, 101 East Gloucester Pike, Barrington, NJ 08007.
- [12] J.P. Freidberg. *Ideal Magnetohydrodynamics*. Plenum Press, New York, NY, 1987.
- [13] J. Gafert, K. Behringer, D. Coster, C. Dorn, A. Kallenbach, R. Schneider, U. Schumacher, and ASDEX Upgrade Team. Spectroscopic investigation of the dynamics of ions and neutrals in the asdex upgrade divertor ii. *Journal of Nuclear Materials*, 266–269:365–369, 1999.
- [14] S. Gangadhara, B. LaBombard, and C. MacLatchy. Impurity transport experiments in the edge plasma of alcator c-mod using gas injection plumes. *Journal of Nuclear Materials*, 290–293:598–603, 2001.
- [15] D.T. Garnier, E.S. Marmor, C.L. Fiore, J.A. Goetz, S.N. Golovato, M.J. Greenwald, A.E. Hubbard, J.H. Irby, P.J. O’Shea, J.J. Ramos, J.E. Rice, J.M. Schachter, P.C. Stek, Y. Takase, R.L. Watterson, S.M. Wolfe, and A. Martynov. Formation and evolution of internal transport barriers in alcator c-mod. In *Proceedings of the 16th IAEA Fusion Energy Conference*, 1996.
- [16] J.A. Goetz, B. LaBombard, B. Lipschultz, C.S. Pitcher, J.L. Terry, C. Boswell, S. Gangadhara, D. Pappas, J. Weaver, B. Welch, R.L. Boivin, P. Bonoli, C. Fiore, R. Granetz, M. Greenwald, A. Hubbard, I. Hutchinson, J. Irby, E. Marmor, D. Mossessian, M. Porkolab, J. Rice, W.L. Rowan, G. Schilling, J. Snipes, Y. Takase, S. Wolfe, and S. Wukitch. High confinement dissipative divertor operation on alcator c-mod. *Physics of Plasmas*, 6(5):1899–1906, 1999.

- [17] M. Greenwald, R. Boivin, P. Bonoli, R. Budny, C. Fiore, J. Goetz, R. Granetz, A. Hubbard, I. Hutchinson, J. Irby, B. LaBombard, Y. Lin, B. Lipschultz, E. Marmor, A. Mazurenko, D. Mossessian, T. Sunn Pedersen, C.S. Pitcher, M. Porkolab, J. Rice, W. Rowan, J. Snipes, G. Schilling, Y. Takase, J. Terry, S. Wolfe, J. Weaver, B. Welch, and S. Wukitch. Characterization of enhanced d_α high-confinement modes in alcator c-mod. *Physics of Plasmas*, 6(5):1943–1949, 1999.
- [18] M. Greenwald, R.L. Boivin, F. Bombarda, P.T. Bonoli, C.L. Fiore, D. Garnier, J.A. Goetz, S.N. Golovato, M.A. Graf, R.S. Granetz, S. Horne, A. Hubbard, I.H. Hutchinson, J.H. Irby, B. LaBombard, B. Lipschultz, E.S. Marmor, M.J. May, G.M. McCracken, P. O’Shea, J.E. Rice, J. Schachter, J.A. Snipes, P.C. Stek, Y. Takase, J.L. Terry, Y. Wang, R. Watterson, B. Welch, and S.M. Wolfe. H-mode confinement in alcator c-mod. *Nuclear Fusion*, 37(6):793–807, 1997.
- [19] M. Greenwald, J.L. Terry, S.M. Wolfe, S. Ejima, M.G. Bell, S.M. Kaye, and G.H. Neilson. A new look at density limits in tokamaks. *Nuclear Fusion*, 28(12):2199–2207, 1988.
- [20] M.M. Guterman and Z.H. Nitecki. *Differential Equations: A First Course*. Saunders College Publishing, New York, NY, 1988.
- [21] N.C. Hawkes, D.V. Bartlett, D.J. Campbell, N. Deliyannis, R.M. Giannella, P.J. Lomas, N.J. Peacock, L. Porte, A. Rookes, and P.R. Thomas. Evolution of edge electric field at the l to h transition in jet. *Plasma Physics and Controlled Fusion*, 38(8):1261–1266, 1996.
- [22] J.D. Huba. Nrl plasma formulary. Technical report, Naval Research Laboratory, Washington, DC, 1994.
- [23] I.H. Hutchinson. Ion collection by probes in strong magnetic fields with plasma flow. *Physical Review A*, 37(11):4358–4366, 1988.
- [24] I.H. Hutchinson. The connected presheath: One-dimensional models of neighboring objects in magnetized plasmas. *Physics of Fluids B*, 3(3):847–856, 1991.

- [25] Interactive Data Language (IDL), Research Systems Inc., 4990 Pearl East Circle, Boulder, CO 80301.
- [26] R.C. Isler, N.H. Brooks, W.P. West, A.W. Leonard, G.R. McKee, and G.D. Porter. Spectroscopic analysis of normal and reversed ion flows in the diiii-d divertor. *Physics of Plasmas*, 6(2):541–549, 1999.
- [27] R.C. Isler, N.H. Brooks, W.P. West, A.W. Leonard, G.R. McKee, and G.D. Porter. Spectroscopic measurements of impurity temperatures and parallel ion flows in the diiii-d divertor. *Journal of Nuclear Materials*, 266–269:376–379, 1999.
- [28] D. Jablonski. *Local Gas Injection as a Scrape-off Layer Diagnostic on the Alcator C-Mod Tokamak*. PhD thesis, M.I.T., 1996.
- [29] R.K. Janev, W.D. Langer, K. Evans Jr, and D.E. Post Jr. *Elementary Processes in Hydrogen-Helium Plasmas*. Springer-Verlag, New York, NY, 1987.
- [30] R.K. Janev, D.E. Post, W.D. Langer, K. Evans, D.B. Heifetz, and J.C. Weisheit. Survey of atomic processes in edge plasmas. *Journal of Nuclear Materials*, 121:10–16, 1984.
- [31] M.V. Klein. *Optics*. John Wiley & Sons, New York, NY, 1970.
- [32] M.V. Klein. *Optics*, pages 124–125. John Wiley & Sons, New York, NY, 1970.
- [33] B. LaBombard. An interpretation of fluctuation induced transport derived from electrostatic probe measurements. *Physics of Plasmas*, 9(4):1300–1311, 2002.
- [34] B. LaBombard, R.L. Boivin, M. Greenwald, J. Hughes, B. Lipschultz, D. Mossessian, C.S. Pitcher, J.L. Terry, and S.J. Zweben. Particle transport in the scrape-off layer and its relationship to discharge density limit in alcator c-mod. *Physics of Plasmas*, 8(5):2107–2117, 2001.
- [35] B. LaBombard, S. Gangadhara, B. Lipschultz, S. Lisgo, D.A. Pappas, C.S. Pitcher, P.C. Stangeby, and Terry J. A novel tracer-gas injection system for

- scrape-off layer impurity transport and screening experiments. *Journal of Nuclear Materials*, 266–269:571–576, 1999.
- [36] B. LaBombard, S. Gangadhara, B. Lipschultz, and C.S. Pitcher. Toroidal rotation as an explanation for plasma flow observations in the alcator c-mod scrape-off layer. *Journal of Nuclear Materials*, 2003. To be published.
- [37] B. LaBombard, J.A. Goetz, I. Hutchinson, D. Jablonski, J. Kesner, C. Kurz, B. Lipschultz, G.M. McCracken, A. Niemczewski, J. Terry, A. Allen, R.L. Boivin, F. Bombarda, P. Bonoli, C. Christensen, C. Fiore, D. Garnier, S. Golovato, R. Granetz, M. Greenwald, S. Horne, A. Hubbard, J. Irby, D. Lo, D. Lumma, E. Marmor, M. May, A. Mazurenko, R. Nachtrieb, H. Ohkawa, P. O’Shea, M. Porkolab, J. Reardon, J. Rice, J. Rost, J. Schachter, J. Snipes, J. Sorci, P. Stek, Y. Takase, Y. Wang, R. Watterson, J. Weaver, B. Welch, and S. Wolfe. Experimental investigation of transport phenomena in the scrape-off layer and divertor. *Journal of Nuclear Materials*, 241–243:149–166, 1997.
- [38] B. LaBombard, M.V. Umansky, R.L. Boivin, J.A. Goetz, J. Hughes, B. Lipschultz, D. Mossessian, C.S. Pitcher, J.L. Terry, and Alcator Group. Cross-field plasma transport and main-chamber recycling in diverted plasmas on alcator c-mod. *Nuclear Fusion*, 40(12):2041–2060, 2000.
- [39] B. LaBombard, private communication.
- [40] B. LaBombard, private communication.
- [41] B. LaBombard. An algorithm to determine the intersection point of a light ray with a plane. Located in `/user10/labombard/edge/modelling/`.
- [42] Labsphere Inc., P.O. Box 78, North Sutton, NH 03260.
- [43] L.L. Lao, H. St. John, and R.D. Stambaugh. Reconstruction of current profile parameters and plasma shapes in tokamaks. *Nuclear Fusion*, 25(11):1611–1622, 1985.

- [44] Larson Electronic Glass, 2840 Bay Road, Redwood City, CA 94064.
- [45] C. MacLatchy, B. LaBombard, and S. Gangadhara. 3-d reconstruction of ionised gas plumes in alcator c-mod. *Bulletin of the American Physical Society*, 44(7):209, 1999.
- [46] Maier Photonics Inc., P.O. Box 890, Lincoln Avenue, Manchester Center, VT 05255.
- [47] Matrox Electronic Systems Ltd., 1055, boul. St-Regis, Dorval (Quebec), Canada H9P 2T4.
- [48] G.F. Matthews, D.N. Buchenauer, D.N. Hill, M.A. Mahdavi, M. Rensink, and P.C. Stangeby. Impurity transport at the diii-d divertor strike points. In *Proceedings of the 18th European Conference on Controlled Fusion and Plasma Physics, Volume III*, pages 229–232, 1990.
- [49] G.M. McCracken, U. Samm, S.J. Fielding, G.F. Matthews, R.A. Pitts, C.S. Pitcher, D. Gray, Y.T. Lie, R.A. Moyer, G. Bertschinger, A. Pospieszczyk, D. Rusbuldt, P.C. Stangeby, B. Schweer, and D. Elder. A study of impurity transport in the plasma boundary of textor using gas puffing. *Journal of Nuclear Materials*, 176–177:191–196, 1990.
- [50] M.A. Meier, R.D. Bengtson, G.A. Hallock, and A.J. Wootton. Adiabatic electron thermal pressure fluctuations in tokamak plasmas. *Physical Review Letters*, 87(8):085003, 2001.
- [51] H. Meister, A. Kallenbach, A.G. Peeters, A. Kendl, J. Hobirk, S.D. Pinches, and ASDEX Upgrade Team. Measurement of poloidal flow, radial electric field and $\mathbf{E} \times \mathbf{B}$ shearing rates at asdex upgrade. *Nuclear Fusion*, 41(11):1633–1644, 2001.
- [52] Meridian Technologies Inc., 700 Elmont Road, Elmont, NY 11003.
- [53] C.S. Pitcher, J.A. Goetz, B. LaBombard, B. Lipschultz, J.L. Weaver, and B.L. Welch. The role of friction in sol pressure balance in alcator c-mod. *Journal of Nuclear Materials*, 266–269:1009–1014, 1999.

- [54] C.S. Pitcher, P.C. Stangeby, D.H.J. Goodall, G.F. Matthews, and G.M. McCracken. Carbon impurity transport around limiters in the dte tokamak. *Journal of Nuclear Materials*, 162–164:337–342, 1989.
- [55] J.E. Rice, M. Greenwald, I.H. Hutchinson, E.S. Marmor, Y. Takase, S.M. Wolfe, and F. Bombarda. Observations of central toroidal rotation in icrf heated alcator c-mod plasmas. *Nuclear Fusion*, 38(1):75–85, 1998.
- [56] J. Roth, E. Vietzke, and A.A. Haasz. Erosion of graphite due to particle impact. *Atomic and Plasma Material Interaction Data for Fusion*, 1:63–78, 1991.
- [57] RTV 108 silicone rubber adhesive sealant, General Electric Silicones, Waterford, NY 12188.
- [58] Schott Fiber Optics, 122 Charlton Street, Southbridge, MA 01550.
- [59] J.A. Snipes, B. LaBombard, M. Greenwald, I.H. Hutchinson, J. Irby, Y. Lin, A. Mazurenko, and M. Porkolab. The quasi-coherent signature of enhanced d_α h-mode in alcator c-mod. *Plasma Physics and Controlled Fusion*, 43(4):L23–L30, 2001.
- [60] M.R. Spiegel. *Theory and Problems of Advanced Mathematics for Engineers and Scientists*, chapter 4. Schaum’s Outline Series. McGraw-Hill, Inc., New York, NY, 21 edition, 1992.
- [61] L. Spitzer. *Physics of Fully Ionized Gases*, chapter 5. Interscience Publishers, Inc., New York, NY, 1956.
- [62] P.C. Stangeby. *The Plasma Boundary of Magnetic Fusion Devices*, pages 298–303. Institute of Physics Publishing, Philadelphia, PA, 2000.
- [63] P.C. Stangeby. *The Plasma Boundary of Magnetic Fusion Devices*, pages 542–543. Institute of Physics Publishing, Philadelphia, PA, 2000.
- [64] P.C. Stangeby. *The Plasma Boundary of Magnetic Fusion Devices*, pages 187–192. Institute of Physics Publishing, Philadelphia, PA, 2000.

- [65] P.C. Stangeby, C. Farrell, S. Hoskins, and L. Wood. Monte carlo modelling of impurity ion transport for a limiter source/sink. *Nuclear Fusion*, 28(11):1945–1962, 1988.
- [66] J.A. Stillerman, T.W. Fredian, K.A. Klare, and G. Manduchi. Mdsplus data acquisition system [for pulsed experiments]. *Review of Scientific Instruments*, 68(1):939–942, 1997.
- [67] J.A. Stillerman. Software development for the plume imaging system.
- [68] J.C. Strikwerda. *Finite Difference Schemes and Partial Differential Equations*, pages 1–7. Chapman & Hall, New York, NY, 1989.
- [69] H.P. Summers. Atomic data and analysis structure (adas). <http://adas.phys.strath.ac.uk/>.
- [70] H. Van Goubergen, R.R. Weynants, S. Jachmich, M. Van Schoor, G. Van Oost, and E. Desoppere. A 1d fluid model for the measurement of perpendicular flow in strongly magnetized plasmas. *Plasma Physics and Controlled Fusion*, 41(6):L17–L22, 1999.
- [71] J.L. Weaver. The development of a reciprocating langmuir probe system for alcator c-mod. B.S. Thesis, 1992. Department of Physics, M.I.T.
- [72] F. Weschenfelder, J. Winter, U. Kögler, H.G. Esser, V. Philipps, A. Pospieszczyk, B. Schweer, J. von Seggern, M.Z. Tokar', and P. Wienhold. Investigation of transport processes close to limiter surfaces in textor-94. *Plasma Physics and Controlled Fusion*, 38(12A):A311–A323, 1996.
- [73] A.J. Wootton. Edge turbulence. *Journal of Nuclear Materials*, 176–177:77–88, 1990.
- [74] C.R. Wylie and L.C. Barrett. *Advanced Engineering Mathematics*, chapter 10. McGraw-Hill, Inc., New York, NY, 1982.
- [75] Xybion Systems Inc., 8380 Miralani Drive, San Diego, CA 92126.

- [76] S.J. Zweben and D.P. Stotler. Edge turbulence imaging in the alcator c-mod tokamak. *Physics of Plasmas*, 9(5):1981–1989, 2002.